

Nano-scale 4D mapping by Scanning Transmission X-ray Microscop

Nano-scale 4D mapping by Scanning Transmission X-ray Microscopy

By

Juan Wu, M.Sc.

A Thesis

Submitted to the School of Graduate Studies

in Partial Fulfillment of the Requirements

for the Degree of

Doctor of Philosophy

McMaster University

© Copyright by Juan Wu, 2018

All Rights Reserved

DOCTOR OF PHILOSOPHY (2018) McMaster University

(Material Science and Engineering) Hamilton, Ontario

TITLE: Nano-scale 4D mapping by Scanning Transmission X-ray Microscopy

AUTHOR: Juan Wu, M.Sc. (Huazhong University of Science and Technology)

SUPERVISOR: Professor Adam P. Hitchcock

NUMBER OF PAGES: xxiii / 232

ABSTRACT

Proton exchange membrane fuel cells (PEMFC) are a promising green energy resource for automotive applications. The cathode is a key rate limiting component of PEMFC. Typical cathodes are composed of Pt catalyst decorated carbon support particles, mixed with a perfluorosulfonic acid (PFSA) polymer. As the proton conduction medium in the cathode, the distribution of the PFSA ionomer will affect PEMFC efficiency, Pt utilization, and degradation kinetics. Optimization of ionomer loadings and distributions is a major goal of PEMFC research.

In this thesis, Scanning transmission X-ray microscopy (STXM) has been used to measure the porosity and component distributions in 3D. Initial studies of PEMFC materials by STXM tomography have been presented. The high energy resolution of STXM collects an extra dimension of component information to be added to the 3 dimension of volume imaging. Multi chemical 3D imaging is defined as 4D imaging. To reduce the radiation damage to PFSA, the compressed sensing (CS) algorithm has been used. The results show that the total radiation damage can be reduced below the critical dose, and better reconstruction results with less measured angles are achieved using CS algorithm.

On the other side, we have tried to measure the PFSA materials by ptychography STXM tomography to improve the spatial resolution. The spatial resolution was improved from 30 nm to < 15 nm at ~ 700 eV. 4D imaging using ptychography STXM tomography is presented.

Highly porous materials with functional coatings were also characterized by soft X-ray spectro-ptycho-tomography. The sample were Al_2O_3 aerogel samples coated with ZnO or TiO_2 by atomic layer deposition (ALD). Quantitative analysis shows the ZnO ALD

coatings are non uniform. Comparisons are made to electron microscopy imaging and X-ray fluorescence analysis of the same ZnO/ Al₂O₃ aerogel material. Together the results provide useful feedback for optimization of ALD coated alumina aerogels.

ACKNOWLEDGEMENTS

Firstly, I would like to express my sincerest gratitude to my supervisor, Prof. Adam Hitchcock, for the continuous support of my Ph.D study, for his patience, motivation, and immense knowledge. He gave me excellent guidance and support throughout my thesis research. His advice on both research as well as on my career has been invaluable.

Besides, I would like to thank my supervisory committee members, Prof. Gianluigi Botton and Prof. Kathryn Grandfield, for their scientific advice and insightful comments.

Special thanks to my collaborators: Mirna Lerotic for coding development, Prof. Paul Midgley group (Cambridge University) for algorithm development, Dr Jonathan Lee and his group (Lawrence Livermore National Laboratory) for preparing excellent samples, sharing their ideas and providing support in writing papers and proposals. The completion and success of this project would not be possible without their valuable contributions.

My sincere thanks also goes to all the beamline scientists at the Canadian Light Source (CLS) and Advanced Light Source (ALS) for their technical support and assistance. I especially thank Drs Jian Wang and Jan Geilhufe for maintaining and developing STXM instrument at SM beamline at the CLS, Dr. Tolek Tyliczszak for developing and maintaining STXM instrument 11.0.2 beamline, and Dr. David Shapiro for mantaining STXM instrument 5.3.2.2 and developing ptychography beamline 5.3.2.1 at the ALS.

Thanks to all people that provide excellent help: Marcia West from McMaster University for sample preparation by microtomy, Dr. Martin Obst from Bayreuth University for tomography sample rotator development, Dr. Lukas Helfen from European Synchrotron Radiation Facility for laminography reconstruction method development, Travis Casagrande for FIB of aerogel.

Furthermore, I am grateful to all of my group members: Xiaohui Zhu, Lis Melo, Lucas Nagard, Vinod Prabu, Zhsheng Qin, Dr. Vincent Lee, Dr. Glyn Cooper. Thanks to all of your support and help during my studies.

Finally, I would like to thank my families. Thanks to my hunsband for the companionship. Thanks to my mother and mother in law who both came from China to help me. Special thanks to my little loving daughter, Ivy.

Juan Wu

TABLE OF CONTENTS

ABSTRACT	iii
ACKNOWLEDGEMENTS	v
TABLE OF CONTENTS	vii
LIST OF FIGURES	x
LIST OF TABLES	xx
LIST OF ABBREVIATIONS AND SYMBOLS	xxi
Chapter 1 Introduction	1
1.1 What is 3D/4D chemical imaging and why is it needed?	1
1.2 3D/4D imaging methods and applications	2
1.3 Proton Exchange Membrane Fuel Cells (PEMFC)	7
1.4 Previous 3D/4D imaging technique for PEMFC research.....	11
1.5 Scanning Transmission X-ray Microscopy	12
1.6 STXM 3D/4D imaging and applications	16
1.7 Research objectives	20
Chapter 2 Techniques and Principles	21
2.1 X-ray micro and nano tomography.....	21
2.2 Electron tomography	22
2.3 Scanning Transmission X-ray Microscopy (STXM) Tomography.....	24
2.4 Ptychographic X-ray computed tomography.....	26
2.5 Laminography.....	29
2.6 Cryo electron tomography (Cryo-ET)	31
2.7 Cryo STXM tomography.....	31
2.8 STXM and Near Edge X-ray Absorption Spectroscopy (NEXAFS)	32
2.9 Radiation damage and dose estimation.....	36
2.10 Tomography data analysis	39
Chapter 3 Experimental Methods.....	43
3.1 Materials and sample preparation.....	43
3.1.1 Polymer electrolyte membrane fuel cell samples	43
3.1.2 Aerogel	45
3.2 STXM Data acquisition and analysis	47

3.3	STXM Tomography	50
3.3.1	Experimental set up	50
3.3.2	Sample preparation	51
3.3.3	Data acquisition	53
3.3.4	Data analysis procedures	56
3.3.5	Data analysis procedures using Mantis	62
3.4	STXM Laminography	65
3.4.1	Experimental apparatus	65
3.4.2	Sample preparation	66
3.4.3	Data acquisition	67
3.4.4	Data analysis	69
3.5	Ptychography for Imaging, Spectroscopy and Tomography	69
3.5.1	Experimental apparatus	69
3.5.2	Sample mounting	71
3.5.3	Data acquisition and data analysis	72
3.6	Cryo STXM and cryo spectrotomography at CLS	74
3.6.1	Sample preparation	76
3.6.2	Data acquisition and analysis	77
3.7	STXM beamlines	77
Chapter 4 Optimization of Three-Dimensional (3D) Chemical Imaging by Soft X-Ray Spectro-Tomography Using a Compressed Sensing Algorithm		79
4.1	Introduction	80
4.2	Methods	81
4.3	Results	85
4.4	Discussion	92
4.5	Summary	93
Chapter 5 4D Imaging of Polymer Electrolyte Membrane Fuel Cell Catalyst Layers by Soft X-Ray Spectro-Tomography		103
5.1	Introduction	104
5.2	Materials and Methods	105
5.3	Results	109
5.4	Discussion	112
5.5	Future development	114

Chapter 6	High-Resolution Imaging of Polymer Electrolyte Membrane Fuel Cell Cathode Layers by Soft X-ray Spectro-Ptychography	133
6.1	Introduction	134
6.2	Experimental section	135
6.3	Results	138
6.4	Discussion.....	141
6.5	Conclusion.....	141
Chapter 7	4D Imaging of ZnO Coated Alumina Aerogels by Scanning Transmission X-Ray Microscopy and Ptychographic Tomography	149
7.1	Introduction	149
7.2	Materials and Methods	153
7.2.1	Samples.....	153
7.2.2	Measurements.....	153
7.2.3	Ptychographic tomography and reconstruction	154
7.2.4	Tomographic reconstruction.....	155
7.3	Results	156
7.3.1	Spectroscopy of the aerogel samples.....	156
7.3.2	Conventional STXM spectro-tomography of ZnO/Al ₂ O ₃ aerogel, sample A.....	158
7.3.3	Spectro-ptychography and spectro-ptycho-tomography of ZnO/Al ₂ O ₃ aerogel	163
7.3.4	Transmission Electron Microscopy (TEM) of ZnO/Al ₂ O ₃ Aerogel.....	174
7.4	Discussion.....	175
7.5	Summary.....	179
Chapter 8	Summary and Future Work	181
8.1	Summary.....	181
8.2	Suggestions for future research	183
8.2.1	Ambient STXM of PEMFC MEAs at the S 1s edge	183
8.2.2	Cryo STXM tomography.....	185
8.2.3	Cryo soft X-ray ptychography tomography	189
8.2.4	Other STXM 4D imaging applications.....	189
REFERENCE	191
Appendix I	List of software.....	224
Appendix II	Laminography	225

LIST OF FIGURES

Figure 1.1 (a) 1D C 1s X-ray absorption spectra, (b) 2D image, (c) 3D stack, (d) 3D chemical map, (e) 4D stack, (f) 4D chemical image of a sample consisting of polyacrylate-filled polystyrene microspheres in water inside a pulled glass capillary. The 3D stacks at each scan angle contained 23 energy images.....	3
Figure 1.2 (a) 2D projection images of a solid; (b) 3D reconstruction from the 2D images.....	4
Figure 1.3 Techniques used for 3-D and 4-D materials science versus length scale.....	4
Figure 1.4 Industrial fields of application for CT.....	6
Figure 1.5 Schematic diagram of a PEMFC.....	7
Figure 1.6 Schematic diagram of PEMFC cathode catalyst.....	10
Figure 1.7 (a) A cube of 340 nm side length of the SEM reconstruction. (b) The reconstructed Pt volume information in the same spatial area as the SEM reconstruction. (c) The superposition of (a) and (b) and visualizes the location of Pt catalyst particle volume and surface information within the porous carbon matrix.	11
Figure 1.8 SM beam line photos: (a) STXM; (b) SM beamline. SR light propagates from right to the left; (c) EPU.	15
Figure 1.9 a) Volume renderings of protein, all-Ca and hot-spot Ca of a calcifying bacterium. (b) correlation of Ca 2p and C 1s signal in cell envelope showing the aragonite-like Ca is uniformly distributed but calcite forms at hotspots. (d) slice through centre of cell, colorized by the indicated regions in Ca-organic_C space.	18
Figure 1.10 Projection images of chemically specific three dimensional datasets acquired at the O 1s edge (a–c), Fe 2p edge (d) and an overlay (e) of hydrated Acidovorax sp. strain BoFeN1 bacteria in the stage of precipitating Fe(III)-(oxyhydr)oxide. The line profile (shown in d) across the Fe-precipitate encrusted periplasm (f) shows a thickness of the crust of ~40 nm (full-width at half-maximum). I, inside cell; O, outside cell. Scale bar is 500 nm	19
Figure 2.1 Schematic illustration of different beam configurations of X-ray computed tomography facility	23

Figure 2.2 (a) Three representative orthoslices of the reconstruction of STEM tomography of a PEMFC cathode; (b) 3D-rendered volume: the blue and grey regions correspond to the Cs ⁺ -stained ionomer and to the carbon support, respectively	24
Figure 2.3 3D chemical maps in 0°, 30°, 60°, 90° degree projections extracted from reconstructed volume with different threshold.	26
Figure 2.4 Schematic of ptychography. A 60 nm coherent soft X-ray spot, focused by zone plate, is scanned over the sample in 40 nm increments.....	28
Figure 2.5 (a) CL and CT scanning geometries for the parallel-beam case. (b,c) missing wedges in CL and CT, respectively, for the missing-information angle $\Psi = 30^\circ$	30
Figure 2.6 At a temperature of 110 K, an intense, 0.2 μm beam spot was left stationary on several locations (noted with arrows) of the biological specimen for several minutes. The image at left was acquired after 10^{10} Gray exposures at these spots, no discernible difference was found compare to an initial image. The specimen was then slowly warmed up to room temperature. The smaller image at right shows the same area as the black box region in the left image after the specimen was slowly warmed up to room temperature.....	32
Figure 2.7 (a) the near edge x-ray absorption fine structure (NEXAFS) arises from electronic transitions of an inner shell electron to energy levels (orbitals in molecules, bands in solids), (b) typical spectrum, (c) O1s spectra of gas, liquid and solid water	33
Figure 2.8 schematic diagram of STXM	34
Figure 2.9 The transmitted photon intensity I_t is related to the incident photon intensity I_0 , mass absorption coefficient μ , the sample density ρ , and the sample thickness t	36
Figure 2.10 NEXAFS spectra of undamaged and soft X-ray and electron beam damaged PET. (a) C 1s edge and (b) O 1s edge.	38
Figure 2.11 Plots of the normalized optical density as a function of radiation dose for PET damaged at 284.8, 286.5, and 288.2 eV by exposure to (a) 300 eV X-rays; (b) 80 keV electrons.....	39
Figure 2.12 3D reconstruction algorithms. (a): WBP. (b): Iterative reconstruction algorithms.	41
Figure 2.13 Compressed sensing model	41

Figure 3.1 Scanning electron microscope image of a polymer electrolyte membrane fuel cell (PEMFC) membrane electrode assembly (Image supplied by Darija Susac, AFCC)	44
Figure 3.2 Cartoon of structure of model sample used to evaluate the ability of STXM tomography to measure 3D distributions and ptychographic to measure non-crystalline soft matter with improved spatial resolution.	45
Figure 3.3 aerogel sample FIB image.....	46
Figure 3.4 STXM stack process of MEA cathode sample. Image stack is measurement by STXM; stack alignment in “Zimba” or “Jacobsen”; convert to OD stack; generate component spectra; stack fit using reference spectra; ROI mask; 3D chemical maps in color map	49
Figure 3.5 (a) the STXM tomography stage mounted in ALS STXM 5.3.2.2; (b) schematic diagram of STXM tomography; (c) STXM tomography stage is composed of a stepper motor attached to a STXM sample plate. The sample is glued to the tip of a 0.8 mm diameter brass sample pin which is held in a chuck (taken from a mechanical pencil) attached to the motor shaft. STXM tomography samples: (d) TEM grid strip; (e) Luxel wet sample pin; (f) pulled glass capillary.....	50
Figure 3.6 (a) the setup for injecting water to make a Luxel tomo wet cell (ALS 11.0.2). A 1 mL syringe connected to a glass micropipette is used as a micro-injector. (b) MEA sample is mounted on the 1-side (bottom) polyimide film Luxel window, then a formvar film is added on top, which forms a closed window. (c) The tip of the glass capillary should stick into the channel of the Luxel pin to define the water path.	52
Figure 3.7 Optical images of TEM grid strip sample rotation.....	54
Figure 3.8 (a) Comparison between predicted and measured X and Z positions of a fiducial point in a STXM tomography measurement. (b) Difference in X, (c) Difference in Z.	56
Figure 3.9 STXM tomography data acquisition and analysis workflow	59
Figure 3.10 Flow diagram of 4D data analysis process in aXis2000.	60
Figure 3.11 Flow diagram of 4D data analysis process using Mantis python code	61
Figure 3.12 Mantis tomography GUI window	63
Figure 3.13 4D analysis of the polymer microsphere in carbon nanopipette sample.....	64
Figure 3.14 (a) STXM Laminography schematic diagram, (b) Laminography stage mounting in the CLS ambient STXM.	65

Figure 3.15 3D rendering from CAD images of modified Laminography sample holder	66
Figure 3.16 Comparison between predicted results and measured results laminography measurement.....	68
Figure 3.17 Schematic of ptychography. (b) computer aided drawing (CAD) rendering of the Nanosurveyor-I Instrument.....	71
Figure 3.18 ptychography sample stage. (left) 2 SiN _x windows or 2 TEM grids can be mounted. (right) grid strip mounted for tomography.	71
Figure 3.19 Diffraction pattern with 720 eV X-rays passing through the cathode.....	73
Figure 3.20 Ptychography processing interface (python script written by David Shapiro)	74
Figure 3.21 Ptychographic reconstructed data measured at 720 eV of a region consisting of the membrane and part of the cathode of a PEMFC. (a) modulus (amplitude) image, (b) phase image, (c) stxm image, (d) (I ₀ -corrected amplitude) absorption and (e) I ₀ -corrected phase image (f) I ₀ -corrected stxm image	74
Figure 3.22 (a) outside (b) inside images of the ptychography tank	75
Figure 3.23 Gatan ‘flyswatter’ sample grid. There are supplied bare and a layer of formvar was added prior to mounting microtomed MEA samples.	76
Figure 4.1 Schematic illustration of the compressed sensing tomographic reconstruction procedure.	84
Figure 4.2 WBP (left), SIRT (middle) and CS (right) electron tomography reconstructions of a Au nanoparticle sample.	85
Figure 4.3 Line intensity profiles through xz planes for (a) WBP, (b) SIRT, (c) CS tomographic reconstructions using 67, 23, and 12 projections as in Figure 2.	86
Figure 4.4 (a) C 1s and (b) F 1s spectra of the components of a model system consisting of a two layer structure; Quantitative 2D projection maps of (c) C-fiber derived from the C 1s image sequence; (d) Pt derived from the C 1s and F 1s image sequences and (e) Teflon fiber derived from the F 1s image sequence. The gray scale in (c-e) is thicknesses in nm. (f) Rescaled color composite.....	87
Figure 4.5 Slices through <i>xy</i> and <i>xz</i> planes of 3D volumes of the C-fiber component reconstructed by (a-c) WBP, (d-f) SIRT, and (g-i) CS-TV methods.	88
Figure 4.6 Isosurface renderings of C-fiber (red), Teflon TM (green), and Pt (blue) components. The surfaces were determined by Otsu automatic thresholding (Otsu	

1975) of the reconstruction volumes and are shown at 0° (left) and 90° (right) for (a-c) CS-TV reconstructions, (d-f) SIRT reconstructions and (g-i) WBP reconstructions.....	89
Figure 4.7 Optimization of the β parameter for CS-TV tomographic reconstructions.....	90
Figure 4.8 (a) C 1s spectra of the components of a sample consisting of acrylate filled polystyrene microspheres inside a carbon nanopipette. Quantitative 2D projection components maps (thicknesses in nm) of (b) acrylate, (c) polystyrene (PS) microsphere shell, and (d) the carbon nanotube pipette. (e) Color-coded composite map showing acrylate in green, PS in blue, and the carbon nanotube pipette in red.	91
Figure 4.9 Evaluation of the effect of the size of the missing wedge on SIRT and CS-TV tomographic reconstructions.	91
Figure 4.10 Line intensity profiles through selected xz planes from (a) WBP, (b) SIRT and (c) CS-TV reconstructions corresponding to the three tilt angle ranges indicated in Figure 9.....	92
Figure 4.S1 Screen shot of the tomography tab in Mantis.	97
Figure 4.S2 Comparison of (a) original image from tilt series at 0°. (b) 2D projection at 0° generated from CS reconstruction. (c) 2D projection at 0° generated from the SIRT reconstruction.	98
Figure 4.S3 CS (left) and SIRT (right) electron tomography reconstructions of a Au nanoparticle sample using all 67 acquired projections.	99
Figure 4.S4 Line intensity profiles through xz plane.	100
Figure 4.S5 Tomographic reconstructions of the STXM images at 290 eV for $\pm 90^\circ$ tilt angle ranges.	101
Figure 4.S6 Tomographic reconstructions using SIRT with a non-negativity constraint of the polystyrene (PS)	102
Figure 5.1 (a) C 1s spectrum of virgin perfluorosulfonic acid (PFSA) code A (table 2). The C 1s spectra of the carbon support and amine epoxy and polystyrene used in these studies are also plotted. (b) F 1s spectrum of undamaged perfluorosulfonic acid (PFSA) and the spectral response of carbon support in the F 1s region.....	107
Figure 5.2 Flow diagram of STXM tomography data acquisition and processing.....	108

Figure 5.3 Component maps of (a) carbon support,(b) PFSA, (c) polystyrene. (d) ionomer in cathode, derived from a stack fit of OD1 reference spectra (Fig. 1), and a constant to a C 1s stack (89 images from 278 to 324 eV), code A.....	109
Figure 5.4 (a) Average F 1s spectra of PFSA in cathode of MEA-A, tomography measurement code C , before and after 3 set spectro-tomography. Optical density image at 694 eV (b) before, and (c) after 3-set tomography.	110
Figure 5.5 2D fluorine maps of MEA-A, tomography measurement code C , from F 1s stack maps.	111
Figure 5.6 F 1s spectra of PFSA (in cathode) of sample MEA-A, tomography measurement code F	112
Figure 5.7 3D distributions of the cathode of sample MEA-A, tomography measurement code F	113
Figure 5.8 D distributions of ionomer in cathode (green) from 3-set tomography sample MEA 11-GDE, tomography measurement code G , viewed at -30°.....	114
Figure 5.S1 Tomo sample mounting.	117
Figure 5.S2 Tomography visualizaiton and sample damage check, code B.	119
Figure 5.S3 Damage evaluation (spectral, imaging) code D.	121
Figure 5.S4 Tomography visualizaiton and changes from set1 to set2 and set2 to set3 code D.	123
Figure 5.S5 Damage evaluation (spectral, imaging) code E.	124
Figure 5.S6 Tomography visualizaiton Code E.....	125
Figure 5.S7 Damage evaluation (spectral, imaging) code G.....	126
Figure 5.S8 Slices from supplemental movie.....	127
Figure 5.S9 Fluorine loss as a function of dose caused by radiaiton damage in tomography for data sets C-G.....	128
Figure 5.S10 Spatial resolution estimated from FRC of a slice for sample Code F.....	129
Figure 5.S11 2D images of ionomer map of sample MEA-11 GDE, code F.....	130
Figure 6.1 Cartoon of structure of the model sample used to evaluate the resolution improvement when using soft X-ray ptychography to measure non-crystalline soft matter.....	135
Figure 6.2 Images of the single layer region of the bilayer model sample.....	137

Figure 6.3 (a) Transmission electron microscopy (TEM) image of a fresh area of the PTFE single layer of the bilayer sample (bright field, 100 keV). (b) Fourier Ring Correlation (FRC) analysis of spatial resolution of the TEM image.....	138
Figure 6.4 Images of the two-layer region of the bilayer model sample (see Fig-1). a. STXM transmission image at 694 eV recorded using a zone plate with 60 nm outer zone width. Ptychography absorption images at b. 684 eV and c. 694 eV. d. Fluorine map obtained by taking the difference between ptychography absorption images at 694 eV (Fig. 3b) and 684 eV (Fig. 3c). e. FRC analysis of spatial resolution of the ptychography fluorine map.....	138
Figure 6.5 Ptychography absorption images of MEA cathode (white rectangle in STXM image shown in Supplemental Fig. S-3).....	139
Figure 6.6 Ptychography F 1s edge full stack (33 energy points) of the fuel cell cathode catalyst layer, analyzed using a two component SVD fit.....	140
Figure 6.7 4D imaging. Volume renderings of the 3D chemical structure of the cathode derived from a compressed sensing tomographic reconstruction of 2-energy F 1s spectro-ptycho-tomography data.s.....	140
Figure 6.8 Multiple slices from the 3D rendered volume of the two components derived from F 1s spectro-ptycho- tomography.. ..	141
Figure 6.9 FRC analysis of an yz slice of the 3D reconstruction of the ptycho-tomography PFSA component signal (Figure 8). b. F 1s spectra of the cathode region.	141
Figure 6.S1 Ptychography absorption and phase difference images	146
Figure 6.S2 STXM optical density image at 694 eV of the cathode region of a PEMFC MEA	147
Figure 7.1 (a) X-ray absorption spectra (XAS) of ZnO/Al ₂ O ₃ aerogel (sample A). (a) Zn L _{2,3} edge, converted to optical density per nm (OD1). The inset shows an expanded view of the near edge L ₃ region. (b) Al K edge, converted to optical density per nm (OD1). The inset shows an expanded view of the near edge.	157
Figure 7.2 STXM 2D chemical maps at 0° tilt angle of a ZnO/Al ₂ O ₃ aerogel (sample A). (a) Al ₂ O ₃ . (b) ZnO. (c) color coded composite map of Al ₂ O ₃ (blue), ZnO (red).	159
Figure 7.3 STXM spectro-tomography derived, 3D volume rendering of Al ₂ O ₃ (blue) and ZnO (red) in the ZnO/Al ₂ O ₃ aerogel FIB sample A	160

Figure 7.4 (a) Surface rendering of color coded composite of the ZnO (red) and Al ₂ O ₃ (blue) 3D distributions from reconstruction of STXM spectro-tomography on ZnO/Al ₂ O ₃ aerogel (sample A), in a 5*5*5 μm ³ cube from the center of Fig. 3 (e). (b) Relative elemental concentration (REC) curves of the two components derived for xy slices averaged through the z direction.	162
Figure 7.5 Ptychography absorption images of ZnO/Al ₂ O ₃ aerogel (sample B) at (a) 1010 eV, (b) 1026.8 eV. (c) ZnO chemical map (OD(1026.8 eV) – OD(1010 eV)). (d) Derived Al ₂ O ₃ chemical map (see text). (e) 4D image color composite of the two component maps, ZnO in red, Al ₂ O ₃ in blue.....	164
Figure 7.6 Check on precision of the reconstruction of the ptychographic tomography data set (sample B).	165
Figure 7.7 3D surface rendering of ZnO and Al ₂ O ₃ from ptychography of ZnO/Al ₂ O ₃ aerogel (sample B).	166
Figure 7.8 Spatial resolution estimated from Fourier Ring Correlation (FRC) of the ZnO and Al ₂ O ₃ ptychography maps (Figs. 5c and 5d). (sample B).	167
Figure 7.9 Histogram of the thickness distribution of (a) Al ₂ O ₃ signal and (b) ZnO signal, in the aerogel sample measured by ptychography (sample B)	169
Figure 7.10 a) Surface rendered color coded composite of the 3D distributions of ZnO and Al ₂ O ₃ from ptychography of ZnO/Al ₂ O ₃ aerogel (sample B). (b) Volume fraction of the two components and their co-localized amounts in xy slices through the z direction of the same volume as Figure 8.	171
Figure 7.11 Views at 6 different tilted angles of the reconstruction of the ptychography sample B . (a) -65°, (b) -35°, (c) -5°, (d) 5°, (e) 35° and (f) 65°.....	172
Figure 7.12 (a) Surface rendering of (1.5 μm) ³ center cube of the reconstructed ptychographic spectro tomography data (sample B). (b) single slices at 0.3 μm, 0.6 μm, 0.9 μm and 1.2 μm depth of the cube. c) plot of the volume fraction per slice, as a function of depth from the xy surface.	173
Figure 7.13 (a) Transmission electron micrograph of an Al ₂ O ₃ aerogel coated with 25 ALD cycles of ZnO. Three morphologies are indicated: ~10 – 30 nm strongly scattering, square/spherical clusters of single crystals (ZnO); elongated, strongly scattering rods (ZnO); and weakly scattering sheet-like material (alumina). (b) High	

resolution TEM showing crystal planes of ZnO. (c) a Z-contrast scanning transmission electron micrograph of the same material in which the higher-Z ZnO coating appears white and the Al ₂ O ₃ appears grey.....	175
Figure 8.1 Evaluation of S 1s STXM of cathodes.....	185
Figure 8.2 2D chemical maps of PFSA of an MEA sample under cryo conditions (-181°C) at different tilted angles, derived from images measured at 684eV and 694 eV. (a) - 70°, (b) -30°, (c) 30°, (d) 65°. (e) 30° tilted view of the 3D reconstructed volume.....	188
Figure 8.3 X-ray transmission images at 694.0 eV of 100 ±14 nm thick PEM fuel cell sample. The membrane region is on the right and the cathode is on the left for all images, which are all on the same spatial scale. (a) Image of a sample region immediately after X-ray exposure at 296 K. (b) Image of a different sample region immediately after X-ray exposure at 95 K, using otherwise identical exposure conditions as a). (c) Same region as b), imaged after allowing the sample to warm up to 296 K.	188
Figure 8.4 (a) TEM image of MV-1 magnetotactic bacteria cells. The scale bar is 400 nm; (b) STXM image of the sample in a Luxel tomography holder. Scale bar is 200 μm (c) color composite of component maps of a wet MT sample, measured at O 1s edge (525eV-550eV) and Fe 2p edge (710eV). The bacteria cell is in green, water in blue, and magnetosome chain in red	189
Figure 8.5 (a) Low-magnification FE-SEM image; (b) high-magnification FE-SEM image; (c) TEM of an individual anatase-titania–cellulose composite nanofibre isolated from the assembly	190
Figure A.1 (a) spectrum of magnetite; (b) 2D images at 704 eV; (c) 2D images at 709.6eV; (d) Fe map generated by OD(709.6eV)-OD(704eV).....	227
Figure A.2 Fe map of magnetite at 0° , 60° ,120° ,180° ,240° ,300°	227
Figure A.3 (a) laminography measurement region in red box, (b-g) 2D laminography carbon	228
Figure A.4 chemical maps of carbon support (blue) and ionomer (green) at (a) 0°, (b) 90°, (c) 180°, (d) 270°	229
Figure A.5 spectrum of TiO ₂ /Al ₂ O ₃ aerogel: (a) TiO ₂ at Ti 2p edge, (b) Al ₂ O ₃ at Al 1s edge ..	229

Figure A.6 chemical maps of (a) TiO ₂ generated by OD (520eV)-OD (450eV) (b) Al ₂ O ₃ generated by OD (1570eV)-OD (1560eV).....	230
Figure A.7 chemical maps of TiO ₂ (red) Al ₂ O ₃ (blue) at rotation position (a) 0°, (b)90°, (c)180°, (d)270°	230
Figure A.8 (a) 2D images of the magnetite at 0°; (b) 0°view of the 3D reconstructed volume	231
Figure A.9 STXM laminography geometry.....	232
Figure A.10 (a) 2D images of the TiO ₂ / Al ₂ O ₃ aerogel sample at 0°; (b) 0°view of the 3D reconstructed volume.....	232

LIST OF TABLES

Table 1.1 Various applications of PEMFC	9
Table 1.2 3D/4D imaging of PEMFC	13
Table 3.1 Summary of tomography data sets measured for this thesis.....	58
Table 3.2 STXM beamlines status	78
Table 4.1 Reconstruction Parameters Used for Simultaneous Iterative Reconstruction Technique (SIRT) and Compressed Sensing (CS)	82
Table 5.1 Properties of the MEA samples examined in this work.....	105
Table 5.2 Summary of conditions for experimental measurements	106
Table 5.3 Accumulated radiation dose and volume fractions in the F 1s stacks in the low dose experiment (code F, 200 nm sample).....	111
Table 6.1 Summary of Conditions and Total Dose for Each Measurement Reported	136
Table 6.2 Spatial Resolution of Ptychography and STXM Measurements	137
Table 7.1 Sample and measurement details.....	153
Table A.1 List of experimental STXM laminography data set.....	226

LIST OF ABBREVIATIONS AND SYMBOLS

2D	Two dimensions
3D	Three dimensions
4D	Four dimensions
A _o	Distance between sample and order-sorting aperture
AFCC	Automotive Fuel Cell Cooperation Corporation
ALS	Advanced Light Source
CAD	Computer Aided Design
CaRPE-FC	Catalysis Research for Polymer Electrlyte Fuel Cells
CCEM	Canadian Centre for Electron Microscopy
CCD	Charge Coupled Device
CCM	Catalyst Coated Membrane
CDI	Coherent Diffractive Imaging
CL	Computed Laminography
CLS	Canadian Light Source
COSMIC	Coherent Scattering and Microscopy
CS	Compressed Sensing
CT	Computed Tomography
δr_N	Width of the Most Outer Zone (Nth) of a Zone Plate
Δr	Diffraction Limited Spatial Resolution
D	Zone Plate Diameter
E	Energy
EDS	Energy Dispersive Spectroscopy
EELS	Electron Energy-Loss Spectroscopy
EFTEM	Energy-Filtered Transmission Electron Microscopy
ET	Electron Microscopy based Tomography
EPU	Elliptically Polarizing Undulator
f	Focal Length
FIB	Focused Ion Beam
FIB-SEM	Focused ion beam scanning electron microscopy

GDL	Gas Diffusion Layer
HAADF	High-Angle Annular Dark Field
HOR	Hydrogen Oxidation Reaction
HR-TEM	High-Resolution Transmission Electron Microscopy
I_t	Transmitted Photon Intensity
I_0	Incident Photon Intensity
k_B	Boltzmann constant, 1.38×10^{-16} erg/K
λ	Wavelength of light
$\mu(E)$	Energy Dependent Mass Absorption Coefficient
MEA	Membrane Electrode Assemblies
MTB	Magnetotactic Bacteria
NEXAFS	Near Edge X-Ray Absorption Fine Structure
OD	Optical Density
OSA	Order Sorting Aperture
ORR	Oxygen Reduction Reaction
δr	Outmost zone
PEM	Proton-Exchange Membrane
PEMFC	Proton-Exchange Membrane Fuel Cells or Polymer Electrolyte Membrane Fuel Cells
PFSA	Perfluorosulfonic Acid
PMT	Photomultiplier Tube
PS	Polystyrene
ROI	Region of Interest (in STXM images)
ρ	Sample Density
σ	Energy-dependent Mass Absorption Coefficient
s	Second
SEM	Scanning Electron Microscopy
SEMt	Scanning Electron Microscopy Tomography
SIRT	Simultaneous Iterative Reconstruction Technique
SM	Spectro-Microscopy
SR	Synchrotron Radiation

STEM	Scanning Transmission Electron Microscopy
STXM	Scanning Transmission X-Ray Microscopy
SVD	Singular Value Decomposition
t	Sample Thickness
T	Temperature
TEM	Transmission Electron Microscopy
TTE	Amine Epoxy Resin
VLM	Visible Light Microscope
WBP	Weighted Back-Projection
XAS	X-ray Absorption Spectroscopy
XANES	X-ray Absorption Near Edge Structure
XCL	X-ray Computed Lanimography
ZP	Fresnel Zone Plate

Chapter 1

Introduction

Chapter 1 describes the concept of 4D imaging. It introduces Proton Exchange Membrane Fuel Cell (PEMFC) systems and X-ray microscopy methods. A summary of recent research in 4D imaging is given.

1.1 What is 3D/4D chemical imaging and why is it needed?

An image shows heterogeneity of specimens in 2 dimensions (x, y) by different contrast mechanisms. If the image contrast mechanism provides explicit sensitivity to chemical species through e.g. spectroscopy, then one can refer to the method as a type of 3D or “chemical imaging”. With appropriate chemical detection technologies, chemical imaging provides the possibility of qualitative and quantitative research, like the composition of the specimen, distribution and the amount of each component. However 2 dimensional (2D) imaging does not detect changes in distributions in the z-direction. 3D imaging (x, y, z) methods have been developed to fully visualize spatial structure of heterogeneous materials. 3D imaging has found applications in many fields, including material science (Salvo et al. 2010), medicine (Cretoiu, Hummel et al. 2014, Bonanno, Coppo et al. 2015), cultural heritage (Sansoni et al. 2009), archaeology (Papadopoulos et al. 2007), reverse engineering (Sansoni et al. 2004), virtual environment (Xia et al. 2000), etc. To the base of 3D imaging, extra dimensions can be added, such as chemistry (Wu et al. 2018), time (Lockwood et al. 1998, Mor-Avi et al. 2004), density (Lee Jin et al. 2003), pressure (Slowko and Krysztof 2014), temperature (Anand et al. 2007), etc.. With an extra

dimension of information, 4D imaging (Zewail 2010, Campbell 2002, Brune 2010) is obtained. In my thesis research 4D imaging involves chemical imaging in three spatial dimensions (x, y, z, E). 4D imaging measures the 3D spatial distribution of each chemical species of a mixture. **Figure 1** outlines different dimensional information (1D, 2D, 3D, 4D) extracted from the same data set. Generally, 4D (3D chemical) imaging provides a quantitative understanding of the distribution of multiple chemical species in three dimensions including the internal structure, interfaces, and surfaces of micro and nanoscale systems.

1.2 3D/4D imaging methods and applications

Tilt-angle tomography is a 3D imaging method in which a sample is viewed from a wide range of angles with some type of penetrating radiation (**Figure 1.2** (a)), such as visible light, X-rays, electrons, neutrons, etc. A three-dimensional image of the internal structure of a solid object is then generated by mathematically manipulating the set of 2D projection images into a representation (reconstruction) of the 3D structure (**Figure 1.2** (b)). The term “tomography” was coined by Mayer in 1914 to describe the derivation of 3D information from 2D X-radiographs (Seynaeve 1995). In the 1970s, with the improvement of electronics enabling computational reconstruction of radiographs, tomography advanced. Since then, the term has been applied to many techniques (Seynaeve 1995). Nowadays, in concert with the development of micron and nano-scale microscopy, tomography is being performed at the micro- and nano-scale. **Figure 1.3** presents different techniques used for 3D/4D imaging at a range of length scale.

Computed tomography (CT) (Brenner and Hall 2007, Khadivi 2006) usually refers to X-ray computed tomography, which measures X-ray images from a series of angles and

produces a 3D image. There are many applications of CT in medicine (Abrams and McNeil 1978, Rustin et al. 2007, Haydel et al. 2000) and industry (De Chiffre et al. 2014).

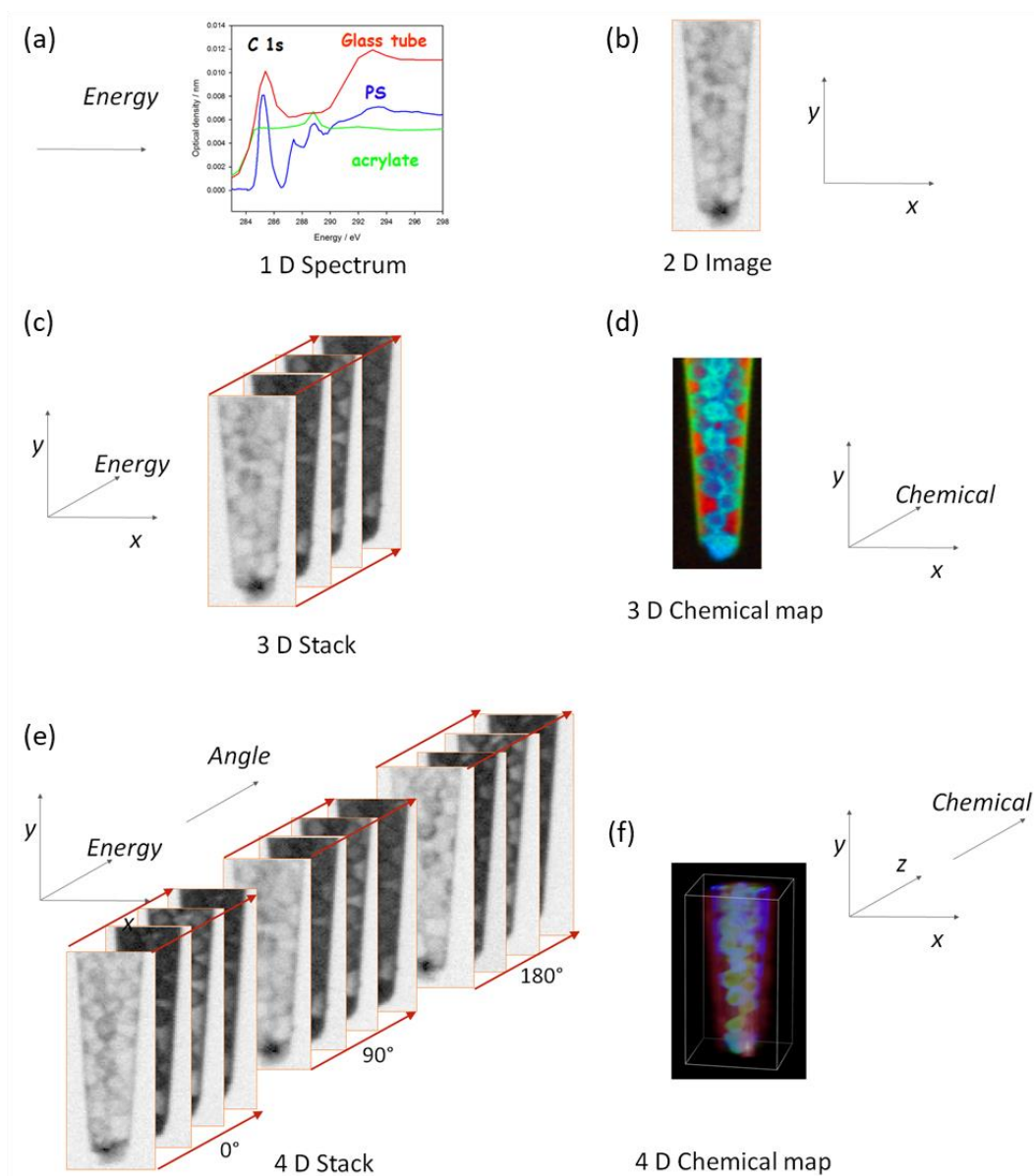


Figure 1.1 Image of a sample consisting of polyacrylate-filled polystyrene microspheres in water inside a pulled glass capillary (a) 1D C 1s X-ray absorption spectra, (b) 2D image, (c) 3D stack, (d) 3D chemical map, (e) 4D stack, (f) 4D image. The 3D stacks (e) at each scan angle contained 23 energy images.

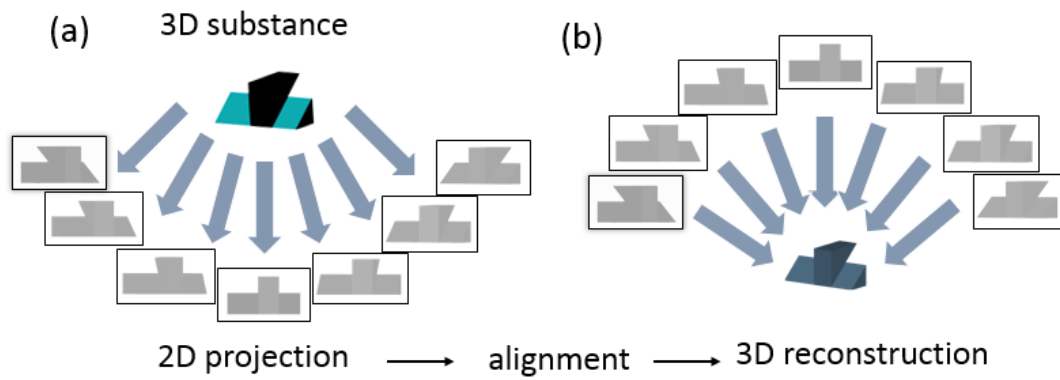


Figure 1.2 (a) 2D projection images of a solid; (b) 3D reconstruction from the 2D images

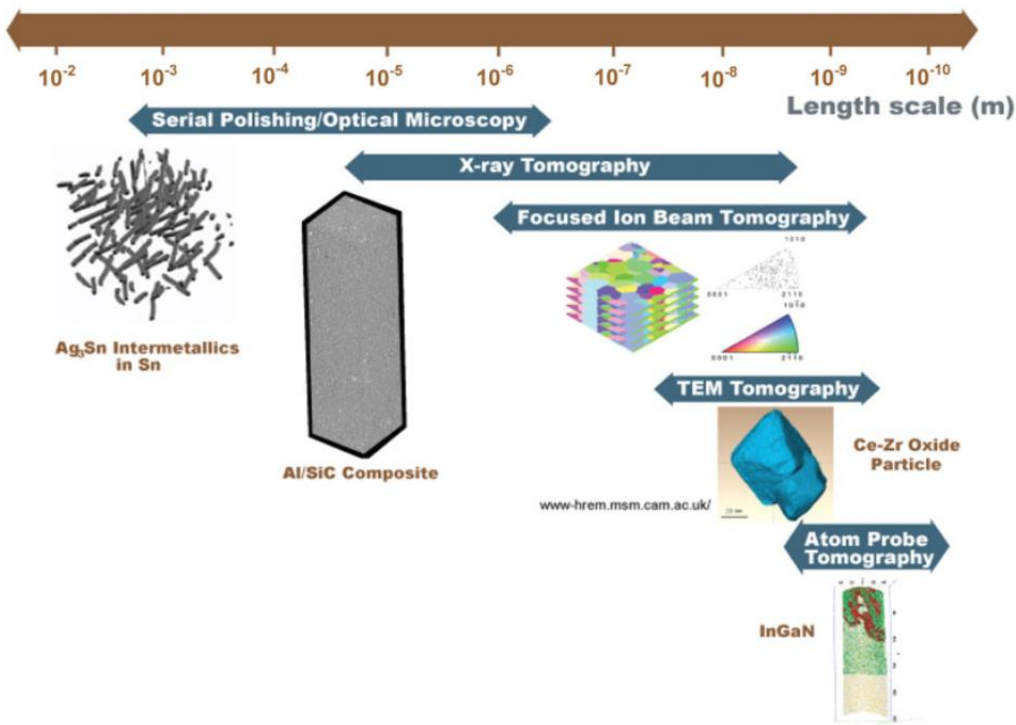


Figure 1.3 Techniques used for 3-D and 4-D materials science at various length scales

Time resolved CT (a 4D imaging method with time as the fourth dimension) has contributed to significant advances in medical research (Ruijiang et al. 2009, Pan et al. 2004, Beddar et al. 2008, Zhang et al. 2005, Colgan et al. 2008, Segars et al. 2008). Figure 1.4 presents different fields of application for CT technology in industry. According to different requirements, CT visualization can be classified into voxel based (volume rendering) or surface based (surface rendering). Simple visualization and non-destructive testing (NDT) with qualitative evaluation can be presented on a voxel basis. Digitization and dimensional metrology with quantitative analysis require surface based evaluation.

Synchrotron based X-ray tomography uses a high intensity, monochromatic beam over a wide range of photon energy. Full field transmission X-ray microscopy (TXM) tomography using hard X-rays (5–11 keV) (Nelson et al. 2011, Andrews et al. 2010, Chen et al. 2010, Awaji et al. 2002), and soft X-rays (250 eV-1.8 keV) (Chao et al. 2005, Parkinson et al. 2008) is efficient and has provided 3D structural data sets on time scale of seconds to minutes. Scanning Transmission X-ray microscopy (STXM) tomography using soft X-ray (~100-2.7 keV) (Haddad et al. 1994, Obst et al. 2009a, Hitchcock et al. 2010, Wu et al. 2018) is effective for chemical mapping but is considerably slower since it contains multi-images per data set. X-ray laminography is an alternative 3D imaging method to tomography. Laminography is especially useful for 3D imaging of flat, laterally extended objects such as integrated circuits (Saida et al. 2012, Hoshino et al. 2011, Helfen et al. 2005, Moffat et al. 2010).

Focused Ion Beam (FIB) tomography is a serial sectioning technique combined with scanning electron microscopy (SEM). FIB tomography can achieve spatial resolutions in the range of tens of nm and has the ability to measure a large volume of specimen (~ 50 x

50 x 10 μm) (Holzer and Cantoni 2012, Prieto 2015). FIB nanotomography is often used for the characterization of porous and granular materials (Inkson et al. 2001, Vivet et al. 2011, Lasagni et al. 2008, Lasagni et al. 2007). Transmission Electron microscopy (TEM) tomography (Weyland and Midgley 2004) is now well established and widely used in materials sciences and in particular in polymer sciences (She et al. 2010, Jinnai and Spontak 2009). When combined with electron energy loss (EELS) as in the STEM-EELS technique, or with energy dispersive spectroscopy (STEM-EDS), chemically resolved 4D imaging can be obtained (Möbus et al. 2003, Jarausch et al. 2009, Yedra et al. 2014, Haberfehlner et al. 2014).

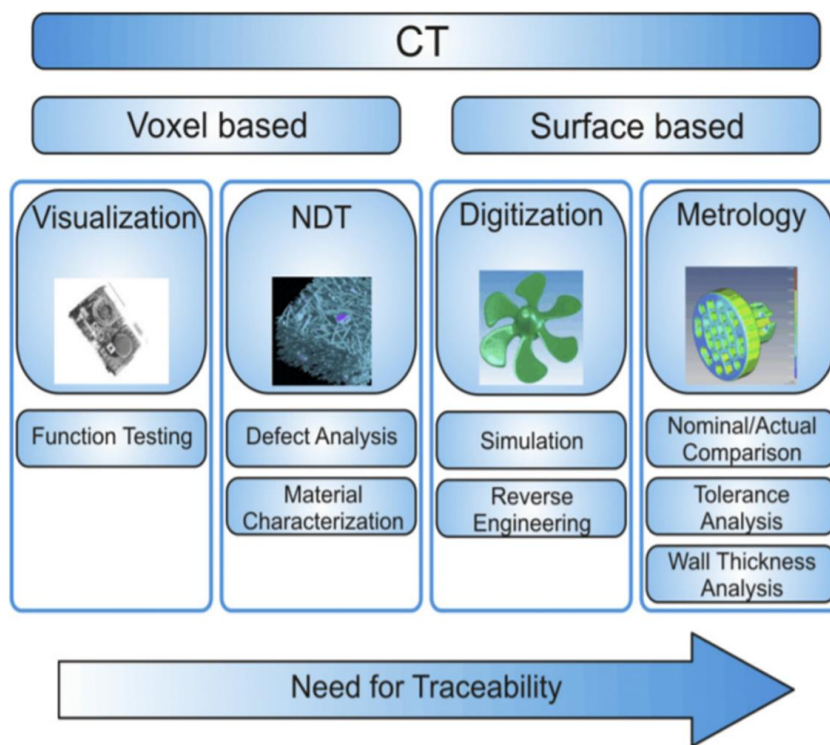


Figure 1.4 Industrial fields of application for X-ray CT

1.3 Proton Exchange Membrane Fuel Cells (PEMFC)

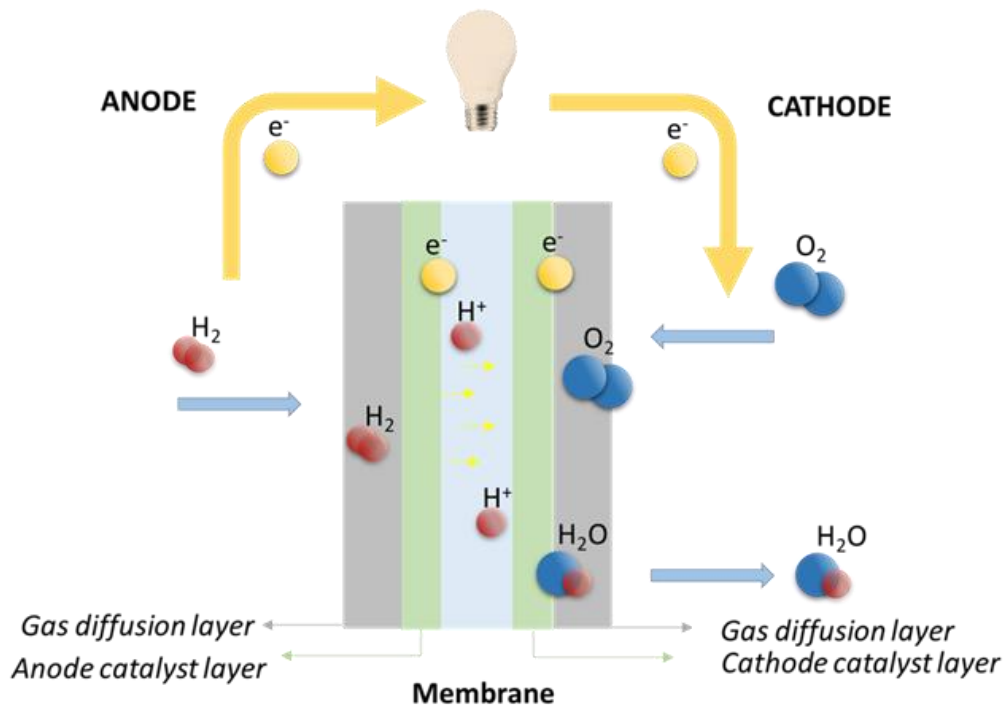


Figure 1.5 Schematic diagram of a PEMFC

Proton exchange membrane fuel cells (PEMFCs) are a promising green resource for stationary and automotive power applications (Wang et al. 2011a). PEMFCs were first employed in space vehicles (Plauche 1978). Recently, other applications of PEMFC have been developed, including hybrid power buses (Folkesson et al. 2003), powered bicycles (Hwang et al. 2004), stationary power generators (Wang et al. 2005) and mobile power (Tüber et al. 2003). More applications are listed in **Table 1.1**. The advantages of PEMFC include compact construction, large current density, solid electrolyte, low working temperature, and fast start-up. When hydrogen is the fuel, the cell reactions at the anode and cathode are as follows:

Anode: Hydrogen Oxidation Reaction (HOR)



Cathode: Oxygen Reduction Reaction (ORR)



The ORR at the cathode is the key rate limiting reaction in PEMFC. Typical cathodes are composed of carbon support particles decorated with Pt catalyst particles, mixed with a proton conducting perfluorosulfonic acid (PFSA) polymer. **Figure 1.6** (Litster and McLean 2004) shows a schematic diagram of the PEMFC cathode catalyst layer, which is attached to the polymer electrolyte membrane (PEM), and is also in contact with a gas diffusion layer (GDL). The PFSA acts as the proton conduction media in the cathode, and thus the distribution of the PFSA ionomer will affect PEMFC efficiency, Pt utilization, and degradation kinetics. Optimization of ionomer loadings and distributions is a major goal of PEMFC research. Methods for directly observing the internal structures and chemical states of the cathode catalyst layer in membrane electrode assemblies (MEAs) are necessary to help optimize PEMFC technology. Because PFSA is very radiation sensitive, it is difficult to directly provide high spatial resolution three dimensional information on the structure/morphology, distribution, and chemical states of Pt nanoparticle cathode catalysts in MEAs.

Table 1.1 Various power system applications of PEMFC (Wee 2007) (reproduced with permission from Elsevier)

Application	Power	Fuel	Comments	Reference
Hybrid power bus	50 kW	Compressed hydrogen in cylinder	Efficiency: 40%, Mean power consumption: 17–24 kW	(Folkesson et al. 2003)
Powered bicycle	300 W	Hydrogen stored in the metal hydrides	Efficiency: 35%, Distance-to-fuel ratio: 1.35 km/g	(Hwang et al. 2004)
Lightweight powered vehicle	5 kW	High pressure gaseous hydrogen in cylinder	Drive over a 100 km run at a speed of 18 km/h	(Hwang et al. 2005)
Sailing yacht	300 W	Hydrogen produced by LPG via a series of processor on-board system	Used as auxiliary power units using bottled LPG as fuels	(Beckhaus et al. 2005)
Stationary power generator	5 kW	Commercially available 15 MPa hydrogen cylinder	Efficiency: more than 30% in fully loaded operation. Operated 3 h at 5 kW with two 50 liter hydrogen cylinders	(Wang et al. 2005)
Uninterrupted power supply	2 kW	Hydrogen produced by methanol via fuel processing	Total cost was strongly dependent on the service time.	(Lin et al. 2005)
Portable computer	46 W	Hydrogen stored in the metal hydrides	Trouble-free start-up of the portable computer	(Tüber et al. 2003)
portable power generation	450W	Methanol steam	higher fuel cell temperature has highest fuel cell performance	(Herdem et al. 2015)
leave-in-place sensor systems	30W	Ultrapure H ₂ supplied from compressed gas cylinders	careful control of the chemical delivery must be ensured	(Higier et al. 2017)
Hydrogen bicycle	500WA	Metal hydrides tank Hydroge	economic analysis to reduce the cost	(Minutillo et al. 2018)
Fuel cell hybrid electric vehicle	90 kW	Hydrogen tank	power efficiency of 96.2%	(Fathabadi 2018)

The overarching theme of my research is 4D imaging method development. My research project was funded partly by the (recently disbanded) Automotive Fuel Cell Cooperation Corporation (AFCC) and by the currently disbanded Catalysis Research for Polymer Electrolyte Fuel Cells) (CaRPE-FC) network. In the context of the network and industry collaboration, my project is motivated by the need to assist PEMFC optimization by 4D characterization of PEMFC catalyst layers. I have developed or improved a number of different 4D imaging methods in order to evaluate their individual advantages and limitations, thereby identifying an optimal solution for 4D imaging of ionomer in PEMFC cathodes.

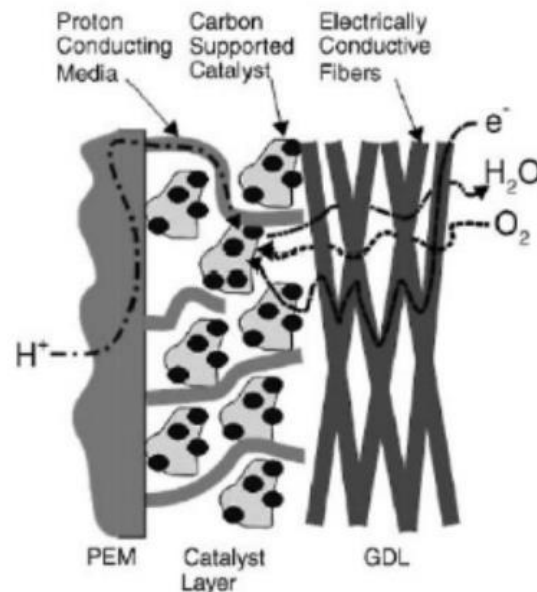


Figure 1.6 Schematic diagram of PEMFC cathode catalyst (Litster and McLean 2004)
(reproduced with permission from Elsevier)

1.4 Previous 3D/4D imaging technique for PEMFC research

CT at 2-10 micron spatial resolution has been used to investigate the structure of gas diffusion layers, and the water distribution in the GDL and the electrode (Fishman et al. 2010, Zenyuk et al. 2015). Neutron tomography has been used to measure the water distribution in fully assembled fuel cell stacks, benefitting by the deep penetration ability. The porous structure and solid phase of the PEMFC cathode layer has been measured at the nanoscale using X-ray tomography (Garzon et al. 2007), but without chemical information.

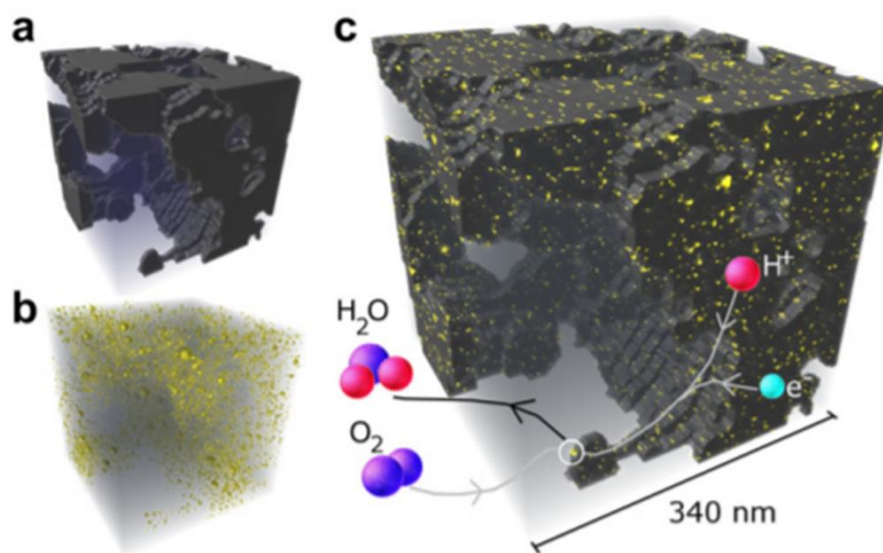


Figure 1.7 (a) A cube of 340 nm side length of the SEMt reconstruction. (b) The reconstructed Pt volume information in the same spatial area as the SEMt reconstruction. (c) The superposition of (a) and (b) and visualizes the location of Pt catalyst particle volume and surface information within the porous carbon matrix. (Thiele et al. 2013)(reproduced with permission from Elsevier)

Electron tomography has been used to measure the Pt particle and carbon support distribution (Gontard et al. 2008, Yu et al. 2012). PEMFC cathodes have been studied by SEM-FIB tomography, combined with TEM tomography (Thiele et al. 2013) (Figure 1.4). TEM tomography was used for volume and surface area distributions of platinum catalyst particles, while FIB-SEM tomography was used to characterize porosity, pore-size and grain-size distributions. Spectro-tomography in a scanning transmission X-ray microscope (STXM) was developed by the Hitchcock group (Johansson et al. 2006). Prior to the start of my thesis it had been applied to measurements of the carbon support and ionomer distributions in cathode layers (Berejnov et al. 2013). Recent 3D imaging studies of PEMFC are listed in Table 1.2.

1.5 Scanning Transmission X-ray Microscopy

Scanning transmission X-ray microscopy (STXM) is a synchrotron-based X-ray microscopy. A Fresnel zone plate is used to focus the X-ray beam to a small spot. The sample is placed in the plane of the spot and images are formed by scanning the sample and measuring the transmitted flux point by point or line by line. Transmitted X-ray intensity is recorded for each pixel. By recording images at a sequence of energies, absorption spectra can be obtained for every pixel. Such spectra are also called near edge X-ray absorption fine structure (NEXAFS) or X-ray absorption near edge spectra (XANES). STXM is a combination of spatially resolved spectroscopy and relatively high spatial resolution imaging with spectral sensitivity.

Table 1.2 3D/4D imaging of PEMFC

Technique	Spatial resolution	Research project	Comments	Reference
Microscale computed tomography	2.44 μm	GDL porosity distribution	provides valuable insight into the heterogeneous porosity distributions of paper, felt, and cloth GDL materials	(Fishman et al. 2010)
Nanometer-Scale X-ray Computed Tomography	50 nm	Microstructure of Polymer Electrolyte Fuel Cell Electrodes	volumetric distributions of the effective secondary pore and agglomerate diameters	(Epting et al. 2011)
Synchrotron X-ray tomography	10 μm	water content in gas diffusion media	demonstrate the feasibility of using X-ray microtomography to quantify liquid water distribution at the component level	(Sinha et al. 2006)
FIB-SEM tomography	3 \times 2 \times 20 nm	correlations between carbon corrosion and microstructure	the predictive capability of degradation models are improved	(Star and Fuller 2017)
Neutron tomography	300 μm	water distributions in polymer electrolyte membrane fuel cell stacks	the water distribution after switch-off was imaged over a time period of 36 h quasi in-situ tomography technique	(Markötter et al. 2012)
TEM tomography and FIB-SEM tomography	0.37nm 2.5 \times 2.5 \times 13.6nm	Analyze volume and surface area distributions of platinum catalyst particles by TEMt. Characterize	Using TEMt and SEMt combined, the visualization of the location and morphological properties of the Pt nanoparticles	(Thiele et al. 2013)

		porosity, pore-size and grain-size distribution by SEMt.	embedded in the porous carbon matrix at very different length scales.	
TEM tomography	voxel size of $0.86 \times 0.86 \times 0.17$ nm	catalyst powders	Reveal useful information on catalyst distribution, available surface area, and particle size distribution	(Jankovic et al. 2013)
Cryo Electron Tomography	spot size of ~ 1 nm	Morphology of Hydrated As-Cast Nafion	first nanoscale 3D views of the internal structure of hydrated Nafion obtained by a direct-imaging approach	(Allen et al. 2015)
X-ray Lanimography	$1.5 \times 1.5 \times 5$ μ m	Cathode Catalyst Layer	XANES combined with the XCL method has been successfully developed for the 4D visualization of the cathode catalyst layer	(Saida et al. 2012)

STXM was first developed at NSLS-I (Brookhaven National Lab) by researchers from the State University of New York at Stony Brook during 1972~1982 (Kirz and Jacobsen 2009). Although initial work focused on imaging biological samples in the ‘water window’ (at ~520 eV), in the early 1990s the first spectromicroscopy studies were published (Ade et al. 1990, Ade et al. 1992, Howells et al. 1987, McNulty et al. 1992). After that, STXM started major expansion. **Figure 1.5** shows photos of the spectromicroscopy (SM) beamline at the Canadian Light Source (CLS) which was developed as one of the CLS phase 1 beamlines and began operation in 2007 (Kaznatcheev et al. 2007).

STXM has been used for the characterization of biological specimens (Shapiro et al. 2005, Cosmidis et al. 2015, Obst et al. 2009b), polymeric materials (Morin et al. 2001, Hitchcock et al. 2005, George et al. 2016) and fuel cell membrane electrode assemblies (MEA) (Berejnov et al. 2011, Susac et al. 2011, Lee et al. 2013). A bibliography of soft X-ray microscopy worldwide has been prepared by my supervisor. It was initially published as a supplement to a review paper (Ade and Hitchcock 2008), and is periodically updated and made available at http://unicorn.mcmaster.ca/xrm-biblio/xrm_bib.html



Figure 1.8 SM beam line photos: (a) STXM; (b) SM beamline. SR light propagates from right to the left; (c) Elliptically polarizing undulator (EPU). (reproduced with permission from (Kaznatcheev et al. 2007) Elsevier)

1.6 STXM 3D/4D imaging and applications

It has been demonstrated recently that STXM tomography is well suited to chemically probe the interior structure of materials due to its excellent spectroscopic capabilities, depth of focus, penetration depth and spatial resolution. (Hitchcock et al. 2010, Berejnov et al. 2013, Obst et al. 2009b, Wang et al. 2011b, Obst and Schmid 2014, Schmid et al. 2014, Hilhorst et al. 2012). STXM 4D imaging can be done in a variety of ways, including serial sectioning (Hitchcock et al. 2003), laminography (Helfen et al. 2005) and tilt-series tomography (Hitchcock et al. 2010). STXM tomography has been used for 3D observations of biomaterials (Parkinson et al. 2008, Johansson et al. 2006, Wang et al. 2011c, Hagen et al. 2014, Otón et al. 2014, McDermott et al. 2012, Sun et al. 2014), and other polymeric systems (Hitchcock et al. 2008, Ohigashi et al. 2017). The advantage of STXM tomography for biological measurement does not require any staining or fixation protocols for cells, so that cells or tissue can be imaged in a near native state (Parkinson et al. 2008). STXM tomography has also been applied for industrial research. Aramburo et al. measured the coordination and distribution of aluminum in Zeolites by STXM tomography at the single-particle level for the first time, and 4D results have been obtained. (Aramburo et al. 2013)

STXM spectro-tomography has been performed on dry samples on single TEM grids (Obst et al. 2009b). **Figure 1.9a** presents volume rendering of a tomography data set for protein, all-calcium and intense-Ca signals in a single *Synechococcus leopoliensis* PCC 7942 bacterium. The data was recorded at the C 1s and Ca 2p edges. Figure 1.9b and Fig. 1.9c shows the compositional correlations of the Ca²⁺ and the organic carbon signal. The

3D results revealed that aragonite is a rather uniformly distributed layer while calcite forms at specific Ca-rich hot spots.

STXM 3D imaging has been applied to wet samples in pulled glass capillaries (Figure 1.1) and in Luxel tomo cells (Friday Harbor, WA, USA) (**Figure 1.10**) that consist of a metal frame coated with polyimide membranes on both sides. The sample is cells of nitrate-reducing *Acidovorax sp.* strain BoFeN1 isolated from anoxic freshwater sediments of Lake Constance which were cultured under anoxic conditions. Figure 1.10 shows the 3D volumes of the Fe(III)-(oxyhydr)oxide, protein and water components, which were derived from O 1s edge, and iron generated by $OD_{723.3\text{eV}}-OD_{704\text{eV}}$ from the Fe 2p edge. The overlay map (Fig. 1.10e) is the relative distribution of different components. Figure 1.10f shows the thickness distribution of the iron. The 3D imaging results reveal iron distributions inside 2 different cells and outside the cells.

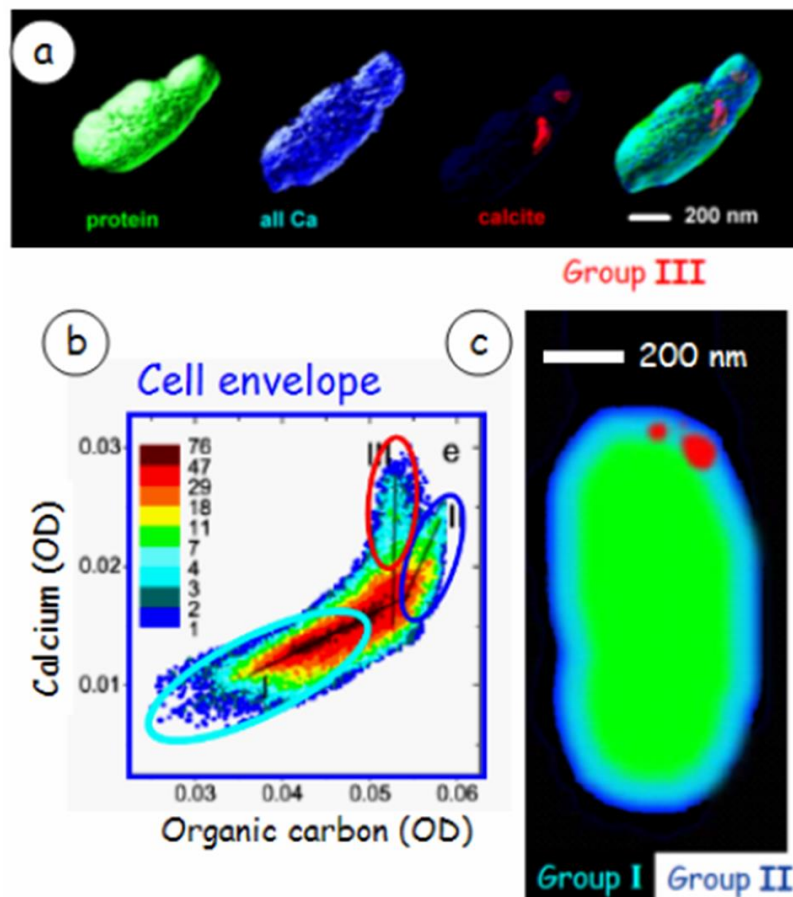


Figure 1.9 a) Volume Renderings of protein, all-Ca and hot-spot Ca of a calcifying bacterium. (b) correlation of Ca 2p and C 1s signal in cell envelope showing the aragonite-like Ca is uniformly distributed but calcite forms at hotspots. (d) slice through centre of cell, colored by the indicated regions in Ca-organic_C space. (Hitchcock et al. 2010) (Reproduced with permission from Microscopy and Microanalysis)

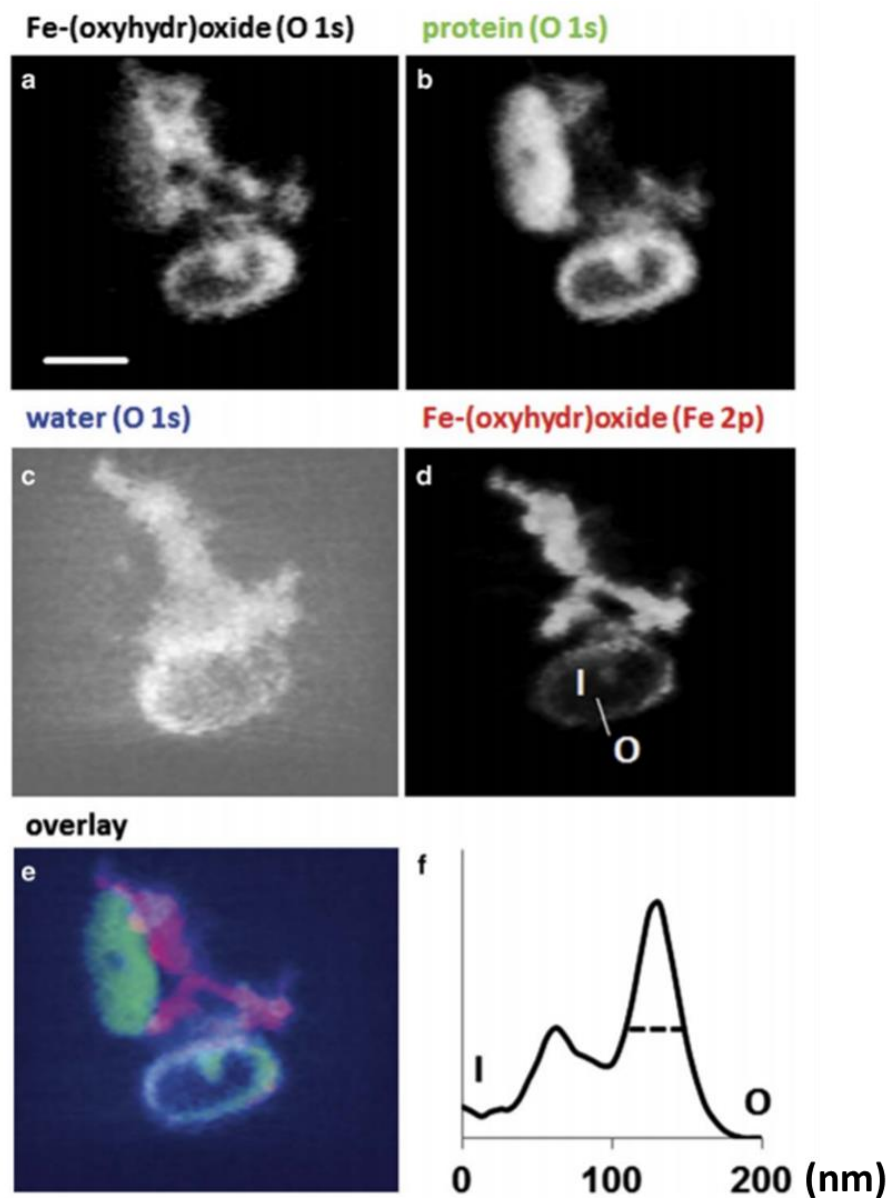


Figure 1.10 Projection images of chemically specific three dimensional datasets acquired at the O 1s edge (a–c), Fe 2p edge (d) and an overlay (e) of hydrated *Acidovorax* sp. strain BoFeN1 bacteria in the stage of precipitating Fe(III)-(oxyhydr)oxide. The line profile (shown in d) across the Fe-precipitate encrusted periplasm (f) shows a thickness of the crust of ~40 nm (full-width at half-maximum). I, inside cell; O, outside cell. Scale bar is 500 nm. (Schmid et al. 2014) (Reproduced with permission from Microscopy and Microanalysis)

1.7 Research objectives

The aim of my PhD research is to develop methods of 4D imaging which could be used to study PEMFC cathodes. All methods are based on scanning transmission x-ray microscopy (STXM). My results are compared to other 3D and 4D microscopy techniques, such as electron microscopy based tomography (ET) for 3D and EDS or EELS-based ET for 4D.

The detailed work performed includes:

- (1) Optimized spectro-tomography methods based on ambient STXM.
- (2) Improved the reconstruction quality by using a novel compressed sensing algorithm, in collaboration with Mirna Lerotic (2nd Look Consulting).
- (3) Developed spectro-laminography by STXM, including instrument improvements.
- (4) Improved the 3D imaging resolution by using the new method of spectro ptychography tomography in collaboration with David Shapiro (ALS).
- (5) Used cryo-STXM tomography to evaluate its potential to decrease the impact of radiation damage on 3D chemical imaging of radiation sensitive samples including dry PEMFC cathodes.
- (6) Laminography method development and application to PEMFC and aerogel sample.

Chapter 2

Techniques and Principles

Chapter 2 describes 3D and 4D imaging methods by various techniques, including X-ray microscopy, electron microscopy, ptychographic X-ray microscopy, cryo electron microscopy and cryo X-ray microscopy. The principles of scanning transmission X-ray microscopy (STXM) and the challenges and measurement of radiation damage by STXM are discussed in this chapter.

2.1 X-ray micro and nano tomography

X-ray microtomography is based on the same principle as X-ray computed tomography (CT) (Willi 2006). A CT reconstruction data set is composed of voxels whose gray levels correspond to X-ray attenuation which in turn, reflects the proportion of X-rays scattered or absorbed as the X-ray beam passes through a volume. Different configurations of CT are shown in Figure 2.1 (Kyle and Ketcham 2015). The modern laboratory CT systems use a cone beam configuration (Figure 2.1(b)) rather than the planar fan beam configuration (Figure 2.1(a)). A linear detector is used for the fan beam configuration while a planar detector is used for the cone beam configuration. The planar detector is more efficient, so more tilted images can be acquired which improves reconstruction quality and thus higher spatial resolution is obtained. Figure 2.1(c) shows near-parallel beam imaging (Fig. 1c), which is possible at synchrotron X-ray sources or a synchrotron-inspired configuration pioneered by Xradia, Inc. (Sunnyvale, California), now Zeiss. This configuration can provide sharper images with high signal-noise ratio, and high spatial

resolution. The spatial resolution of a clinical CT device is 200-500 μm (Burghardt et al., 2011) . For X-ray microtomography, the spatial resolution can range from 50 μm to approximately 1 μm (Wildenschild et al. 2002). Micro-CT based on hard X-rays was first developed for ceramic automotive materials in the 1980s by the Ford Motor Company. It was then applied to quantitative evaluation of bone, cartilage, and cardiovascular structures, with applications in fundamental structure-function analysis, disease, tissue engineering, and numerical modeling (Boerckel et al. 2014). The advantage of hard X-ray micro-CT is the ability to study thick samples including small animals and bio-materials in cm thickness ranges. The application of micro-CT to PEMFC materials has mostly been in characterizing gas diffusion layers (Mack et al. 2014). With the recent development of specialized X-ray lenses, nanometer-scale X-ray computed tomography (nano-CT) with <50 nm resolution is now available (Tkachuk et al. 2009). Nano-CT has been used for to measure 3D distributions of solid agglomerates and pores in PEMFC cathode layers (Epting et al. 2012).

2.2 Electron tomography

Electron tomography extends the 2D imaging capabilities of Transmission Electron Microscopy (TEM) to the third spatial dimension. Tomography using scanning transmission electron microscopy (STEM) in the high-angle annular dark field (HAADF) detection mode is a powerful 3D chemical-sensitive method (Haberfehlner et al. 2014). The image contrast mechanism has atomic number sensitivity and STEM mode is not affected by diffraction contrast. When combined with energy-filtered TEM (EFTEM), energy-dispersive X-ray spectroscopy (EDS) or electron energy-loss spectroscopy (EELS) (Yedra et al. 2014), spectroscopic and element-sensitive tomography methods, true 4D imaging,

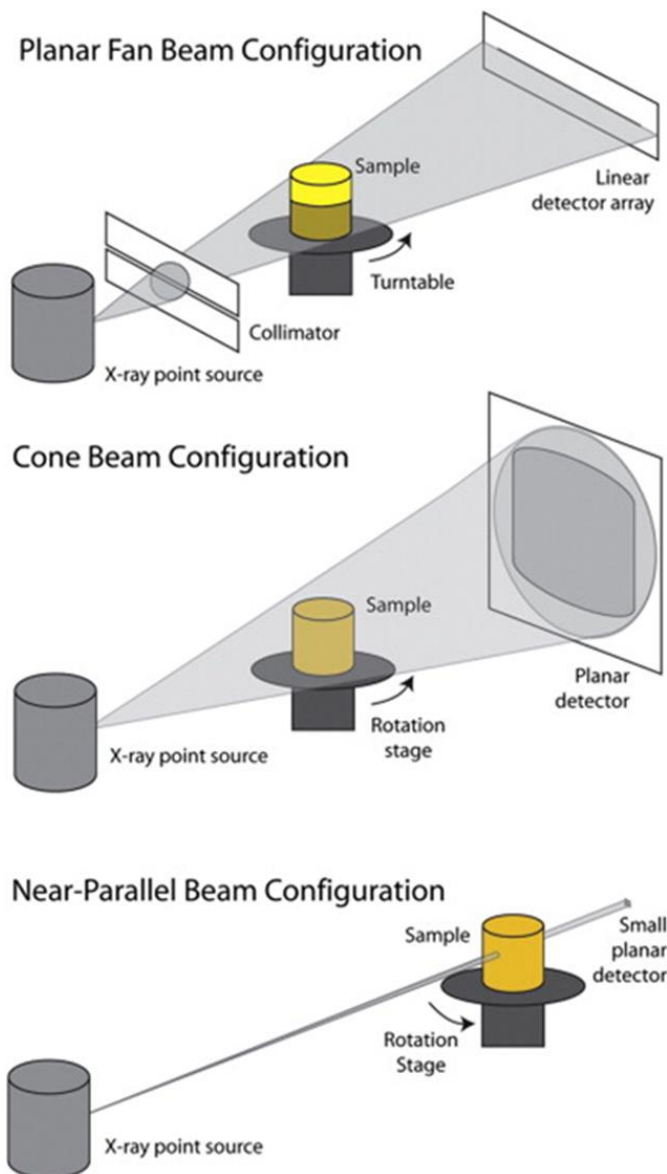


Figure 2.1 Schematic illustration of different beam configuration of X-ray computed tomography facility(Kyle and Ketcham 2015) (reproduced with permission from Elsevier)

has been demonstrated (Haberfehlner et al. 2014, Nan et al. 2011). Because of its high spatial resolution (<0.1 nm), electron tomography is quite widely used in the study of nanoparticle distributions in different catalyst support materials, including fuel cell electrodes (Vivet et al. 2011, Grothausmann et al. 2011). Many studies of cathode catalyst

layers of PEMFC have been reported (Yu et al. 2012, Ziegler et al. 2011). Recently, Lopez-Haro et. al. reported the 3D morphology of the PFSA thin layer surrounding the carbon particles using electron tomography (Lopez-Haro et al. 2014). By staining the ionomer with Cs^+ ions, a 7 nm thick Cs -ionomer was observed covering the surface of the carbon-support particles (Fig. 2.2). However, electron tomography of soft materials without staining is very difficult, especially for systems which are sensitive to radiation damage. PFSA is one of those types of materials. Radiation damage to PFSA in cathodes has been identified as a major challenge in applying analytical electron microscopy to PEMFC cathodes (Porat et al. 1995, He et al. 2014, Cullen et al. 2014).

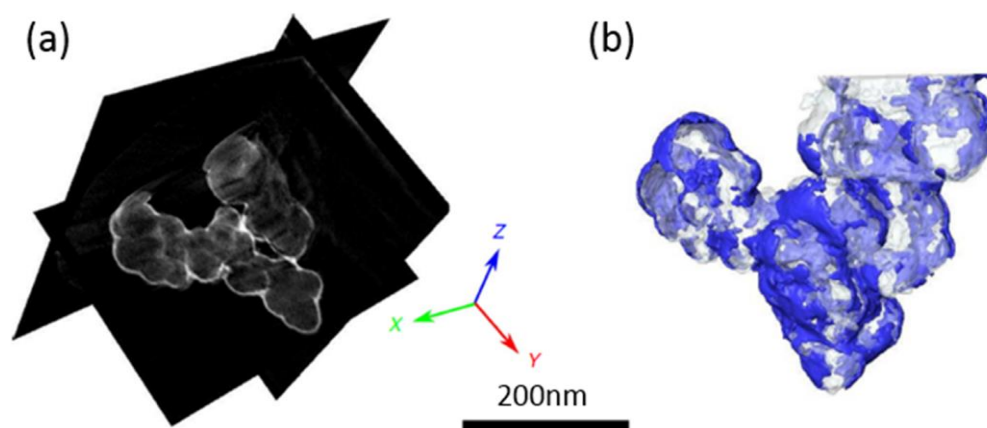


Figure 2.2 (a) Three representative orthoslices of the reconstruction of STEM tomography of a PEMFC cathode; (b) 3D-rendered volume: the blue and grey regions correspond to the Cs^+ -stained ionomer and to the carbon support, respectively (Lopez-Haro et al. 2014) (reproduced with permission from Springer Nature)

2.3 Scanning Transmission X-ray Microscopy (STXM) Tomography

STXM has been demonstrated to be a useful tool for studies of cathode catalyst layer of PEMFC (Susac et al. 2013). Over the last few years, our group has been working to

extend the 2D and 3D cathode catalyst research to 4D. In 2012, STXM spectro-tomography was applied to two types of pristine catalyst coated membranes (CCM) at the C 1s and F 1s edge (Berejnov et al. 2013). Focused ion beam (FIB) and conventional microtoming were used to prepare samples of the same catalyst coated membrane (CCM). The study found a very different amount of fluorine in the two samples, because of sample damage in the sample preparation by FIB (Bassim et al. 2012), (Melo et al. 2014). Fig. 2.3 shows 3D chemical maps of the FIB sample. The red volume is the carbon-support network, which is reconstructed from the difference of optical density images at 285 and 278 eV, while the blue is the radiation damaged PFSA polymer, which is reconstructed from the difference of the optical density image at 296 eV and the carbon support chemical map. The two volumes are visualized in surface rendering using different threshold values. The quantitative thickness of the F component is only 1-2 nm while that of the carbon-support is ~90 nm. The F signal is much too low, which was identified as ion beam damage from the FIB procedure (Berejnov et al. 2013, Melo 2014 et al.). For the microtomed sample, the total fluorine thickness is 15-20 nm, and the carbon thickness is 190-230 nm. This study (Berejnov et al. 2013) indicates that STXM spectro-tomography, combined with microtoming sample preparation, is suitable for PEMFC cathode catalyst 3D imaging, but FIB preparation is not suitable. Radiation damage still exists in STXM (Wang et al. 2009a), and is especially problematic for STXM tomography of PFSA. Overcoming this challenge is a major outcome of my thesis research.

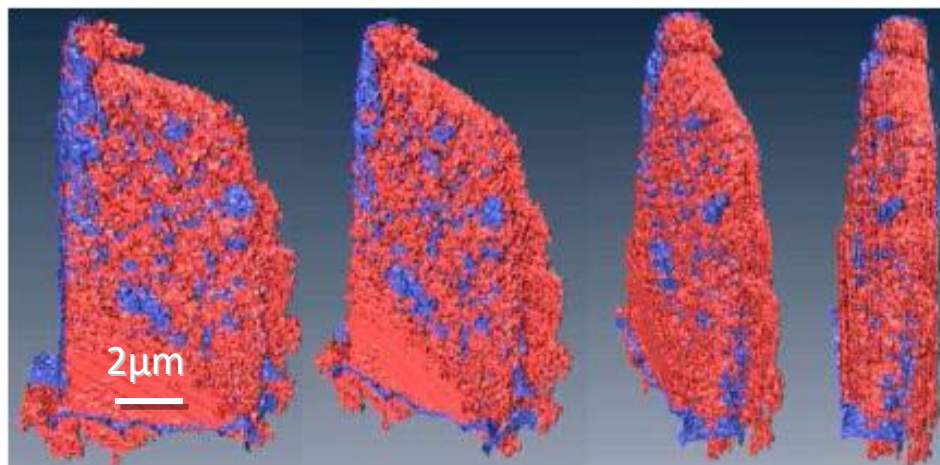


Figure 2.3 3D chemical maps in 0°, 30°, 60°, 90° degree projections extracted from reconstructed volume with different threshold. The red signal represents the carbon support ($OD_{285}-OD_{278}$) and the blue one shows the ionomer ($OD_{296} - (OD_{285}-OD_{278})$) (Berejnov et al. 2013). (reproduced with permission from ECS Transactions) 50(2): 361-368. Copyright 2013, The Electrochemical Society)

2.4 Ptychographic X-ray computed tomography

Ptychography is a type of coherent diffractive imaging (CDI) which provides quantitative phase and amplitude information about the sample and the illumination. Its spatial resolution is not limited by the limitations of the probe forming optics (Rodenburg 2008, Dierolf et al. 2010), and has the potential to achieve diffraction limited resolution (Edo et al. 2013, Miao et al. 2015) which is given by the Raleigh diffraction limit of the X-rays used, which is $\lambda / (2 \cdot NA)$, where λ is the X-ray wavelength, and NA is the numerical aperture. $NA = n \cdot \sin\theta$, where n is the diffraction order, and θ is the convergent angle of the incident X-rays. The image is reconstructed from coherent scattering patterns, which are generated in a series of overlapping exposures (Rodenburg et al. 2007, Thibault et al. 2009,

Thibault et al. 2014). The overlap of adjacent sampled areas provides a major constraint to the iterative reconstruction algorithm which converges much faster and more reliably than other CDI methods (Bunk et al. 2008). Ptychography developed over a decade ago in the hard X-ray regime, where high sensitivity X-ray cameras are readily available, diffraction is stronger, wavelength is very short, and high penetration depths facilitate ease of implementation (Takahashi et al. 2011). Ptychography in the soft X-ray is still under development. The first soft X-ray ptychography paper imaged a fossil diatom at 517 eV in the “water window” (Giewekemeyer et al. 2010). Soft X-ray ptychographic tomography using phase contrast at a single wavelength has been reported (Venkatakrisnan et al. 2016). The first soft X-ray spectro-ptychography measurement was reported in 2011 (Beckers et al. 2011). Recently, multi-energy, soft X-ray spectro-ptychography has been used to characterize magnetotactic bacteria (Zhu et al. 2016), cement hydrates (Bae et al. 2015), nanocatalysts (Wise et al. 2016), lithium battery systems (Yu et al. 2015) and fuel cell membrane electrode assemblies (Hitchcock et al. 2016, Putz et al. 2016). Ptychography can be combined with tomography to produce high-resolution 3D nanostructure characterization. Holler *et al.* recorded a series of 2D ptychographic images of a porous Ta₂O₅ film sample at different tilt angles and achieved a 3D spatial resolution of 16 nm using 0.2 nm wavelength X-rays (Holler et al. 2014). Yu *et al.* have recently reported the first detailed, soft X-ray spectro-tomo-ptychography study in which the 3D chemical structure of Li_xFePO₄ battery electrode material was measured at the Fe L-edge, as a function of the charge/discharge state (Yu et al. 2017).

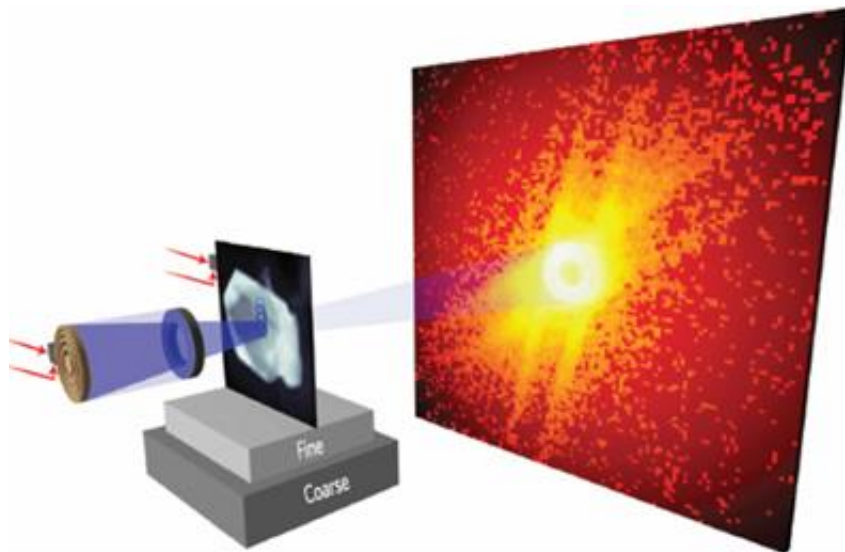


Figure 2.4 Schematic of ptychography. A 60 nm coherent soft X-ray spot, focused by zone plate, is scanned over the sample in 40 nm increments. (Shapiro *et al.*, 2014) (reproduced with permission from Springer Nature)

Ptychographic X-ray microscopy and tomography is well developed in the hard X-ray region (Dierolf *et al.* 2010, Esmaeili *et al.* 2013), while ptychographic soft X-ray imaging tomography is being developed at the ALS (5.3.2.1,11.0.2) and CLS (10ID1) (Hitchcock 2015). As part of this thesis, soft X-ray spectro-ptycho-tomography was performed using the Nanosurveyor I instrument at ALS bend magnet beamline 5.3.2.1. Recently the ALS COherent Scattering and MICROscopy (COSMIC) undulator beam line has completed commissioning. It is equipped with Nanosurveyor I and Nanosurveyor II ptychography endstations.

2.5 Laminography

Laminography is an alternative to tomography, which overcomes the problem of strong absorption by the sample at high tilt angles. For laminography, the rotational axis of a planar sample, is at an angle with respect to the optical axis of the x-ray beam (**Fig. 2.5 (a)**). Computed laminography (CL), has been developed specifically for imaging flat samples (Helfen et al. 2005). In CL, each projection has the same transmission depth, while in CT the path length increase with increasing tilt angle, so that, at some point, the absorption becomes saturated. For STXM samples with fixed OD of ~ 1 at normal incidence, this occurs at $60^\circ - 70^\circ$. This results in a wedge of missing data at high angles where projection images are not meaningful due to strong absorption. A missing wedge still exists in CL (**Fig. 2.5(b)**), but the missing information distribution is different and the excluded region is much smaller (Xu et al. 2012a). The technique has already been applied using hard X-ray synchrotron radiation (Helfen et al. 2005) and neutron imaging (Salvemini et al. 2015). Synchrotron radiation CT and CL of a wire-bonded integrated circuit have been compared (Helfen et al. 2011). The scanning range for CT was $\pm 60^\circ$, while for CL, the full $0-360^\circ$ range was sampled with a 60° tilt angle of the rotation axis relative to the X-ray optical axis. The reconstructed CL data showed better quality than CT due to more isotropic scanning around the through-plane direction of the specimen. High resolution CL has been used to perform 3D imaging of microsystem devices and to study the microstructure of materials (Helfen et al. 2011).

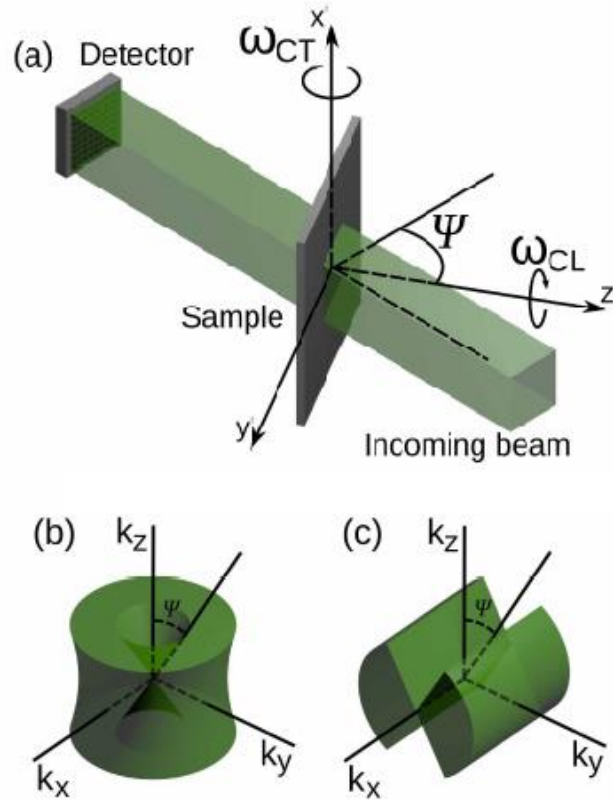


Figure 2.5 (a) CL and CT scanning geometries for the parallel-beam case. ω_{CT} presents the tomographic rotation axis and ω_{CL} is the laminographic rotation axis. The specimen coordinate frame (x', y', z') is defined with (x', y') spanning the in-plane direction and z' being parallel to the specimen surface normal. (b,c) missing wedges in CL and CT, respectively, for the missing-information angle $\Psi = 30^\circ$. (Reproduced with permission from (Xu et al. 2012a) The Optical Society)

Recently, 3D laminography based on Pt L_3 X-ray absorption fine structure (XAFS) was used to study PEMFC cathode catalyst layers under operational conditions (Saida et al. 2012). The distribution of Pt catalysts was observed and quantified from the difference in the intensity of X-ray absorption at 11.572 keV and 11.496 keV. Because of the inclination of the rotational axis, in the laminography reconstruction, a different spatial resolution was

achieved depending on the direction of the reconstructed three-dimensional image: the spatial resolution in the reconstructed X–Y plane was 1.5 μm , while the spatial resolution in the depth (Z) direction was about 5 μm .

2.6 Cryo electron tomography (Cryo-ET)

Cryo electron tomography is based on cryo electron microscopy, which was developed to reduce the impact of radiation damage for biological specimens (Murphy and Jensen 2007). With rapid freezing techniques, biological materials can be imaged in a fully hydrated, close-to-physiological state (Lučić et al. 2013). Cryo-ET have been applied to different biological samples, such as thick intact cells at lower spatial resolution (Ortiz et al. 2010), and cellular fractions in higher spatial resolution (Medalia et al. 2002).

2.7 Cryo STXM tomography

Reduced radiation damage in cryo scanning transmission X-ray microscopy was demonstrated by Maser et al. (Maser et al. 2000) in a soft X-ray cryo STXM developed by the Jacobsen group at the National Synchrotron Light Source NSLS-I, beamline X1A. Images from that study are reproduced in Fig. 2.6. A frozen hydrated specimen of 3T3 fibroblast with a thickness of up to 10 μm was measured at 100 K. The results demonstrated that biological specimens do not suffer mass loss or morphological changes at radiation doses up to about 10^{10} Gray when measured at 110 K. A tomography dataset measured at 24 angles and an energy of 516 eV was measured on mouse 3T3 fibroblasts on TEM grid. The combination of cryo tomography and X-ray absorption spectroscopy by cryo-STXM was also discussed (Wang et al. 2000), but 4D (STXM spectro-tomography) results were

never published from the Stony Brook cryo-STXM at NSLS-I beamline XIA, which was dismantled in 2014.

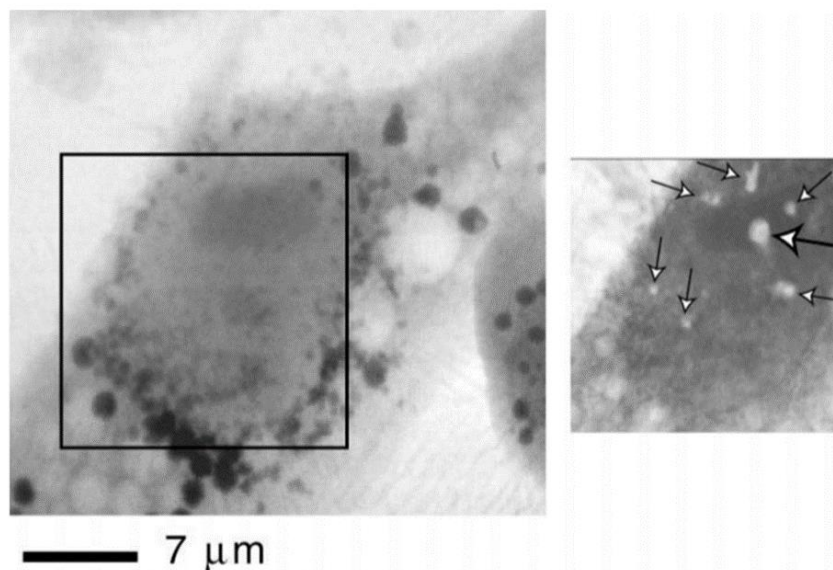


Figure 2.6 At a temperature of 110 K, an intense, 0.2 μm beam spot was left stationary on several locations (noted with arrows) of the biological specimen for several minutes. The image at left was acquired after 10^{10} Gray exposures at these spots, no discernible difference was found compare to an initial image. The specimen was then slowly warmed up to room temperature. The smaller image at right shows the same area as the black box region in the left image after the specimen was slowly warmed up to room temperature. The heavily dosed regions lost significant mass, presumably due to the reaction of radiation-produced free radicals as the temperature approached room temperature. (Maser et al. 2000) (reproduced with permission from John Wiley and Sons)

2.8 STXM and Near Edge X-ray Absorption Spectroscopy (NEXAFS)

The image contrast in Scanning Transmission X-ray microscopy (STXM) is based on near-edge x-ray absorption fine structure (NEXAFS) (Stöhr 1992). Prior to availability of synchrotron radiation X-ray absorption spectroscopy was described in terms of absorption edges, which are the onsets of inner-shell ionization. With the development of

synchrotron radiation and high performance soft X-ray beamlines, tunable X-rays can be used to measure electronic excitation and ionization processes in which an inner-shell electron is excited to unfilled molecular orbitals or conduction bands (see figure 2.7). It is possible to identify the chemical species in materials and sometimes its phase (figure 2.7 (c)), from the fine details of the absorption spectrum at each edge.

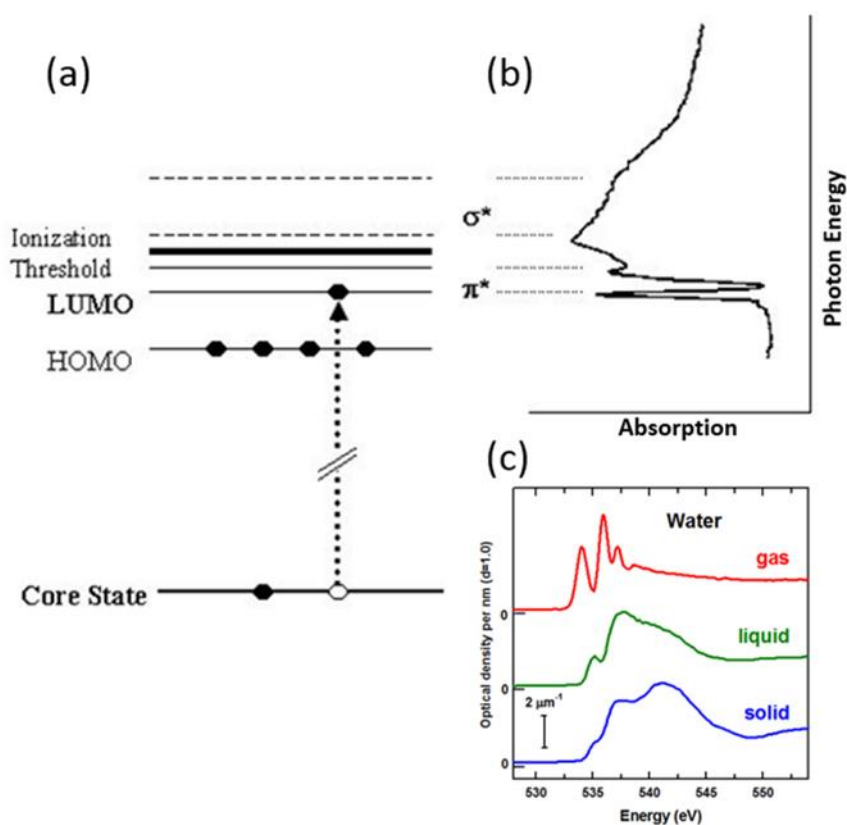


Figure 2.7 (a) The near edge x-ray absorption fine structure (NEXAFS) arises from electronic transitions of an inner shell electron to energy levels (orbitals in molecules, bands in solids), (b) typical spectrum, (c) O1s spectra of gas, liquid and solid water.

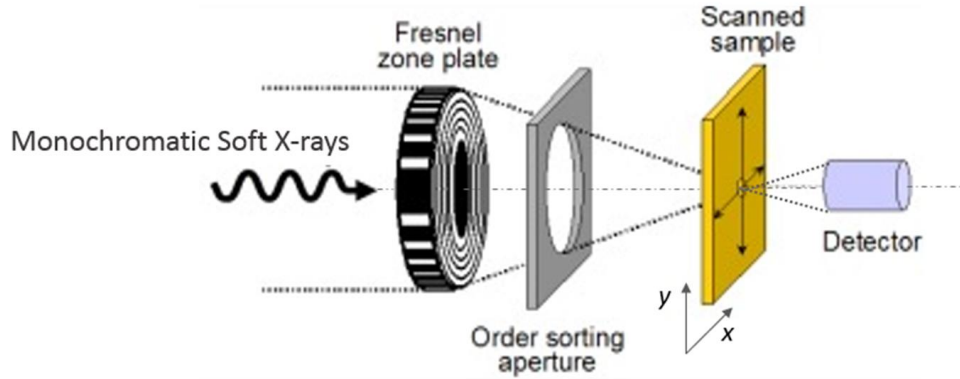


Figure 2.8 Schematic diagram of STXM.

A schematic diagram of STXM is shown in Figure 2.8. A Fresnel zone plate (ZP) is used to focus monochromatic X-rays, and the focused first order light focused is selected by an order sorting aperture (OSA). The size of the focal point (Δr) depends on the properties of the zone plate ($\Delta r \sim 1.22\delta_r$, where δ_r is the width of the outmost zone). At present the typical STXM spot size is 30 nm, while the record published spatial resolution in soft X-ray STXM is 10 nm (Chao et al. 2012). The focal length (f) depends on the ZP properties and photon energy as follows:

$$f = \frac{D\delta_r}{\lambda} \quad (2.1)$$

where D is the zone plate diameter, δ_r is the outmost zone width, λ is the wavelength of the incident light [E (eV) = $hc/\lambda = 1,240/\lambda$ (nm)].

An image is generated by detecting the transmitted photons while a thin section of a specimen is raster-scanned in (x,y) at the focus of the x-rays. The transmitted photons are measured by a detector consisting of a phosphor converter of X-ray to visible light converter and a high performance photomultiplier tube (PMT), operated in single photon

counting mode. The X-ray absorption spectrum (XAS) is measured by recording the transmitted signal as a function of photon energy. XAS can be measured at a point, along a line, over an area, or through a volume. In the “stack” method (C. Jacobsen et al. 2000) , images are acquired at a sequence of closely spaced intervals in X-ray energy over a small spatial region. The transmitted photon intensity is converted to optical density using Lambert - Beer’s law:

$$OD = \ln(I_0/I_t) \quad (2.2)$$

Where I_0 is the incident X-ray flux, and I_t is the flux transmitted through the sample. The OD can be related to the sample density and thickness (Figure 2.9).

$$OD = \mu(E)\rho t \quad (2.3)$$

where $\mu(E)$ is the mass absorption coefficient at X-ray energy E , ρ is the density and t is the sample thickness.

The mass absorption coefficient for a given material is an inherent characteristic. It can be derived from measurements of the NEXAFS spectrum of the pure material. The OD spectrum of 1 nm of pure material (OD1) is used for quantitative analysis. The OD is proportional to sample thickness t . The optimum OD for a good quality spectrum is ~ 1 . To achieve this in the soft X-ray region (150-1500 eV), samples should be thin. For $\rho \sim 1 \text{ g/cm}^3$ materials at the C 1s edge, the optimal thickness is 80-150 nm, although this varies with the nature of the sample, its density, and the incident energy.

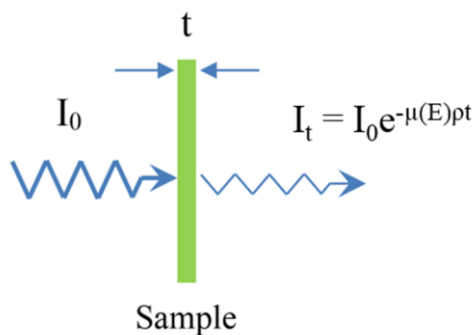


Figure 2.9 The transmitted photon intensity I_t is related to the incident photon intensity I_0 , mass absorption coefficient μ , the sample density ρ , and the sample thickness t .

2.9 Radiation damage and dose estimation

For both electron microscopy and X-ray microscopy, radiation damage can be a significant concern since it results in chemical modification (often of a reductive character) and / or mass loss. The exact nature of the radiation damage will depend not only on the elemental composition of the raw material but on its bonding, its physical state, and its environment. Radiation damage of various organic and inorganic materials has been studied for decades (Cosslett 1978, Glaeser and Taylor 1978, Egerton et al. 2004, Egerton 2013). Polymers can be cross-linked or degraded, which will also change the physical properties of these polymer (Egerton et al. 2004). The factors that affect radiation damage have also been examined. The amount of radiation damage is proportional to the absorbed dose (dose is absorbed energy/mass).

Soft X-ray spectromicroscopy is increasingly being applied to organic materials (Kaznatcheyev et al., 2002; Hitchcock et al., 2005; Ade & Hitchcock, 2008) and biological

samples.(Dynes *et al.*, 2006a, Dynes *et al.*, 2006b). Using near edge X-ray absorption spectroscopy (NEXAFS), the changes caused by radiation damage can be quantified. Compared to electron energy loss spectroscopy in transmission electron microscopes (TEM-EELS), for similar amounts of useful analytical information, it has been shown that STXM-XAS is about 100-1000 times less damaging than TEM-EELS (Rightor *et al.* 1997, Wang *et al.* 2009b) or TEM-EDX (Melo *et al.* 2017). For example, radiation damage of polyethylene terephthalate (PET) by soft X-rays and high energy electrons was examined by (Wang *et al.*, 2009b). Soft X-ray damage to PET was made by patterned exposure at 300 eV and at 531.6 eV for a series of exposure times. Electron beam damage was generated by 80 keV electrons and analysed by STXM. (Note, although not stated explicitly in Wang *et al.* (2009), efforts to measure the spectral changes as a function of exposure/dose by TEM-EELS were not successful as 1 critical dose of damage was induced by the time the first EELS spectrum was measured). The spectra of undamaged and damaged PET at the C 1s and O 1s edges are shown in Fig. 2.10. It was found that the spectral changes were similar for damage by electrons and X-rays, indicating the radiation chemistry is dominated by secondary processes, not the primary event. The changes due to radiation damage are plotted as a function of dose in Figure 2.11. The results show that electron beam damage has a similar critical dose as X-ray radiation damage to PET. However, when compared to the dose needed for analytically useful spectral information, X-rays achieve similar results with ~100 times lower dose. Radiation damage calculations can be found in Chapter 5.

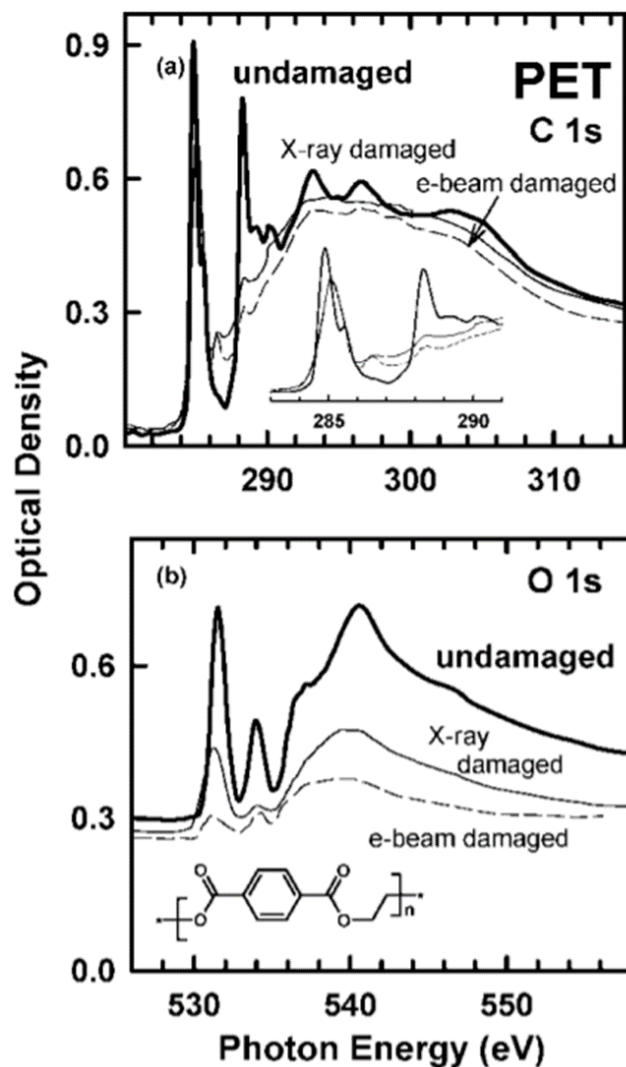


Figure 2.10 NEXAFS spectra of undamaged and soft X-ray and electron beam damaged PET. (a) C 1s edge and (b) O 1s edge. In each plot the solid thick line is the undamaged spectrum, the thin solid line is the X-ray spectrum from a region damaged at 3 (C 1s) or 2 (O 1s) times the critical dose, and the thin dashed line is the electron beam damaged spectrum from a region damaged at 2 times the critical dose. The insert shows an expanded region of the C 1s spectra, illustrating there are significant changes in the shape of the C 1s $\rightarrow \pi^*$ peak (~ 285 eV) associated with Ph-COOR bond breaking. (Wang *et al.*, 2009b) (reproduced with permission from American Chemical Society)

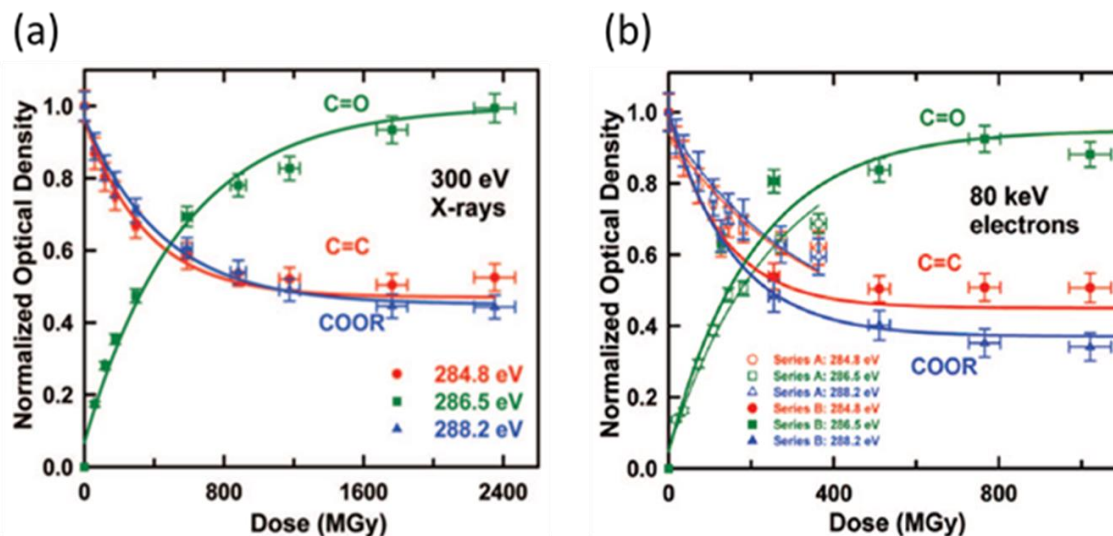


Figure 2.11 Plots of the normalized optical density as a function of radiation dose for PET damaged at 284.8, 286.5, and 288.2 eV by exposure to (a) 300 eV X-rays; (b) 80 keV electrons (Wang *et al.*, 2009b) (reproduced with permission from American Chemical Society)

To record high resolution images and discover the true chemical distribution, the measurements should be made with a dose significantly smaller than the critical radiation dose (perhaps less than 20%). Glaeser *et al.* (1978) point out that at cryogenic temperatures (< 100 K) the rate for radiation damage to hydrated, large biomolecules, particularly proteins can be reduced as much as 10-fold compared to the damage rate at room temperature (Glaeser and Taylor 1978). Cryo-ET and cryo STXM tomography was introduced in this chapter.

2.10 Tomography data analysis

Image alignment, conversion to OD, spectral analysis and chemical map generation was done using **aXis2000** (Hitchcock 2018, <http://unicorn.mcmaster.ca/aXis2000.html>).

Mantis (Lerotic et al. 2014, <http://spectromicroscopy.com/>) was used for 3D reconstruction using Simultaneous Iterative Reconstruction Technique (SIRT) and Compressed Sensing (CS) algorithms. **ImageJ** can also be used for alignment and 3D reconstruction. Weighted back projection (WBP), and SIRT reconstructions were carried out using **TomoJ**. The principles of WBP and SIRT are shown in **Figure 2.12** (Bilbao-Castro et al. 2006). For WBP, the specimen mass is projected back into a reconstruction volume (backprojected). For iterative reconstruction algorithms, the projection and backprojection calculation will iterate n times to optimize the reconstruction results. For both WBP and SIRT, increasing the # of tilt angles number will increase the reconstruction quality. A smaller angular range or # of angles can give as good results by SIRT, as compared to a full data set analysed by WBP (Wu et al. 2017).

The principle of Compressed Sensing (CS) is presented in **Fig. 2.13** (Shalaby et al. 2017). Schematic illustration of the compressed sensing tomographic reconstruction procedure can be found in Fig. 4.1. A detailed comparison of the relative reconstruction quality of CS, SIRT and WBP is presented in Chapter 4. The angle range effect for the reconstruction quality has also been evaluated in Chapter 4. After reconstruction, the 3D /4D volumes were rendered using **Avizo** in both volume based and surface based procedures. The threshold of the imaging was set using auto Otsu thresholding (Otsu 1979). Volume fraction, porosity, co-localization of components are calculated on surface base in Avizo. Details for data analysis are described in Chapter 3.

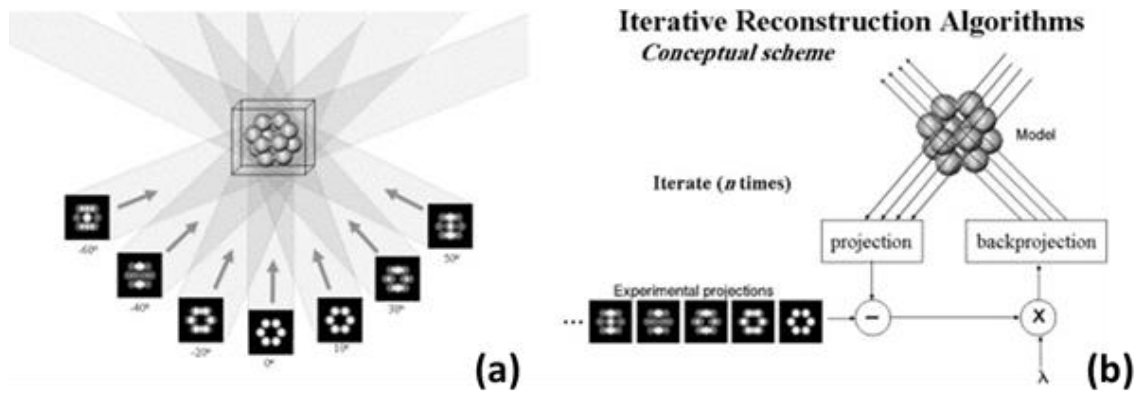


Figure 2.12 3D reconstruction algorithms. (a): WBP. (b): Iterative reconstruction algorithms.

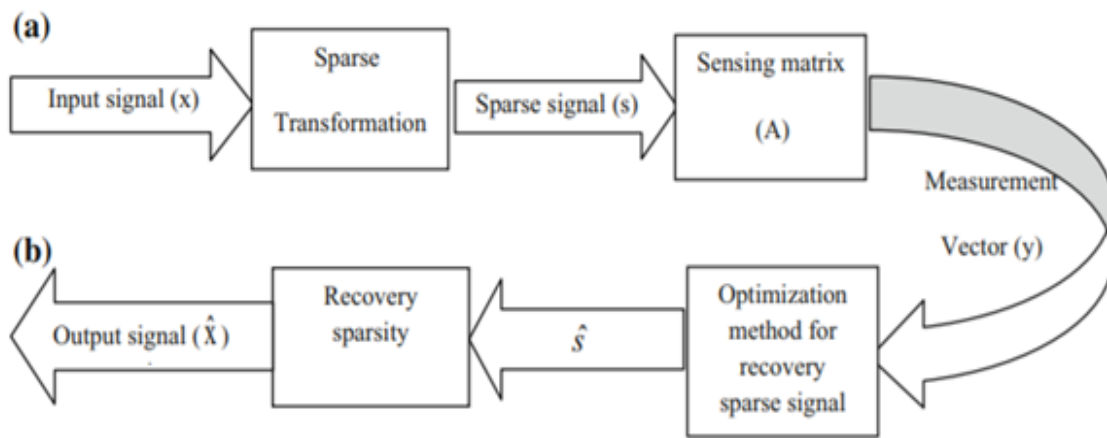


Figure 2.13 Compressed sensing model.

Chapter 3

Experimental Methods

Chapter 3 describes in detail the materials used for this study, sample preparation, data acquisition and data analysis procedures,

3.1 Materials and sample preparation

3.1.1 Polymer electrolyte membrane fuel cell samples

Several different fuel cell samples were supplied by our collaborators at the Automotive Fuel Cell Co-operation Corporation (AFCC). **Figure 3.1** shows a scanning electron microscopy (SEM) image of a cross-section of a fuel cell membrane electrode assembly (MEA). The MEA sample is a catalyst coated membrane (CCM), combined with anode and cathode gas diffusion layers (GDL). The CCM consists of a proton conducting, electrically insulating membrane with two catalyst impregnated electrodes, the anode and the cathode, on each side of the membrane. Samples for STXM and ptychography were prepared by Marcia West in the electron microscopy facility in the Department of Pathology, McMaster University. The CCMs were cut into small rectangular pieces and embedded in an amine epoxy resin (called TTE for short), prepared by mixing trimethylolpropane triglycidyl ether and 4,4'-methylenebis(2-methylcyclohexylamine) in a 1:1 weight ratio and cured at 70 °C overnight (Li et al. 2009). The embedded samples were microtomed using a DiATOME diamond knife at room temperature with a Leica Ultracut UCT to provide sections with nominal thicknesses between 100 to 300 nm. The sections

were transferred from the surface of a water bath to formvar coated 3 mm diameter Cu TEM grids.

A PEMFC model sample, prepared by Dr. Viatcheslav Berejnov (AFCC) in collaboration with Marcia Reid (McMaster), was used to evaluate 3D reconstruction and the strength of ptychographic scattering signal from soft polymeric materials. The PEMFC model system comprised two layers of polymer films. One layer is Pt decorated carbon fibers embedded in TTE epoxy, the other layer is Teflon™ fibers embedded in TTE epoxy. The two layers were microtomed individually and transferred to a formvar coated TEM grid layer by layer. The two layers are positioned in a criss-cross fashion. The sample contains both 2-layer and 1-layer regions, as shown in **Figure 3.2**.

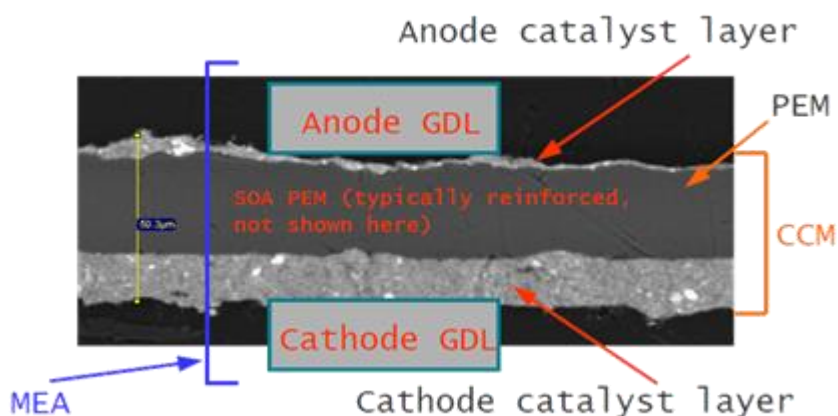


Figure 3.1 Scanning electron microscope image of a polymer electrolyte membrane fuel cell (PEMFC) membrane electrode assembly (Image supplied by Darija Susac, AFCC)

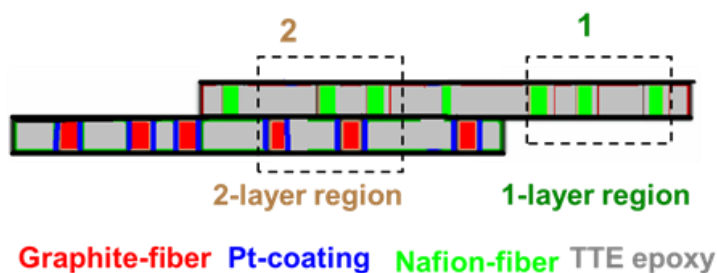


Figure 3.2 Cartoon of structure of model sample used to evaluate the ability of STXM tomography to measure 3D distributions and ptychographic to measure non-crystalline soft matter with improved spatial resolution. The dashed boxes indicate the types of areas measured for the data presented in chapter 5

3.1.2 Aerogel

Several different aerogel samples were supplied by Jon Lee from Lawrence Livermore National Laboratory (LLNL). The alumina (Al_2O_3) aerogel samples are prepared by a two step sol-gel process method. Following supercritical drying, the monolith aerogel parts had a bulk density of $\sim 0.04 \text{ g/cm}^3$ versus $\sim 4 \text{ g/cm}^3$ from bulk Al_2O_3 . Coating of the alumina aerogels with ZnO was achieved via atomic layer deposition (ALD) according to established protocols (Poco et al. 2001, Biener et al. 2011a, Biener et al. 2013). The alumina aerogels were exposed to 6 or 25 ALD cycles composed of ZnEt_2 and H_2O precursor half-cycles in a warm wall reactor (wall and stage temperature of $110 \text{ }^\circ\text{C}$). To facilitate handling, the aerogels were kept in their molds during ALD coating. Long pump (20 s), pulse (500 s at $\sim 133 \text{ Pa}$), and nitrogen purge cycles (500 s) during each ALD half-cycle were used to promote uniform coating throughout the porous material. The aerogel samples were prepared for STXM and ptychography measurement by two different methods. First, the sample was crushed using a clean scalpel blade, then dispersed in distilled water to get a low concentration dispersion of aerogel powder. A few μL of the

solution was dropped on a formvar coated TEM grid and air dried. After drying, a single grid strip with the region of interest was excised using a single pair of a new, sharp scalpel. The second aerogel sample preparation was focused ion beam (FIB) milling, carried out by Travis Casagrande in the Canadian Centre for Electron Microscopy (CCEM). A 5 nm carbon layer was deposited on a piece of the aerogel for thermal conduction. The sample was FIB sectioned into a $20\ \mu\text{m} \times 30\ \mu\text{m} \times 30\ \mu\text{m}$ cube as shown in **Fig. 3.3**, and then mounted on the tip of a strip of TEM grid. The grid strip was then glued to a brass pin for STXM tomography or to the sample support piece for ptychography, and mechanically attached to the STXM or ptychography rotation system. The preparation of the aerogel for laminography was similar, except the full 3 mm Cu grid was used. A formvar film was placed on top to prevent the powder from being ejected from the formvar by electrostatics (X-ray absorption charges samples positively).

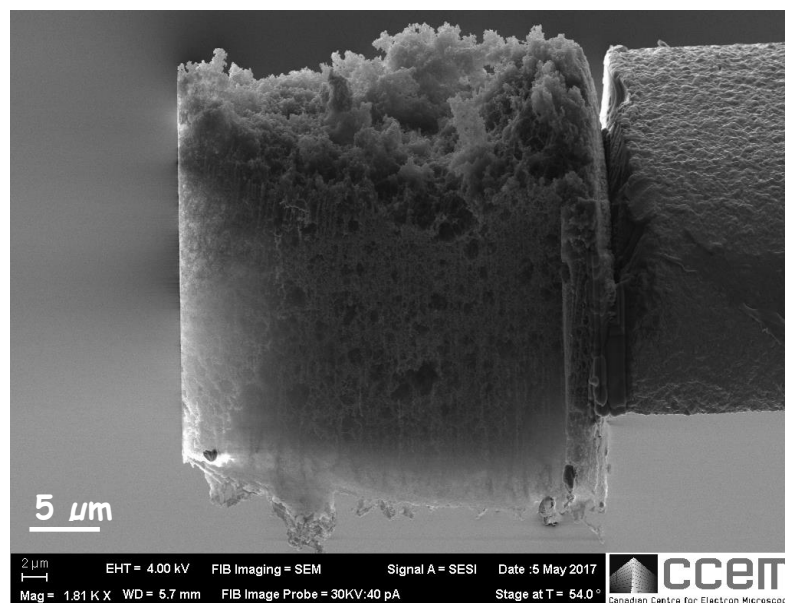


Figure 3.3 Scanning electron microscope (SEM) image of FIB sample of ZnO/Al₂O₃ aerogel sample

3.2 STXM Data acquisition and analysis

STXM records transmission signals in different modes. Point scan mode is used to record the spectrum of one or multiple points. The line scan spectrum mode records a line at a set of photon energies, resulting in a spectrum at each point along the line. For the image mode one or more spatial regions are defined in the STXM control software using either graphical or numerical inputs to define the center position and the size of each rectangular region. The step size (distance in nm between adjacent pixels) determines the spatial sampling of the image. If a single energy is selected then the images will only be recorded at that energy. By setting a series of energies, a spectral image series, also called a stack (Jacobsen et al. 2000), will be recorded (see Fig. 3.4). The data is recorded image by image at the sequence of energies, rather than recording a full spectrum at each point (as is done in EELS spectral imaging (Möbus et al. 2003, Kimoto et al. 2007)). The spectrum at each point or an arbitrary region in the image can be obtained using post-acquisition analysis. The user defines the centre position, X, Y size, pixel spacing, photon energies and a single per-pixel dwell time. For image mode acquisitions, the typical dwell/pixel is 1 ms, although larger dwells are used if better statistical precision is required. The STXM_Control software has provision for automatically adjusting the zone plate position so as to use a controlled defocus of the spot size, which is very useful to reduce the radiation damage, although at the expense of lowered spatial resolution.

Image stacks are aligned using either the ‘Zimba’ or ‘Jacobsen stack analyse’ Fourier cross-correlation methods which are implemented in aXis2000. The I_0 must be measured from a region without the components of interest, but with all other aspects, including any sample support material. For the PEMFC MEA samples on a formvar

support, the spectrum of a region of formvar is used for the I_0 . Having the I_0 region in the stack area is the best type of I_0 . The I_0 is used to convert transmission images into optical density (OD) images (see Eqn. 2.2), on either a single image basis or for a full stack. Spectra can be extracted from single component regions of an OD stack and used as reference spectra to generate maps for each chemical component, using either the singular value decomposition (SVD) (Koprinarov et al. 2002, Hitchcock et al. 2005, Ade et al. 1992) or stack fit methods implemented in aXis2000. The SVD algorithm, which is used in both SVD and stack fit procedures, is an efficient matrix method equivalent to an optimized least squares fit for cases where the data is highly over-sampled, as is always the case in STXM. There are $10^4 - 10^5$ spectra in a typical stack, but there is usually less than 6 statistically significant components. For stack fit, there is a constant (energy independent) term, which accounts for background in the spectra, which can arise when the I_0 is recorded at a different time than the stack. In the SVD method, the energy independent term is not included. If the intensity scales of the reference spectra are converted to an absolute response (OD1, or OD per 1 nm thickness of the material at standard density) then the gray scale of the resulting component maps gives absolute thickness in nm (Hitchcock 2012). Sets of component maps can be combined into a color composite map to show the relationships among the spatial distributions of the components. Only 3-component Red, Green, Blue (RGB) composites are implemented in aXis2000, but a larger number of components can be represented using other image processing packages such as PaintShop, ImageJ etc.

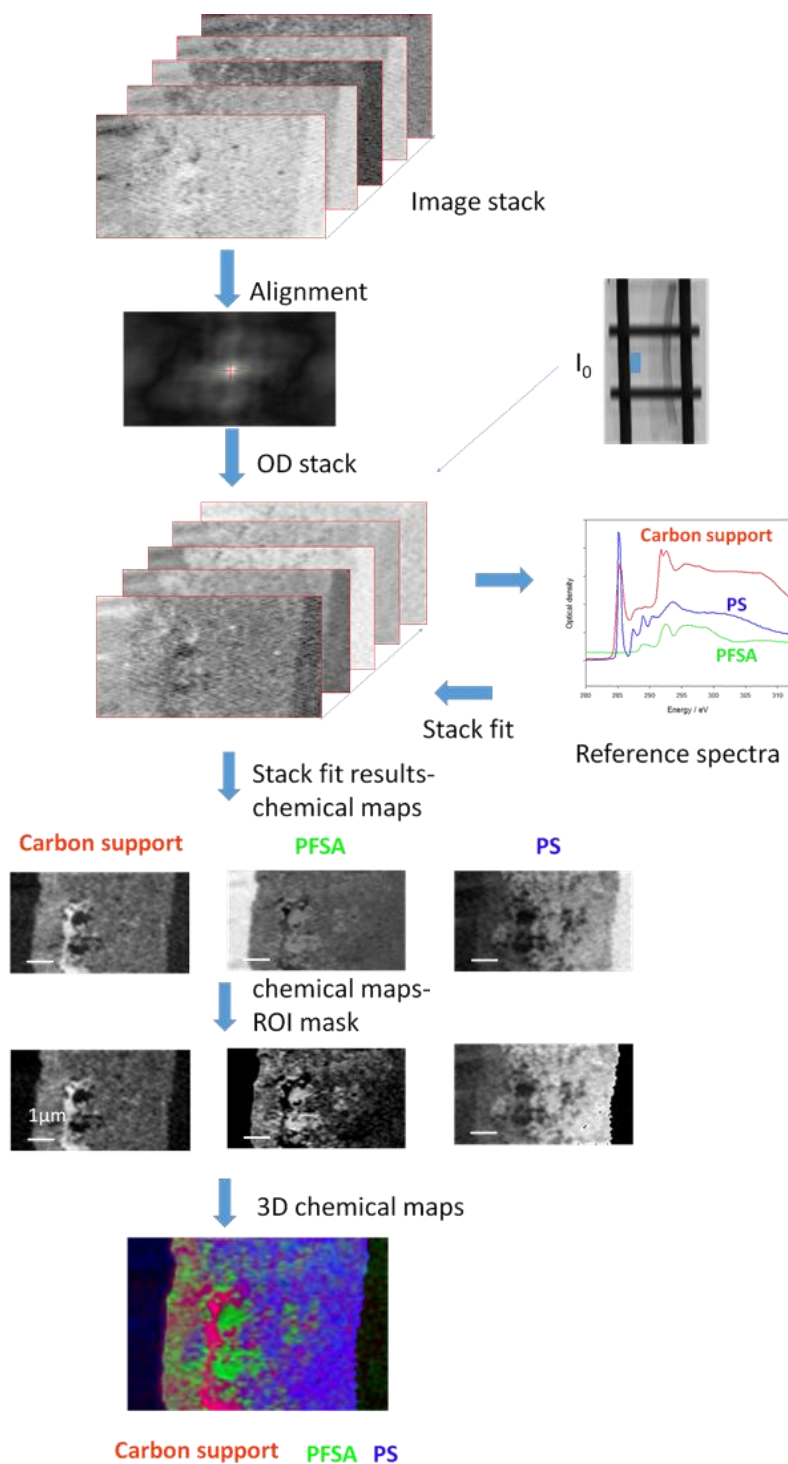


Figure 3.4 Outline of processing of a STXM stack process of an MEA cathode sample. The image stack is measured in transmission mode by STXM; stack alignment in “Zimba” or “Jacobsen”; convert to OD stack; generate component spectra; stack fit using reference spectra; ROI mask; 3D chemical maps in color map

3.3 STXM Tomography

3.3.1 Experimental set up

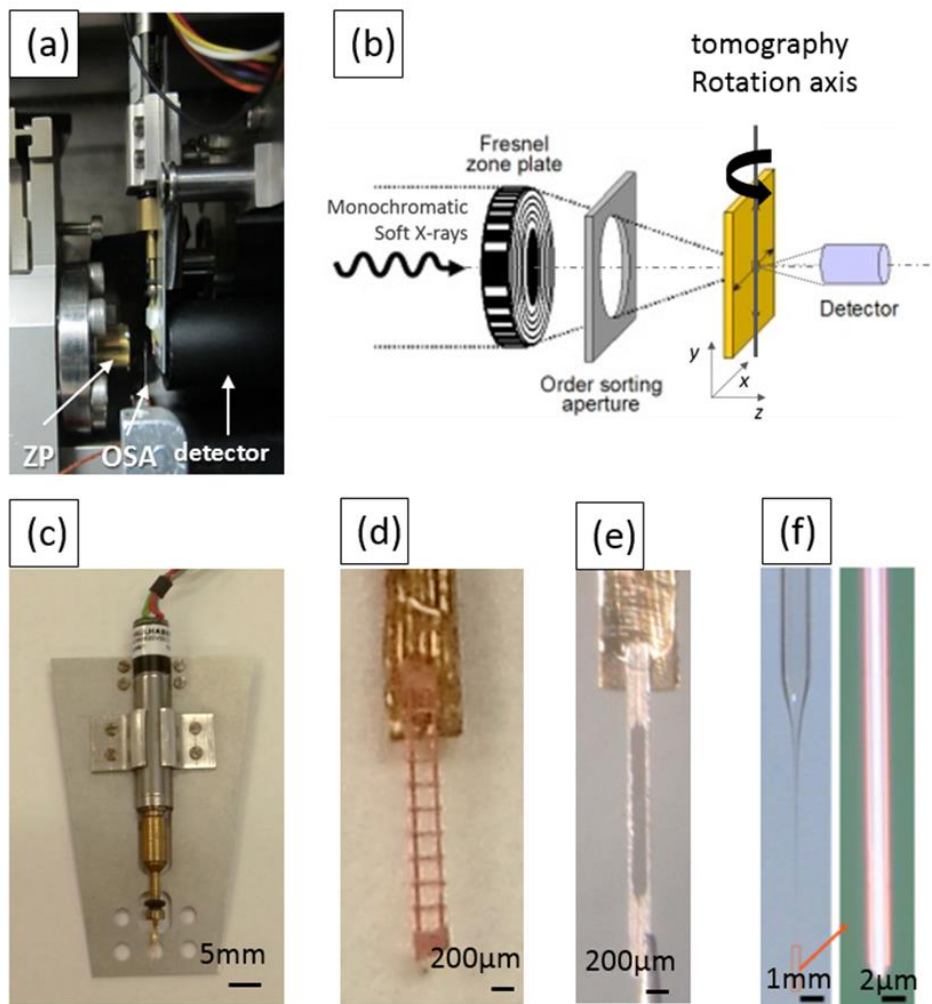


Figure 3.5 (a) The STXM tomography stage mounted in ALS STXM 5.3.2.2; (b) schematic diagram of STXM tomography; (c) STXM tomography stage is composed of a stepper motor attached to a STXM sample plate. The sample is glued to the tip of a 0.8 mm diameter brass sample pin which is held in a chuck (taken from a mechanical pencil) attached to the motor shaft. STXM tomography samples: (d) TEM grid strip; (e) Luxel wet sample pin; (f) pulled glass capillary.

The STXM angle-scan tomography rotation stage used in this thesis (**Fig.3.5 (c)**) was made by Dr. Martin Obst while he was at Tuebingen University. A rotation motor (Faulhaber ADM0620, Faulhaber, Schoenaich, Germany) is used. The 0.8 mm wide sample pin is inserted in a chuck from a mechanical pencil which is mounted on the motor shaft. The orientation of the pin can be adjusted with tweezers under visual light microscopy (VLM), and aligned to the rotation axis, which is perpendicular to the incident X-ray beam.

3.3.2 Sample preparation

There are various approaches for preparing samples for tomography. One is to inject fluid samples into pulled glass capillaries or carbon nanopipettes (Kim et al. 2005, Johansson et al. 2007) (**fig.3.5 (f)**). The diameter of the tip of the glass capillaries or carbon nanopipettes can be thinned down to a few micrometers (glass) or a few hundred nanometers (carbon nanopipettes), so these samples can be rotated over the full 360°, and thus can be used to collect datasets without missing wedge artifacts. However it is not possible to insert microtomed samples into glass capillaries or carbon nanopipettes. Another method is to cut a single strip from a TEM grid, then mount the strip on the tip of the brass rod (**Fig.3.5 (d)**). To avoid conflicts between the sample and the OSA during tomography measurement, the strip has to be mounted in the middle of the brass pin, and aligned to be co-linear with the axis of the brass pin. A needle frame “tomo-pin” from Luxel (**fig.3.5 (e)**) in which the sample is enclosed by thin polyimide and formvar films, allows studies of wet samples (Schmid et al. 2014, Schmid et al. 2016). The latter two approaches were used in this project for flat film samples. For the TEM strip method, a slice of a PEMFC MEA is cut by ultra-microtomy to a thickness of 100~300 nm (the ultra-microtomy is performed by Marcia Reid, Dept of Pathology, McMaster), and mounted on a

3 mm TEM grid. The region of interest is identified by visible light microscopy (VLM). Then the strip containing that region is carefully excised using a new scalpel blade. **Fig. 3.6** shows the process of wet cell assembly. The MEA sample was mounted on the 1-sided (bottom) polyimide film Luxel window by Marcia Reid, then a formvar film was added on top, to form a sealed cell. A 1 mL syringe connected to a water filled glass micropipette is used as a micro-injector. After injection, the top and bottom fill ports are sealed with epoxy. Wet cell samples are stored in a humid box to reduce the chance of drying out before the measurements can be made.

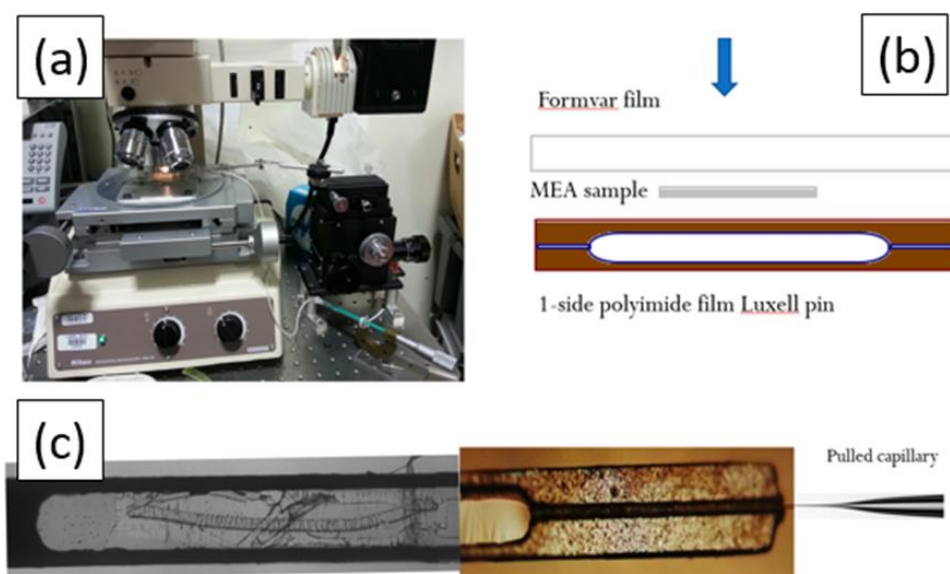


Figure 3.6 (a) The setup for injecting water to make a Luxel tomo wet cell (ALS 11.0.2). A 1 mL syringe connected to a glass micropipette is used as a micro-injector. (b) MEA sample is mounted on the 1-side (bottom) polyimide film Luxel window, then a formvar film is added on top, which forms a closed window. (c) The tip of the glass capillary should stick into the channel of the Luxel pin to define the water path.

3.3.3 Data acquisition

For STXM tomography on flat samples, due to limited penetration at high angles, the maximum rotation angle measured was $\sim 80^\circ$, and usually the angle range is limited to $\pm 70^\circ$. In order to minimize radiation damage and acquisition time, a 3° to 6° degree angle increment was initially used for a total of 30~40 tilt angles. This is the minimum number needed for meaningful reconstructions using the weighted back projection (WBP) or simultaneous iterative reconstruction technique (SIRT) algorithms. As part of this thesis, I worked with scientists in Paul Midgey's group (Cambridge) and with Mirna Lerotic (2nd Look consulting) to develop methods to apply a compressed sensing (CS) algorithm for reconstruction of STXM tomography data sets (see chapter 4, Wu et al. 2017). Because the CS reconstruction algorithm is more efficient and robust relative to missing wedge artefacts, 8° to 10° degree angle increments can be used, for a total of only 14-16 tilt angles, which was a key factor in developing approaches allowing tomography of PEMFC MEAs with minimal radiation damage. Energy stacks (4 or more energies) or stack maps (2 or 3 energies) are measured at each tilt angle. Since the energy scales of synchrotron beamlines are often out-of-calibration by 0.5-2 eV, a full spectroscopy stack is first measured and analysed to determine the correct energies. The stack is taken in a similar, or sometimes the same, region as the tomography area, and 20-60 images are measured at closely spaced energy intervals to get good spectra. When the tomography area is measured with full stack spectroscopy (see chapter 5, Wu et al. 2018), the X-ray beam is defocused to 100-200 nm and a step size equal to the spot size is used so as to minimize radiation damage.

Many energy (20-30) spectra are obtained in full stack tomography (e.g. acrylate-filled PS microspheres in a CNT nanopipette, presented in chapter 4, (Wu et al. 2017). In the

stack map tomography approach, images are acquired at a chemically specific peak energy and an energy below the onset of the inner shell absorption edge is used for each species of interest. For analysis of PFSA in PEMFC cathodes, 278 / 285.3 eV for C-support (for PEMFC embedded in TTE resin) and 684/ 694 eV or 684/ 704 eV were used.

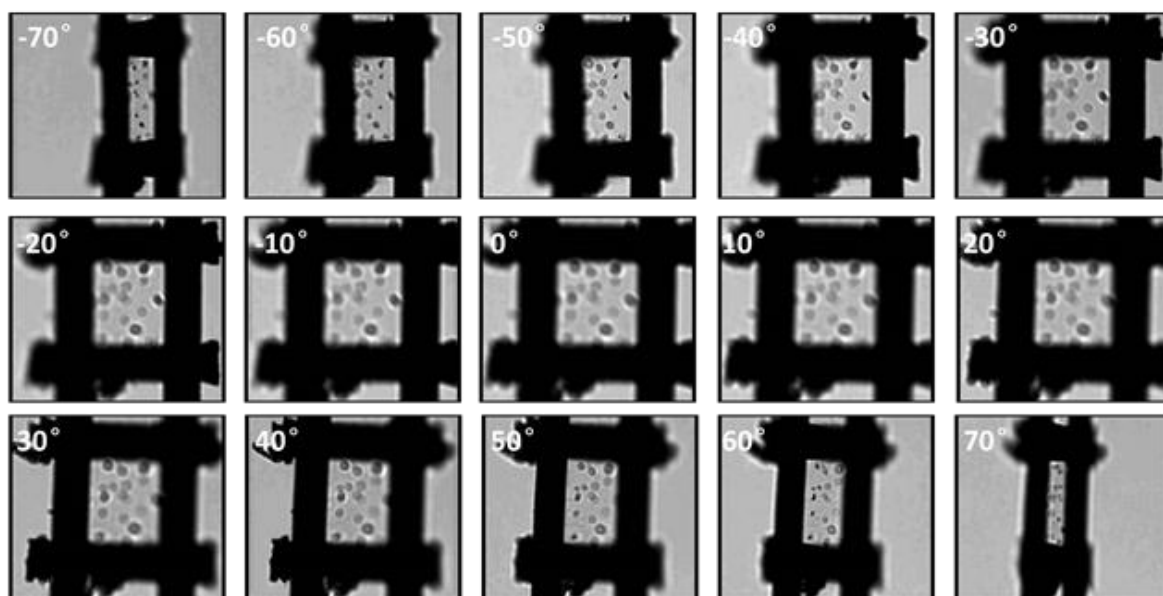


Figure 3.7 Optical images of TEM grid strip sample rotation

For the ambient STXM, VLM has been used to align the sample to minimize the wobble of the sample rotation. The rotation of the sample can be observed under VLM (**Fig. 3.7**), the region of interest of the sample can be adjusted to be close to the eucentric center by using tweezers to carefully bend the grid strip while it is attached to the brass tomo pin. Since there is no eucentric adjustment system for the ambient STXM tomography set-up, after each step of rotation, the (x,z) position of the sample will change and has to be found manually. A predictor excel sheet was used to predict the trajectory of the rotation. To

calibrate the (x,z) prediction spreadsheet, the coordinates of a fiducial point are recorded at 3 widely spaced tilted angles (-50, 0, +50), and then equations for an ellipse in 3D are used to predict the intermediary positions. **Figure 3.8** plots the difference between the predicted and measured (x,z) positions (NB the y-axis is along the rotation axis and there is very little change in its value with tilt angle). The predicted positions match the measured positions quite well, with a standard deviation in x of $\pm 6 \mu\text{m}$, and in z of $\pm 4 \mu\text{m}$. In order to obtain an accurate prediction, the 3 pre-known points have to be dispersed. Errors in the actual angle of the 3 selected points will decrease the accuracy of the prediction. In principle the prediction can reduce the measurement time for finding the sample after changing the tilt angle. In practice, because the numerical scales are changed each time STXM_control is stopped and re-started, and since software crashes happen a few times in each 8-16 hour tomo measurement, it usually turned out to be easier to ‘chase’ the displaced sample. In general, the practical protocol of tomography measurement is as follows:

1. Change to the **next tilt angle** using the stepper motor controller;
2. **Find** the region of interest;
3. **Frame** by imaging the tomography region trying to centre on the rotation axis;
4. **Focus** to the middle of the tomography region;
5. **Check** by doing an undersampled scan to check the position and the focus;
6. **Run** the multi energy stack with full pixels at this tilt angle.

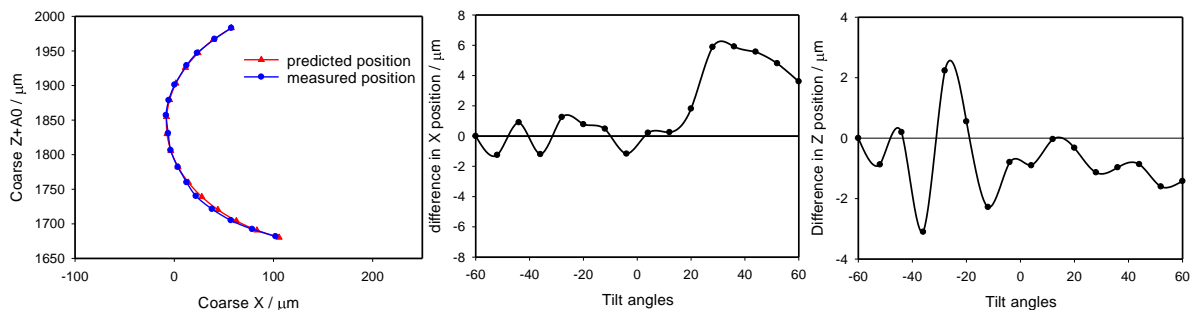


Figure 3.8 (a) Comparison between predicted and measured X and Z positions of a fiducial point in a STXM tomography measurement. (b) Difference in X, (c) Difference in Z.

3.3.4 Data analysis procedures

Figure 3.9 outlines the workflow for analysis of STXM tomography and spectrotomography data. The initial steps of analysing STXM spectrotomography data are carried out in aXis2000 (Hitchcock 2018). The stack map images at each tilt angle are aligned and converted to OD using a suitable I_0 signal. In some cases, such as the FIB aerogel sample (Chapter 6), a suitable I_0 region existed in the region measured. If not, the I_0 was acquired before and after (and often in the middle) of the tomography measurements by measuring a point spectrum on a suitable no-sample area, such as the formvar support, in the case of grid strip measurements of MEAs supported on formvar. Chemical maps at each angle are obtained from the difference of the ON (typically a peak energy, but sometimes a continuum energy) OD image and OFF (pre-edge energy) OD image. If a full stack is measured at each tilt angle, each energy stack is aligned, converted to OD, and fit to suitable reference spectra to obtain a set of chemical component maps at each tilt angle. In some cases OD difference maps would be converted to absolute thickness (h) using $\Delta OD1$ values from suitable OD1 reference spectra, where $h = \Delta OD / \Delta OD1$. Angle stacks

consisting of chemical maps generated at every angle for each component are then assembled using a stack list of the file names. The usual energy axis in a stack is replaced with the values of the tilt angle of each image. This angle stack is then aligned in aXis2000 using the ‘Zimba’ or ‘Jacobsen stack analyse’ Fourier cross-correlation methods. Usually this must be followed by an additional manual alignment in aXis2000, which lets the user identify the position of the same fiducial point in the image / map at each tilt angle. aXis2000 is then used to convert the (*.ncb) format angle stack to a (*.mrc) file. 3D reconstruction software, such as Imod, TomoJ or Mantis, is then used for final alignment and reconstruction. Imod (as implemented in the ImodJ plug-in in ImageJ) uses alignment by a robust fitting method, which gives lower or no weight to points with high deviations from the fit (residual error). Standard reconstruction algorithms such as Weighted Back Projection (BWP) and Simultaneous Iterative Reconstruction Technique (SIRT) as implemented in the ImodJ and TomoJ plug-ins to ImageJ are used to reconstruct a 3D model of the volume from the optimally aligned image or chemical map tilt series. Generally, in order to get high quality of 3D reconstruction results, 30-40 tilted images are needed if SIRT is used, and many more (90-180) for high quality results using BWP. The largest number of tilt angles measured in my STXM tomography studies was 36 (see **Table 3.1** for a listing of ALL my data sets).

Table 3.1 Summary of tomography data sets measured for this thesis

Date	measurement	energies	angles	unicorn/data/xrm	reconstruction results/method
17/06	cryo-STXM MEA 11 GDE	684eV/694eV	-70° - +65°/10°	/CLS-cryo-STXM/2017/17-06/06-08/0tomo	√ CS
17/05	cryo-STXM MEA 11 GDE	680eV/710eV	-60° - +20°/10°	/CLS-cryo-STXM/2017/17-05	√ CS
17/05	ambient STXM FIB aerogel tomo	1015eV/1055eV 1555eV/571eV	0° - +180°/10°	/stxm-cls/2017/17-05/FIB-TOMO	√ CS
16/11	MEA A tomo	280eV/285.2eV 684eV/704eV	-63° - +63°/9°	/stxm5322/2016/16-11/tomography-analysis	√ CS
16/10	MEA A 3sets tomo	684eV/705eV	-66° - +60°/9° -69° - +57°/9° -72° - +54°/9°	/stxm5322/2016/16-10/tomography-analysis	√ CS
16/08	MEA 11 GDE tomography	684eV/704eV	-63° - +57°/9° -66° - +54°/9°	/stxm-cls/2016/16-08/2016-aug-tomo	√ CS
16/06	aerogel tomo	450eV/462.5eV/ 520eV /528.9eV/530.4eV/ 550eV	-65° - +70°/5°	/stxm5322/2016/16-06a/aerogel-tomo	√ CS
16/03	MEA A tomography/2 sets	278eV/285.4eV 684eV/694eV	-64° - +64°/8°	/stxm-cls/2016/16-03/2nd-tomo-set-&16Feb1102	√ CS
16/02	MEA 2 sets tomo @CLS	278eV/285.4eV 684eV/694eV	-60° - +60°/8°	/stxm-11/2016/16-02/tomo-analysis	√ CS
15/07	MEA 3 sets tomo	684eV/693eV	-66° - +60°/9° -63° - +63°/9° -60° - +66°/9°	/stxm-11/2015/15-07/tomo-analysis	√ CS
15/07	MEA A wet tomo	528eV/531.1eV/ 535.4eV 684eV/694eV	-60° - +60°/6°	/stxm5322/2015/15-07/wet-tomo	√ CS
15/04	MEA 3 sets tomo	684eV/693.2eV	-66° - +60°/9° -63° - +63°/9° -60° - +66°/9°	/stxm5322/2015/15-04/tomo-analysis	√ CS
14/10	MEA wet tomo	278eV/284.5eV/ 285.2eV 684eV/694eV	-72° - +68°/4°	/stxm5322/2014/14-10/tomo-analysis	√SIRT
14/08	MTB wet cell tomo	528eV- 539.1eV/6 points	-60° - +44°/4°		√SIRT
14/05	AFCC 2-layer tomo	278eV/285.2eV 684eV/694eV	-72° - +72°/4°	/stxm-cls/2014/14-05/AFCC-2-layer	√SIRT
14/04	MEA tomo	278eV/285.2eV 684eV/694eV	-72° - +72°/4°	/stxm5322/2014/14-04/tomo-analysis	√SIRT
13/12	AFCC-2layer-tomo	278eV/285.2eV 684eV/694eV	-60° - 0°	/stxm5322/2013/13-12/2-layer-tomo	

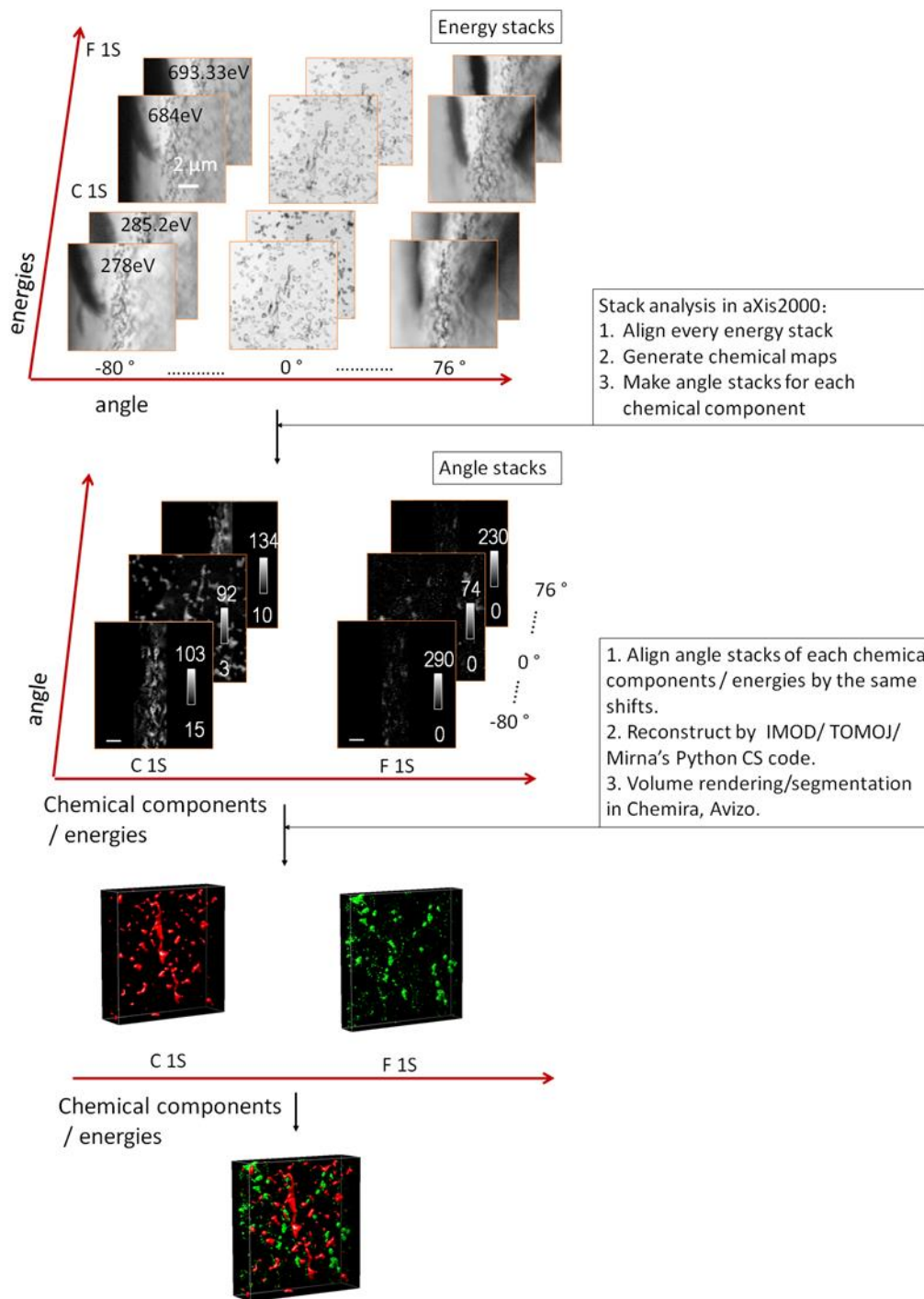


Figure 3.9 STXM tomography data acquisition and analysis workflow

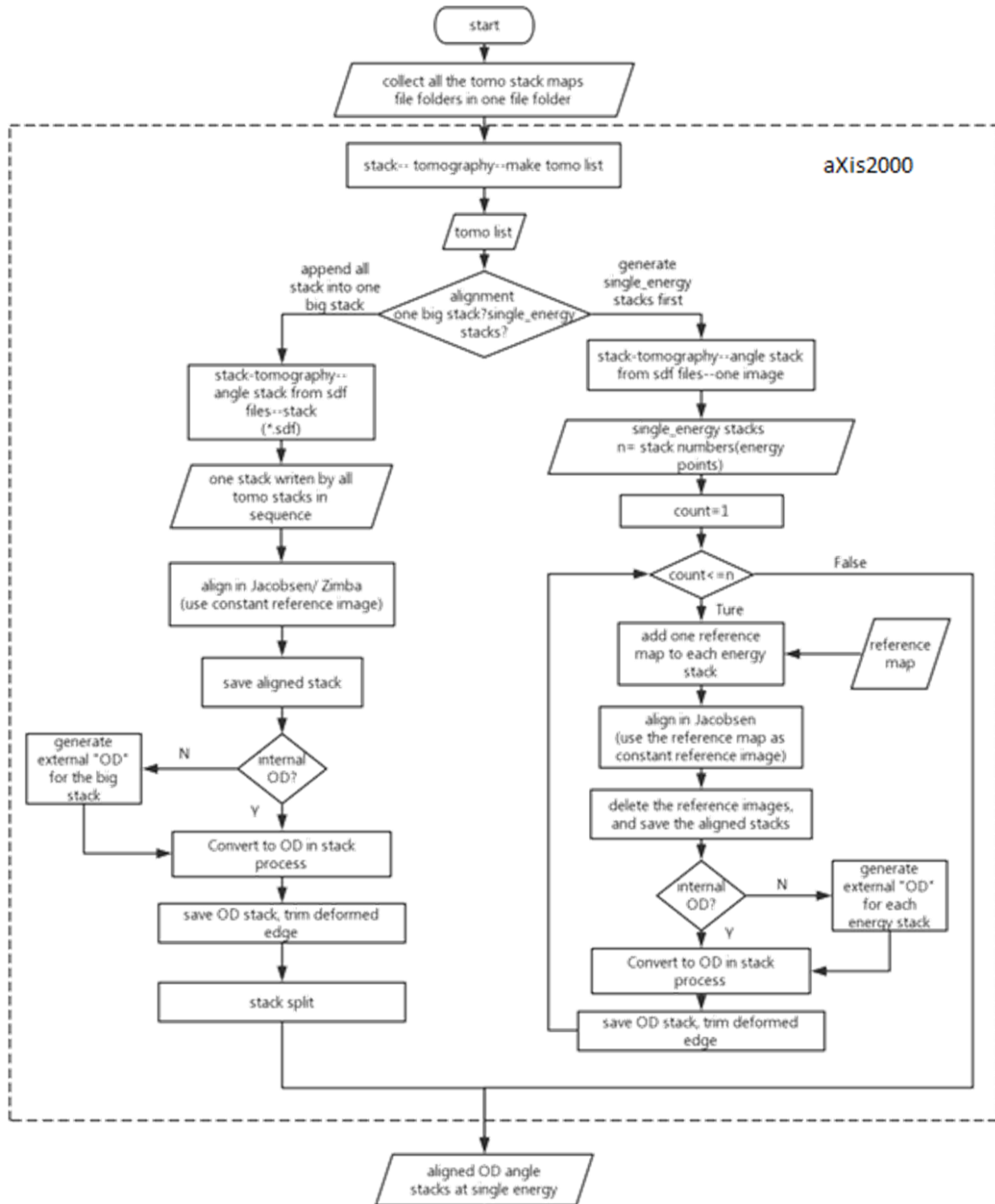


Figure 3.10 Flow diagram of 4D data analysis process in aXis2000.

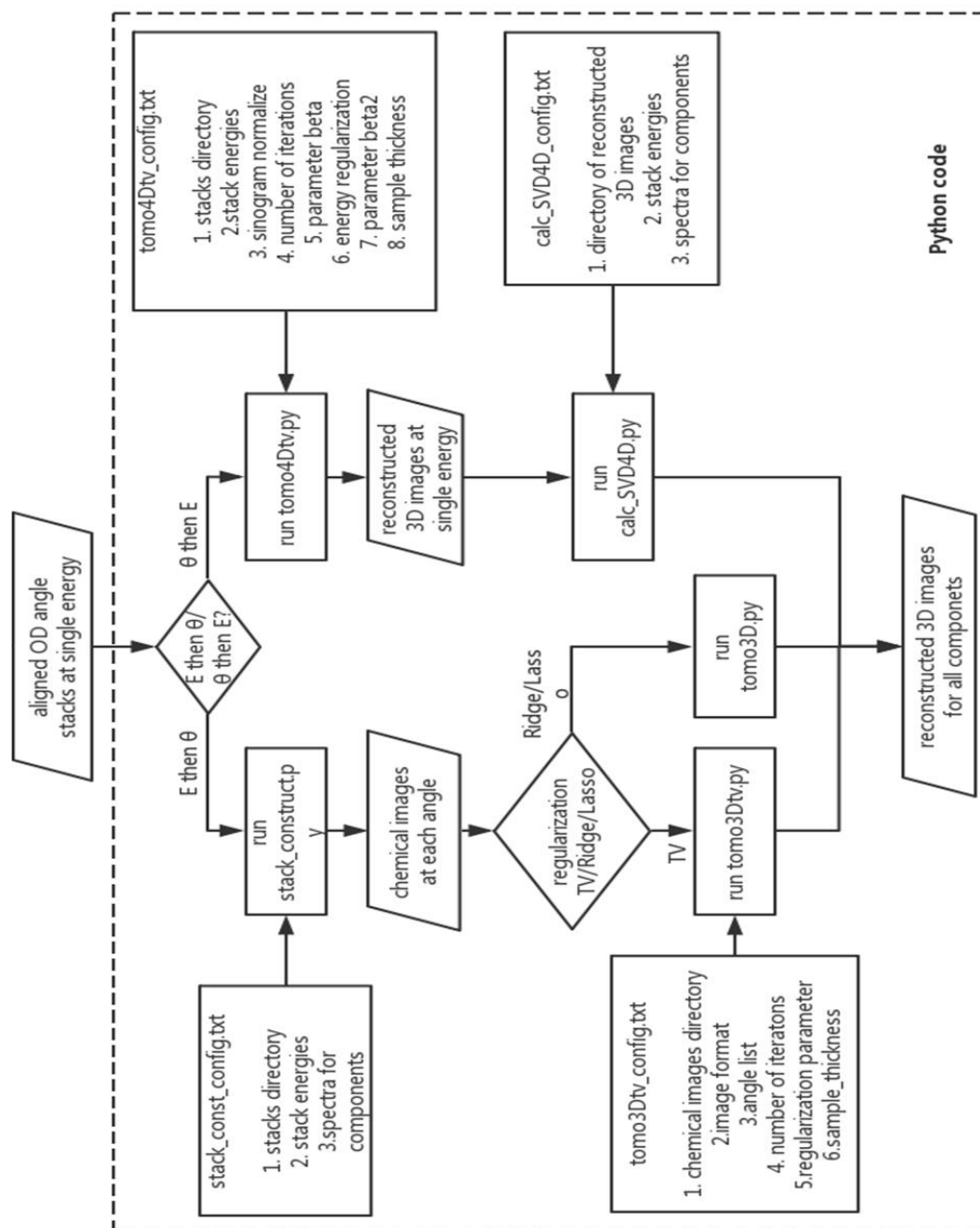


Figure 3.11 Flow diagram of 4D data analysis process using Mantis python code

3.3.5 Data analysis procedures using Mantis

Another method of 4D data analysis was developed in collaboration with Mirna Lerotic (2nd look consulting). Flow diagrams of the 4D tomography analysis procedure are shown in **Fig. 3.10** and **Fig. 3.11**. Alignment, OD conversion and chemical analysis are done in aXis2000 (Fig. 3.10). Two reconstruction paths are available in the Mantis python code (Fig. 3.11). These procedures are available in the Mantis spectromicroscopy data analysis package (source and executable files are available for free at <http://spectromicroscopy.com/>) (Lerotic et al. 2014). In one of the two approaches it is possible for the user to generate a segmented set of voxel locations, and then work backward through the data analysis so as to generate the NEXAFS spectrum of that set of selected voxels. To my knowledge this is the first example of true 4D voxel spectrum data analysis. This is very powerful since it allows the user to verify the 3D chemical analysis which is based on quality of match between the voxel spectrum and the linear combination of reference spectra that were used to fit, and thus generate the 3D reconstructed chemical maps. This function is available in Mantis 2.3.03 and later versions. The Mantis tomography GUI window is shown in **Fig 3.12**. To enable extraction of voxel spectra, the 3D reconstruction for each energy has to be calculated first. One changes the slider bar at the top of the xy view of the 3D reconstruction to scan through the reconstruction results for all energies. The left slider bar scans the xy view through the z direction. The 'select ROI', allows selection of lower and upper voxel values to select a specific region of the 3D volume, At the end of this selection process the spectrum of the 3D volume ROI is extracted and can be saved to a file. 3D ROI files generated from other programs (TomoJ, Chimera, Aviso etc) can be read to identify the voxel set of interest. It is noteworthy that

the 3D voxel set does not have to be continuous. Its properties are defined by the voxel intensity values in Mantis, and can be defined in many other ways in other software packages such as Avizo.

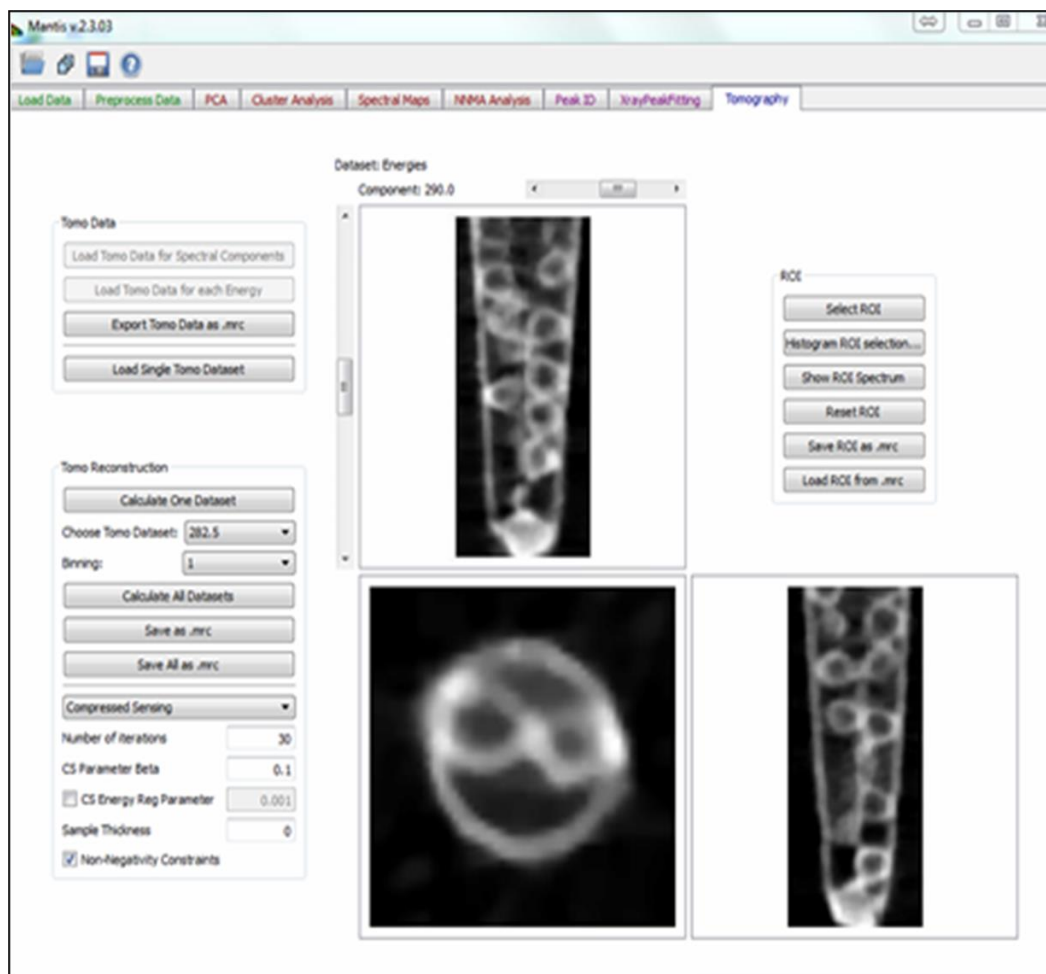


Figure 3.12 Mantis tomography GUI window

Figure 3.13 shows an example of this type of 4D analysis in the case of a polymer microsphere sample (Hitchcock et al. 2008) which consists of an aqueous suspension of 0.8 μm diameter polymer particles enclosed in a carbon nanopipette. The microspheres inside the nanopipette consisted of a dilute linear polyacrylate (PA) water solution

enclosed in a hollow polystyrene (PS) shell. The 3D rendering image is from the reconstruction result at 292.0 eV and shows 3 volumes in black, light blue and red. The spectra of these 3 different volumes of the reconstruction are displayed at the right side of Fig. 3.13. For more detail please see **Chapter 4**.

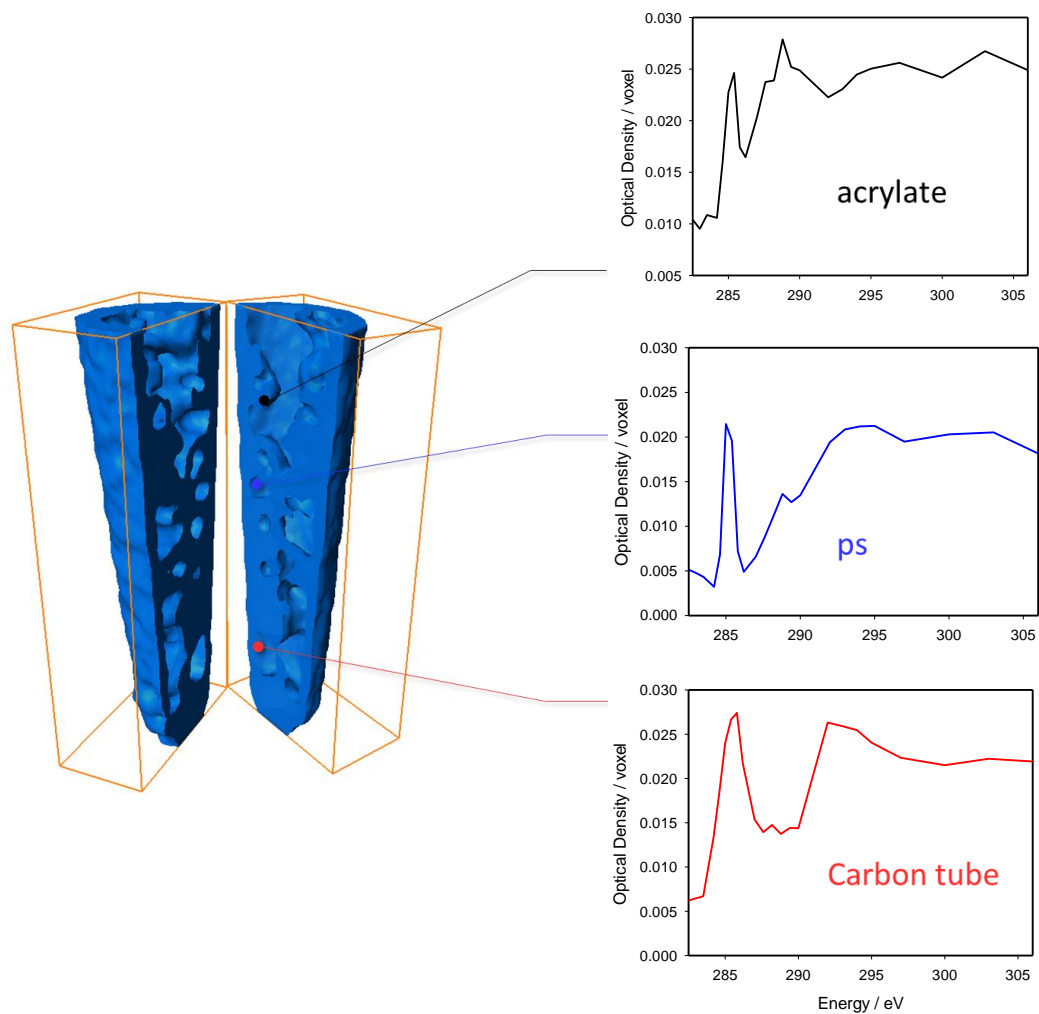


Figure 3.13 4D analysis of the polymer microsphere in carbon nanopipette sample.

Chimera (University of California, San Francisco, UCSF) (Pettersen et al. 2004) and Avizo (Thermo Fischer) (Westenberger 2008) are used for volume rendering and segmentation. (Fig. 3.7)

3.4 STXM Laminography

3.4.1 Experimental apparatus

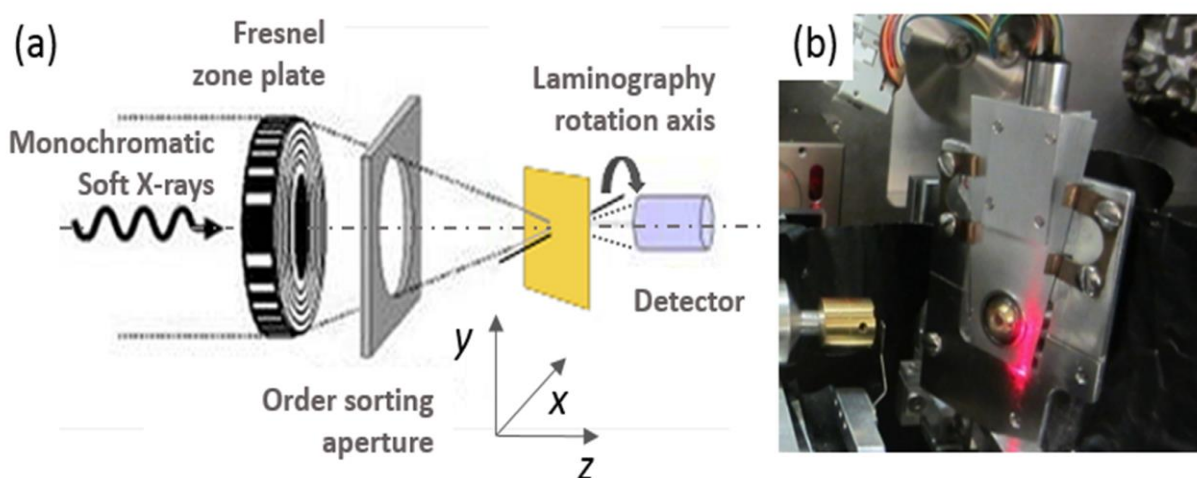


Figure 3.14 (a) STXM Laminography schematic diagram, (b) Laminography stage mounting in the CLS ambient STXM.

A schematic of the set-up used for laminography was shown in Chapter 2, Figure 2.5. For STXM laminography, the sample plate holder is tilted by up to 30° degrees. A 2-stage stepper motor (MicroMo ARSAPE model AM1020-A-0,25-8) is used for azimuthal rotation in the STXM laminography stage. A pair of bevel wheels changes the rotation axis from vertical to horizontal. The previous azimuthal rotator system developed for linear dichroism studies (Hernández-Cruz, et al. 2007) has a cylindrical hole to let the X-ray beam to pass through. With a ~30° tilted geometry, most of the beam will be blocked by the inside wall of the cylindrical hole. To solve this problem, the cylindrical hole was changed

to a cone shaped hole in the middle of the rotation brass piece which allowed most of the X-ray beam to pass through to the detector, even at 40°. A raised boss was included to ensure the sample can approach very close to the OSA without collision with the sides of the laminography rotation system. The edge of the boss was designed to avoid conflict between the rotator and the zone plate holder. A computer aided design (CAD) rendered image of the modified laminography sample rotator is shown in **Fig. 3.15** Samples mounted on 3 mm TEM grid are used.

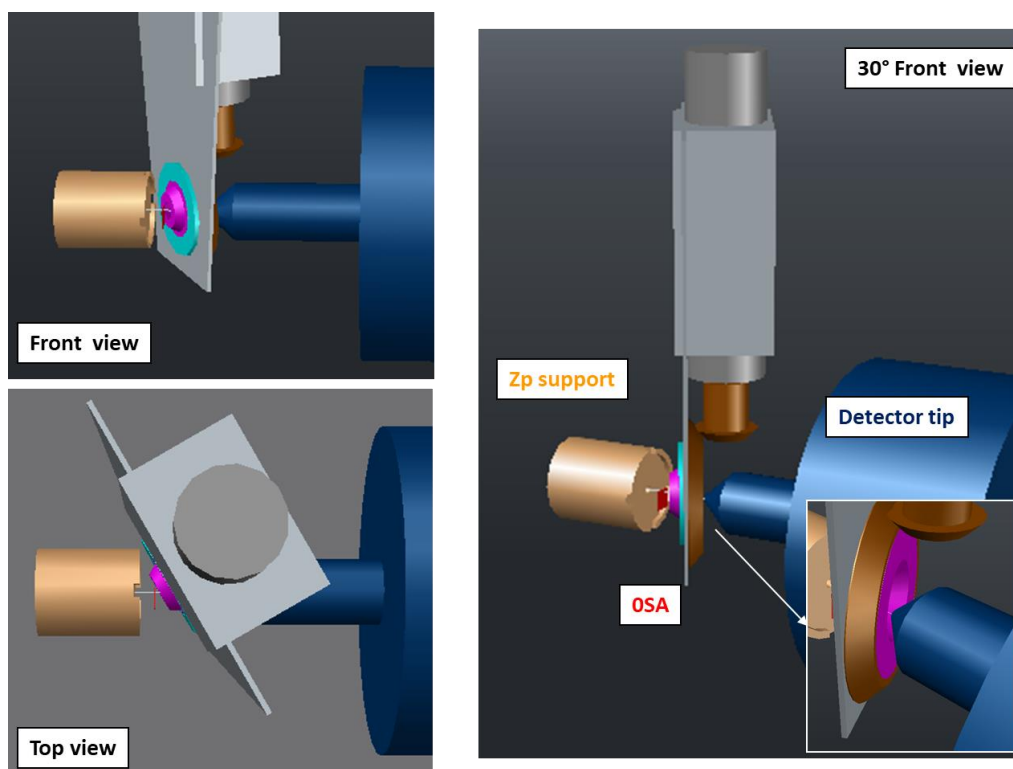


Figure 3.15 3D rendering from CAD images of modified Laminography sample holder

3.4.2 Sample preparation

In laminography the sample is rotated by 360° about an axis tilted relative to the X-ray axis by (typically in this work) 30°. When the sample is rotated azimuthally the X-ray spot

traces an elliptical trajectory in the xy plane of the sample as shown in **Fig. 3.16**. If the region of interest (ROI) of the sample is close to the axis of rotation (typically close to the center of the TEM grid) the offset between subsequent azimuthal rotation angles is smaller. Choosing an ROI near the rotation axis will also decrease the possibility of collision between sample holder and detector. After modification, the total thickness of the sample rotator is about 4.3 mm. Although the cone design of the sample mounting hole has been used, the detector has to be moved backward by 1 to 2 mm. If the ROI of the sample is far from the rotation center, then the tip of detector will be close to the wall of the conical hole of the sample rotator. Furthermore, in this situation, the movement of the sample while searching for the ROI after each change in azimuthal angle will be larger, which can lead to collisions. When preparing samples for laminography it is best to place the ROI as close to the center of the TEM grid as possible. Also during sample mounting, the sample ROI can be adjusted to be at the rotation center by displacing the TEM grid from the centre position.

3.4.3 Data acquisition

As opposed to tomography, the thickness of the sample does not change during laminography and the sample can be rotated freely from 0° to 360° . In order to reduce radiation exposure and measurement time, a 10° increment is usually used, resulting in measurements at 37 azimuthal angles. The prediction excel sheet can also be used to predict new co-ordinates of ROI for laminography measurement. **Figure 3.16** shows the 3D trajectory of a laminography measurement, in which the measured position is in red and the predicted position is in blue. The 0° , 60° and 120° coordinates were used for the prediction. As in STXM tomography measurements, full energy stacks are measured and analysed first to determine the exact energies. Pre-edge and peak/post edge energies were then

selected for laminography angular stack map measurements. For the PEMFC MEA samples, 278 eV and 285.3 eV (if TTE resin was used to embed) or 284.3 eV (if PS sandwich was used) were used for carbon-support and 684 eV and 694 eV (or 704 eV) were used for the ionomer for 4 energy laminography measurements. For the ZnO/Al₂O₃ aerogel sample, 1015 eV and 1055 eV were used to map the ZnO at the Zn 2p edge, while 1555 eV and 1571 eV were used to map the Al₂O₃ at the Al 1s edge. The chemical maps were generated by converting transmission images to OD, aligning them, then subtracting the pre edge signal from the peak/post edge signal. Alignment of the angle stacks was done in aXis2000 manually.

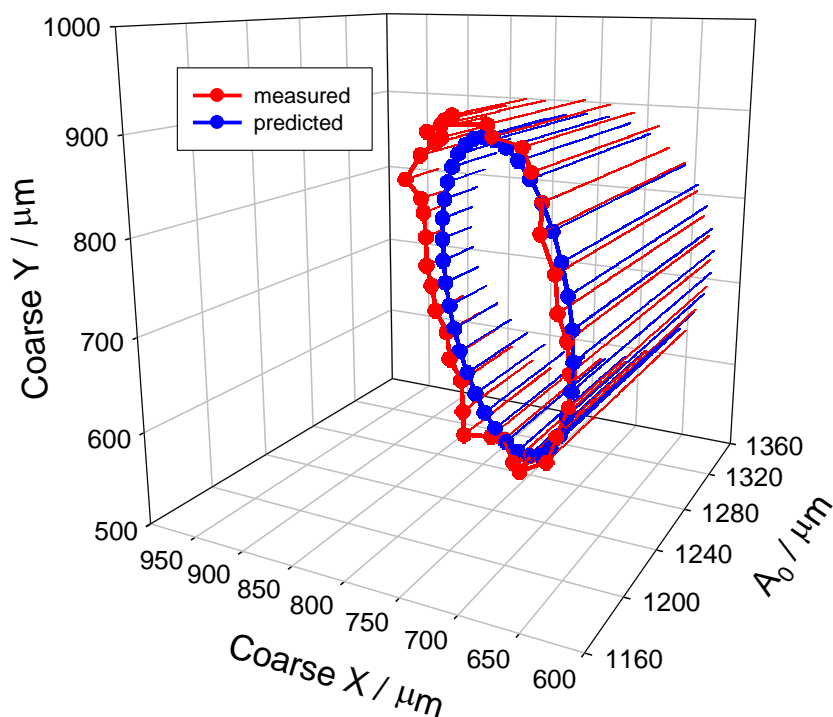


Figure 3.16 Comparison between predicted results and measured results laminography measurement

3.4.4 Data analysis

The code for laminography reconstruction was developed by Mirna Lerotic (2nd Look Consulting) with help from Lukas Helfen (ESRF). The WBP algorithm has been used, which requires more tilt angle images (hundreds ideally) for the reconstruction. In the current STXM measurement condition, we usually measure about 36 images with 10° increment. The compressed sensing algorithm needs to be adapted to laminography and used to allow reasonable reconstructions with very few laminography angles. That code is still under development.

3.5 Ptychography for Imaging, Spectroscopy and Tomography

3.5.1 Experimental apparatus

Ptychographic measurements were carried out using the Nanosurveyor I instrument (Shapiro et al. 2016, David et al. 2017) mounted on the 5.3.2.1 bending magnet beamline at the ALS. Some measurements were also performed using the STXM on beamline 1102 at the ALS, modified for ptychography. **Fig. 3.17a** is a cartoon of the Nanosurveyor-I instrument while **Fig.3.17b** is a CAD rendered image of the system. In order to record the coherent scattered signal, the bright field STXM detector is replaced with a custom-built fast-frame rate charge-coupled device (CCD) (Denes et al. 2009) which can transfer a megapixel image in ~10 ms. The sample can be positioned or raster scanned using a stepper motor stage for coarse positioning and a piezo-electric stage for fine positioning. Both zone plate and sample stages can be fine scanned, with ZP scanning used for ptychography measurements. A phosphor photomultiplier tube (PMT) detector is also incorporated, mounted at a 45° angle from the inboard side, which can be advanced for conventional

STXM measurements, or retracted for ptychography measurements. The design has decreased the mass around the sample, which has increased stability and minimized vibrations during scanning. The OSA is stationary, which limits the fine scan region to $20\ \mu\text{m} \times 20\ \mu\text{m}$. Another core component is the laser interferometry feedback system which is important to achieve long term stability and precise positioning (Denes et al. 2009). In prior interferometer controlled STXMs such as ALS 5.3.22 (Kilcoyne et al. 2003), and CLS aSTXM (Kaznatcheev et al. 2007) an Agilent interferometer is used with 2 nm position measurement which achieves stabilizations of 5-10 nm up to 100 Hz. Nanosurveyor I uses a Renishaw interferometer system with 0.2 nm position measurement precision. It achieves stabilizations of 2 - 4 nm up to 100 Hz. Since the goal of soft X-ray ptychography is to achieve spatial resolution at the wavelength diffraction limit ($\lambda/2NA$ or ~ 4 nm at the C 1s edge, ~ 2 nm at F 1s edge, ~ 0.8 nm at the Si 1s edge), the stability of the relative positioning of the sample and the ZP focusing optic must be much better than this spatial resolution target. A SmarAct rotation stage underneath a 2-axis piezo sample stage for eucentric positioning is used for tomography measurements. A combination of coarse positioning and fine positioning systems is used to position the sample ROI at the eucentric center of the tomography rotator, where the rotation axis intersects with focused X-ray beam. With care, less than $3\ \mu\text{m}$ wobble can be achieved, which allows fully automated tomography measurements above 500 eV where the depth of focus is $>5\ \mu\text{m}$. For multi-energy spectro-tomography measurements, the eucentric adjustment system did not work well enough to allow for automatic multi-tilt angle measurements. Thus manual tilt angle changes, followed by framing and refocusing on the ROI was still needed to remove the wobble before each tilt angle in spectro-ptychography tomography measurements.

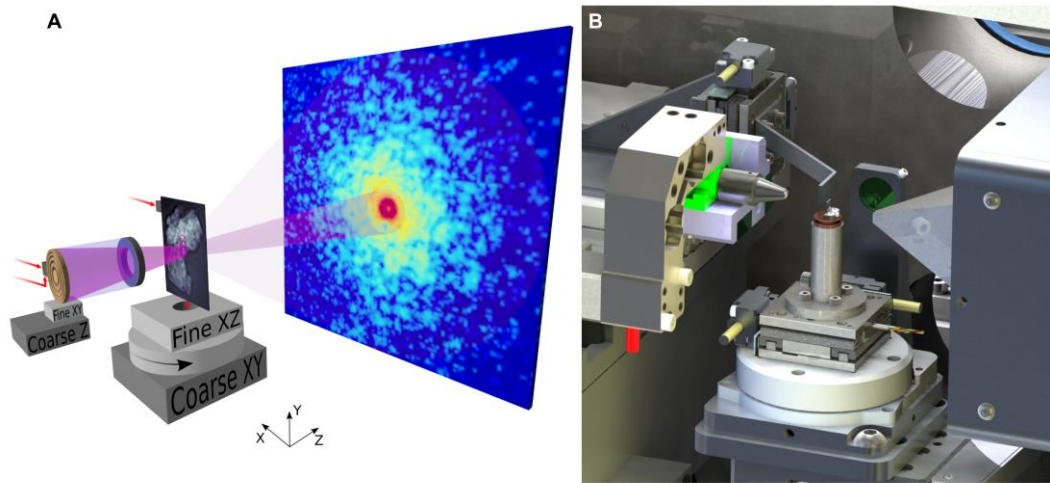


Figure 3.17 Schematic of ptychography. (b) computer aided drawing (CAD) rendering of the Nanosurveyor-I Instrument. (David et al. 2017)

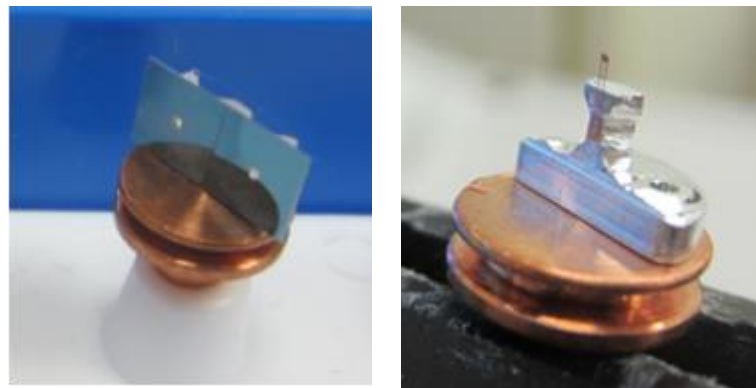


Figure 3.18 Ptychography sample stage. (left) 2 SiN_x windows or 2 TEM grids can be mounted. (right) grid strip mounted for tomography.

3.5.2 Sample mounting

The ptychography sample stage is shown in **Fig. 3.18**. The regular ptychography sample stage is on the left, with two silicon nitride (SiN_x) windows (Norcada Inc., Canada)

mounted. For tomography measurement, the two sides of the sample holder are removed, then the single strip of TEM grid with sample is mounted in the middle of the sample holder as shown in Fig. 3. 18(b).

3.5.3 Data acquisition and data analysis

The zone plates used for ptychography have larger outer zone radius (either 70 or 100 nm) than those used for conventional STXM (20 - 35 nm), in order to have a larger X-ray spot size and thus achieve a larger measurement area with a given number of pixels and thus beamtime. This does reduce spatial resolution somewhat relative to what would be achieved with a finer ZP. Typically ptychography achieves a factor of 10-15 improvement in spatial resolution relative to the spot size used. In ptychography measurements in March 2018 with Nanosurveyor I on the COSMIC beamline at ALS, 40 nm outer zone zone plates are being used and spatial resolutions of 5 nm have been achieved (Shapiro, private communication).

Fig. 3.19 shows an example of a coherent diffraction pattern detected by the CCD camera when a 720 eV X-ray beam is passing through a PEMFC cathode. A set of such diffraction patterns are recorded for an array of overlapping points on the sample. Overlapping factors of at least 40% are used. Since each image is 1 Mpixel, a single 50 x 50 point ptychography data set is about 2.5 Gb in size. Multi-dimensional data – 3D energy stacks, or 4D ptycho-spectro-tomography data sets - are many 100s of Gb in size. The ptychography data corresponding to a single real space image is processed at the ALS using the SHARP software (CaMERA, Marchesini et al. 2017), accessed via a python script (see **Fig. 3.20**). The reconstructed data for each image are saved as separate TIFF files for modulus, phase, stxm, complex and intensity images.

Figure 3.21 displays the output of the reconstruction of the ptychographic data for a single image for a region of a PEMFC cathode measured at 720 eV. **Figure 3.21a** is the modulus (amplitude) image, **Fig.3.15b** is the phase image, **Fig.3.15c** is the STXM image derived from the ptychography. **Fig.3.21d**, and **Fig.3.21e** are absorption and phase images of the amplitude and phase after correction for I_0 . **Fig.3.21f** is the I_0 corrected STXM image. For ptychography tomography measurements, 15 tilt angles with 9° or 10° increment from $\sim -65^\circ$ to $\sim +65^\circ$ were measured. The dwell time used for each coherent diffraction image was 100 ms. Attempts to reduce the dwell below 100 ms when using Nanosurveyor I on 5.3.2.1 gave poor quality results, probably because of the limited coherent flux on this bend magnet beamline. (Dwells of 40 ms are giving excellent results with Nanosurveyor I on COSMIC (Shapiro, private communication)). After reconstruction, the chemical map for each component at each tilt angle was generated by subtracting the pre-edge from the peak energy ptychography absorption image. Angular stacks of the chemical maps were then aligned using aXis2000, and that set of tilt angle data was then reconstructed in Mantis using the compressed sensing (CS) method (Wu et al. 2017).



Figure 3.19 Diffraction pattern with 720 eV X-rays passing through the cathode.

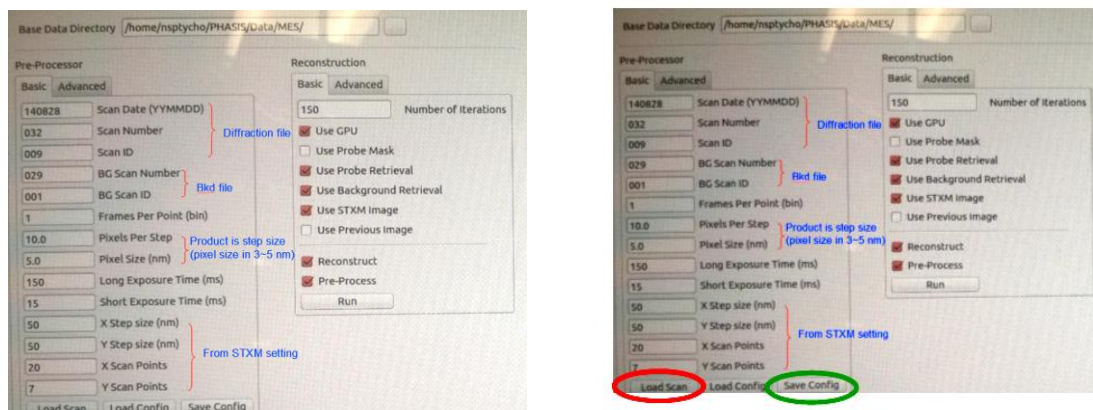


Figure 3.20 Ptychography processing interface (python script written by David Shapiro).

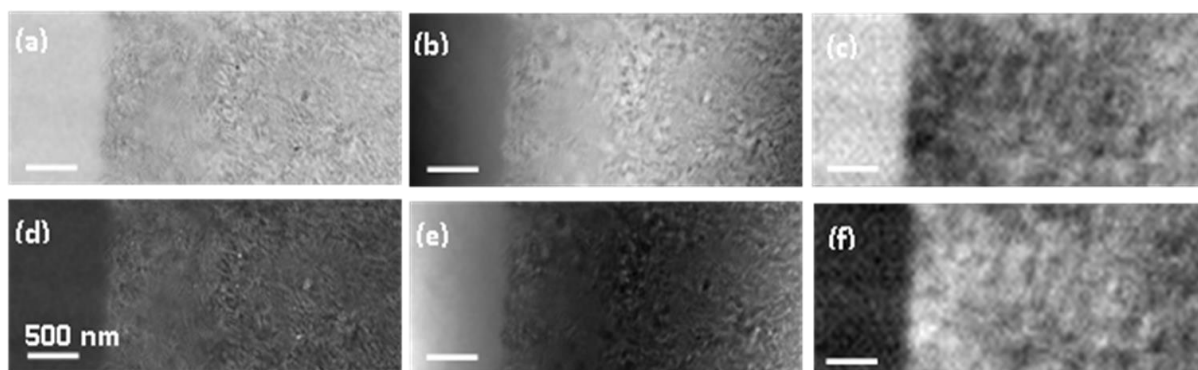


Figure 3.21 Ptychographic reconstructed data measured at 720 eV of a region consisting of the membrane and part of the cathode of a PEMFC. (a) modulus (amplitude) image, (b) phase image, (c) stxm image, (d) (I_0 -corrected amplitude) absorption and (e) I_0 -corrected phase image (f) I_0 -corrected stxm image (5.3.2.1 run of May 2016, data set 2016-05-20-021)

3.6 Cryo STXM and cryo spectrotomography at CLS

As part of a major CFI-funded upgrade to the spectromicroscopy facility at CLS, a new STXM with cryo-tomography capability was designed, fabricated and assembled

(2013-2015) (Leontowich et al 2018). It was installed in June 2015, and completed its commissioning in March 2018. **Figure 3.22** shows exterior and interior views of the cryo-STXM at the CLS ID10.1 beamline. A Gatan 630 cryo-transfer holder, mounted on a JEOL compustage is used as the cryo sample holder. A sample temperature of -180°C (93 K) is achieved when the sample is under good vacuum ($< 1 \times 10^{-9}$ torr) and the sample cryo-pot is filled with liquid nitrogen. The cryo sample holder can be tilted from -70° to $+70^{\circ}$. A long working distance camera is used for visual adjustment of the sample with the X-ray microscope. In addition a blue laser can be directed co-axial with the X-ray beam to facilitate sample alignment and to test the instrument when there is no X-ray beam. This is only the second cryo-STXM in the world. The first was built by the Jacobsen group (Maser et al. 2000, Wang et al. 2000, Osanna et al. 2001, Beetz 2003) and used at beamline X1A at NSLS-I from $\sim 2000 - 2010$. I took part in the first cryo-tomography measurement with the CLS cryo-STXM in May 2017.

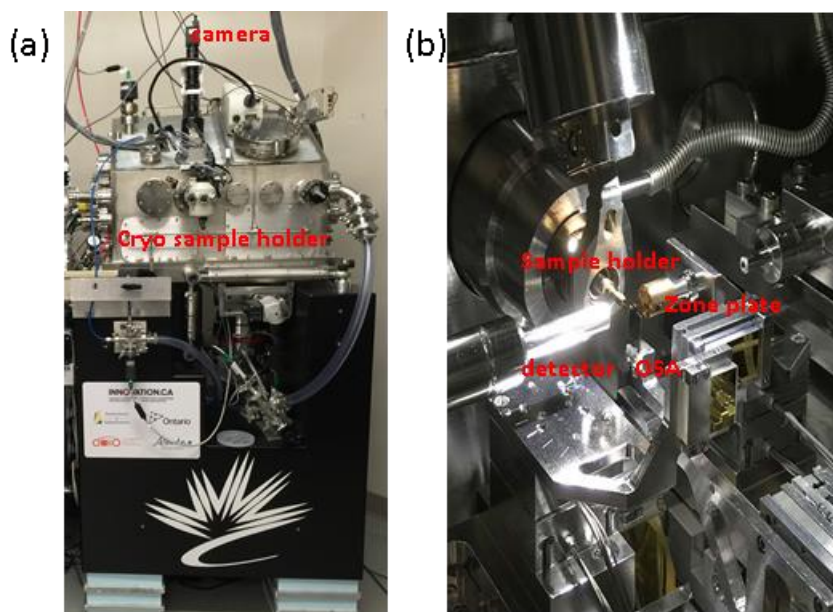


Figure 3.22 (a) Outside (b) inside images of the ptychography tank

3.6.1 Sample preparation

Gatan high tilt, ‘flyswatter’ sample grids (Gatan, Inc.) were used to mount samples, as shown in **Fig. 3.23a**. **Figure 3.23b** shows a magnified view of the sample grid with microtomed sections of a PEMFC MEA sample visible. The sample strip is positioned to be parallel to the grid bar, so the whole cathode will keep in the center of the image at all rotation angles. Note that the rotation axis is the x-axis (horizontal) in c-STXM whereas STXM tomography and ptycho-tomography are performed with rotation about the z-axis (vertical).

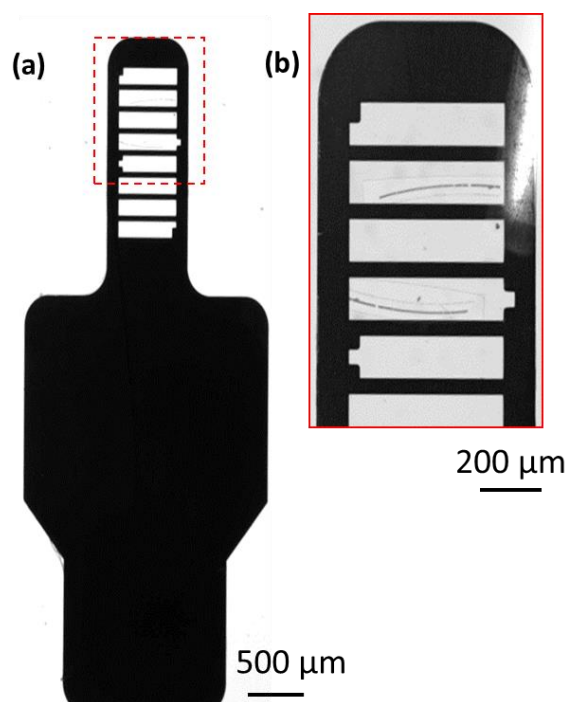


Figure 3.23 Gatan ‘flyswatter’ sample grid. There are supplied bare and a layer of formvar was added prior to mounting microtomed MEA samples. (a) Full grid, (b) expand tip shown an MEA sample on formvar

3.6.2 Data acquisition and analysis

The rotation range of the sample holder is from -70° to $+70^\circ$. A $5\text{-}10^\circ$ increment was used for the tomography measurements. The PEMFC cathode was measured at 684 eV, 694 eV and 704 eV at the F 1s edge. Chemical maps were generated by subtracting the pre-edge OD image from the peak (694 eV) or continuum (704 eV) OD images after prior alignment in aXis 2000. 3D reconstruction of the chemical maps was performed in Mantis using the CS method.

Recently, automatic measurement of cryo STXM tomography data sets has been achieved (Leontowich et al. 2018). For cryo-STXM eucentric correction, the GoniZ (or sample straightness) is very critical. A combination of GoniZ motion and sample repositioning can (in favourable cases) achieve a eucentric rotation condition of sufficient quality that a full tilt angle data set can be acquired without operator intervention to frame and refocus at each tilt angle. However, a very large sample region must be scanned in order to keep the ROI in the measured image. Automated tomography with ZP-z automatic adjustment is possible and has been tested. If the sample region of interest is not located in the middle of GoniY, sample motion up to $30\ \mu\text{m}$ as a function of tilt angle is expected and relatively easy to follow, with GoniY being changed systematically to the new location with each sample rotation angle.

3.7 STXM beamlines

STXM tomography measurements were performed using CLS SM 10ID-1 (Hilhorst et al. 2012), ALS STXM 5.3.2.2 (Obst and Schmid 2014), ALS STXM 11.0.2 (Aramburo et al. 2013), and ALS STXM 5.3.2.1 (Farmand et al. 2017, Wu et al. 2018). The STXM

laminography measurements were performed using CLS SM 10ID-1. Table 3.2 shows the status of these STXM beamlines.

Table 3.2 STXM beamlines status

	CLS	ALS	ALS	ALS
beamline	SM 10ID-1	5.3.2.2	5.3.2.1	11.02
Staff scientist	Jian Wang Yingshen Lu Jan Geilhufe	Matthew Marcus David Shapiro	Young-Sang Yu	David Shapiro Hendrik Bluhm
Energy range	130 - 2700 eV	250eV – 780eV	600-2000eV	90 - 2000 eV
EPU capabilities	EPU gap can be scanned synchronously with the PGM both in step-by-step and continuous (up to 10 eV/s) spectral acquisition.			EPU5
2 nd order reduction	~5% at 270 eV, achieved using Ti filter	Second-order suppression by a factor of 10 has been achieved with a modest reduction in flux of about 50%.	Second-order suppression by a factor of 10 has been achieved with a modest reduction in flux of about 50%.	
detector	PMT-based	PMT-based	CCD	PMT-based
Detector eff	0.85/F1s	0.75/F1s		0.7/F1s
experiments	Tomography laminography	tomography	Ptychography tomography	Ptychography tomography
reference	(Kaznatcheev et al. 2007)	(Kilcoyne et al. 2003)	(Kilcoyne et al. 2003)	(Tyliszczak et al. 2004)

Chapter 4

Optimization of Three-Dimensional (3D) Chemical Imaging by Soft X-Ray Spectro-Tomography Using a Compressed Sensing Algorithm

Juan Wu, Mirna Lerotic, Sean Collins, Rowan Leary, Zineb Saghi, Paul Midgley, Slava Berejnov, Darija Susac, Juergen Stumper, Gurvinder Singh and Adam P. Hitchcock

This chapter presents the results of three dimensional reconstruction by compressed sensing algorithm for soft X-ray spectro tomography. The reconstruction quality have been compared to weighted back-projection and simultaneous iterations reconstruction technique.

This work is a collaboration with Mirna Lerotic who wrote the code for the reconstruction, and Sean Collins, Rowan Leary, Zineb Saghi, Paul Midgley who gave guidance for the algorithm development and provided the Transmission Electron Microscopy tomography dataset for coding test. My role was to provide feedback to Mirna Lerotic on performance and user friendliness of the Mantis implementation of the CS algorithm, and test the data sets. I wrote the first draft of the paper. The paper was written in collaboration with major contributions from Rowan Leary, Adam Hitchcock, Sean Collins and Mirna Lerotic. (Wu et al..2017) (Reproduced with permission from Microscopy and Microanalysis)

Microsc. Microanal. 23, 951–966, 2017
doi:10.1017/S1431927617012466

Microscopy AND
Microanalysis
© MICROSCOPY SOCIETY OF AMERICA 2017

Optimization of Three-Dimensional (3D) Chemical Imaging by Soft X-Ray Spectro-Tomography Using a Compressed Sensing Algorithm

Juan Wu,¹ Mirna Lerotic,² Sean Collins,³ Rowan Leary,³ Zineb Saghi,³ Paul Midgley,³ Slava Berejnov,⁴ Darija Susac,⁴ Juergen Stumper,⁴ Gurvinder Singh,⁵ and Adam P. Hitchcock^{1,*}

¹Department of Chemistry & Chemical Biology, McMaster University, Hamilton, ON L8S 4M1, Canada

²2nd Look Consulting, Hong Kong

³Department of Materials Science and Metallurgy, University of Cambridge, Cambridge CB2 1TQ, UK

⁴Automotive Fuel Cell Cooperation (AFCC) Corporation, Burnaby, BC V5J 5J8, Canada

⁵Department of Materials Science and Engineering, Norwegian University of Science and Technology, Trondheim N-7491, Norway

Abstract: Soft X-ray spectro-tomography provides three-dimensional (3D) chemical mapping based on natural X-ray absorption properties. Since radiation damage is intrinsic to X-ray absorption, it is important to find ways to maximize signal within a given dose. For tomography, using the smallest number of tilt series images that gives a faithful reconstruction is one such method. Compressed sensing (CS) methods have relatively recently been applied to tomographic reconstruction algorithms, providing faithful 3D reconstructions with a much smaller number of projection images than when conventional reconstruction methods are used. Here, CS is applied in the context of scanning transmission X-ray microscopy tomography. Reconstructions by weighted back-projection, the simultaneous iterative reconstruction technique, and CS are compared. The effects of varying tilt angle increment and angular range for the tomographic reconstructions are examined. Optimization of the regularization parameter in the CS reconstruction is explored and discussed. The comparisons show that CS can provide improved reconstruction fidelity relative to weighted back-projection and simultaneous iterative reconstruction techniques, with increasingly pronounced advantages as the angular sampling is reduced. In particular, missing wedge artifacts are significantly reduced and there is enhanced recovery of sharp edges. Examples of using CS for low-dose scanning transmission X-ray microscopy spectroscopic tomography are presented.

Key words: 3D chemical mapping, X-ray tomography, compressed sensing, STXM, electron tomography

INTRODUCTION

Tilt series tomography is now a popular and well-developed method for measuring the three-dimensional (3D) morphology and spatial distribution of materials (Baruchel et al., 2006; Boudin et al., 2010; Leary et al., 2012; Ercius et al., 2015). A typical tilt series tomography data set is composed of a set of two-dimensional (2D) projection images collected at different sample rotation angles. A reconstruction algorithm is then applied to the set of projection images to generate 3D information. The fidelity of the resulting tomographic reconstruction is related to both the image collection and the reconstruction algorithm.

Scanning transmission X-ray microscopy (STXM) (Howells et al., 2007; Ade & Hitchcock, 2008; Hitchcock, 2012) provides chemical speciation and high-resolution quantitative mapping in projection with a routine resolution of ~30 nm and a state-of-the-art resolution of 10 nm (Chao et al., 2012). STXM spectro-tomography (multi-angle tomographic acquisition at multiple X-ray energies) (Johansson et al., 2006; Johansson et al., 2007; Wang et al.,

2011; Schmid et al., 2016) provides four-dimensional (4D) information, in the form of chemical mapping in 3D, with a spatial and chemical resolution dependent on sampling and data processing. Near-edge X-ray absorption fine structure (NEXAFS) (Stöhr, 1992) provides a high degree of chemical sensitivity and provides readily quantifiable chemical information. 4D spectro-microscopic analysis has been achieved for environmental and biological (Obst et al., 2009; Obst & Schmid, 2014; Schmid et al., 2014) and polymer samples (Hitchcock et al., 2008). Although radiation damage rates vary greatly among different samples, for any given sample, when compared with electron energy-loss spectroscopy in a transmission electron microscope (TEM-EELS), STXM provides lower radiation damage for a given core level spectroscopy measurement (Wang et al., 2009a, 2009b). Thus, STXM can offer advantages over analytical TEM for studies of radiation-sensitive materials such as biological samples and polymers.

Currently, common algorithms used to reconstruct tomographic data sets include weighted back-projection (WBP) (Vainshtein, 1970; Xu & Wang, 2005) and various iterative reconstruction methods, such as the simultaneous iterative reconstruction technique (SIRT) (Gilbert, 1972; Penczek, 2010). Both methods have been used previously in

Received February 12, 2017; accepted July 17, 2017
*Corresponding author. aph@mcmaster.ca

STXM tomography (Berejnov et al., 2013). However, two key challenges arise in conventional STXM tomography when there is under-sampling in projection data acquisition. First, images are acquired at a limited number of discrete sample rotation angles (tilt angles) and so the information recorded is incomplete. The tilt increment and number of tilt angles is typically set by considerations of instrument and sample stability, radiation dose, and acquisition time. Second, samples for soft X-ray STXM tomography must be relatively thin (<300 nm) to allow X-ray penetration. When a flat sample is rotated to a high angle, the incident X-ray may be fully absorbed by the sample or may become shadowed by a support grid. As a result, 180° rotation cannot be achieved, leaving a missing wedge of information in the tilt series. Typically, SIRT is more robust than WBP to the effects of the missing wedge and limited angular sampling (Gilbert, 1972; Penczek, 2010) and generally yields higher-quality 3D reconstructions (Bangliang et al., 2000). Nevertheless, the highly under-sampled measurements typical of STXM tomography still lead to significant artifacts in both WBP and SIRT reconstructions.

The relatively recently developed information recovery method known as compressed sensing (CS) can substantially reduce the number of measurements needed to recover a signal (Candès et al., 2006; Donoho, 2006; Blumensath & Davies, 2009). CS and related methods have been deployed efficaciously to reduce the number of images needed for tomographic reconstruction (Sidky & Pan, 2008), and to reduce artifacts arising from the missing wedge and thus reduce the overall dose needed for a given quality of 3D chemical imaging. CS has been shown to give high-fidelity reconstructions even when very few tilt angles are used (Saghi et al., 2011; Leary et al., 2013; Saghi et al., 2016), as small as nine angles in some cases (Saghi et al., 2011). In CS, prior knowledge of sample properties, such as the local homogeneity of constituent phases, is used to enable robust reconstructions from highly under-sampled measurements. CS approaches to electron tomography have demonstrated substantial achievements, including successful reconstructions of morphological and chemical signals from highly limited tilt series data (Nicoletti et al., 2013; Haberehner et al., 2014; Torruella et al., 2016). Here, we present CS tomography applied to 4D STXM analysis of high radiation-sensitive samples.

Many polymer samples are too beam sensitive for electron tomographic characterization. For these systems, chemical mapping is preferably performed in STXM. Proton exchange membrane fuel cells (PEM-FCs) represent a major emerging area in STXM characterization, and are industrially of considerable importance. PEM-FC technology is a promising green resource for stationary and automotive power applications (Folkesson et al., 2003; Wang et al., 2005). The oxygen reduction reaction at the cathode, in which oxygen, protons, and electrons combine to form water in a catalyzed reaction, is the key rate-limiting step in PEM-FC. The cathode consists of carbon support particles decorated with Pt catalyst particles, surrounded by proton

conducting perfluorosulfonic acid (PFSA) polymer (referred to as the ionomer when in the cathode) and inter-particle pores. Since a proton conductor such as PFSA is required to transport protons from the membrane-cathode interface throughout the cathode, the distribution of ionomer in the cathode plays a critical role in PEM-FC. Optimization of ionomer loadings and distributions requires direct observations of the internal structures and chemical states of the cathode catalyst layer in membrane electrode assemblies. STXM has been applied as an effective method for mapping ionomer in 2D (Susac et al., 2011; Susac et al., 2013) and there has been some exploration of the potential for 3D ionomer mapping (Berejnov et al., 2013). The radiation sensitivity of PFSA has made it difficult to measure the 3D chemical structure, morphology, and quantitative distribution of ionomer in PEM-FC cathodes. Methods to reduce the dose by reducing the number of tilt angles are required for meaningful 3D chemical imaging.

In this work, we compare the results of WBP, SIRT, and CS reconstructions applied to several tomography data sets. In order to identify the benefits and characteristics of the compressed sensing approach, we have used readily available conventional approaches for the comparative WBP and SIRT analyses. First, we demonstrate the efficacy of CS tomography in the case of a high-angle annular dark-field scanning TEM (HAADF-STEM) tomography study of Au nanoparticles. This study highlights the performance of CS tomography in tilt series data comprising few projections and exhibiting the characteristic missing wedge in electron tomography and shows robustness to data corruptions including diffraction effects in crystalline samples. Second, a bilayer thin film was fabricated specifically to test the capability of STXM tomography to derive the correct 3D distribution of chemical components important in the analysis of PEM-FC electrodes. The model system contains components with spectral signatures similar to those in a PEM-FC cathode. A third sample, consisting of a complex polymer microsphere system (Johansson et al., 2007; Hitchcock et al., 2008) composed of a low-density linear acrylate in a polystyrene shell inside a carbon nanopipette (Schrlau et al., 2008), illustrates the application of STXM tomography to a sample with multiple overlapping chemical spectral signatures present. Full 180° rotation was possible for this sample, enabling an exploration of the effects of the size of the missing wedge on CS and other reconstruction methods. Together, these analyses establish CS tomography as a powerful technique for STXM tomography of radiation-sensitive materials.

METHODS

Electron Tomography

Electron tomography tilt series data was acquired using an FEI Tecnai F20 FEG-TEM (Hillsboro, OR, USA) operated at 200 kV. Gold nanoparticles were prepared by a modified seed-mediated growth process as reported by

Bandhopadhyay et al. (2017). The sample was drop cast onto 200 mesh copper TEM grids coated with a continuous carbon film. A tilt series of HAADF-STEM images was acquired from -68° to $+64^\circ$ in 2° increments. The tilt series image stack was first aligned using cross-correlation methods followed by alignment of the tilt axis, performed using Inspect3D (FEI).

STXM Tomography

STXM tomography was carried out at the ambient STXM on beamline 10IDI (SM) at the Canadian Light Source (CLS) and at beamline 5.3.2.2 at the Advanced Light Source (ALS). The tomography sample holder and rotation system was initially developed by Johansson et al. (2006). For the PEM-FC study in this work, we used an improved device with a smaller stepper motor and a simpler, more reliable mounting system (Schmid et al., 2014). In this system, the rotation is driven by a two-phase micro-stepper motor (Faulhaber ADM0620; Faulhaber, Schoenaich, Germany). The sample is a single strip cut from a 100 mesh, 3 mm TEM grid using a fresh scalpel. This strip is glued using nail polish to the tip of a 0.6-mm diameter brass rod, and the rod is mounted to the stepper motor using the chuck from a mechanical pencil using 0.6 mm graphite. The full sample width is around $250\ \mu\text{m}$. This narrow sample is necessary due to spatial constraints imposed by the order sorting aperture, which is only $250\ \mu\text{m}$ upstream from the X-ray focal point when using C 1s photon energies (270–330 eV). The projection images were measured with the samples at room temperature, after the STXM tank was pumped to a residual vacuum of ~ 1 mbar, then back filled with He to 0.2 bar. Further details on the experimental methodology are included in Supplementary Table 1.

Supplementary Table 1

Supplementary Table 1 can be found online. Please visit journals.cambridge.org/jid_MAM.

The PEM-FC model system comprised a two-layer polymer film with Pt decorated carbon fibers in one layer and Teflon™ fibers in a second layer. The fibers in each layer were embedded in an epoxy. A STXM spectro-tomography data set was recorded

from -72° to $+72^\circ$ at 4° intervals. At each angle images were measured at four energies: 278 and 285 eV at the C 1s edge, to map the carbon fibers, and 684 and 694 eV at the F 1s edge, to map the Teflon™ fibers. The F 1s images were recorded before the C 1s images to reduce the impact of radiation damage on the quantitation of the Teflon™.

The polymer microsphere sample (Johansson et al., 2007; Hitchcock et al., 2008) consisted of an aqueous suspension of $0.8\ \mu\text{m}$ diameter polymer particles enclosed in a carbon nanopipette (Schrlau et al., 2008). The wall of the carbon nanopipette consisted of fused multiwalled carbon nanotubes grown inside a tapered glass capillary. The tube wall was 45-nm thick and had an internal diameter which tapered from 3 to $0.5\ \mu\text{m}$. The microspheres inside the nanopipette were composed of a rigid, hollow polystyrene (PS) shell which encapsulated a dilute linear polyacrylate (PA) water solution. The entire sample was initially suspended in water at the time of preparation. A significant portion of the water was lost during preparation and some of the acrylate diffused out of the microspheres, resulting in a layer of PA on the inner surface of the nanopipette. Images of the nanopipette sample were acquired for 23 energies from 282.5 to 306 eV in the C 1s absorption edge. For tomography, the combined energy-image stack was acquired in a tilt series from -90° to $+90^\circ$ with a 4° increment.

The image contrast in STXM is based on NEXAFS (Stöhr, 1992), which provides sensitivity to the chemical structure due to creation of inner-shell excited and ionized states. In STXM, X-ray absorption is measured by recording the transmitted signal (I_t) as a function of photon energy. The transmitted signal is then converted to absorption signal [optical density (OD)] by Lambert–Beer’s law:

$$\text{OD} = \ln(I_0/I_t) \quad (1)$$

where I_0 is the incident photon flux, typically measured in an area without the sample but with all underlying sample support materials present.

Axis2000 (Hitchcock, Hamilton, Canada) was used for the initial analysis of both STXM data sets. After alignment and conversion from transmission to absorption, chemical maps at each angle were obtained from the difference of the peak energy image and the pre-edge energy image. Angle stacks consisting of chemical maps generated at every angle for each component were then assembled and further aligned. The full number of angles and parameters used in the SIRT and CS

Table 1. Reconstruction Parameters Used for Simultaneous Iterative Reconstruction Technique (SIRT) and Compressed Sensing (CS) Analysis of the Three Data Sets for Different Numbers of Angles or Angle Ranges

Parameters	Au Nanoparticle Sample			PEM-FC Model Sample			PS-Acrylate Sample		
	1			4			23		
No. of energies	1			4			23		
No. of angles/range	67	23	12	37	19	10	$\pm 90^\circ$	$\pm 74^\circ$	$\pm 62^\circ$
SIRT Iteration n	20	20	20	20	20	20	20	20	20
CS β	0.7	0.4	0.2	0.3	0.1	0.06	0.2	0.08	0.05
Iteration n	100	100	100	100	100	100	30	30	30

PEM-FC, Proton exchange membrane fuel cells; PS, polystyrene; SIRT, simultaneous iterative reconstruction technique; CS, compressed sensing.

954 Juan Wu et al.

reconstructions are summarized in Table 1. The 3D reconstruction software IMOD (Kremer et al., 1996) was used for WBP and SIRT reconstructions. A python-based implementation was used for the CS reconstructions. The CS code used in this study uses a total variation (TV)-based, compressed sensing algorithm (<https://github.com/emmanuelle/tomo-tv>), employing a real space projection operator. It has been implemented in a dedicated X-ray spectromicroscopy processing tool called Mantis (Lerotic et al., 2014), available at <http://spectromicroscopy.com>. Mantis is an open-source tool developed in Python for spectromicroscopy data analysis. Recently a new tab for spectro-tomography has been added which allows tomographic reconstruction of single energy data sets as well as energy-by-energy or component-by-component reconstruction. An image of the layout of the spectro-tomography interface in Mantis is provided in Supplementary Figure 1; both CS and SIRT are supported. The reconstructed 3D volume is visualized within Mantis by xy , xz , and yz orthoslices. For spectro-tomography data, reconstructions can be done for each energy. In those cases spectral information for each voxel of the resulting volume is available and can be inspected with an ROI tool.

Supplementary Figure 1

Supplementary Figure 1 can be found online. Please visit journals.cambridge.org/jid_MAM.

Visualization

Chimera (University of California, San Francisco, UCSF) (Pettersen et al., 2004) and Fiji (ImageJ) (Schneider et al., 2012), were used for volume rendering and visualization. The z -direction labeled on the reconstruction visualizations is parallel to the optic axis (the missing wedge direction), the y -direction is parallel to the tilt axis and the x -direction perpendicular to these.

Compressed Sensing

The concept of compression is pervasive in contemporary data handling, forming the foundation for important image file formats such as the ubiquitous JPEG format. The success of compression relies on the fact that most natural images can be described very well by a small number of coefficients in some basis. A basis consists of a set of functions that can be used to represent the image when combined with appropriate weighting factors or coefficients. Popular bases used for image compression are the discrete cosine transform (used in the JPEG format) and the discrete wavelet transform (used in the JPEG-2000 format). In the context of image compression, an image is first fully sampled (i.e., a measurement is recorded at each pixel in the image) before a transform is applied to the image data to determine the coefficients in the selected basis. To compress the image data, only the largest coefficients are retained and the small coefficients are discarded. Given that the majority of information in the image is contained in far fewer coefficients in the

chosen basis than pixels in the original image, the data is said to be compressed. The stored coefficients can in turn be used to recover the image data with minimal information loss by inverting the transform used in the compression process.

In symbolic notation, the transform can be written as an operator Ψ , which, when applied to an image \mathbf{x} , returns a list of coefficients, a vector \mathbf{c} :

$$\mathbf{c} = \Psi\mathbf{x}. \tag{2}$$

If the coefficients are mostly zero, the vector \mathbf{c} is said to be sparse. The number of non-zero elements in \mathbf{c} can be counted, k , and then the vector is said to be k -sparse. In compression, sparsity is enforced by setting small coefficients to zero, giving an approximate but nearly complete representation of the original image data. In this case, the coefficient vector is only approximately sparse, but the compressed image still contains the most important information.

In CS, the goal is to directly target the non-zero coefficients in \mathbf{c} rather than the fully sampled image. If it can be assumed that the number of coefficients in \mathbf{c} is small for a complete or nearly complete representation of the fully sampled data, then taking measurements directed at determining this small number of coefficients allows for taking fewer measurements during data acquisition. However, the way these few measurements are taken is critical in CS to ensure recovery of the most important coefficients in \mathbf{c} .

In general, the signal measured experimentally is of the form

$$\mathbf{b} = \Phi\mathbf{x} \tag{3}$$

where \mathbf{b} is the measurements recorded on the object \mathbf{x} . The operator Φ defines how the measurements are taken. In the case of tomography, Φ describes line integrals through the 3D object \mathbf{x} which return projection data \mathbf{b} . In the framework of CS, the sampling equation (3) is modified to give

$$\mathbf{b} = \Phi\Psi^*\mathbf{c} \tag{4}$$

where Ψ^* denotes the inverse transform. Equation (4) follows from combining equations (2) and (3).

Two key requirements underpin the mathematical theory for CS: (i) \mathbf{x} is sparse in the transform domain Ψ and (ii) Φ and Ψ are incoherent. The requirement for sparsity emerges in a straight-forward way from the concept of compression. In order for a limited number of measurements to recover the important coefficients, it is critical that the number of coefficients sought is small. The concept of incoherence can be considered in two ways. In the first, incoherence ensures that individual measurements of \mathbf{b} provide information about many coefficients of \mathbf{x} . In the second, the incoherence requirement can be understood to establish that artifacts due to under-sampling appear as noise during the reconstruction of \mathbf{x} , allowing the significant coefficients to stand out.

Given a set of measurements, CS aims to recover the sparse coefficient vector \mathbf{c} . Direct minimization of the number of non-zero coefficients is generally computationally intractable. However, it has been shown that the computationally feasible problem of minimizing the ℓ_1 -norm returns

the sparsest solution. The ℓ_1 -norm is defined as the sum of the absolute values of the i elements of the vector \mathbf{c} :

$$\|\mathbf{c}\|_1 = \sum_i |c_i|. \quad (5)$$

The CS reconstruction can be written as a regularized minimization problem:

$$\operatorname{argmin}_{\mathbf{x}}(\mathbf{x}) = \{ \|\Phi\mathbf{x} - \mathbf{b}\|_2^2 + \beta \|\Psi\mathbf{x}\|_1 \}, \quad (6)$$

where the squared ℓ_2 -norm, taken as

$$\|\mathbf{q}\|_2^2 = \sum_i q_i^2, \quad (7)$$

for any vector \mathbf{q} , compares the reconstructed signal \mathbf{x} with the experimental measurements \mathbf{b} , and the second term, using the ℓ_1 -norm, promotes sparsity of the signal in a selected transform domain. In the combined minimization, the first term establishes data fidelity and the second term acts as a penalty term directing the reconstruction toward the sparsest solution. The factor β is an adjustable weighting parameter that is tuned according to the intrinsic sparsity and the relative magnitudes of the signals in the minimization. In its most pure form, the CS approach is designed to overcome artifacts due to under-sampling.

The operator for the sparse transform domain, Ψ , should generally be selected in accordance with prior knowledge of the structure in the object. In the simplest case, if the object can be represented by a small, finite number of volume elements (voxels), then the identity transform would be a suitable operator, Ψ . Another sparse transform domain for many materials samples in the physical sciences is the gradient domain, since many samples consist of homogeneous regions of near constant density with sharp boundaries. In the gradient domain, such samples are

represented by a small number of pixels at the boundaries between different homogeneous regions. Figure 1a illustrates such a transformation of an image into the gradient domain. The ℓ_1 -norm of spatial finite differences in an image serves to describe this sparse domain for computational purposes and is also called the TV-norm. For chemical samples, this TV-norm is applied in the spatial domain (typically for separated chemical phases); that is, the sparsity in the spatial gradient domain is used to improve tomographic reconstruction. Alternative sparsifying transforms may also be suitable for CS approaches in tomography, such as total generalized variation (Bredies et al., 2010), wavelets and related transforms (Mallat, 2008), and adaptive strategies such as dictionary-learning techniques (Duarte-Carvajalino & Sapiro, 2009). In this study the sparseness of the data was described by the TV-norm that was applied with different degrees using the factor β that was tuned for each data set.

Regarding the second requirement for CS, that of incoherence, insight can be gained most readily by considering tilt series tomographic sampling in terms of a radial sampling of Fourier space via the Fourier slice theorem (Kak & Slaney, 1988), which seminal studies have shown satisfies the incoherence requirement (Candès et al., 2006; Lustig et al., 2007). The use of radial Fourier sampling in CS is further supported by recent theoretical work on optimized CS sampling regimes (Adcock et al., 2017). In this regard, CS tomographic reconstruction can be approached using Fourier or real space based projection operators, with the latter being used in this work. Figure 1 visually summarizes the algorithmic approach to solving equation (6) for the CS-TV tomography in this study, using a simple 2D phantom object similar to the PEM-FC material studied by STXM tomography.

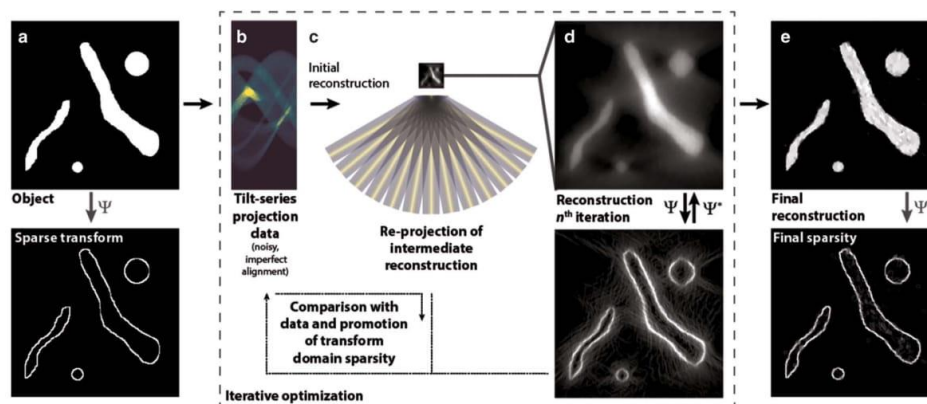


Figure 1. Schematic illustration of the compressed sensing tomographic reconstruction procedure. **a:** A transform domain is selected that represents the object in a sparse way (e.g., gradient domain sparsity shown). **b:** Tilt series projection data is acquired and (c) an initial reconstruction is performed by back projection or other methods. This intermediate reconstruction is likewise transformed, exhibiting less sparsity as the under-sampling artifacts are spread in a noise-like manner throughout the sparse domain. The transformed reconstruction and re-projections are refined by an iterative optimization algorithm to yield (d) the final reconstruction with (e) high sparsity in the transform domain.

RESULTS

Compressed Sensing Electron Tomography

CS tomography has seen widespread application in electron microscopy to achieve high-quality tomographic reconstructions from limited and challenging data sets. Here, in developing CS-TV methods for STXM tomography, we first highlight the performance of the reconstruction algorithm for handling missing wedge artifacts and diffraction contrast in electron tomography using a crystalline Au nanoparticle sample. This sample also provides a means for illustrating the robust performance of the CS-TV tomography approach when under-sampling a conventional tilt series by increasing the increment between tilt angles. Figure 2 compares orthogonal slices (“orthoslices”) extracted from tomographic reconstructions using a common WBP and SIRT implementation (IMOD) with those from the CS-TV algorithm (Mantis). Figures 2a–2c shows the *xy* slices for WBP, SIRT, and CS-TV reconstructions from the full 67-angle set,

whereas Figures 2d–2f presents the *xz* slices of the same reconstruction. The *xz* slices are emphasized as these show most prominently the artifacts resulting from the missing wedge due to the limited tilt range. Aside from angle-specific diffraction in 2D images at specific tilt angles, there is good agreement between the 2D projection generated from the reconstructions with the original data, as shown for a tilt angle of 0° in Supplementary Figure 2.

Supplementary Figure 2

Supplementary Figure 2 can be found online. Please visit journals.cambridge.org/jid_MAM.

To compare the reconstruction results with a reduced number of tilt angles, sub-sets of 23 angles (with 6° increments) and 12 angles (with 12° increments) were analyzed. As summarized in Figures 2d–2i, the WBP and SIRT reconstructions for all three sets of projection angles used showed “streaking” artifacts, characteristic of the under-sampling between adjacent tilts and the missing wedge. The surface of the Au particles became less well defined as the number of tilt angles was decreased. In contrast, the results from the CS-TV reconstruction were similar, and overall of much higher quality, for all three sampling regimes. The *xy* slices for both SIRT and CS-TV reconstructions showed some banding in the intensities throughout the volume, which are attributed to diffraction contrast effects, that is modulations of signal intensity at or near Bragg conditions of the Au crystals. Although for an individual particle such diffraction contrast contributions would only modulate the relative intensity of the particle, in the ensemble of particles, which overlap significantly at high tilt, the effect of the diffraction contrast gives rise to the observed bands. The difference in brightness of particles should not be interpreted as missing intensity but rather is a result of inconsistent intensities in the input tilt series.

The CS-TV reconstruction deals with the diffraction artifacts in the tilt series somewhat differently from the WBP and SIRT reconstructions in that the CS-TV reconstructions show larger regions of flatter intensity. At the top and bottom of the orthoslice in Figure 2c, particles appear relatively brighter than in the middle of the particle aggregate, due to changes in the total signal magnitude relative to the TV-regularization parameter for each 2D reconstruction in the planes perpendicular to the tilt axis (see also Compressed Sensing section). 3D TV-regularization methods, additionally incorporating the gradient along the tilt axis in the TV-norm, have been applied in electron tomography of samples exhibiting high levels of diffraction contrast, and these 3D CS-TV methods further reduce diffraction effects by promoting particle densities that are homogeneous throughout the full reconstruction volume (Leary et al., 2016). However, there is a trade-off in the computational efficiency in 3D compared with 2D reconstruction which may be undesirable for applications in spectroscopic STXM

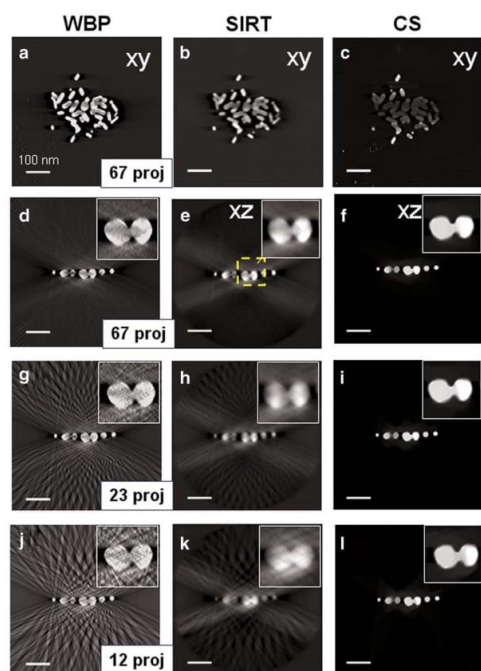


Figure 2. Weighted back-projection (WBP) (left), simultaneous iterative reconstruction technique (SIRT) (middle), and compressed sensing (CS) (right) electron tomography reconstructions of a Au nanoparticle sample. Selected slices through the *xy* plane of (a) WBP, (b) SIRT, and (c) CS reconstructions using all 67 acquired projections. Slices through the *xz* plane are compared for three different tilt increments: (d–f) reconstructions using all 67 acquired projections, (g–i) reconstructions using 23 projections, (j–l) reconstructions using 12 projections. The insets highlight the particles near the center of the volume. See Supplementary Figure 2 for comparison of the original 2D projection image at 0° with that generated from the SIRT and CS reconstructions.

tomography where computational requirements are already higher due to the use of signals at multiple energies.

Figure 3 presents line intensity profiles in horizontal and vertical directions from the reconstructions for all three tilt angle ranges. The WBP vertical profile shows a high noisy background along the vertical missing wedge direction, in agreement with Figures 2d, 2g, 2j. For the SIRT reconstructions, the intensity in the horizontal profile is reduced as the number of projections is reduced. However, there is no significant change in the CS profiles as the number of projections is reduced. Both the horizontal and vertical profiles of CS have very low background intensity and the surfaces of the Au particles are well reconstructed. We note that the SIRT analysis can be improved. There are many different ways to implement SIRT. Alternative SIRT strategies include

those described in the overview by Elfving et al. (2012), which outlines the approaches first reported by Cimmino (1938) and Landweber (1951). Other iterative based methods such as those proposed by Andersen & Kak (1984), Gregor & Benson (2008), and Censor et al. (2008), may offer further improvements to a SIRT type of analysis. Any one of these may work better or worse for a given data set. We are using a readily available and widely used SIRT implementation. Our main goal was to show the difference between a typical SIRT implementation and what the addition of prior knowledge in the form of TV in CS does in terms of the reconstruction quality. Supplementary Figures 3 and 4 present SIRT results with addition of compact support and non-negativity constraints. When these same approaches are also applied to the CS analysis, there is still clearly a significant benefit to using CS.

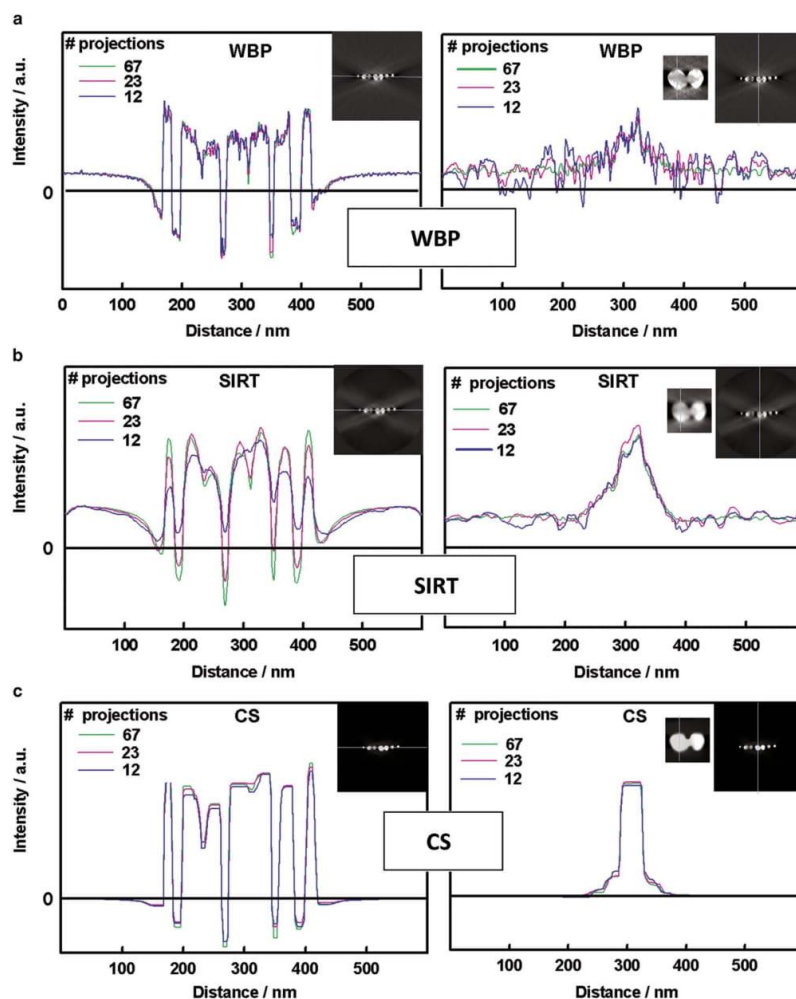


Figure 3. Line intensity profiles through xz planes for (a) weighted back-projection (WBP), (b) simultaneous iterative reconstruction technique (SIRT), and (c) compressed sensing (CS) tomographic reconstructions using 67, 23, and 12 projections as in Figure 2. The insets show the locations of the selected lines.

958 Juan Wu et al.

Adding the non-negativity constraints improves the SIRT results. In the same way, there may also be other ways of improving CS, including applying non-negativity. It is critical that fair comparisons be made and these comparisons should include equivalent constraints (only change one thing at a time, in this case moving from SIRT to CS is meant to only add the TV constraint). In fact, CS continues to develop as a field, suggesting other possible improvements to come that are beyond the scope of the present work.

Supplementary Figures 3 and 4

Supplementary Figures 3 and 4 can be found online. Please visit journals.cambridge.org/jid_MAM.

These electron tomography results illustrate key performance characteristics of CS reconstruction methods. They present a useful starting point for transferring CS tomography approaches to STXM and for comparing performance characteristics in considering missing wedge and under-sampling artifacts common to electron and X-ray tomography.

STXM Tomography of a Model PEM-FC Sample

Figures 4a and 4b shows the individual component X-ray absorption reference spectra used to analyse the bilayer model carbon-fluorine fiber sample. For spectral analysis, and to explore an optimized 2D projection analysis for comparison with 3D chemical imaging using a restricted set of photon energies, a region of the bilayer sample was measured over a range of photon energies at the C 1s and F 1s edges. Data were acquired in the form of a sequence of images at varying photon energies, also called stacks (Jacobsen et al., 2000) on a transverse cross-section of the bilayer sample. After alignment, the intensity at a given pixel through the stack gives a transmission spectrum of the material at that pixel. The C-fiber map (Fig. 4c) was generated from the C 1s stack data whereas the F-fiber (Teflon™) map (Fig. 4e) was generated from the F 1s stack data, in each case using stack fit (Hitchcock, 2012), a quantitative chemical analysis process in which reference spectra and a constant are used in a singular value decomposition (Zhang et al., 1996) of the multi-energy absorption data set. The Pt-shell map (Fig. 4d) was derived from the constant map of the C 1s stack fit. Figure 4f presents a color-coded composite highlighting the distribution of Teflon™ relative to the distributions of the carbon fiber and the Pt shell. Signals arising from the carbon fiber are shown in red, the Teflon™ fiber is shown in green, and the Pt shell is shown in blue. Areas without color correspond to regions of embedding resin. From the full C 1s and F 1s spectra, component-specific peak energies and pre-edge energies were identified. The first peak in the C 1s spectrum corresponds to C 1s → π* transitions, which only occur in the graphitic carbon fiber. Thus the carbon fiber map was obtained by subtracting a pre-edge absorption image (278 eV) from the image at the π* peak (285.3 eV). The Teflon™ fibers, simulating the PFSA component of PEM-FC

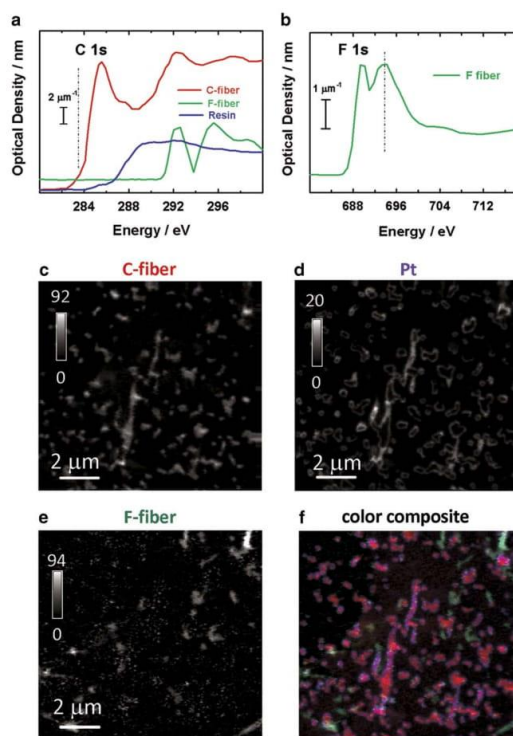


Figure 4. a: C 1s and (b) F 1s spectra of the components of a model system consisting of a two-layer structure in which one layer consists of Pt decorated graphitic carbon fibers embedded in epoxy and the second layer consists of Teflon™ fibers embedded in epoxy. The sample is a microtomed slice perpendicular to the plane of the two layers. Quantitative 2D projection maps of (c) C-fiber derived from the C 1s image sequence, (d) Pt derived from the C 1s and F 1s image sequences, and (e) Teflon™ fiber derived from the F 1s image sequence. The gray scale in (c–e) is thicknesses in nm. f: Rescaled color composite (C-fiber in red, Teflon™ fiber in green, Pt in blue). The black regions in the component maps and color composite are regions filled with epoxy.

electrodes, were selectively probed at the F 1s edge, since the Teflon™ fibers are the only component containing fluorine. The C 1s pre-edge image (278 eV) was dominated by contributions from Pt and F. An estimate for the Pt signal was generated from the C 1s pre-edge image and the F 1s map using the procedure outlined by Hitchcock et al. (2014). In order to limit radiation damage, tilt series images were recorded only at 278.0, 285.3, 684.0, and 693.0 eV at each scan angle. Due to limited penetration at high angles, the maximum rotation angle was ±72°, and this range was sampled with a 4° increment.

In order to compare the reconstruction quality of WBP, SIRT, and CS-TV algorithms with varied sub-sampling, two sub-sets from the complete 37-projection set, consisting of 19 projections and 10 projections, were reconstructed by each method. Figure 5 presents *xy* and *xz* orthoslices from

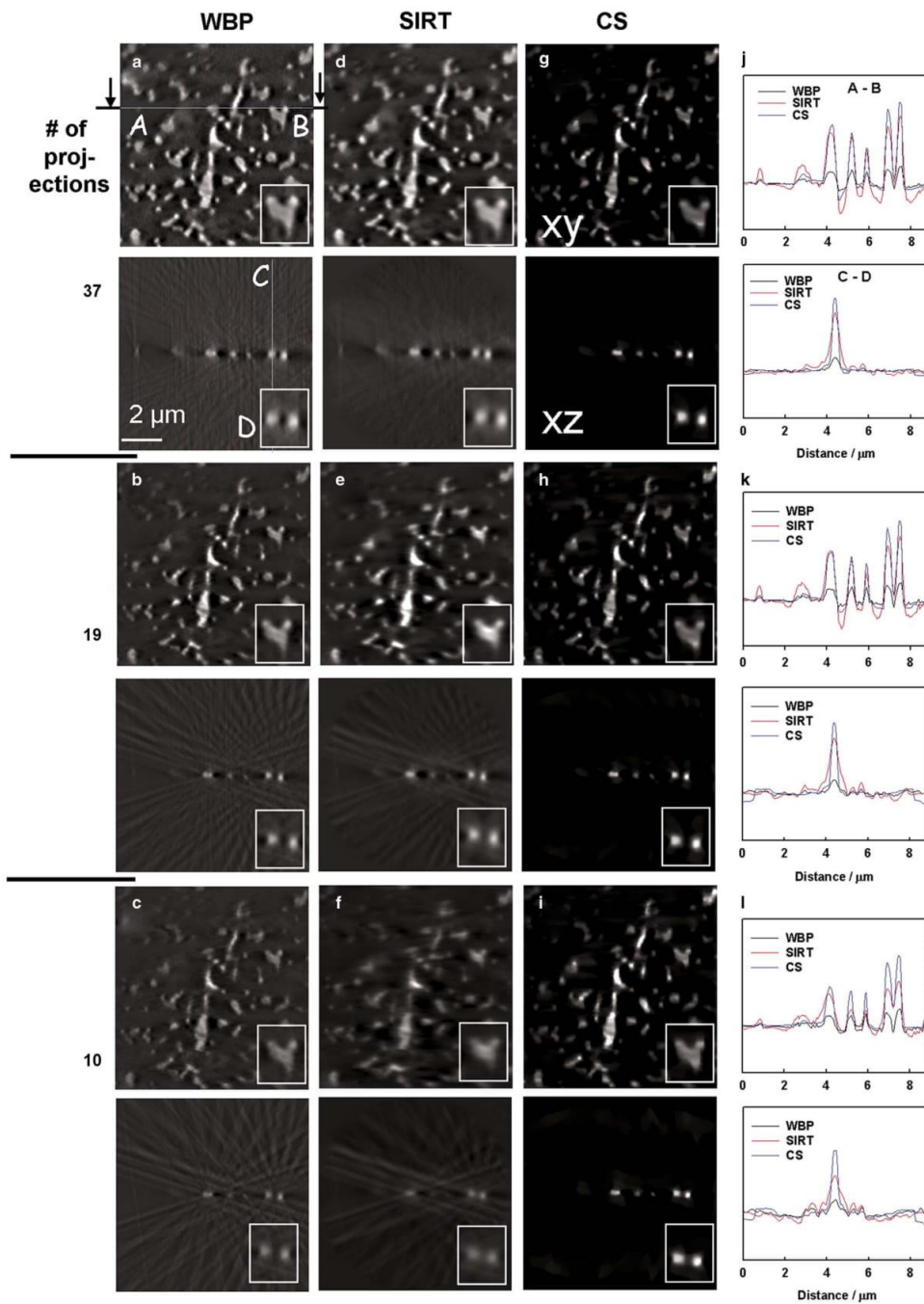


Figure 5. Slices through xy and xz planes of three-dimensional volumes of the C-fiber component reconstructed by (a–c) weighted back-projection (WBP), (d–f) simultaneous iterative reconstruction technique (SIRT), and (g–i) compressed sensing total variation (CS-TV) methods. The reconstructions were performed using (a,d,g) all 37 tilt angles, (b,e,h) 19-tilt angles, and (c,f,i) 10-tilt angles. The insets highlight a selected sub-region intersected by both the xy and xz planes as shown by the white dashed line. j–l: The line profile of each row. The upper images of each set is the A–B line for the xy slice, the lower images of each set is the C–D line for the xz slice.

960 Juan Wu et al.

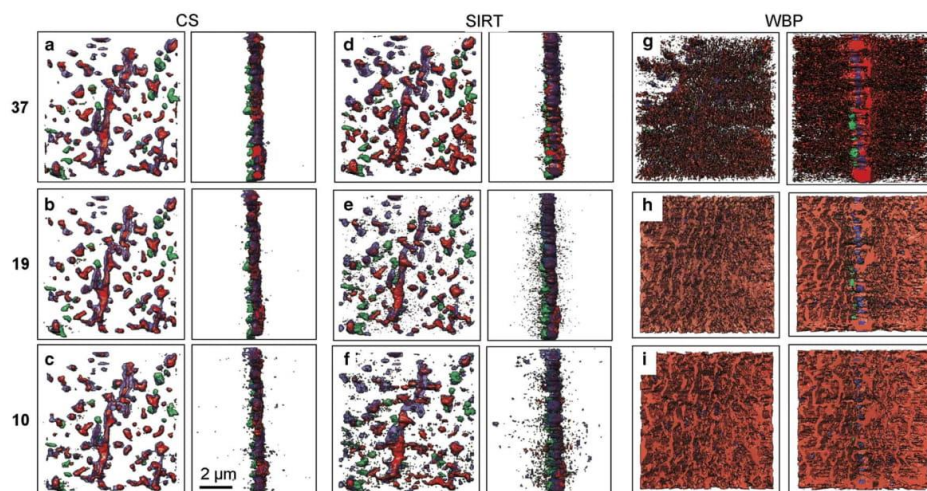


Figure 6. Isosurface renderings of C-fiber (red), Teflon™ (green), and Pt (blue) components. The surfaces were determined by Otsu automatic thresholding (Otsu, 1975) of the reconstruction volumes and are shown at 0° (left) and 90° (right) for (a–c) compressed sensing total variation (CS-TV) reconstructions, (d–f) simultaneous iterative reconstruction technique (SIRT) reconstructions, and (g–i) weighted back-projection (WBP) reconstructions. The reconstructions were performed using (a,d,g) 37 projections, (b,e,h) 19 projections, and (c,f,i) 10 projections.

the 3D reconstructed volume for the carbon fiber. The other components showed similar results and are displayed as multi-component surface renderings in Figure 6. When all 37 projection tilt angles were used, the WBP and SIRT reconstructions reproduced the carbon support fiber distribution to a reasonable approximation (Figs. 5a and 5d). However, even at this degree of sampling, the CS-TV reconstructions were of substantially higher quality, with a much lower level of artifacts than the SIRT result, greatly easing interpretation of the carbon fiber support morphology (Fig. 5g). When profiles along the A–B line in *xy* and the C–D line in *xz* slices were compared, the intensity distribution from the WBP reconstruction was much lower than that in the SIRT and CS reconstructions, and the SIRT reconstruction contained more negative signal. As the tilt increment was increased and the number of projections decreased, the quality of the reconstruction results from the WBP and SIRT methods showed substantial degradation. This was especially noticeable in the *xz* slices (Figs. 5c and 5f lower) revealing missing wedge effects. Streaking artifacts were more prominent, blurring in the missing wedge direction was greater, the particles became elongated in the missing wedge direction, and gray levels were more distributed throughout the volume. In the *xy* slices (Figs. 5b, 5c, 5e, 5f upper), both the density and the shape were distorted. In contrast to the WBP and SIRT results, the CS-TV reconstructions did not show substantial changes using 19 (Fig. 5h) or only 10 projections (Fig. 5i). For the CS-TV reconstructions, the distribution and morphology of the carbon fibers remained nearly identical to that in the reconstruction using the full projection series. Similar conclusions can be obtained from the line profile plot results. As

the number of projections was decreased, the WBP and SIRT reconstruction line profiles changed, especially for the 10-projection reconstruction, while the line profiles for the 10-projection CS reconstruction were similar to those from the 37-projection reconstruction. The intensity of the SIRT reconstruction signal decreased by ~50% from the 37- to the 10-projection, and the background became noisier. The success of CS-TV reconstruction relative to WBP and SIRT became increasingly pronounced as the number of projections was reduced.

Figure 6 presents color-composite isosurface renderings of WBP, SIRT, and CS-TV reconstructions for all three chemical components. Note that the epoxy contributed minimally to the Teflon™ fiber, carbon fiber, or Pt maps because those maps were derived from optical density differences at energies where the spectrum of the epoxy does not change (Fig. 4a). In Figures 4 and 6, the empty regions are uniformly filled with epoxy. The isosurface renderings were obtained using the Otsu automatic threshold method (Otsu, 1975) implemented in ImageJ. Figure 6 compares 0° and 90° views of the CS-TV and SIRT reconstructions shown in Figure 5, and reinforces the trends seen there. For the full 37-tilt angle set (Figs. 6a, 6d, 6g), the SIRT, CS-TV, and WBP reconstructions exhibited similar morphology and spatial distributions for the three components. However, even with the full set of angles, the WBP reconstruction showed high background levels (Fig. 6g). The isosurfaces showed compact structures with sharp edges, consistent with a relatively high signal-to-noise ratio (SNR) in the reconstruction volume. The results from CS-TV for the 19-tilt angle (Fig. 6b) and 10-tilt angle (Fig. 6c) sets remained of high quality, showing only small changes relative to the

analysis of the 37-tilt angle set. However, in the corresponding SIRT reconstructions, substantial speckle and a gradual smearing of the edges appeared in the reconstructions as the number of projections was reduced (Figs. 6e and 6f). The signal from the WBP reconstructions of 19-projection (Fig. 6h) and 10-projection (Fig. 6i) sets was basically lost in the noise. The missing wedge problem strongly affects WBP, as has been noted elsewhere (Penczek, 2010).

As highlighted in equation (6), the CS-TV method requires the selection of the parameter β , the weighting factor for the TV-norm in the reconstruction process. In principle, the optimal value for β is defined by the intrinsic sparsity of the object and the relative magnitudes of the signals in the reconstruction. Experimentally, the value of β will also be influenced by noise or other artifacts in the data set. Moreover, the true sparsity of the object will not be known in general. As a result, β must be optimized for each data set. Figure 7 illustrates the effects of different choices of β for CS-TV reconstruction of the 37-projection data set of the bilayer model sample (carbon fiber map). When β was set too low (Figs. 7a and 7d) there was little effect of TV regularization and the reconstruction showed negligible benefit of CS. When β was set too high (Figs. 7c and 7f), the effect of the TV penalty term was over-emphasized, resulting in a flattened image with plateaus in the reconstructed signal and background which did not represent physical structures in the sample. This is clearly seen in the line profiles across the projections (Figs. 7g and 7h).

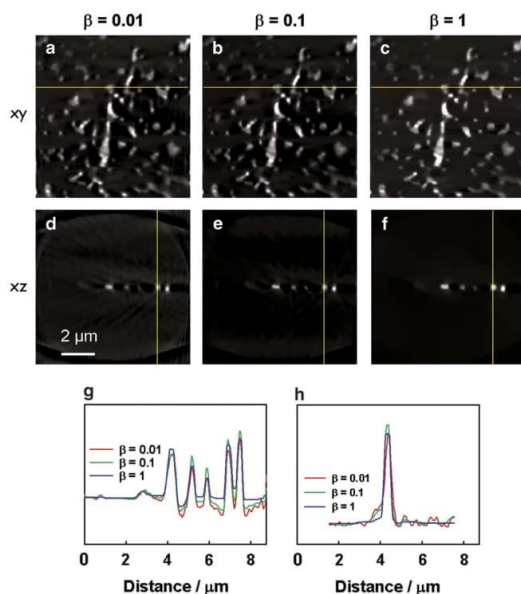


Figure 7. Effect of different choices of the β parameter for compressed sensing total variation (CS-TV) tomographic reconstructions. Slices through the xy (upper) and xz (middle) planes are shown for reconstructions using (a,d) $\beta = 0.01$, (b,e) $\beta = 0.1$, and (c,f) $\beta = 1$. **g:** Line intensity profiles through the indicated line on the xy slices. **h:** Line intensity profiles through the indicated line on the xz slices.

In general, the optimal β value will be larger for greater signal magnitudes, for example, if more projections are included in the input data set. In this case, the data fidelity term in equation (6) is larger, and the penalty term requires greater weight to have the same effect. The sparsity of the object will also affect the optimal β , as will the noise level and the presence of other inconsistencies in the data. Although these heuristics provide some guidelines for selecting β , often empirical optimization of the β parameter is needed. In principle, the β parameter could be normalized relative to the term accounting for consistency with the experimental data, removing some of the dependence on the number of tilt angles. The implementation presented here maintains the behavior of the β parameter from earlier work for consistency in the application of CS-TV to STXM tomography. For a day-to-day user, the effect remains the same: β is necessarily optimized for the particular data set at hand. Typically, this optimization may be carried out on a representative xz slice from a given sample, and then the more time- and computationally-intensive volume reconstruction can be carried out with the selected optimal β value.

3D Mapping Acrylate/Polystyrene in a Nanopipette

The microsphere-nanopipette sample allowed exploration of CS-TV tomography using a data set with a richer spectral dimension than that of the bilayer model sample. This case exhibits gradient domain sparsity (TV-sparsity) in the spatial dimensions, making use of a separate decomposition of the finite number of chemical phases in the spectral dimension. In this sample, multiple carbon-based compounds with overlapping signals were present, demonstrating the power of 4D imaging using STXM spectro-tomography. In addition, the needle-like sample geometry enabled evaluation of CS-TV tomography with a data set acquired over a complete 180° tilt range, which allowed examination of the effect of varying the angular range by artificially introducing a missing wedge *post facto*.

The C 1s spectra of the components extracted from the C 1s stacks are shown in Figure 8a. The X-ray absorption was saturated at several photon energies around the intense 285 eV C 1s $\rightarrow \pi^*$ peak because both the carbon nanotube pipette and PS absorb strongly at this energy, so that the total absorption became too large when the X-rays passed through more than one microsphere. Figures 8b to 8d presents the chemical maps for the acrylate, PS, and carbon nanopipette components derived from SVD analysis of one angle projection, using all energies except those at 285.0 and 285.5 eV where the absorption saturation distortion occurs. Figure 8e is a color composite of these three component maps. The carbon nanopipette map was expected to show signal from the exterior tube only. The acrylate should show a larger density inside the microspheres, although it is known that acrylate leaked from some of the hollow PS particles in this particular sample (Johansson et al., 2007). If so, as the water was lost, the acrylate dried on to the interior of the PS particles or onto the interior of the carbon nanopipette.

962 Juan Wu et al.

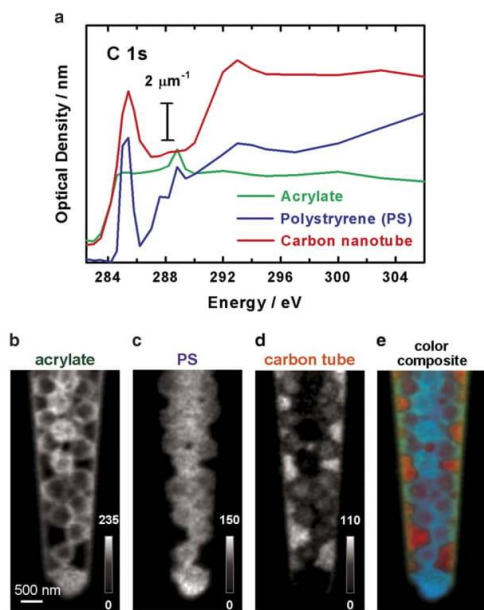


Figure 8. a: C 1s spectra of the components of a sample consisting of acrylate filled polystyrene microspheres inside a carbon nanopipette. Quantitative two-dimensional projection components maps (thicknesses in nm) of (b) acrylate, (c) polystyrene (PS) microsphere shell, and (d) the carbon nanotube pipette. e: Color-coded composite map showing acrylate in green, PS in blue, and the carbon nanotube pipette in red.

Figure 9 presents the 3D reconstructions of the acrylate maps obtained using WBP, CS-TV, and SIRT for tilt angle ranges of $\pm 90^\circ$, $\pm 74^\circ$, and $\pm 62^\circ$. The results from the $\pm 90^\circ$ tilt set showed hollow acrylate distributions inside the tube in the xy slice and no missing wedge artifacts in the xz slice (Figs. 9a, 9d, 9g). Using presently available STXM tilt-series data-acquisition technology and standard processing techniques, WBP and SIRT methods yielded reconstructions with intensities with both negative and positive values. Such artifacts represent a key limitation for analytical tomography where intensity represents concentration, motivating the development of alternative reconstruction techniques. In contrast, using only the addition of the TV-minimization constraint in CS, the reconstructions were significantly improved, with physically interpretable intensities. When the analysis was performed using reduced tilt angle ranges, missing wedge artifacts appeared in the WBP, SIRT, and CS-TV reconstructions, though the artifacts were much less severe in the CS-TV reconstructions (Figs. 9g, 9h, 9i). Figure 10 presents line intensity profiles along the missing wedge direction for the WBP (Fig. 10a), SIRT (Fig. 10b), and CS-TV (Fig. 10c) results for each of the three tilt angle ranges. For WBP and SIRT reconstructions, the line profiles showed significant broadening in the missing wedge direction as the size of the missing wedge was increased (highlighted with arrows in Figs. 10a and 10b). The intensity distributions in

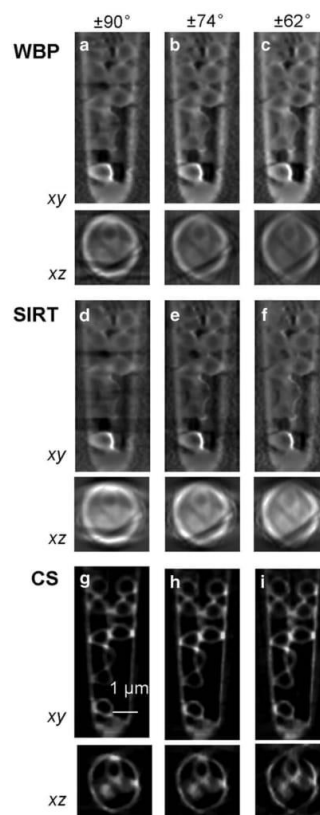


Figure 9. Evaluation of the effect of the size of the missing wedge on simultaneous iterative reconstruction technique (SIRT) and compressed sensing total variation (CS-TV) tomographic reconstructions of the acrylate maps. Comparisons of (a–c) weighted back-projection (WBP), (d–f) SIRT, and (g–i) CS-TV results for three different tilt angle ranges: (a,d,g) $\pm 90^\circ$, (b,e,h) $\pm 74^\circ$, and (c,f,i) $\pm 62^\circ$. Slices through the xy (top) and xz (bottom) planes are shown for each reconstruction.

line profiles from the $\pm 90^\circ$ and $\pm 74^\circ$ tilt sets reconstructed using CS-TV were similar (Fig. 10c). For CS-TV reconstructions, effects of the missing wedge appeared as a slight broadening of features only when the tilt angle range was reduced to $\pm 62^\circ$. Moreover, changes appeared in isolated regions of the CS-TV reconstructions, whereas for SIRT reconstructions all peaks were affected by the increased missing wedge. Overall, CS-TV reconstructions maintained data fidelity to a reasonable level, whereas WBP and SIRT showed a significant reduction in reconstruction quality. Supplementary Figure 5 presents WBP, SIRT, and CS reconstructions of the images recorded at a single photon energy (290 eV), in order to explore if the analysis in the spectral domain, to generate component maps, had an effect. When only a single energy is analysed, the clarity of the reconstructions is improved for each method, but similar results with respect to the relative quality of WBP, SIRT, and

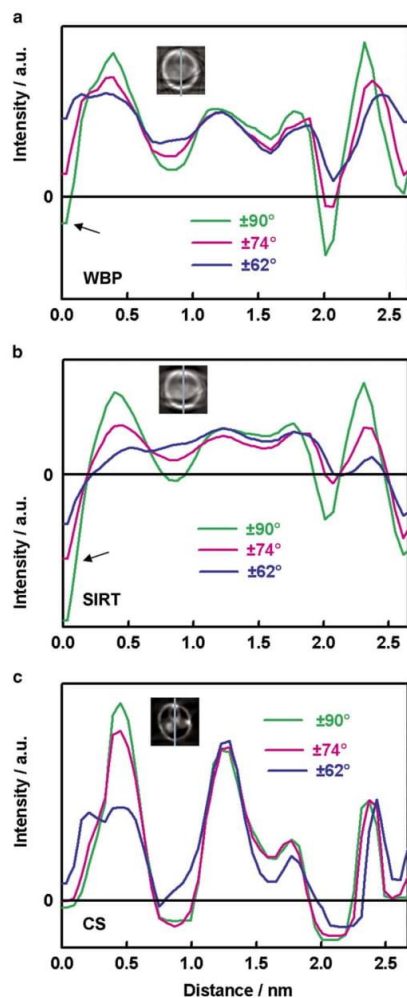


Figure 10. Line intensity profiles through selected xz planes from (a) weighted back-projection (WBP), (b) simultaneous iterative reconstruction technique (SIRT), and (c) compressed sensing total variation (CS-TV) reconstructions corresponding to the three tilt angle ranges indicated in Figure 9. The insets show the location of the selected lines.

CS are obtained as for the reconstructions of the component maps. Supplementary Figure 6 presents SIRT analyses with a non-negativity constraint of the PS and carbon nanotubes component maps, at three different tilt angle ranges ($\pm 90^\circ$, $\pm 74^\circ$, $\pm 62^\circ$). As found for the Au dumbbell electron tomography analysis, applying the non-negativity constraint does improve the SIRT reconstructions and reduces its sensitivity to changes in the tilt angle range analysed.

Supplementary Figures 5 and 6

Supplementary Figures 5 and 6 can be found online. Please visit journals.cambridge.org/jid_MAM.

DISCUSSION

The demonstration of a CS-TV tomography algorithm for STXM presented here outlines ways for improving the quality of STXM tomography reconstructions and opens up new possibilities for dose-rationing in STXM tilt series spectro-tomography. The geometry of STXM optics means that many samples impose an upper limit on the tilt range accessible for tomography, introducing a missing wedge of information, as in electron tomography. The CS-TV approach applied to STXM tilt series data of a PEM-FC model sample and a chemically complex microsphere sample has shown significant benefits over conventional WBP and SIRT methods for data sets with a missing wedge.

Furthermore, the CS-TV tomography approach has been shown to be robust to substantial under-sampling by increasing the angular increment in a tilt series. For STXM of radiation-sensitive materials, this CS-TV approach makes available several new acquisition strategies for minimizing dose. For a given SNR in each tilt series projection, the total dose may be reduced by acquiring fewer images at larger tilt increment. Alternatively, for a fixed total dose, the SNR of each individual projection may be increased by acquiring fewer images, each for a longer time. Each of these approaches may offer advantages for different samples, for imaging at different ionization edges, or at different spatial resolutions. Critically, enabling these techniques will allow 3D chemical imaging of samples that cannot be imaged with electron tomography, even with CS techniques, due to their radiation sensitivity. Our model sample analyses demonstrate the capability of CS-TV to produce high-fidelity tomographic reconstructions using a very small number of tilt angles. The feasibility of STXM tomography using limited projection data is a critical and promising result for 3D chemical imaging of the ionomer in PEM-FC cathodes, since PFSA is highly radiation sensitive (Susac et al., 2013; Melo et al., 2016) and excessive mass loss and ionomer redistribution can occur when more than ~ 10 angles are measured. We anticipate that CS-TV methods will become widespread and routine in STXM tomography, particularly for radiation-sensitive materials such as the ionomer in PEM-FC cathodes. Reliable mapping of PEM-FC cathodes, and the corresponding quantitative reliability of 3D mapping of PFSA will be possible with 12–15 projections instead of 30–40 projections or more, as in more conventional approaches to STXM tomography.

At its core, the CS-TV algorithm is widely adaptable to many materials samples. The TV-norm requires the sample to be composed of at least approximately homogeneous chemical phases. This assumption is readily satisfied by many chemistries where individual compounds are present in separate sub-volumes. The CS-TV approach is, moreover, often more flexible than other advanced tomographic approaches like the discrete algebraic reconstruction technique (DART) (Batenburg & Sijbers, 2007). DART assumes a known, finite number of gray levels in the reconstruction volume. The CS-TV approach does not impose knowledge of

the number of different homogeneous phases. On the other hand, samples containing continuous chemical gradients, for example, may not be suitable for CS-TV STXM tomography methods. In those cases the CS framework allows alternatives to the TV-norm to be used for CS reconstructions. Identity and wavelet transforms have been applied to cases in electron tomography (Saghi et al., 2011; Nicoletti et al., 2013) and these sparsity transforms can be combined for improved results (Leary et al., 2012; Saghi et al., 2016). Total generalized variation techniques (Al-Afeef et al., 2015a) and dictionary-learning approaches (Al-Afeef et al., 2015b, 2016) to CS tomography also present alternatives for dealing with continuous intensity variations and other types of structure in data. By applying transform domains that are appropriate to the structure in the data, CS can be widely adapted to different types of samples. Here, the CS-TV approach is broadly applicable to many common sample types encountered in STXM.

The high chemical sensitivity of spectroscopic STXM, well illustrated in the microsphere sample, represents another key advance for 3D chemical imaging. The wealth of chemical detail available in NEXAFS can now be recovered for 3D micro- and nano-scale analysis using advanced tomography techniques like the CS-TV algorithm. The many STXM modalities, including developments in ptychographic STXM imaging, will likely also benefit from combination with CS-TV tomography methods.

SUMMARY

An implementation of the CS-TV algorithm for analysis of STXM tomography data sets was presented, and its performance was evaluated relative to WBP and SIRT analyses of three different data sets. In each case, significant improvements were demonstrated, especially for highly under-sampled tilt series. The results show that CS-TV can be used to derive high-fidelity 3D morphology even when radically fewer projections are used. This approach provides a method to improve the reliability of 3D mapping of ionomer in PEM-FC cathodes and many other radiation-sensitive materials by using fewer projections and thus decreasing radiation damage. CS-TV should also be applicable to ptychographic tomography (Holler et al., 2014) and spectro-ptycho-tomography.

ACKNOWLEDGMENTS

The authors thank Marcia Reid (McMaster University) who prepared samples and Martin Obst (University of Bayreuth) who made the tomography rotation stage. The authors are grateful for excellent instrumentation support from CLS staff, Jian Wang, and Jay Dynes; and the ALS staff, Tolek Tyliczszak, and David Kilcoyne. Tomography and other data were acquired at beamlines 5.3.2.2 and 11.0.2 at the Advanced Light Source, which is supported by the Director of the Office of Science, Department of Energy, under Contract no. DE-AC02-05CH11231. Some

results were also obtained with the ambient STXM on beamline 10ID1 at the Canadian Light Source, which is supported by the Canadian Foundation for Innovation. The research leading to these results has received funding from the European Research Council under the European Union's Seventh Framework Program (FP7/2007-2013)/ERC grant agreement no. 291522-3DIMAGE, as well as from the European Union Seventh Framework Program under Grant Agreement 312483-ESTEEM2 (Integrated Infrastructure Initiative – I3). R.L. acknowledges a Junior Research Fellowship from Clare College.

REFERENCES

- ADCOCK, B., HANSEN, A.C., POON, C. & ROMAN, B. (2017). Breaking the coherence barrier: A new theory for compressed sensing. *Forum of Mathematics, Sigma*, **5**, e4.
- ADE, H. & HITCHCOCK, A.P. (2008). NEXAFS microscopy and resonant scattering: Composition and orientation probed in real and reciprocal space. *Polymer* **49**, 643–675.
- AL-AFEEF, A., ALEKSEEV, A., MACLAREN, I. & COCKSHOT, P. (2015a). Electron tomography based on a Total Generalized Variation minimization reconstruction technique. *31st Picture Coding Symposium*, Cairns, Australia.
- AL-AFEEF, A., BOBYNKO, J., COCKSHOT, W.P., CRAVEN, A.J., ZUAZO, I.U., BARGES, P. & MACLAREN, I. (2016). Linear chemically sensitive electron tomography using DualEELS and dictionary-based compressed sensing. *Ultramicroscopy* **170**, 96–106.
- AL-AFEEF, A., COCKSHOT, W.P., MACLAREN, I. & MCVITIE, S. (2015b). Electron tomography image reconstruction using data-driven adaptive compressed sensing. *Scanning* **38**, 251–276.
- ANDERSEN, A.H. & KAK, A.C. (1984). Simultaneous algebraic reconstruction technique (SART): A superior implementation of the ART algorithm. *Ultrason Imaging* **6**, 81–94.
- BANDHOPADHYAY, S., SINGH, G. & GLOMM, W.R. (2017). Shape tunable synthesis of anisotropic gold nanostructures through binary surfactant mixtures. *Materials Today Chemistry* **3**, 1–9.
- BANGLIANG, S., YIHENG, Z., LIHUI, P., DANYA, Y. & BAOFEN, Z. (2000). The use of simultaneous iterative reconstruction technique for electrical capacitance tomography. *Chem Eng J* **77**, 37–41.
- BARUCHEL, J., BUFFIERE, J.-Y., CLOETENS, P., DI MICHEL, M., FERRIE, E., LUDWIG, W., MAIRE, E. & SALVO, L. (2006). Advances in synchrotron radiation microtomography. *Scripta Materialia* **55**, 41–46.
- BATENBURG, K.J. & SIBERS, J. (2007). Dart: A fast Heuristic algebraic reconstruction algorithm for discrete tomography. In *Proceedings of the 2007 IEEE International Conference on Image Processing*. Piscataway, NJ: IEEE. doi:10.1109/ICIP.2007.4379972.
- BEREJNOV, V., SUSAC, D., STUMPER, J. & HITCHCOCK, A.P. (2013). 3D chemical mapping of PEM fuel cell cathodes by scanning transmission soft X-ray spectro-tomography. *ECS Trans* **50**, 361–368.
- BLUMENSATH, T. & DAVIES, M.E. (2009). Iterative hard thresholding for compressed sensing. *Appl Comput Harmonic Anal* **27**, 265–274.
- BOUDIN, F., HOURS, M., LACRONIQUE, J.-F., SALVO, L., SUÉRY, M., MARMOTTANT, A., LIMODIN, N. & BERNARD, D. (2010). 3D imaging in material science: Application of X-ray tomography. *C R Phys* **11**, 641–649.
- BREDIES, K., KUNISHI, K. & POCK, T. (2010). Total generalized variation. *SIAM J Imaging Sci* **3**, 492–526.

- CANDÈS, E.J., ROMBER, J. & TAO, T. (2006). Robust uncertainty principles: Exact signal reconstruction from highly incomplete frequency information. *IEEE Trans Inform Theory* **52**, 489–509.
- CENSOR, Y., ELFVING, T., HERMAN, G.T. & NIKAZAD, T. (2008). On diagonally relaxed orthogonal projection methods. *SIAM J Sci Comput* **30**, 473–504.
- CHAO, W., FISCHER, P., TYLISZCZAK, T., REKAWA, S., ANDERSON, E. & NAULLEAU, P. (2012). Real space soft x-ray imaging at 10 nm spatial resolution. *Optics Express* **20**, 9777–9783.
- CIMMINO, G. (1938). Calcolo approssimato per le soluzioni dei sistemi di equazioni lineari. *La Ricerca Scientifica, XVI, Series II, Anno IX* **1**, 326–333.
- DONOHO, D.L. (2006). Compressed sensing. *IEEE Trans Inform Theory* **52**, 1289–1306.
- DUARTE-CARVAJALINO, J.M. & SAPIRO, G. (2009). Learning to sense sparse signals: Simultaneous sensing matrix and sparsifying dictionary optimization. *IEEE Trans Image Process* **18**, 1395–1408.
- ELFVING, T., HANSEN, P.C. & NIKAZAD, T. (2012). Semiconvergence and relaxation parameters for projected SIRT algorithms. *SIAM J Sci Comput* **34**, A2000–A2017.
- ERCIUS, P., ALAIDI, O., RAMES, M.J. & REN, G. (2015). Electron tomography: A three-dimensional analytic tool for hard and soft materials research. *Adv Mater* **27**, 5638–5663.
- FOLKESSON, A., ANDERSSON, C., ALVFORS, P., ALAKÜLA, M. & OVERGAARD, L. (2003). Real life testing of a hybrid PEM fuel cell bus. *J Power Sources* **118**, 349–357.
- GILBERT, P. (1972). Iterative methods for the three-dimensional reconstruction of an object from projections. *J Theoretical Biol* **36**, 105–117.
- GREGOR, J. & BENSON, T. (2008). Computational analysis and improvement of SIRT. *IEEE Trans Med Imag* **27**, 918–924.
- HABERFELHNER, G., ORTHACKER, A., ALBU, M., LI, J. & KOTHEITNER, G. (2014). Nanoscale voxel spectroscopy by simultaneous EELS and EDS tomography. *Nanoscale* **6**, 14563–14569.
- HITCHCOCK, A.P. (2012). Soft X-ray imaging and spectromicroscopy. In *Handbook of Nanoscopy*, Tendeloo G.V., Dyck D.V., & Pennycook S.J. (Eds.), pp. 745–791. Weinheim, Germany: Wiley-VCH Verlag GmbH & Co. KGaA.
- HITCHCOCK, A.P., BEREJNOV, V., LEE, V., WEST, M.M., DUTTA, M., COLBOW, V. & WESSEL, S. (2014). Carbon corrosion of proton exchange membrane fuel cell catalyst layers studied by scanning transmission X-ray microscopy. *J Power Sources* **266**, 66–78.
- HITCHCOCK, A.P., JOHANSSON, G.A., MITCHELL, G.E., KEEFE, M.H. & TYLISZCZAK, T. (2008). 3-D chemical imaging using angle-scan nanotomography in a soft X-ray scanning transmission X-ray microscope. *Appl Phys A* **92**, 447–452.
- HOLLER, M., DIAZ, A., GUIZAR-SICAÍROS, M., KARVINEN, P., FÄRM, E., HÄRKÖNEN, E., RITALA, M., MENZEL, A., RAABE, J. & BUNK, O. (2014). X-ray ptychographic computed tomography at 16 nm isotropic 3D resolution. *Sci Rep* **4**, 3857.
- HOWELLS, M., JACOBSEN, C., WARWICK, T. & VAN DEN BOS, A. (2007). Principles and applications of zone plate X-ray microscopes. In *Science of Microscopy*, Hawkes, P.W. & Spence, J.C.H. (Eds.), pp. 835–926. New York, NY: Springer.
- JACOBSEN, C., WIRICK, S., FLYNN, G. & ZIMBA, C. (2000). Soft X-ray spectroscopy from image sequences with sub-100 nm spatial resolution. *J Microsc* **197**, 173–184.
- JOHANSSON, G.A., DYNES, J.J., HITCHCOCK, A.P., TYLISZCZAK, T., SWERHONE, G.D. & LAWRENCE, J.R. (2006). Chemically sensitive tomography at 50 nm spatial resolution using a soft X-ray scanning transmission X-ray microscope. *Microsc Microanal* **12**, 1412–1413.
- JOHANSSON, G.A., TYLISZCZAK, T., MITCHELL, G.E., KEEFE, M.H. & HITCHCOCK, A.P. (2007). Three-dimensional chemical mapping by scanning transmission X-ray spectromicroscopy. *J Synchrotron Rad* **14**, 395–402.
- KAK, A.C. & SLANEY, M. (1988). *Principles of Computerized Tomographic Imaging*, Society for Industrial and Applied Mathematics, New York: IEEE Press.
- KREMER, J.R., MASTRONARDE, D.N. & MCLINTOSH, J.R. (1996). Computer visualization of three-dimensional image data using IMOD. *J Struct Biol* **116**, 71–76.
- LANDWEBER, L. (1951). An iteration formula for Fredholm integral equations of the first kind. *Am J Math* **73**, 615–624.
- LEARY, R.K., KUMAR, A., STRANEY, P.J., COLLINS, S.M., YAZDI, S., DUNIN-BORKOWSKI, R.E., MIDGLEY, P.A., MILLSTONE, J.E. & RINGE, E. (2016). Structural and optical properties of discrete dendritic Pt nanoparticles on colloidal Au nanoprisms. *J Phys Chem C* **120**, 20843–20851.
- LEARY, R., MIDGLEY, P.A. & THOMAS, J.M. (2012). Recent advances in the application of electron tomography to materials chemistry. *Acc Chem Res* **45**, 1782–1791.
- LEARY, R., SAGHI, Z., MIDGLEY, P.A. & HOLLAND, D.J. (2013). Compressed sensing electron tomography. *Ultramicroscopy* **131**, 70–91.
- LEROTIC, M., MAK, R., WIRICK, S., MEIRER, F. & JACOBSEN, C. (2014). MANTiS: A program for the analysis of X-ray spectromicroscopy data. *J Synchrotron Rad* **21**, 1206–1212.
- LUSTIG, M., DONOHO, D. & PAULY, J.M. (2007). Sparse MRI: The application of compressed sensing for rapid MR imaging. *Magn Reson Med* **58**, 1182–1195.
- MALLAT, S. (2008). *A Wavelet Tour of Signal Processing*, 3rd ed. Cambridge, MA: Academic Press.
- MELO, L.G.A., HITCHCOCK, A.P., BEREJNOV, V., SUSAC, D., STUMPER, J. & BOTTON, G.A. (2016). Evaluating focused ion beam and ultramicrotome sample preparation for analytical microscopies of the cathode layer of a polymer electrolyte membrane fuel cell. *J Power Sources* **312**, 23–35.
- NICOLETTI, O., DE LA PEÑA, F., LEARY, R.K., HOLLAND, D.J., DUCATI, C. & MIDGLEY, P.A. (2013). Three-dimensional imaging of localized surface plasmon resonances of metal nanoparticles. *Nature* **502**, 80–84.
- OBST, M. & SCHMID, G. (2014). 3D chemical mapping: Application of scanning transmission (soft) X-ray microscopy (STXM) in combination with angle-scan tomography in bio-, geo-, and environmental sciences. In *Electron Microscopy*, Kuo, J. (Ed.), pp. 757–781. New York: Humana Press.
- OBST, M., WANG, J. & HITCHCOCK, A.P. (2009). Soft X-ray spectro-tomography study of cyanobacterial biomineral nucleation. *Geobiology* **7**, 577–591.
- OTSU, N. (1975). A threshold selection method from gray-level histograms. *Automatica* **11**, 285–296, 23–27.
- PENCZEK, P.C. (2010). Fundamentals of three-dimensional reconstruction from projections. *Methods Enzymol* **482**, 1–33.
- PETTERSEN, E.F., GODDARD, T.D., HUANG, C.C., COUCH, G.S., GREENBLATT, D.M., MENG, E.C. & FERRIN, T.E. (2004). UCSF Chimera—A visualization system for exploratory research and analysis. *J Comput Chem* **25**, 1605–1612.
- SAGHI, Z., DIVITINI, G., WINTER, B., LEARY, R., SPIECKER, E., DUCATI, C. & MIDGLEY, P.A. (2016). Compressed sensing electron tomography of needle-shaped biological specimens – Potential for improved reconstruction fidelity with reduced dose. *Ultramicroscopy* **160**, 230–238.

966 Juan Wu et al.

- SAGHI, Z., HOLLAND, D.J., LEARY, R., FALQUI, A., BERTONI, G., SEDERMAN, A.J., GLADDEN, L.F. & MIDGLEY, P.A. (2011). Three-dimensional morphology of iron oxide nanoparticles with reactive concave surfaces. A compressed sensing-electron tomography (CS-ET) approach. *Nano Lett* **11**, 4666–4673.
- SCHMID, G., OBST, M., WU, J. & HITCHCOCK, A.P. (2016). 3D chemical imaging of nanoscale biological, environmental and synthetic materials by soft X-ray spectro-tomography. In *X-Ray and Neutron Techniques for Nanomaterials Characterization*, Kumar, C.S.S.R. (Ed.), pp. 43–94. Berlin: Springer.
- SCHMID, G., ZEITVOGEL, F., HAO, L., INGINO, P., KUERNER, W., DYNES, J.J., KARUNAKARAN, C., WANG, J., LU, Y., AYERS, T., SCHIETINGER, C., HITCHCOCK, A.P. & OBST, M. (2014). Synchrotron-based chemical nano-tomography of microbial cell-mineral aggregates in their natural, hydrated state. *Microsc Microanal* **20**, 531–536.
- SCHNEIDER, C.A., RASBAND, W.S. & ELICEIRI, K.W. (2012). NIH Image to ImageJ: 25 years of image analysis. *Nature Methods* **9**, 671–675.
- SCHRLAU, M.G., FALLS, E.M., ZIOBER, B.L. & BAU, H.H. (2008). Carbon nanopipettes for cell probes and intracellular injection. *Nanotechnology* **19**, 015101.
- SIDKY, E.Y. & PAN, X.C. (2008). Image reconstruction in circular cone-beam computed tomography by constrained, total-variation minimization. *Phys Med Biol* **53**, 4777–4807.
- STÖHR, J. (1992). *NEXAFS Spectroscopy*. Berlin: Springer-Verlag.
- SUSAC, D., BEREJNOV, V., HITCHCOCK, A.P. & STUMPER, J. (2011). STXM study of the ionomer distribution in the PEM fuel cell catalyst layers. *ECS Trans* **41**, 629–635.
- SUSAC, D., BEREJNOV, V., HITCHCOCK, A.P. & STUMPER, J. (2013). STXM characterization of PEM fuel cell catalyst layers. *ECS Trans* **50**, 405–413.
- TORRUELLA, P., ARENAL, R., DE LA PEÑA, F., SAGHI, S., YEDRA, L., ELJARRAT, A., LÓPEZ-CONESA, L., ESTRADER, M., LÓPEZ-ORTEGA, A., SALAZAR-ALVAREZ, G., NOGUÉS, J., DUCATI, C., MIDGLEY, P.A., PEIRÓ, F. & ESTRADÉ, S. (2016). 3D visualization of the iron oxidation state in FeO/Fe₃O₄ core-shell nanocubes from electron energy loss tomography. *Nano Lett* **16**, 5068–5073.
- VAINSHTEIN, B.K. (1970). Finding the structure of objects from projections. *Sov Phys Crystallogr* **15**, 781–787.
- WANG, C., MAO, Z., BAO, F., LI, X. & XIE, X. (2005). Development and performance of 5 kW proton exchange membrane fuel cell stationary power system. *Int J Hydrogen Energy* **30**, 1031–1034.
- WANG, J., BOTTON, G.A., WEST, M.M. & HITCHCOCK, A.P. (2009b). Quantitative evaluation of radiation damage to polyethylene terephthalate by soft X-rays and high-energy electrons. *J Phys Chem B* **113**, 1869–1876.
- WANG, J., HITCHCOCK, A.P., KARUNAKARAN, C., PRANGE, A., FRANZ, B., HARKNESS, T., LU, Y., OBST, M. & HORMES, J. (2011). 3D chemical and elemental imaging by STXM spectrotomography. *AIP Conf Proc*, **1365**, 215–218.
- WANG, J., MORIN, C., LI, L., HITCHCOCK, A.P., SCHOLL, A. & DORAN, A. (2009a). Radiation damage in soft X-ray microscopy. *J Electron Spectrosc Relat Phenom* **170**, 25–36.
- XU, M. & WANG, L.V. (2005). Universal back-projection algorithm for photoacoustic computed tomography. *Phys Rev E* **71**, 016706.
- ZHANG, X., BALHORN, R. & MAZIRIMAS, J. (1996). Mapping and measuring DNA to protein ratios in mammalian sperm head by XANES imaging. *J Struct Biol* **116**, 335–344.

Supplemental Information for Optimization of 3D chemical imaging by soft X-ray spectro-tomography using a compressed sensing algorithm

Juan Wu,¹ Mirna Lerotic,² Sean Collins,³ Rowan Leary,³ Zineb Saghi,³ Paul Midgley,³
 Slava Berejnov,⁴ Darija Susac,⁴ Juergen Stumper,⁴ Gurvinder Singh⁵ and Adam P.
 Hitchcock¹

Microscopy & Microanalysis

Tomo-CS-supplemental-2nd-revision.doc

Last changed: 26 June 2017

1 Experimental conditions for tomography data acquisition

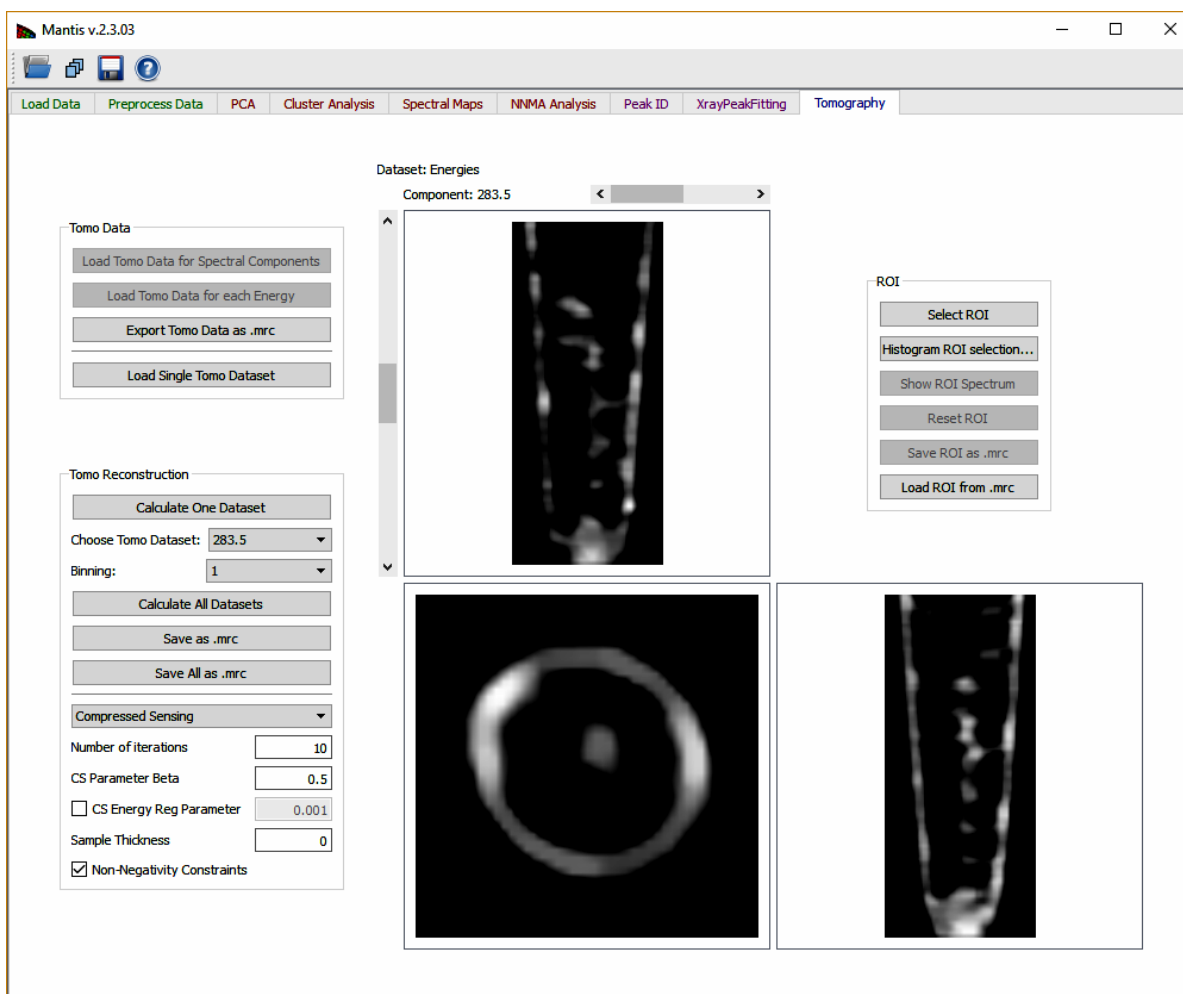
Table S-1 summarizes the key parameters used for acquiring the 3 tomographic data sets presented in this paper. The Au dumbbell sample was measured at a single energy in STEM while the polymer bilayer and nanopipette samples were measured at multiple energies in STXM.

Table S-1 Experimental details

Property	Au dumbbells	Polymer bilayer	Nanopipette
Instrument	FEI Tecnai F20 FEG-TEM, 200 keV	C 1s - ALS STXM 5322 F 1s - CLS a-STXM	ALS STXM 5322
Detection mode	dark field STEM	transmission	transmission
Energies (eV)	Not applicable	278, 285, 684, 694 eV	282-306 eV, 23 energies
Energy step	Not applicable	irregular	irregular
Energy resolution (meV)	Not applicable	C 1s – 300 F 1s - 200	300
Image step (nm)	0.59	100	60
Beam size (nm)	≤ 1	30	30
Spatial resolution (nm)	probe size	50 or spot size	50 or spot size
Exposure time/pixel	12 μs	1 ms	1 ms
Detector	Fischione Annular Dark Field Detector	Phosphor – PMT [1]	Phosphor – PMT [1]

[1] S. Fakra, S., A.L. Kilcoyne, and T. Tyliszczak, “Scintillator Detectors for Scanning Transmission X-ray Microscopes at the Advanced Light Source,” in Synchrotron Radiation Instrumentation 2003: Eighth International Conference on Synchrotron Radiation Instrumentation, T. Warwick, J. Stohr, H.A. Padmore, J. Arthur, AIP Conf Proc. 705, 973-976 (2004)

2 Compressed sensing reconstruction implemented as a tab in Mantis



Supplemental Figure S-1: Screen shot of the tomography tab in Mantis which provides access to CS and SIRT reconstructions with selectable parameters, on single energy, multiple energy, and multiple chemical map, tomography data sets. The reconstruction calculation can be tuned for each dataset by changing the algorithm parameters and by selectively imposing non-negativity constraints. There is provision for ROI voxel subset selection based on thresholding and subsequent extraction of the spectral signature of the voxel ROI, if multi-energy data set is being analyzed.

3 Comparison of original images with result from the tilt series

Figure S-2 presents the original 2D projection image at 0° (Fig. S2a) with that generated from the CS (Fig. S2b) and SIRT (Fig. S2c) reconstructions of the Au dumbbell STEM data set using all 67 acquired projections. The CS result shows more uniform density, while the SIRT result has background and diffraction artefacts not seen in the original 0° tilt angle image.

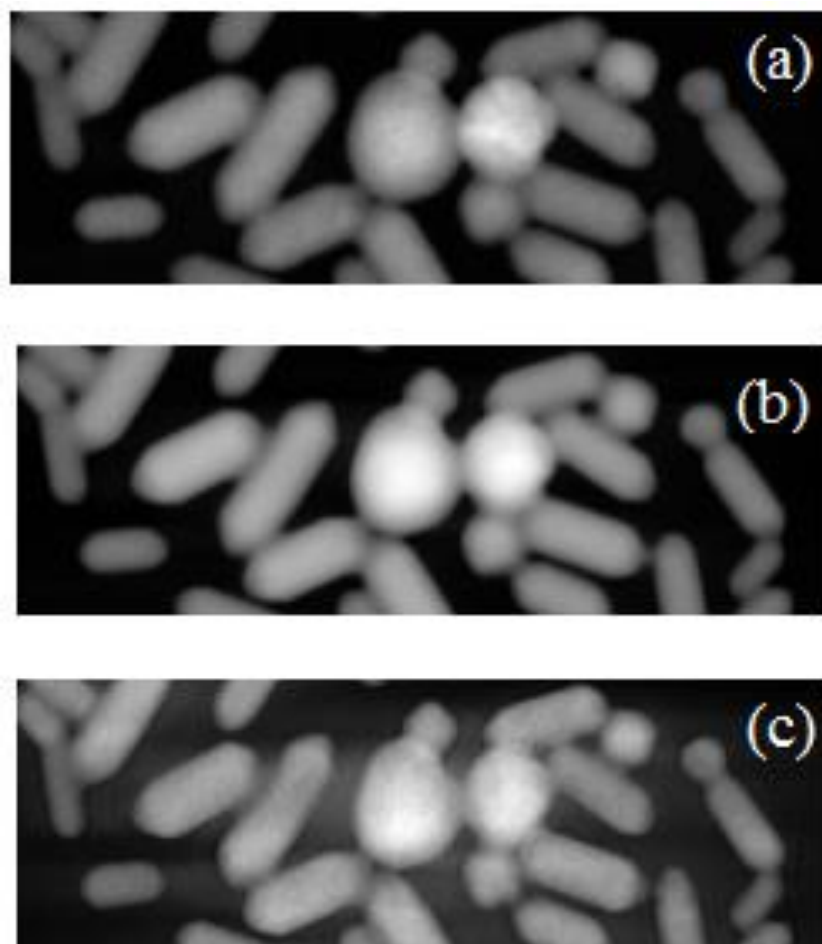


Figure S-2 Comparison of (a) original image from tilt series at 0° . (b) 2D projection at 0° generated from CS reconstruction. (c) 2D projection at 0° generated from the SIRT reconstruction. All 67 tilt angles were used.

4 Alternate approaches to SIRT reconstruction

Figure S-3 and **Figure S-4** presents results from CS and SIRT analysis of the Au dumbbell STEM data set using all 67 acquired projections. As compared to the reconstruction used to generate Fig.2 of the paper, the background level of the input images have been set to zero (an implementation of a compact support constraint) and overall normalization and non-negativity constraints have been applied. The CS results are more homogeneous in fig. S3 (a) as compared to Fig. 2(c). The intensity profiles plotted in the panels (a) - (d) in Fig. S3 show zero background intensity, and clean background signals around the particles. Even with implementation of additional constraints, the SIRT analysis shows significant missing wedge artefacts that are not present in the CS result.

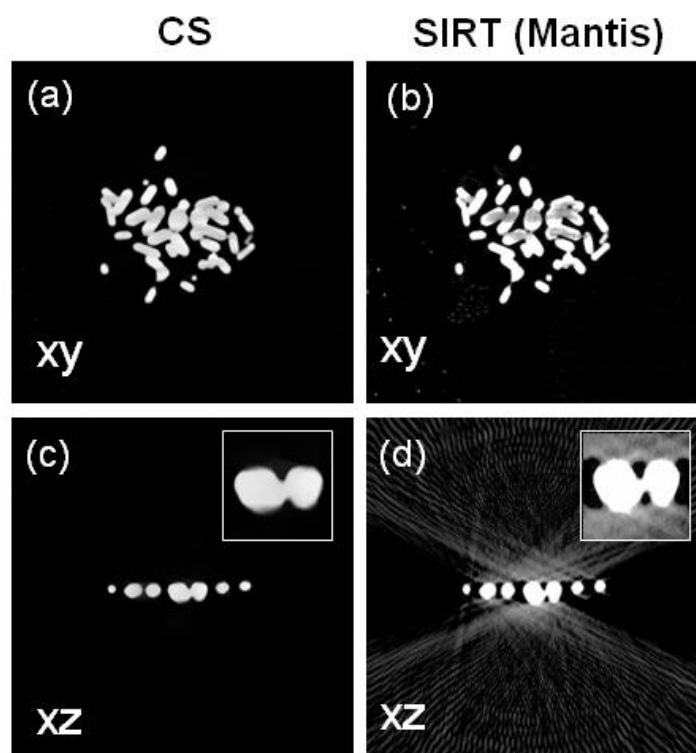


Fig. S-3: CS (left) and SIRT (right) electron tomography reconstructions of a Au nanoparticle sample using all 67 acquired projections. Selected slices through the xy plane of (a) CS, (b) SIRT and xz plane of (c) CS, (d) SIRT. The insets highlight the particles near the center of the volume.

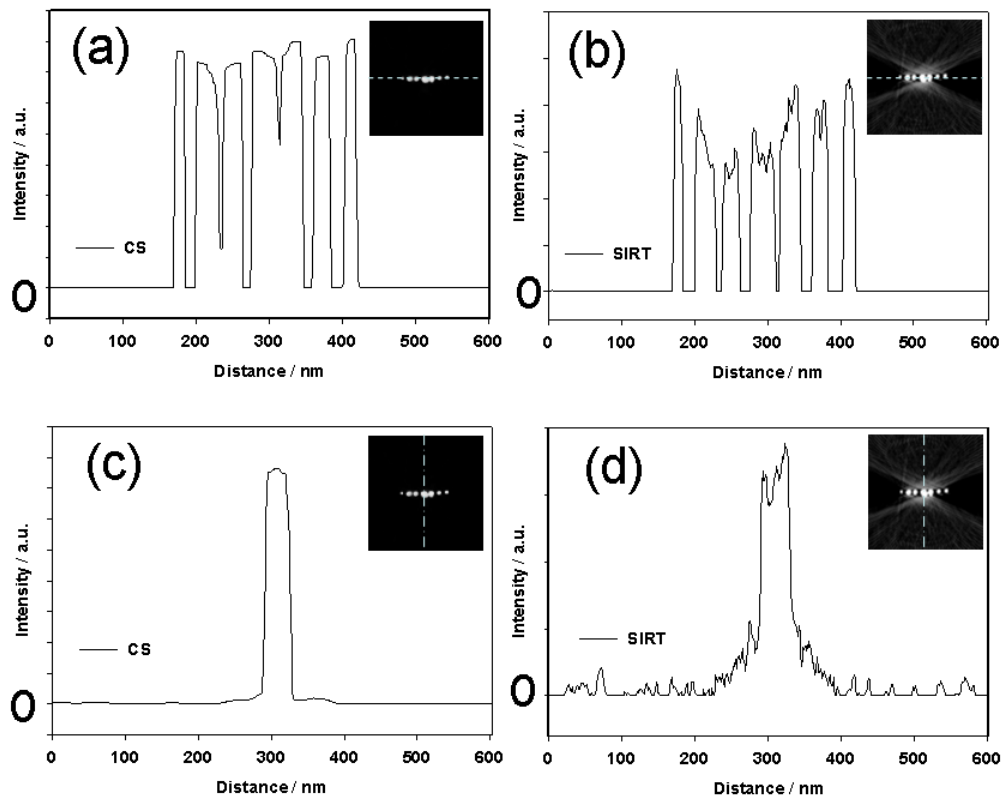


Fig. S-4: Line intensity profiles through xz plane from the (a),(c) CS and (b),(d) SIRT reconstructions shown in Fig. S-3

Figure S-5 presents results from analysis of the nanopipette data set using CS reconstruction of all 37 tilt angles at a single photon energy of 290 eV. (Note the results in Fig. 9 of the main paper are for reconstruction of component maps, derived from fitting the images recorded at multiple photon energies to reference spectra).

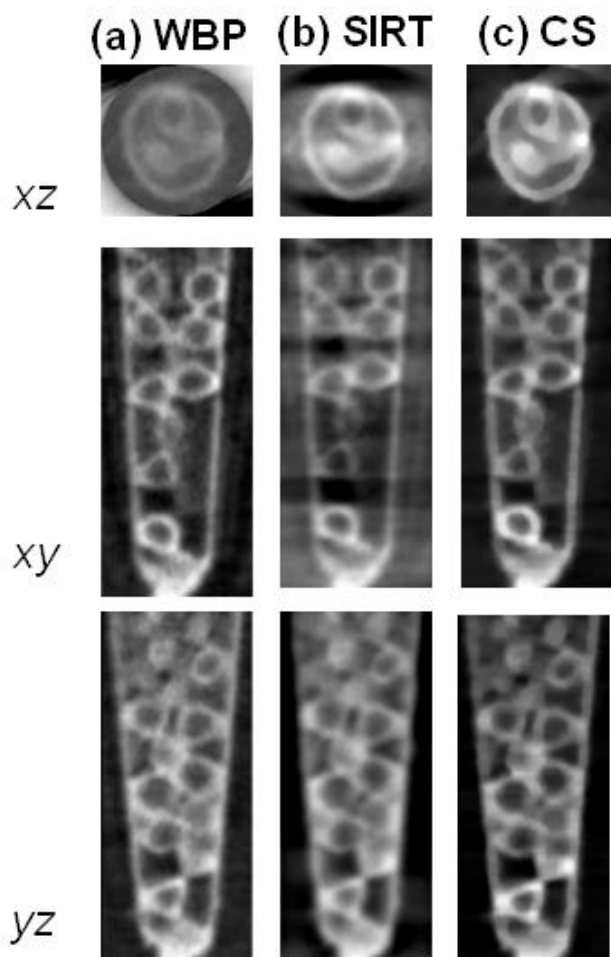


Fig. S-5: Tomographic reconstructions of the STXM images at 290 eV for $\pm 90^\circ$ tilt angle ranges using (a) WBP, (b) SIRT and (c) CS-TV. Slices through the xz (top), xy (middle) and yz (bottom) planes are shown for each reconstruction.

Figure S-6 presents results of SIRT analyses of the polystyrene and carbon nanotube chemical map tomography data sets over 3 different tilt angle ranges using a non-negative constraint.

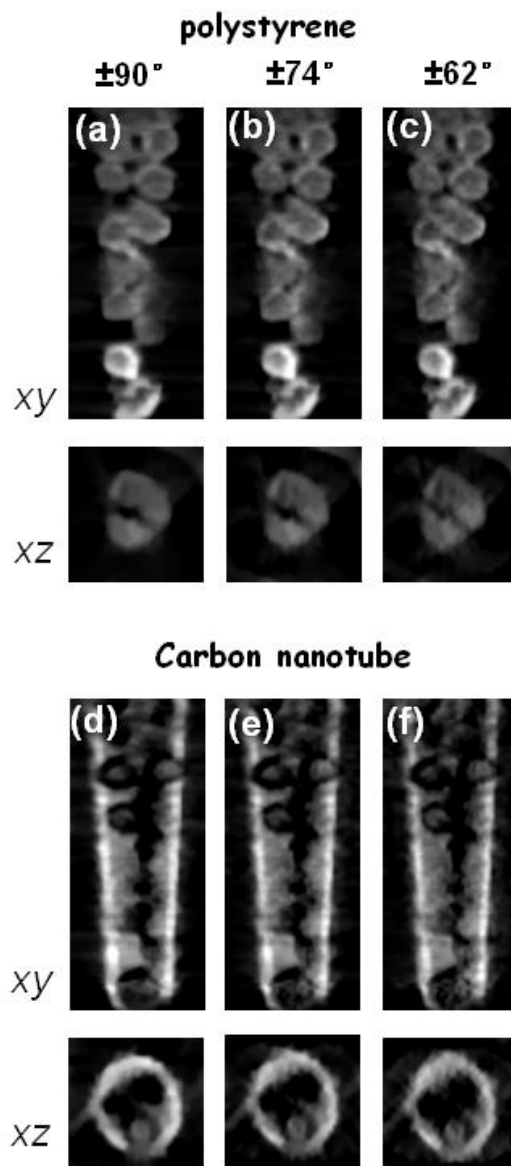


Fig. S-6: Tomographic reconstructions using SIRT with a non-negativity constraint of the polystyrene (PS) (a,b,c) and carbon nanotube component s(d,e,f) for three different tilt angle ranges (a,d) $\pm 90^\circ$, (b,e) $\pm 74^\circ$, and (c,f) $\pm 62^\circ$. Slices through the xy (top) and xz (bottom) planes are shown for each reconstruction.

Chapter 5

4D Imaging of Polymer Electrolyte Membrane Fuel Cell Catalyst Layers by Soft X-Ray Spectro-Tomography

JuanWu, Lis G.A.Melo, XiaohuiZhu, Marcia M.West, Viatcheslav Berejnov, Darija Susac,
Juergen Stumper, Adam P.Hitchcock

This chapter presents the results of four dimension (4D) imaging of PFSA in polymer electrolyte membrane fuel cell catalyst layers by soft X-ray spectro tomography. The amount and 3D distribution of PFSA radiation damage is measured.

*This work is a collaboration with Lis Melo who performed the radiation dose calculations, and Dr. Xiaohui Zhu who performed with the spatial resolution calculation, Marcia West microtomed samples. Viatcheslav Berejnov, Darija Susac, Juergen Stump provided the PEMFC CCM samples, and Adam Hitchcock who suggested the idea of multi-set measurements and assisted with many of the tomography measuremnts. My role was measuring all of the data sets, processing all the spectroscopy and tomography data, preparing all figures and writing the first draft. The paper writing was done by me, in collaboration with Adam Hitccock, Lis Melo and Viatcheslav Berejnov. (Wu et al., 2018)(
Reproduced with permission from Elsevier)*



Contents lists available at ScienceDirect

Journal of Power Sources

journal homepage: www.elsevier.com/locate/jpowsour



4D imaging of polymer electrolyte membrane fuel cell catalyst layers by soft X-ray spectro-tomography



Juan Wu^a, Lis G.A. Melo^a, Xiaohui Zhu^a, Marcia M. West^b, Viatcheslav Berejnov^c, Darija Susac^c, Juergen Stumper^c, Adam P. Hitchcock^{a,*}

^a Dept. of Chemistry & Chemical Biology, McMaster University, Hamilton, L8S 4M1, Canada

^b Dept. of Pathology, McMaster University Hamilton, L8N 3Z5, Canada

^c Automotive Fuel Cell Cooperation (AFCC) Corp., Burnaby, V5J 5J8, Canada

HIGHLIGHTS

- Soft X-ray tomography at multiple X-ray energies is used to map ionomer in PEM-FC.
- Compressed sensing processing allows valid reconstruction with ~15 tilt angles.
- Multi-set tomograms are used to guide dose reduction to get low damage measurements.
- Changes in 3D ionomer distribution occur due to radiation damage.
- Conditions to achieve low damage (< 5%) are identified and used for 4D imaging.

ARTICLE INFO

Keywords:

X-ray microscopy
Tomography
3D ionomer distributions
STXM
Compressed sensing
Radiation damage

ABSTRACT

4D imaging - the three-dimensional distributions of chemical species determined using multi-energy X-ray tomography - of cathode catalyst layers of polymer electrolyte membrane fuel cells (PEM-FC) has been measured by scanning transmission x-ray microscopy (STXM) spectro-tomography at the C 1s and F 1s edges. In order to monitor the effects of radiation damage on the composition and 3D structure of the perfluorosulfonic acid (PFSA) ionomer, the same volume was measured 3 times sequentially, with spectral characterization of that same volume at several time points during the measurements. The changes in the average F 1s spectrum of the ionomer in the cathode as the measurements progressed gave insights into the degree of chemical modification, fluorine mass loss, and changes in the 3D distributions of ionomer that accompanied the spectro-tomographic measurement. The PFSA ionomer-in-cathode is modified both chemically and physically by radiation damage. The 3D volume decreases anisotropically. By reducing the incident flux, partial defocusing (50 nm spot size), limiting the number of tilt angles to 14, and using compressed sensing reconstruction, we show it is possible to reproducibly measure the 3D structure of ionomer in PEM-FC cathodes at ambient temperature while causing minimal radiation damage.

1. Introduction

Quantitative imaging of the chemical components of polymer electrolyte membrane fuel cell (PEM FC) electrodes is needed to analyze catalyst layer (CL) fabrication quality and failure modes [1]. The 3D distribution of the components in CLs determines porosity and thus permeability for fuels and products; electrochemical effectiveness, and thermo-mechanical properties. Analytical electron microscopy and X-ray microscopy both have the spatial resolution and chemical sensitivity to provide useful analytical information about CL components.

However, the electron and X-ray beams cause radiation damage [2–4] in soft materials such as biological materials [5] and polymers [4,6,7] and is a major limitation in analytical microscopes which use ionizing radiation. Radiation damage brings into question the reliability of the quantitation, especially for the perfluorosulfonic acid (PFSA) ionomer component which is extremely radiation sensitive [8–10]. The electron beam in Transmission Electron Microscopy (TEM) and the photon beam in X-ray microscopy (XRM) both inject energy into the sample and cause radiation damage, the severity of which depends on the sample and method used [2,3]. Changes to the chemical composition, structure

* Corresponding author.

E-mail address: aph@mcmaster.ca (A.P. Hitchcock).

<https://doi.org/10.1016/j.jpowsour.2018.01.074>

Received 10 November 2017; Received in revised form 21 January 2018; Accepted 24 January 2018

Available online 09 February 2018

0378-7753/© 2018 Elsevier B.V. All rights reserved.

and spatial distributions caused by radiation damage can limit effective spatial resolution and definitely limit analytical accuracy. In order to obtain meaningful analytical results, it is important to understand how the analytical spectral signal changes both qualitatively and quantitatively, and to characterize the physical and chemical changes that occur.

This study focuses on the PEMFC cathode catalyst layer, which is composed of graphitic carbon support particles decorated with Pt catalyst, and the ionomer proton conductor, perfluorosulfonic acid (PFSA). The spatial distribution of catalyst particles and ionomer in a PEM-FC cathode affects the efficiency of the fuel cell device since the oxygen reduction reaction (ORR) at the cathode is the rate limiting process. For the ORR to occur, protons must be transported along a continuous pathway of PFSA from the membrane/cathode boundary to all of the ORR catalyst sites throughout the cathode. Since the reaction only happens at the interface of PFSA, catalyst particles, conductive carbon support, and with access via a porous network to O₂ reactant and product water removal, it is important to accurately measure the distribution of PFSA and pores, not only in 2D [11–16], but also in 3D [17–20].

Hard X-ray tomography in the laboratory [21,22] and at synchrotrons [23] is well-developed, and has been used for 3D characterization of the gas diffusion layer (GDL) [24] as well as tracking liquid water transport in model PEM-FC structures [25,26]. The microstructure of the solid phase of PEMFC electrodes [22] and changes in PEM-FC membranes following transient operation [26] have also been studied by X-ray computed tomography. However, the lab and most synchrotron hard X-ray methods do not provide chemical analysis and have a spatial resolution of ~1 µm at best. Saida et al. [27] have used full field X-ray microscopy, and spectro-laminography at the Pt L₃ edge, to characterize the oxidation state of the Pt catalyst in fresh and degraded PEM-FC MEAs, with a spatial resolution of 1.5 µm (x,y) and 5 µm (z). Very recently, Matsui et al. [28] have reported *operando* spectro-tomography at the Pt L₃ edge, thereby providing 3D chemical maps of Pt in the catalyst layer before and after *in situ* accelerated degradation testing (total of 20,000 cycles). Again the spatial resolution was a few µm. In both cases [27,28] complete Pt L₃ spectra were acquired. These are outstanding measurements which provide important chemical state information on the Pt catalyst but little or no information on the morphology and chemical state of the low-Z support, ionomer and membrane components of the membrane.

Soft X-ray tomography has higher spatial resolution (~30 nm [29]) than hard X-ray tomography and excellent analytical capability if tomograms at multiple photon energies are measured. 3D density based imaging using full field transmission soft X-ray microscopes is well developed [30]. However it has not been applied to PEM-FC to our knowledge, and does not provide spectroscopy in most implementations. Soft X-ray STXM tomography using multiple photon energies for direct 3D chemical mapping, was pioneered by Johansson et al. [31–35]. A comprehensive review of soft X-ray STXM spectro-tomography, which includes results on PEM-FC and related materials, was published recently [36].

Soft X-ray STXM [37–40] has been demonstrated to be a useful method for quantitative chemically sensitive imaging of the PEM-FC

cathode catalyst layer, and in particular, for giving accurate 2D projection maps of the ionomer in PEM-FC cathodes with negligible radiation damage [10–16,40]. Over the last few years, our group has been working to extend STXM characterization of cathode catalyst layers to 4D imaging which involves multi-photon energy tomography, or imaging in four dimensions (x, y, z, E). 4D imaging measures the spatial distribution of each chemical species of a heterogeneous sample in 3D. Prior to this study, STXM tilt-series spectro-tomography at the C 1s and F 1s edges was applied to two types of pristine catalyst coated membranes (CCM), demonstrating that the ionomer in the cathode could be visualized in 3D [19]. However, the 3D spatial resolution was somewhat less than the 2D spatial resolution, and the morphology and ionomer amount was significantly modified by the large radiation doses used in those studies [19]. The doses used in that early work were large – many 100's of MGy – because the same volume was measured repeatedly at multiple photon energies and multiple tilt angles, using maximum usable incident flux.

The objective of the research reported in this paper is to find ways of performing room temperature STXM spectro-tomography with significantly reduced dose so as to perform 4D imaging of the PFSA ionomer in a real PEM-FC cathode sample without extensive fluorine mass loss, without modification to the ionomer distribution, and without changes to the local chemical structure of the PFSA. To guide the operational changes that have allowed us to achieve this goal, we have developed a multi-set tomography method which tracks the mass loss, chemical transformation, and 3D structural reorganization of PFSA in PEM-FC cathodes during tomography. A major improvement was the use of a new reconstruction method called compressed sensing [41]. By combining compressed sensing tomographic reconstruction, reducing the number of tilt angles, and a 50-fold reduction in incident flux, we show that it is possible to measure meaningful, quantitative 3D ionomer-in-cathode distributions of real PEM-FC samples using STXM spectro-tomography at ambient temperature.

2. Materials and methods

2.1. Samples

Several different fuel cell PEM-FC catalyst coated membrane (CCM) samples were used in this study. Table 1 summarizes their compositions and properties. The CCMs were cut into small rectangular pieces and embedded in an amine epoxy resin (called TTE for short), prepared by mixing trimethylolpropane triglycidyl ether and 4,4'-methylenebis(2-methylcyclohexylamine) in a 1:1 wt ratio and cured at 70 °C overnight [42]. The embedded samples were microtomed at room temperature using a DiATOME™ diamond knife with a Leica Ultracut UCT to generate sections with nominal thicknesses between 100 and 300 nm. The sections were transferred from the surface of a water bath to formvar coated 100-mesh Cu TEM grids, which were then used for STXM studies.

There are size constraints in the STXM chamber which are important for tomography measurements [36]. The distance from the sample to the order sorting aperture (OSA), which is the first optical element upstream from the sample, is only 250 µm when measuring at

Table 1
 Properties of the MEA samples examined in this work.

Sample label	source	Membrane	C_support	Ionomer	I/C ^a	Pt load (mg/cm ²) ^a	Cathode fabrication method
MEA "C" 2071 TMP	Gore	ePTFE micro-reinforced; Gore-Select, 18 µm	Gore LSAC	Gore		0.4	Slot-die coating
MEA "A"	AFCC	Continuous; NRE-211, 25 µm, 1100EW	LSAC	Nafion 117	1.44	0.25	Mayer bar coating
MEA "B"	AFCC	Continuous; NRE-211, 25 µm, 1100EW	LSAC	Nafion 115	0.57	0.25	Mayer bar coating
MEA 11 GDE	Ballard	Continuous; NRE-211, 25 µm, 1100EW	LSAC	Nafion 117	1.07	0.6–0.7	Screen print

^a Target values, defined from ink composition.

Table 2
 Summary of conditions for experimental measurements.^a

Code	sample	STXM	Type	Fig(s)	Energies (eV)	Angles (°)/#	Io (MHz) ^b	Beam diam (nm)	Step size (nm)	Thickness (nm) ^c	Total dose (MGy) ^{c,d}
A1	MEA-C in PS	ALS 5.3.2.2	2D C 1s	1	C 1s: 278–324/86	0	15.6 ^e	120	120	110	9
A2	MEA-C in PS	ALS 5.3.2.2	2D F 1s	1	F 1s: 680–740/70	0	4 ^f	150	150	110	4
B1	MEA-C in PS	ALS 5.3.2.2	3D lo-dose 1-set	S-3	C 1s: 278.0, 284.5, 285.3	–72 to +64/35 total	7.7	80	80	110	8
B2	MEA-C in PS	ALS 5.3.2.2	3D lo-dose 1-set	S-3	F 1s: 684, 694	–72 to +64/35 total	3.4	80	80	110	13
C	MEA-A in TTE	ALS 5.3.2.2	3D hi dose 3-set (3°) ^g	S-3	F 1s: 684, 694	–66 to +60 /15 per set	9.4	45	45	310	72
D	MEA-A in TTE	ALS 1102	3D hi dose 3-set (3°) ^g	S-4, S-5, S-6	F 1s: 684, 694	–66 to +60 /15 per set	20 ^h	30	30	61	780
E1	MEA-A in TTE	ALS 1102	3D mid dose 2-set (6°) ^{h,i}	S-6, S-7	C 1s: 278, 285.4	–60 to +60 /16 per set	20.6 ^h	40	40	95	52
E1	MEA-A in TTE	ALS 1102	3D mid dose 2-set (6°) ^{h,i}	S-6, S-7	F 1s: 684, 694	–60 to +60 /16 per set	4 ^h	40	40	95	8
E2	MEA-A in TTE	CLS aSTXM	3D lo dose 2-set (6°) ^g	S-6, S-7	C 1s: 278, 285.4	–60 to +60 /16 per set	1.9	50	50	95	4
E2	MEA-A in TTE	CLS aSTXM	3D lo dose 2-set (6°) ^g	S-6, S-7	F 1s: 684, 694	–60 to +60 /16 per set	3.3	50	50	95	6
F1	MEA-A in PS	ALS 5.3.2.2	3D lo dose 3-set (3°) ^g	4–6	F 1s: 684, 705	–66 to +60 /16 per set	4.1	50	50	177	32
F2	MEA-A in PS	ALS 5.3.2.2	3D 1-set	4–6	C 1s: 280, 284.5	–66 to +60/15	5	50	50	177	6
G	MEA-11 GDE	CLS aSTXM	3D lo dose 3-set (3°) ^g	7,8	F 1s: 684, 705	–63 to +54 /14 per set	2.3	50	50	336	10

^a For each image the dwell time per pixel is 1 ms. The voxel size used in the reconstruction is the same as the step size of the images.
^b The Io signal is the measured value divided by the detector efficiency which is different for the different beamlines used. For ALS 5.3.2.2 and CLS a-STXM measured detector efficiencies of 0.7 (F 1s) and 0.3 (C 1s) were used. For 11.0.2 detector efficiencies of 0.4 (F 1s) and 0.15 (C 1s) were used.
^c Thickness and dose estimated for the membrane region.
^d For A, B, E, and F the total dose (sum of C 1s and F 1s) are 13, 21, 70 and 38 MGy.
^e At 319 eV.
^f At 705 eV.
^g Angle increment between individual sets of the multi-set acquisition.
^h For the data collected at 1102, the Io indicated was not normalized by the detector efficiency.
ⁱ Both C 1s and F 1s tomography data was measured for code E at ALS 11.0.2 but it was of poor quality so it was re-measured at CLS. The E1 dose combines dose from both the F 1s and C 1s measurements at ALS 11.0.2.

the C 1s edge [37]. To allow for sample rotation without collisions between the sample and the OSA at high tilt angles, it is necessary to reduce the lateral width of the sample. Thus, the TEM grid was cut using a fresh scalpel to isolate a single, ~250 μm wide strip containing the CCM section of interest. This grid strip was then glued at the tip of a metal pin, which was held in a mechanical pencil chuck, which in turn was secured to the shaft of a stepping motor rotator.

2.2. Instrumentation and methods

STXM measurements were performed at room temperature using the ambient STXM at Canadian Light Source (CLS) beamline 10ID-1 [43] and STXMs on Advanced Light Source (ALS) beamlines 5.3.2.2 [44] and 11.0.2 [45]. The details of STXM instrumentation and principles of operation are described elsewhere [37–39,46]. Image contrast and thus chemical sensitivity in STXM is based on the near-edge X-ray absorption fine structure (NEXAFS) [47] spectral response of the different materials in heterogeneous samples such as PEM-FC cathodes. NEXAFS spectral signals measured in transmission under conditions where the Beer-Lambert law applies provide a high degree of chemical sensitivity and can be used to quantify the amounts of each species at each pixel or voxel (expressed as nm thickness). STXM measurements using 2D projection have been used widely in PEMFC cathode catalyst research [10–16,41]. In this work, the spectro-tomography measurements were performed using only a few specific energies at the C 1s and F 1s absorption edges since these suffice to map spatial distributions of carbon support, PFSA ionomer, Pt catalyst and porosity [10–15].

STXM tomography is performed by mounting the sample on a rotation system, with the rotation axis perpendicular to the propagation direction of the incident X-ray beam. The STXM angle-scan tomography rotation stage (Supplemental Fig. S-1a) uses a two-phase micro-stepper motor (Faulhaber ADM0620, Faulhaber, Schoenaich, Germany). The strip cut from the TEM grid containing the MEA sample is mounted on a 0.8 mm diameter brass pin, inserted in a chuck from a mechanical pencil, which in turn, is mounted on the motor shaft (see Fig.S-1b). The position and orientation of the sample strip is carefully adjusted under an optical microscope to align the sample region of interest with the rotation axis, which is perpendicular to the incident X-ray beam. With care, the extent of off-axis motion during 180° rotation can be reduced to ~50 μm [35].

Due to attenuation of the soft X-ray beam at high angles for flat samples the maximum rotation angle that can be measured is ~80°; usually the angle range is limited to ±70°. Note that with focused ion beam (FIB) pillar or cylindrical samples such as pulled glass pipettes [33] it is possible to rotate over the full 180° range. The range and angle increments for each measurement made in this work are summarized in Table 2. After each rotation, the region of interest had to be located and the microscope refocused. This increases the operation time and results in some additional dose. Good alignment of the spatial orientation of the grid sample strip along the rotation axis decreases this extra operational time since the region of interest stays close to the X-ray beam at all tilt angles. At present, among soft X-ray STXMs, only the Nano-surveyor I system at ALS [48] is equipped with a proper eucentric sample adjustment system, which is needed to fully automate STXM

J. Wu et al.

Journal of Power Sources 381 (2018) 72–83

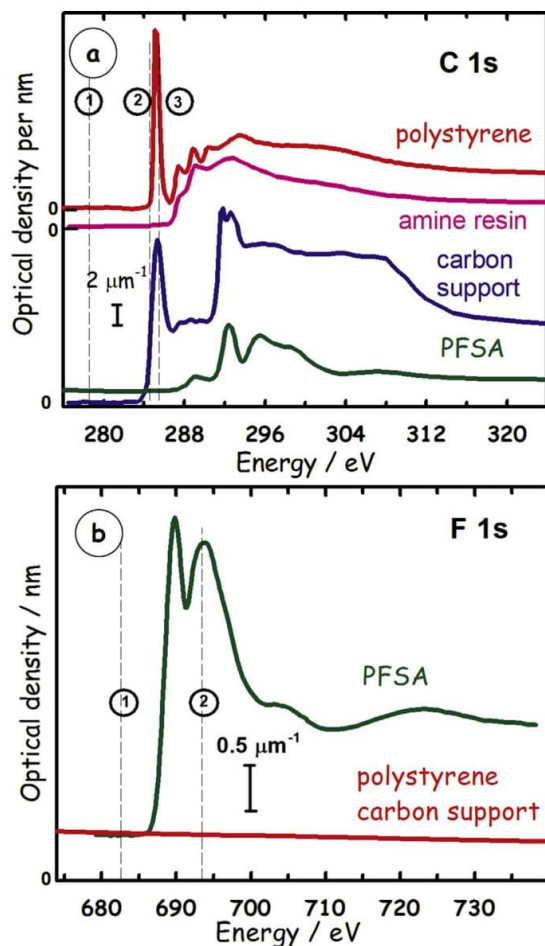


Fig. 1. (a) C 1s spectrum of perfluorosulfonic acid (PFSA), the membrane of a catalyst coated membrane (CCM) of a polymer electrolyte membrane fuel cell (PEM-FC), recorded with scanning transmission X-ray microscopy (STXM) using a defocused beam, with conditions in code A (Table 2). The C 1s spectra of the carbon support and the amine epoxy (TTE) and polystyrene (PS) embedding materials used in these studies are also plotted. The intensity scale is absolute (OD/nm) and offsets are used for clarity. (b) F 1s spectrum of PFSA and the spectral response of carbon in the F 1s region. (measured at ALS 5.3.2.2).

tomography data acquisition. Despite this lacuna of the STXMs used in this work, the trajectory of the rotation can be predicted if one measures several images at large angle changes (e.g. -45° , 0° , $+45^\circ$) and does some simple trigonometry. This approach can save significant measurement time. In the past, most soft X-ray STXM tomography acquired images at 30–40 tilt angles [31–36]. Tomography measurements of a PEM-FC MEA sample at two absorption edges (4 photon energies), 39 tilt angles, $10\ \mu\text{m} \times 10\ \mu\text{m}$ image size with 200×200 pixels takes 10–12 h, despite the actual image data acquisition time being only 3–4 h. However, with the development of compressed sensing 3D reconstruction methods [49,50], good quality reconstructions can be achieved with 10 or even fewer tilt angles [39] which significantly reduces both the beamtime used and the imparted dose. Different experimental conditions and different STXM microscopes and beamlines were used for the various tomography data sets reported in this paper. The parameters for each data set are summarized in Table 2, using code

X as the label for each measurement.

2.3. Spectroscopy and STXM data analysis

Axis2000 [51] is used to convert the measured transmission images to optical density (OD) images by applying the Lambert-Beer law at each image pixel:

$$OD(E) = \ln(I_0(E)/I(E)) = \sum_i \mu_i(E)\rho_i t_i \quad (1)$$

where $I_0(E)$ is the intensity spectrum of the incident X-ray, $I(E)$ is the intensity spectrum of the transmitted beam, $\mu_i(E)$ is the X-ray absorption coefficient ρ_i is the density and t_i is the thickness of component i . If suitable reference spectra are available, and they have been placed on an absolute intensity scale (OD/nm, also called OD1), then the absolute thicknesses of each component at each pixel can be derived, assuming the local density is the same as that of the pure material [39].

The procedure used to derive quantitative component maps at each tilt angle is the same as that used for 2D projection mapping [11–13] – two energies at the C 1s are used to map carbon support, 2 energies at the F 1s are used to map ionomer, and the F 1s data is combined with the pre-C 1s image to map the Pt catalyst [13]. In a few cases (codes, C, D, G) the non-fluorinated 3D distributions of non-fluorinated components were derived from the pre-F 1s edge tomogram, by subtracting a weighted amount of the ionomer tomogram signal, to correct for the absorption by ionomer at the pre-edge energy. Before each tomography measurement, images at a series of photon energies (called a stack [52]) in the C 1s and F 1s regions are acquired and analyzed to determine the optimum energies for the 2-energy (on/off) evaluation. Fig. 1 presents quantitative C 1s and F 1s spectra of the chemical species involved. The calibration and pre-tomography characterization is performed using a full spectral stack (50–70 images), which is measured in a different region to the tomography area, but one with similar morphology. In order to map the PFSA and the carbon support with minimal radiation dose, images are measured at only 4 energies. The on-signal for carbon support is measured at 284.5 eV for polystyrene (PS) embedded samples and 285.2 eV for TTE embedded samples. The on-signal for PFSA ionomer is measured at 694 eV or 705 eV. Initially we used 694 eV, since this peak has high intensity and was very sensitive to radiation damage. However during the course of this study we realized the changes at 694 eV were a combination of electronic/chemical structure changes and fluorine loss, which have similar decay rates at low dose, but diverge at higher doses. Since it was more important to track the amount of fluorine with respect to quantitation, we changed our on-signal energy to 705 eV. At energies in the F 1s continuum such as 705 eV, the F-loss is accurately measured without combining sensitivity to electronic/chemical structure changes. The off-signal is measured at a pre-edge energy where absorption by all components is tracked (278 eV for carbon support, and 684 eV for PFSA). After converting each image to optical density (OD), chemical maps of each component are generated by subtracting the pre-edge image from the absorption peak image (e.g. for a TTE-embedded sample, $OD_{\text{Csup}} = OD_{285.2} - OD_{278}$, and $OD_{\text{PFSA}} = OD_{694} - OD_{684}$).

The methods used to derive doses for each experiment are detailed in Supplemental Information, section S-1.

2.4. Tomography data acquisition and analysis

A flow diagram of the tomography data acquisition and analysis is shown in Fig. 2. Data with various choices of tilt angles were measured in this work in order to systematically find ways to reduce dose while preserving 4D imaging quality. Table 2 summarizes details of each measurement. At each angle, images measured at either or both the C 1s and F 1s edges are converted to quantitative maps of the carbon support and ionomer. The individual images or the chemical maps at a set of projection angles are then aligned in axis2000 using Fourier correlation

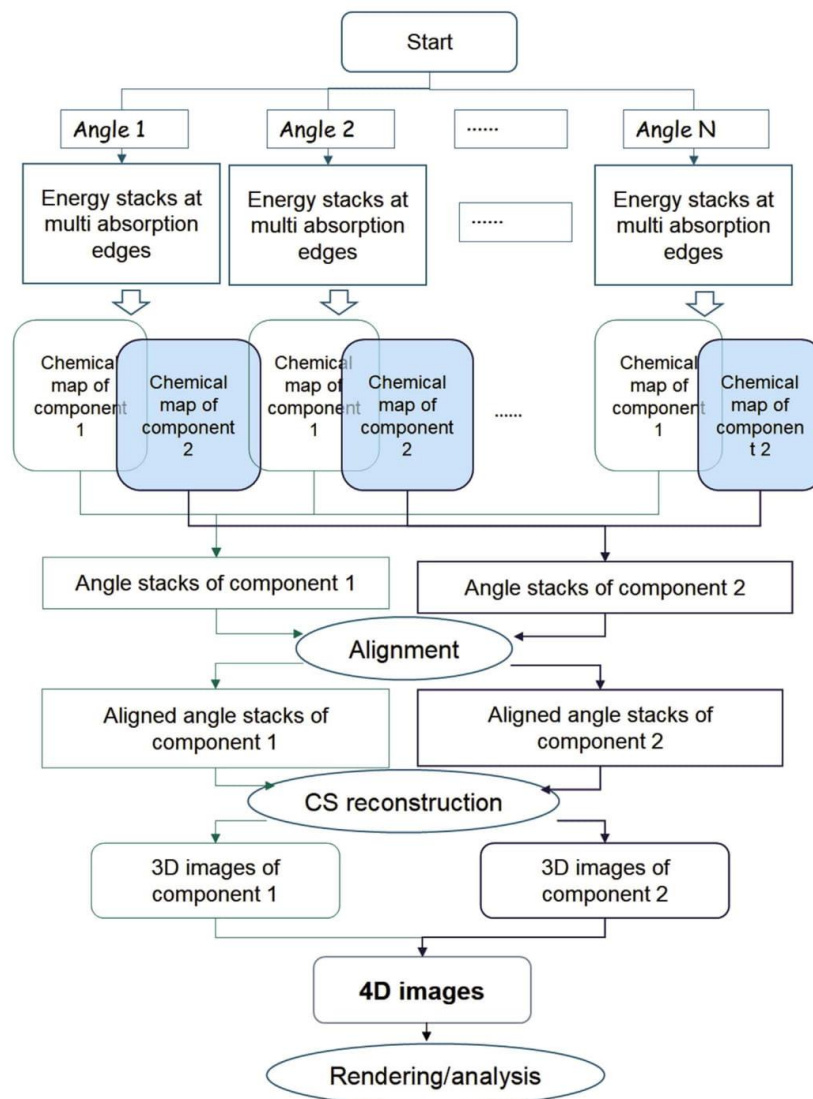


Fig. 2. Flow diagram of STXM tomography data acquisition and processing.

methods. A final alignment based on sinusoidal response optimization is performed using IMod [53] or TomoJ [54]. The fully aligned tilt angle data sets (single energy images or chemical maps) are used for 3D reconstruction by IMod, TomoJ or Mantis [41,55,56]. Different reconstruction algorithms can be employed. One of the most popular 3D reconstruction algorithms is SIRT (Simultaneous Iterative Reconstruction Technique) [57]. However, SIRT requires data from at least 30 tilt angles over a wide-angle range to obtain good quality reconstruction. For STXM tomography, measuring this many tilt angles results in long exposure times and excessive radiation damage to the ionomer. In this study, the 3D reconstructions were performed using a compressed sensing algorithm [58] developed by Lerotic [41] which is available in the Mantis package for spectromicroscopy analysis [56]. The compressed sensing (CS) approach provides high quality 3D reconstructions on data sets with a significantly reduced number of projection angles

[41]. CS is also less sensitive than SIRT to missing wedge artifacts associated with limited tilt angle ranges. By using CS, the tomography measurement time can be significantly decreased because 10 tilt angles over $\pm 70^\circ$ provides a reconstruction quality which is as good or better than SIRT analysis of a 40 tilt angle data set [41]. The compressed sensing algorithm parameters were tested and adjusted for different data sets. For the PEM-FC cathode samples, a β parameter of 0.1, and 30 iterations were typically used. There is another important advantage to use the CS method. Since good quality reconstruction can be obtained using only 10 images [41], we were able to make several tomographic measurements on the same area with gradually increasing dose. This enabled exploration of the effects of radiation damage on the quantitative 3D ionomer distribution and the chemical state of the ionomer.

By merging the reconstructed 3D data sets of the ionomer and carbon support, a 4D image (chemically sensitive 3D imaging) is

J. Wu et al.

Journal of Power Sources 381 (2018) 72–83

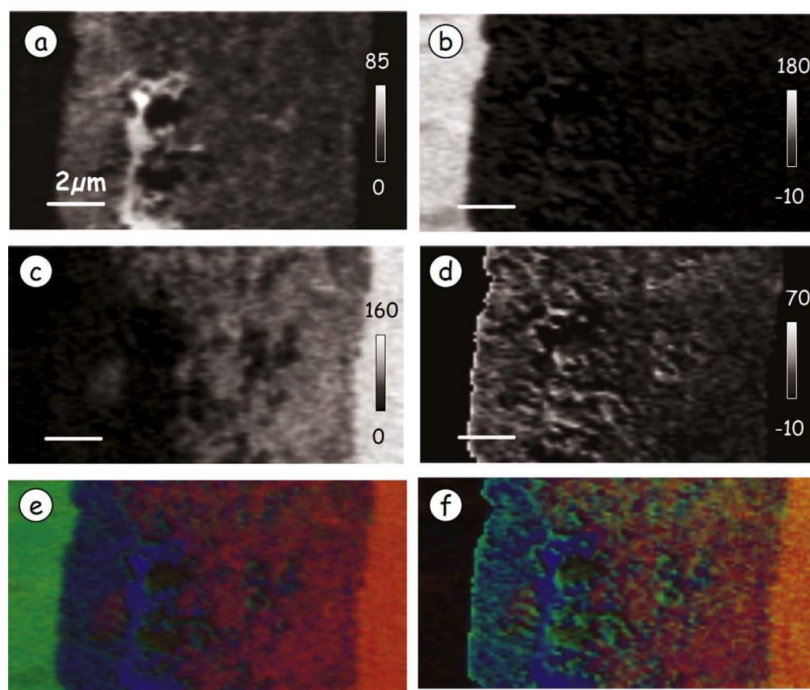


Fig. 3. Component maps of (a) carbon support, (b) PFSA, (c) polystyrene, (d) ionomer in cathode, derived from a stack fit of OD1 reference spectra (Fig. 1), and a constant to a C 1s stack (89 images from 278 to 324 eV), **code A** (see Table 2 for conditions). The intensity gray scale is thickness in nm. The ionomer map was obtained by masking and subtracting the much more intense membrane signal in the PFSA map. (e) Color coded composite using rescale (ie relative distribution) of carbon support (blue), all PFSA (green) and polystyrene (red). (f) Color coded composite of carbon support (blue), ionomer (green) and polystyrene (red) in the cathode. (measured at ALS 5.3.2.2).

generated which consists of the 3D distribution of each component within the same sample volume with accurate spatial registry. Alternatively, it is possible to perform the analysis of all the spectral and angle data in Mantis, such that the spectral data at any set of voxels in the reconstructed volume can be extracted, examined and analyzed [41]. All reconstructions were performed using cubic voxels with a side dimension equal to the step (pixel) size in the 2D images (see Table 2 for details). Segmentation, visualization and rendered displays, both stills and movies, were performed using Chimera [59], TomoJ [54] or Avizo 9.0 [60]. For isolating 3D distributions of specific components the automated Otsu threshold method [61] was used to guide segmentation. The explicit thresholds used for each rendering are listed in the figure captions.

3. Results

3.1. Spectroscopic analysis and tomography of PEM-FC cathodes

Typical C 1s and F 1s X-ray absorption spectra of the chemical components of PEM-FC cathodes, as well as TTE and PS, the two embedding media used in this work, are presented in Fig. 1a. All but the TTE spectrum were measured on sample MEA “C” embedded in PS, using conditions in **code A**, which deposited approximately 9 and 4 MGy for the C 1s and F1s measurement, respectively, and thus negligible damage is expected. The carbon support (typically partially graphitic carbon black), the PFSA, and the embedding media (either polystyrene or amine resin) can be easily differentiated from their C 1s spectra (Fig. 1a). In addition, it is possible to estimate the amount of Pt catalyst present from the pre-C 1s intensity combined with knowledge of the amount of PFSA, as explained and used in a recent study [13]. For the F 1s edge, PFSA is the only F-containing component; the other carbon-rich components have a similar, non-structured shape in the F 1s region (Fig. 1b). Thus, it is straightforward to quantitatively map ionomer-in-cathode from the F 1s spectrum using the 2-energy stack

map procedure [10–12]. As an example of STXM 2D chemical mapping, Fig. 3 presents quantitative component maps of the carbon support, PFSA and the polystyrene (PS) embedding media, derived from a C 1s stack recorded from MEA “C” at 86 energies from 278 to 324 eV. Color composites of these component maps are presented in Fig. 3e (PS – red, membrane & ionomer – green, carbon – blue, over the whole region measured) and Fig. 3f (PS – red, ionomer-in-cathode – green, and carbon – blue). Such color composite maps are very useful to display the relative spatial positions of the components, which is obviously critical to understanding the relationship of processing, distributions of PFSA ionomer in the cathode, and PEM-FC performance. The radiation dose caused by the combined F 1s and C 1s stack measurements is estimated to be 13 MGy, which is about 1/3rd of the PFSA thin film critical dose (Table 2, **code A**). Tomography measurements were also performed as per code B. The tomographic results, damage evaluation and associated discussion are presented in Supplemental Information section S-2, which includes visualization (Fig. S-2).

3.2. Three-set F 1s spectro-tomography of a thick sample with high dose (code C)

A three-set F 1s spectro-tomography study was carried out on a ~300 nm thick MEA “A” sample (measurement as described in **code C** in Table 2), using a radiation dose rate of 750 MGy/s and a total dose of 72 MGy. This is a high dose rate, but is typical of the values used for 2D projection mapping of ionomer in cathode, since high statistical precision can be obtained with less than 5 ms total dwell per pixel [11,12]. Each of the three tilt-angle tomography data sets consisted of measurements at 15 angles. Set 1 was measured from –66° to +60° with 9° increment, while the angles for set 2 were offset by +3°, and those for set 3 were offset by +6°, thereby covering the full range of –66° to +66° for a total of 45 angles. The F 1s spectrum of the cathode was measured using a defocused beam before and after each tomography data collection, using only 3.4 MGy dose per stack. Fig. 4a shows there

J. Wu et al.

Journal of Power Sources 381 (2018) 72–83

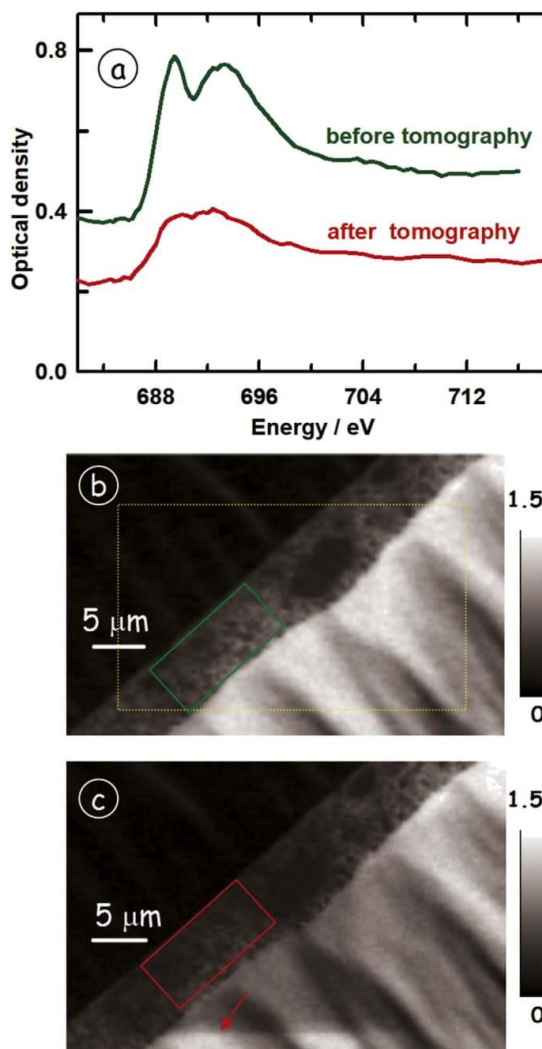


Fig. 4. Average F 1s spectra of PFSA in cathode of MEA-A, tomography measurement code C (Table 2), before and after 3 set spectro-tomography. Optical density image at 694 eV, (b) before, and (c) after 3-set tomography. The rectangular frame in (b) indicates the tomography region, which is evident in (c) from contrast changes at the boundary in the cathode and membrane areas due to radiation damage. The areas from which the cathode F 1s spectra were obtained are also indicated. (measured at ALS 5322).

was a significant reduction in the intensity of the F 1s spectrum of the PFSA cathode after the tomography dataset acquisition, which imparted a total dose of 72 MGy. After the full 3 set tomography measurement, there is only a hint of the two peak spectrum typical for undamaged PFSA, and the F 1s continuum signal has decreased by ~50% relative to the adjacent undamaged area. This extent of fluorine loss would invalidate these results as a quantitative evaluation of the distribution of ionomer in cathodes. The radiation damage causes a significant change in contrast as visualized by comparing an OD image measured at 694 eV before (Fig. 4b) and after (Fig. 4c) the 3-set tomography measurements.

Since three independent tomography measurements were made on the same volume it is possible to test for spatial selectivity in the fluorine loss. Fig. 5a,b,c display the 2D fluorine maps at ~normal

incidence (-3° , 0° , and 3° in the 1st, 2nd and 3rd set, respectively). The average F 1s signal ($OD_{694} - OD_{684}$) decreased by ~20% by the end of the first set, by another ~20% after the second set, and another 10% after the third set. After reconstruction, the Otsu threshold method [61] was used to segment the PFSA distributions in the cathode. Fig. 5d,e,f are 0° projections of the reconstructed ionomer signal. A significant reduction in amount of fluorine signal is evident. Fig. 5g illustrates the change (ionomer lost) in measuring set 1, displayed in red, evaluated from the difference of set 1 and set 2, superimposed on the distribution of set 2. Fig. 5h plots the same for the F loss in both sets 1 and 2, superimposed on the distribution of set 3. Clearly there is spatial selectivity in the ionomer loss, with some areas losing fluorine faster than other areas, as indicated by the non-uniform distribution of the ionomer lost. In general, the greater percent loss occurred in regions with relatively low amounts of ionomer. If the volume of ionomer after set 1 is defined as 100%, the volume of the ionomer decreased to 70% after set 2, and 50% after set 3. The total dose was 72 MGy (24 MGy for each set). The radiation effects and quantitative dose issues are discussed in section 4.

3.3. Results from multi-set spectro-tomography of other samples at high doses (codes D, E)

Supplemental Information section S-3, which includes supplemental Figs. S-3 and S-4, presents results from a three set F 1s spectro-tomography of a thin sample with high dose (code D). Supplemental Information section S-4, which includes supplemental Figs. S-5 and S-6, presents results from a two-set C 1s and F 1s spectro-tomography at medium dose (code E).

3.4. Three-set F 1s spectro-tomography with low dose F (code F)

An additional low dose 3-set tomography measurement was performed on a 200 nm thick section of sample MEA-A, with conditions of code F (Table 2). To further reduce radiation damage while measuring the ionomer at the F 1s edge, the F 1s tomography data was measured first, then the C 1s tomography data was measured, instead of taking 2 F 1s, and 2 C 1s images at each tilt angle. With this approach, the absorbed dose during the F 1s measurement was lower and thus the critical ionomer distribution less affected. The beam spot size was also defocused to 50 nm. The peak energy of the F 1s measurement was changed to 705 eV (in the F 1s continuum) in order to desensitize the 3D distributions to the change in spectral shape from 2-peak to 1-peak that occurs because of radiation damage [62]. Table 3 lists the estimated radiation dose after each step in the 3 set F 1s measurement. The total dose for all 3 F 1s tomograms was only 32 MGy.

The F 1s spectra of the cathode at different times throughout the F 1s 3-set tomography are plotted in Fig. 6. These F 1s spectra were recorded using highly defocused stacks before the tomography, after half of the first tomography set, and after each of the 3 tomography sets. By reducing the total dose to less than 32 MGy, conditions were achieved where the original 2-peak structure of the F 1s spectrum is retained throughout the whole measurement, with relatively little reduction in the F 1s continuum intensity caused by fluorine mass loss. Fig. 7 presents visualizations of the ionomer (Fig. 7a) and carbon support (Fig. 7b) components in the same volume, derived from the CS reconstruction, as well as the 4D image (Fig. 7c) combining the ionomer and carbon support reconstructions. The PFSA signal (green) was derived from $OD_{705} - OD_{684}$ while the carbon support signal (blue) was derived from $OD_{284.5} - OD_{280}$. Fig. 7d,e,f shows views from a 30° viewing angle of the 3D distributions of the ionomer (green) and carbon support (blue) components derived from each of the 3-set tomographic measurements of the same region of the cathode. Because the C 1s measurement of the carbon support was done after the F 1s measurement, there is additional uncertainty in the quantitation. Fig. 7g,h,i presents maps of the overlap (intersection) of the carbon support and

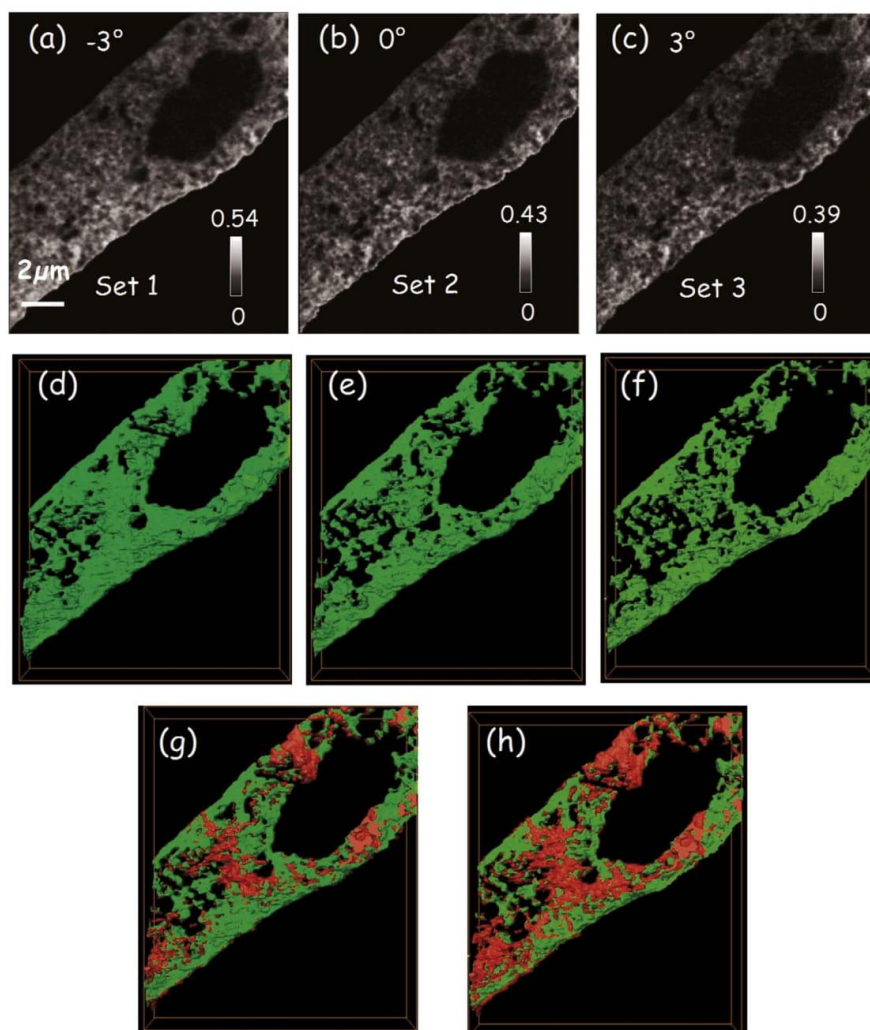


Fig. 5. 2D fluorine maps of MEA-A, tomography measurement **code C**, from F 1s stack maps measured at: (a) -3° in set 1, (b) 0° in set 2, (c) 3° in set 3 (3° offsets of the projection angle scales were used between each set). Surface renderings (indicating location) of the 3D ionomer distribution from CS reconstruction of (d) set 1, (e) set 2, (f) set 3 at 0° . Surface renderings of ionomer loss superimposed on the ionomer distribution of set 1, for ionomer loss derived from (g) difference between set 1 and set 2 in red, and for ionomer loss derived from (h) difference between set 1 and set 3 in red. The thresholds used to segment the ionomer volumes are 0.0040, 0.0050, 0.0055 for sets 1, 2, and 3. (measured at ALS 5.3.2.2).

Table 3

Accumulated radiation dose and volume fractions in the F 1s stacks in the low dose experiment (**code F**, 200 nm sample).

Set#	Radiation dose (MGy) ^a	OD ₇₀₅ - OD ₆₈₂ ^b	Thresh. C _{supp}	Carbon Support (%) ^c	Thresh. PFSA	PFSA in cathode (%) ^c	Intersection of C _{supp.} & PFSA in 3D (%)	Porosity (%) ^d	PFSA off C _{supp} (%)
1 st	12	0.127	0.005	69	0.0070	48	41	23	8
2 nd	21	0.126	0.005	69	0.0033	43	33	27	4
3 rd	30	0.122	0.005	69	0.0036	41	27	30	1

^a Cumulative radiation dose up to and including the indicated measurement from both spectroscopy and tomography measurements.

^b Prior to any measurements OD₇₀₅ - OD₆₈₂ was 0.135.

^c The volume percent for each species is determined after threshold values indicated, which were obtained with guidance from the Otsu auto-threshold method [60].

^d Porosity was determined by requiring the sum (C_{supp} + PFSA_{off}_{supp} + porosity) to equal 100%.

J. Wu et al.

Journal of Power Sources 381 (2018) 72–83

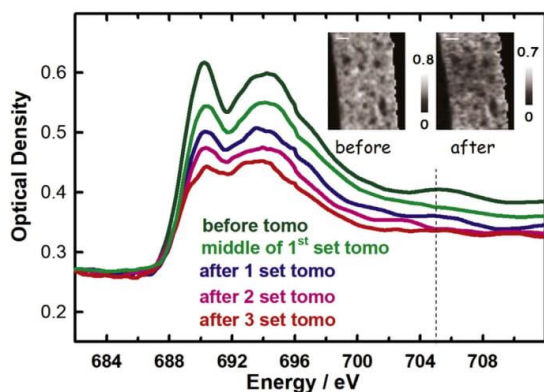


Fig. 6. F 1s spectra of PFSA in the cathode of sample MEA-A, tomography measurement code F (Table 2), taken before tomography, after 1/2 of 1st set, after 1st set, after 2nd set, and after 3rd set of the 3-set spectro-tomography. The insert images are the F maps of the tomography region before, and after the 3-set tomography measurement. (measured at ALS 5.3.2.2).

ionomer (in yellow) for sets 1,2,3, as a means for identifying the parts of the 3D distribution of ionomer that are in close proximity to the carbon support and Pt catalyst, the condition needed for effectiveness of the ionomer. The intersection volume of the carbon support and ionomer is overestimated due to the spatial resolution limitations of STXM tomography. The changes in the volume fraction of ionomer after each set are listed in Table 3. This analysis indicates that the 3D ionomer loss is more significant in regions with less ionomer and starts from areas not in contact with the carbon support. Using this approach of low flux and slightly defocused conditions, 30 tilt angles can be measured with negligible chemical change, as indicated by preservation of the 2-peaked F 1s spectrum (Fig. 6), and negligible structural change (as indicated by similarity of the 3D ionomer maps from 1st and 3rd sets), and only mild fluorine mass loss.

3.5. Three-set F 1s spectro-tomography on a thick sample with minimal dose (code G)

An additional 3-set tomography measurement was performed on a ~300 nm thick section of sample MEA 11-GDE using conditions of code G (Table 2). F 1s spectra of the cathode were recorded using large defocus, low dose conditions, before the start of tomography, at the middle of the first tomography set, then after each tomography set. The total dose after the 3-sets (total of 84 images, or 84 ms of beam at each pixel) is estimated to be 10 MGy. The F 1s spectra of the cathode recorded before, during, and after the tomography are presented in supplemental Figure S-7a. While there was a small reduction in the OD at 694 eV, the shape of the F 1s spectra remained essentially constant. The fluorine loss, as evaluated by $(OD_{705} - OD_{684})$, was only 5%. This, combined with the negligible change of spectral shape, indicates that the 3-set measurement caused negligible changes in the C-F local chemical environment or the amount of ionomer. 2D projection images at 694 eV before the start of the 3-set acquisition and after each set (supplemental Fig. S-7b through S-7e) are consistent with a very low extent of radiation damage.

Component maps of the ionomer in the cathode (obtained from $OD_{704} - OD_{684}$ at 0°) are presented in Fig. S-8(b-e). The average ionomer amount derived from these 2D maps indicates that there was only 4% fluorine mass loss by the end of the 3-set tomography, consistent with the spectral data (Fig. S-7a). Renderings of the 3D distributions of the ionomer from CS reconstruction of these tomography data sets are presented in Fig. 8. There are no significant changes between set 1 (Fig. 8a), set 2 (Fig. 8b) and set 3 (Fig. 8c) tomography results. Volume

differences in the yellow box region for set 2, as (set 2 - set 1) and for set 3 as (set 3 - set 1) are shown in Fig. 8d and Fig. 8e. The ionomer signal lost due to radiation damage is presented in red. Relative to the volume fraction of ionomer in set 1, the amount of ionomer reported in set 2 is 4.5% smaller while that reported in set 3 is 8% smaller. From the difference in total ionomer volume between the first tomography set and the second and third sets, the ionomer loss is not the same in every direction on the surface of each particle, especially during the initial stage of the radiation damage. Thus, despite relatively low radiation damage, rescaling the ionomer/voxel by the mass loss percentage will not properly represent the original 3D ionomer distribution due to selectivity in the locations where the ionomer is preferentially lost.

A movie of an Aviso rendering of the 3D distribution of the ionomer reconstructed from the code G data is presented in supplemental Section S-5. Several frames from this movie are displayed in Supplemental Fig. S-8. The voxels are cubes of 50 nm on a side. In the movie, the ionomer distribution is rotated by 360° about the tilt axis, first as measured from the first tilt angle set. It then superimposes in red the differences between set 1 and set 2 (corresponding to ionomer loss due to radiation damage in set 1), plotted on an enhanced intensity scale, relative to that of the ionomer by ~2. This clearly shows preferential loss of ionomer in the thinner regions. It then displays a 360° rotation about the tilt axis of the ionomer distribution as measured from the second tilt angle set. Finally, the differences between set 3 and set 2 ionomer results is superimposed in red, using the same, expanded intensity scale.

Supplementary video related to this article can be found at <http://dx.doi.org/10.1016/j.jpowsour.2018.01.074>.

The ionomer distributions for all three of the PEM-FC cathode samples measured in this work show large ovoidal regions where there is little or no ionomer, despite the presence of Pt coated carbon support particles in these same ovoidal regions. The origin of these ionomer-depleted regions is likely due to incomplete mixing of the ionomer with other components of the ionomer ink at the relatively large ionomer loadings that were chosen for these samples. In other studies, STXM has been used to show that lower ionomer loadings, different ink formulations, and/or different electrode layer fabrication methods can achieve much more uniform ionomer distributions, with good coverage of the majority of catalyst particles [15].

4. Discussion

Changes in F 1s spectra, integrated amounts of ionomer, and 3D ionomer distributions caused by radiation damage during soft X-ray tomography measurements have been studied. The effects of total dose, sample thickness, number of projection angles, and choice of measurement energies have been explored. High incident flux and/or use of many projection angles, and thus large total dose (> 50 MGy) results in unacceptable levels of spectral (and thus chemical) change, mass loss, and modifications of the 3D spatial distributions. Reducing the incident flux and using a slight defocus (to 50 nm, the same as the pixel step size), results in tomographic data sets in which changes from radiation damage are barely measurable (code F, G). The advanced compressed sensing reconstruction method [41] allowed a significant decrease in the number of tilt angles needed. This greatly decreased the radiation dose, and also decreased the measurement time from ~12 h to ~4 h (of which < 1/3rd is actual beam-on-sample time). CS reconstruction allows good quality reconstructions with astonishingly small numbers of sample tilt angles. Systematically predicting the ROI at each tilt angle and modifying the acquisition software to enable auto positioning and auto focus will allow further reduction of the acquisition time.

Supplemental section S-6 (including Fig. S-10) summarizes the quantitative radiation damage aspects of this study. These results indicate that STXM tomography at room temperature can be used to measure meaningful 3D distributions of ionomer in PEM-FC cathodes if sufficient care is used in making the measurements, and if advanced

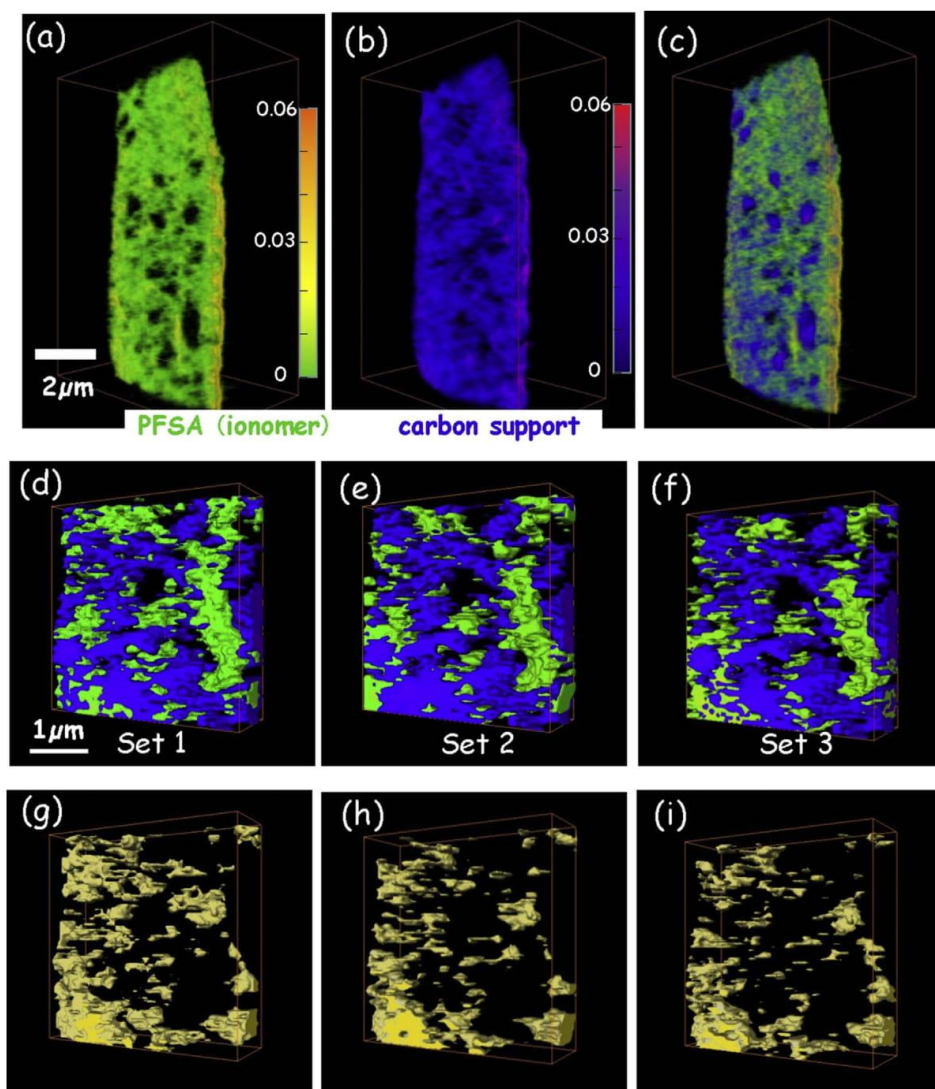


Fig. 7. 3D distributions of the cathode of sample MEA-A, tomography measurement code F (a) PFSA (green) from OD₇₀₅ – OD₆₈₄, (b) carbon support (blue) from OD_{284.5} – OD₂₈₀. The scale bars on the right side of (a), (b) indicate the voxel intensity scale, for a voxel size of (50 nm)³. (c) composite of the 2 components, in each case viewed at -45° . Threshold for ionomer is 0.007, that for carbon support is 0.005. Surface rendered 3D distributions of PFSA (green), carbon support (blue) in a region of the cathode of sample MEA-A, tomography measurement code F, viewed at a tilt of -30° . (d) set 1, (e) set 2, (f) set 3. (g), (h), (i) are surface renderings of the intersection of the maps of the carbon support and ionomer for sets 1, 2 and 3. Thresholds for the ionomer distributions are 0.007, 0.0033, 0.0036 (OD/voxel) for sets 1, 2 and 3, while those for the carbon support were 0.005 for each set. (measured at ALS 5.3.2.2).

reconstruction methods like compressed sensing [41] are used. A major challenge for STXM tomography applied to ionomer-in-cathode distributions is that only limited 3D information can be obtained because of the need to use thin sections on account of the strong absorption at the C 1s (and to a lesser extent) F 1s edges. The resolution in the z-direction is at best 50 nm. Thus only 2–6 unique samplings along the z-direction are being made in these measurements. Although the lateral spatial resolution in 2D projection images can be as small as 30 nm if a 25 nm outer zone diameter zone plate is used, the 3D spatial resolution is lower than that for 2D projection due to a number of factors including: misalignment of images measured at different tilt angles, the missing wedge effect, out-of-focus images at high rotation angles, etc. If

the alignment across tilt angles can be improved this may increase the 3D spatial resolution.

Supplemental section S-7 (including Supplemental Figs. S-10) discusses the 3D spatial resolution of these measurements, which is estimated to be ~ 90 nm, limited by the large pixel size (50 nm) and other factors. Another issue that affects the results is the threshold used for each dataset. The Otsu auto threshold method [61] was used to guide choice of threshold for segmentation in all cases, and in general the threshold chosen was very close to those values. However, the signal to noise level affects the threshold that approach generates. Masking and removing the non-cathode regions (membrane and embedding polymer) before reconstruction and using the same parameters for

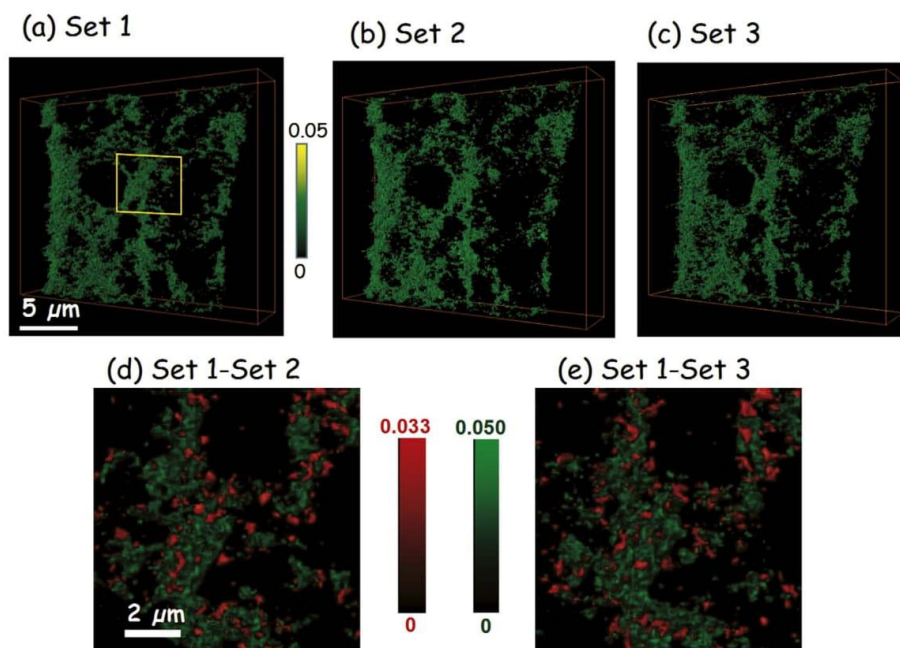


Fig. 8. 3D distributions of ionomer in cathode (green) from 3-set tomography sample MEA 11-GDE, tomography measurement code G, viewed at -30° . Total volume of cathode region of (a) set 1, (b) set 2, (c) set 3. (d) set 2 (green) and the difference between set 1 and set 2. (e) set 3 (green) and the difference between set 1 and set 3 in the yellow box region. In (d) and (e) red displays the ionomer signal present in the earlier measurement that is absent in the later measurement, while green is the signal present in both measurements. Thresholds for each data set are 0.0042, 0.0045 and 0.0046. (measured at CLS a-STXM, 10ID1).

reconstruction, rendering and thresholding will minimize this source of systematic uncertainty. We note that the data sets were measured using different beamlines which have different properties. We have tried as best we could to compensate by e.g. using beamline specific detector efficiencies, in some cases measured using the method reported in Ref. [63].

Supplemental section S7 (with Fig. S-11) provides a check on the accuracy of the 4D imaging by comparing projections of 3D data with 2D measurements.

This work shows that STXM tomography at room temperature can be used to quantify 3D distributions of ionomer in PEM-FC cathodes with negligible radiation damage. This is the first time the 3D distribution of the PFSA ionomer-in-cathode is shown in its original state without chemically staining to enhance contrast [17,18] or modified due to excess radiation damage [19], or by sample preparation technique [64]. We have also demonstrated that the damage caused to the PFSA ionomer due to soft X-rays is not homogenous in 3D. Therefore, a simple extrapolation of the 3D volume of the ionomer to compensate for the damage will not yield accurate information about the sample. Since X-rays and electrons cause similar structural changes to the ionomer due to damage [10], we believe this is of major concern for those performing electron tomography as a means to measure the 3D distributions of ionomer in PEM-FC electrodes.

5. Future developments

STXM tomography with compressed sensing reconstruction was used to measure 3D distributions of ionomer in the cathodes of PEMFC catalyst coated membranes. By systematically reducing total dose and using compressed sensing for 3D reconstruction, 3D ionomer distributions have been measured under conditions where changes from radiation damage are barely measurable. Measuring samples at low

temperature (100 K) can further improve reliability of determining ionomer distributions in 3D since the F-loss should be suppressed [65]. STXM cryo-tomography is now available at the CLS [66] and measurements are underway to verify this claim.

The emerging technique of soft X-ray ptychography [67] has been applied to 4D imaging of PEM-FC cathodes [20,68]. Ptychography has higher spatial resolution than STXM, having achieved better than 5 nm in 2D projection imaging [67]. However, ptycho-tomography uses much higher X-ray doses and thus the radiation damage issue is more severe than conventional ambient temperature STXM tomography. High spatial resolution (12 nm) 2D projection mapping of PFSA ionomer in cathodes of a PEM-FC has been achieved with low dose ptychography [20,68]. We expect that the COSMIC beamline and ptychography end stations presently being commissioned at the ALS will have the potential to perform 4D imaging of ionomer in PEM-FC electrodes with spectro-ptycho-tomography with acceptable doses and extent of radiation damage.

Acknowledgements

We thank Martin Obst (Bayreuth University) for making the tomography rotation stage used in this study. Research was funded by NSERC (RGPIN6141-15), AFCC (10592538), the CaRPE-FC fuel cell network (APCPJ417858-11) and the Canada Research Chair program (CRC-22684). Measurements were made using STXMs on beamlines 5.3.2.2 and 11.0.2 at the Advanced Light Source which is supported by the Division of Basic Energy Sciences of U.S. DoE under contract No. DE-AC02-05CH11231. Measurements were also made using the ambient STXM on beamline 10ID1 at the Canadian Light Source, which is supported by CFI, NSERC, CIHR, NRC and the University of Saskatchewan.

Appendix A. Supplementary data

Supplementary data related to this article can be found at <http://dx.doi.org/10.1016/j.jpowsour.2018.01.074>.

References

- [1] Z. Weber, R.L. Borup, R.M. Darling, P.K. Das, T.J. Dursch, W. Gu, D. Harvey, A. Kusoglu, S. Litster, M.M. Mench, R. Mukundan, J.P. Owejan, J.G. Pharoah, M. Secanell, I.V. Zenyuk, *J. Electrochem. Soc.* 161 (2014) F1254–F1299.
- [2] R.F. Egerton, R.F., P. Li, M. Malac, *Micron* 35 (2004) 399–409.
- [3] R.F. Egerton, *Ultramicroscopy* 127 (2013) 100–108.
- [4] J. Wang, C. Morin, L. Li, A.P. Hitchcock, X. Zhang, T. Araki, A. Doran, A. Scholl, *J. Electron. Spectrosc. Relat. Phenom.* 170 (2009) 25–36.
- [5] S.P. Williams, C.J. Jacobsen, X. Kirz, J. Zhang, J. Van't Hof, S. Lamm, *Proc. SPIE - The International Society for Optical Engineering* 1741 (1993) 318–324.
- [6] D.T. Grubb, *J. Mater. Sci.* 9 (1974) 1715–1736.
- [7] T. Coffey, S.G. Urquhart, H. Ade, *J. Electron. Spectrosc. Relat. Phenom.* 122 (2002) 65–78.
- [8] S. Yakovlev, P.N. Balsara, H.K. Downing, *Membranes* 3 (2013) 424–439.
- [9] D.A. Cullen, R. Koestner, R.S. Kukreja, Z.Y. Liu, S. Minko, O. Trotsenko, A. Tokarev, L. Guetaz, H.M. Meyer, C.M. Parish, K.L. More, *J. Electrochem. Soc.* 161 (2014) F1111–F1117.
- [10] L.G.A. Melo, A.P. Hitchcock, J. Jankovic, J. Stumper, D. Susac, V. Berejnov, *ECS Transactions* 80 (2017) 275–282.
- [11] D. Susac, V. Berejnov, A.P. Hitchcock, J. Stumper, *ECS Transactions* 50 (2012) 405–413.
- [12] D. Susac, V. Berejnov, A.P. Hitchcock, J. Stumper, *ECS Transactions* 41 (2011) 629–635.
- [13] A.P. Hitchcock, V. Berejnov, V. Lee, M.M. West, M. Dutta, V. Colbow, S. Wessel, *J. Power Sources* 266 (2014) 66–78.
- [14] A.P. Hitchcock, V.J. Wu Lee, N. Appathurai, T. Tyliczszak, H.-W. Shiu, D. Shapiro, V. Berejnov, D. Susac, J. Stumper, *Microsc. Microanal.* 22 (S-3) (2016) 1290–1291.
- [15] A.P. Hitchcock, V. Lee, J. Wu, M.M. West, G. Cooper, V. Berejnov, T. Soboleva, D. Susac, J. Stumper, *Am. Inst. Phys. Conf Series* 1696 (2016) 020012 (1–8).
- [16] D. Putz, V. Susac, J. Berejnov, A.P. Wu, Hitchcock, J. Stumper, *J. Electrochem. Soc.* 75 (2016) 3–23.
- [17] H. Uchida, J.M. Song, S. Suzuki, E. Nakazawa, N. Baba, M. Watanabe, *J. Phys. Chem. B* 110 (2006) 13319–13321.
- [18] M. Lopez-Haro, L. Guétaz, T. Printemps, A. Morin, S. Escibano, P.H. Jouneau, P. Bayle-Guillemaud, F. Chandezon, G. Gebel, *Nat. Commun.* 5 (2014) 5229.
- [19] V. Berejnov, D. Susac, J. Stumper, A.P. Hitchcock, *ECS Transactions* 50 (2013) 361–368.
- [20] A.P. Hitchcock, *J. Electron. Spectrosc. Relat. Phenom.* 200 (2015) 49–63.
- [21] U. Bonse, A. Tkachuk, M. Feser, H. Cui, F. Diewer, H. Chang, W. Yun, *SPIE Proceedings* 6318 (2006) 63181D.
- [22] W.K. Epting, W.K., J. Gelb, S. Litster, *Adv. Funct. Mater.* 22 (2012) 555–560.
- [23] Z. Fishman, J. Hinebaugh, A. Bazylak, *J. Electrochem. Soc.* 157 (2010) B1643–B1650.
- [24] P. Krüger, H. Markötter, J. Hausmann, M. Klages, T. Arlt, J. Banhart, C. Hartnig, I. Manke, J. Scholta, *J. Power Sources* 196 (2011) 5250–5255.
- [25] J. Lee, J. Hinebaugh, A. Bazylak, *J. Power Sources* 227 (2013) 123–130.
- [26] F.H. Garzon, S.H. Lau, J.R. Davey, R. Borup, *ECS Transactions* 11 (2007) 1139–1149.
- [27] T. Saida, O. Sekizawa, N. Ishiguro, M. Hoshino, K. Uesugi, T. Uruga, S.-I. Ohkoshi, T. Yokoyama, M. Tada, *Angew. Chem. Int. Ed.* 51 (2012) 10311–10314.
- [28] H. Matsui, N. Ishiguro, T. Uruga, O. Sekizawa, K. Higashi, N. Maejima, M. Tada, *Angew. Chem. Int. Ed.* 56 (2017) 9371–9375.
- [29] W. Chao, B.D. Harteneck, J.A. Liddle, E.H. Anderson, D.T. Attwood, *Nature* 435 (2005) 1210–1213.
- [30] A. Sakidiniwat, D. Attwood, *Nat. Photon.* 4 (2010) 840–848.
- [31] G.A. Johansson, J.J. Dynes, A.P. Hitchcock, T. Tyliczszak, G.D.W. Swerhone, J.R. Lawrence, *Proc. SPIE* 6318 (2006) 11–1–9.
- [32] G.A. Johansson, J.J. Dynes, A.P. Hitchcock, T. Tyliczszak, G.D. Swerhone, J.R. Lawrence, *Microsc. Microanal.* 12 (2006) 1412–1413.
- [33] G.A. Johansson, T. Tyliczszak, G.E. Mitchell, M.H. Keefe, A.P. Hitchcock, *J. Synchrotron Radiat.* 14 (2007) 395–402.
- [34] A.P. Hitchcock, J.J. Dynes, G. Johansson, J. Wang, G. Botton, *Micron* 39 (2008) 311–319.
- [35] A.P. Hitchcock, G.A. Johansson, G.E. Mitchell, M.H. Keefe, T. Tyliczszak, *Appl. Phys. A* 92 (2008) 447–452.
- [36] G. Schmid, M. Obst, J. Wu, A.P. Hitchcock, C.S.S.R. Kumar (Ed.), Chapter 2 in *X-ray and Neutron Techniques for Nanomaterials Characterization*, vol. 5, Springer, Berlin, 2016, pp. 43–94 2016.
- [37] M. Howells, C. Jacobsen, T. Warwick, A. Van den Bos, P.W. Hawkes, J.C.H. Spence (Eds.), *Science of Microscopy*, Springer New York, New York, NY, 2007, pp. 835–926.
- [38] H. Ade, A.P. Hitchcock, *Polymer* 49 (2008) 643–675.
- [39] A.P. Hitchcock, Gustaaf Van Tendeloo, Dirk Van Dyck, Stephen J. Pennycook (Eds.), Chapter 22 in Volume II of the *Handbook of Nanoscience*, Wiley, 2012, pp. 745–791.
- [40] M.G. George, J. Wang, R. Banerjee, A. Bazylak, *J. Power Sources* 309 (2016) 254–259.
- [41] J. Wu, M. Lerotic, S. Collins, R. Leary, Z. Saggi, P. Midgley, V. Berejnov, D. Susac, J. Stumper, G. Singh, A.P. Hitchcock, *Microsc. Microanal.* 23 (2017) 951–966.
- [42] R. Takekoh, M. Okubo, T. Araki, H.D.H. Stöver, A.P. Hitchcock, *Macromolecules* 38 (2005) 542–551.
- [43] K.V. Kaznatcheev, Ch Karunakaran, U.D. Lanke, S.G. Urquhart, M. Obst, A.P. Hitchcock, *Nucl. Inst. Meth. A* 582 (2007) 96–99.
- [44] T. Warwick, H. Ade, A.L.D. Kilcoyne, M. Kraitscher, T. Tyliczszak, S. Fakra, A.P. Hitchcock, P. Hitchcock, H.A. Padmore, *J. Synchrotron Radiat.* 9 (2002) 254–257.
- [45] H. Blumh, K. Andersson, T. Araki, K. Benzerara, G.E. Brown, J.J. Dynes, S. Ghosal, M.K. Gilles, H. Ch. Hansen, J.C. Hemminger, A.P. Hitchcock, G. Ketteler, A.L.D. Kilcoyne, E. Kneedler, J.R. Lawrence, G.G. Leppard, J. Majzlam, B.S. Mun, S.C.B. Myneni, A. Nilsson, H. Ogasawara, D.F. Ogletree, K. Pecher, M. Salmeron, D.K. Shuh, B. Tonner, T. Tyliczszak, T. Warwick, T.H. Yoon, *J. Electron. Spectrosc. Relat. Phenom.* 150 (2006) 86–104.
- [46] A.L.D. Kilcoyne, T. Tyliczszak, W.F. Steele, S. Fakra, P. Hitchcock, K. Franck, E. Anderson, B. Harteneck, E.G. Rightor, G.E. Mitchell, A.P. Hitchcock, L. Yang, T. Warwick, H. Ade, *J. Synchrotron Radiat.* 10 (2003) 125–136.
- [47] J. Stöhr, *NEXAFS Spectroscopy*, Springer, Berlin, 1992.
- [48] D.A. Shapiro, R. Celestre, P. Denes, M. Farmand, J. Joseph, A.L.D. Kilcoyne, S. Marchesini, H. Padmore, S.V. Venkatakrishnan, T. Warwick, Y.-S. Yu, *J. Phys. Conf. Ser.* 849 (2017) 012028.
- [49] D.L. Donoho, *IEEE Trans. Inf. Theor.* 52 (2006) 7–21.
- [50] Z. Saggi, G. Divitini, B. Winter, R. Leary, E. Specker, C. Ducati, P.A. Midgley, *Ultramicroscopy* 160 (2016) 230–238.
- [51] A.P. Hitchcock, **aXis2000 is an IDL Program for Analysis of Spectromicroscopy Data. It is available free for non-commercial use from <http://unicorn.mcmaster.ca/aXis2000.html>.**
- [52] C. Jacobsen, S. Wirick, G. Flynn, C. Zimba, *J. Microsc.* 197 (2000) 10–17.
- [53] J.R. Kremer, D.N. Mastrorade, J.R. McIntosh, *J. Struct. Biol.* 116 (1996) 71–76.
- [54] C. Messaoudi, T. Boudier, C.O.S. Sorzano, S. Marco, *BMC Bioinf.* 8 (2007) 288–312.
- [55] M. Lerotic, M.R. Mak, S. Wirick, F. Meirer, C. Jacobsen, *J. Synchrotron Radiat.* 21 (2014) 1206–1212.
- [56] **MANTIS is a python code for spectromicroscopy data analysis, available free at <http://spectromicroscopy.com>.**
- [57] T. Elfving, P. Hansen, T. Nikazad, *SIAM J. Sci. Comput.* 34 (2012) A2000–A2017.
- [58] E.Y. Sidky, X. Pan, *Phys. Med. Biol.* 53 (2008) 4777–4799.
- [59] E.F. Pettersen, T.D. Goddard, C.C. Huang, G.S. Couch, D.M. Greenblatt, E.C. Meng, T.E. Ferrin, *J. Comput. Chem.* 25 (2004) 1605–1612.
- [60] M. Westerhoff Stalling, H. Hege, H.-C.C.D. Hansen, C.R. Johnson (Eds.), "Amira: a Highly Interactive System for Visual Data Analysis". *The Visualization Handbook*, Elsevier, 2005, pp. 749–767.
- [61] N. Otsu, *Automatica* 11 (1975) 23–27.
- [62] L.G.A. Melo, M. West, V. Berejnov and A.P. Hitchcock, **Radiation Physics and Chemistry, (in preparation).**
- [63] A.F.G. Leontowich, A.P. Hitchcock, T. Tyliczszak, M. Weigand, J. Wang, C. Karunakaran, *J. Synchrotron Radiat.* 19 (2012) 976–987.
- [64] L.G.A. Melo, G.A. Botton, A.P. Hitchcock, *Microsc. Microanal.* 21 (2015) 2443–2444.
- [65] J. Wang, C.J. Jacobsen, J. Maser, J. Osanna, *J. Microsc.* 197 (2000) 80–93.
- [66] A.F.G. Leontowich, R.B., C. Regier, D.M. Taylor, J. Wang, D. Beauregard, J. Geilhufe, J. Swirsky, J. Wu, C. Karunakaran, A. P. Hitchcock, and S. G. Urquhart, *Rev. Sci Inst* (in prep).
- [67] D.A. Shapiro, Y.-S. Yu, T. Tyliczszak, J. Cabana, R. Celestre, W. Chao, K. A.L.D. Kaznatcheev, F. Kilcoyne, S. Maia, Y.S. Marchesini, T. Meng, L.L. Warwick, Yang, H.A. Padmore, *Nat. Photonics* 8 (2014) 765–769.
- [68] J. Wu, X. Zhu, T. Tyliczszak, H.-W. Shiu, D. Shapiro, V. Berejnov, D. Susac, J. Stumper and A. P. Hitchcock, *J. Synchrotron Radiat.* (in prep).

Supplemental Information to 4D imaging of polymer electrolyte membrane fuel cell catalyst layers by soft X-ray spectro-tomography

Juan Wu,¹ Lis Guimaraes de Azeredo Melo,¹ Xiaohui Zhu,¹ Marcia M. West,² Viatcheslav Berejnov,³ Darija Susac,³ Juergen Stumper³ and Adam P. Hitchcock^{1*}

Contents:

Fig S-1 tomo sample mounting

Section S-1 Radiation dose quantification

Section S-2 Evaluation of tomography data for code B and associated radiation damage

Fig S-2 tomography visualization and sample damage check , **code B**

Section S-3 Three set F 1s spectro-tomography of a thin sample with high dose (code D)

Fig S-3 Damage evaluation (spectral, imaging) **code D**

Fig S-4 Tomography visualization and changes from set 1 → 2 and set 2 → 3 **code D**

Section S-4 Two-set C 1s and F 1s spectro-tomography at medium dose (**code E**)

Fig S-5 Damage evaluation (spectral, imaging) **code E**

Fig S-6 Tomography visualization **code E**

Section S-5 damage evaluation and tomography visualization, **code G**

Fig S-7 Damage evaluation (spectral, imaging) **code G**

Fig. S8 Tomography visualization, **code G**

Section S-6 Quantitative radiation damage overview

Fig. S-9 Fluorine loss as function of dose

Section S-7 Evaluation of 3D spatial resolution

Fig. S-10 Fourier ring correlation of xz and yz slices of tomography results, **code F**

Section S-8 Comparison of projections of 3D data with 2D measurements, **code F**

Fig S-11 3D integration compared to 2D projections, Setx 1,2,3, **code F**

Excel spreadsheet: **STXM_dose_calculator.xls** (35 kB dated: 05-Nov-2017)

Movie file: **3sets-scale-17-11-04.mpg** (90,286 kB, dated: 04-Nov-2017)

JOURNAL : J. Power Sources (submitted 10 Nov 2017; revised submitted 19-Jan-2018)

PEM-FC-4D-imaging-Supplemental.doc last changed: 19 Jan 2018

* Corresponding author. aph@mcmaster.ca Tel: 1-905-525-9140 ext 24749

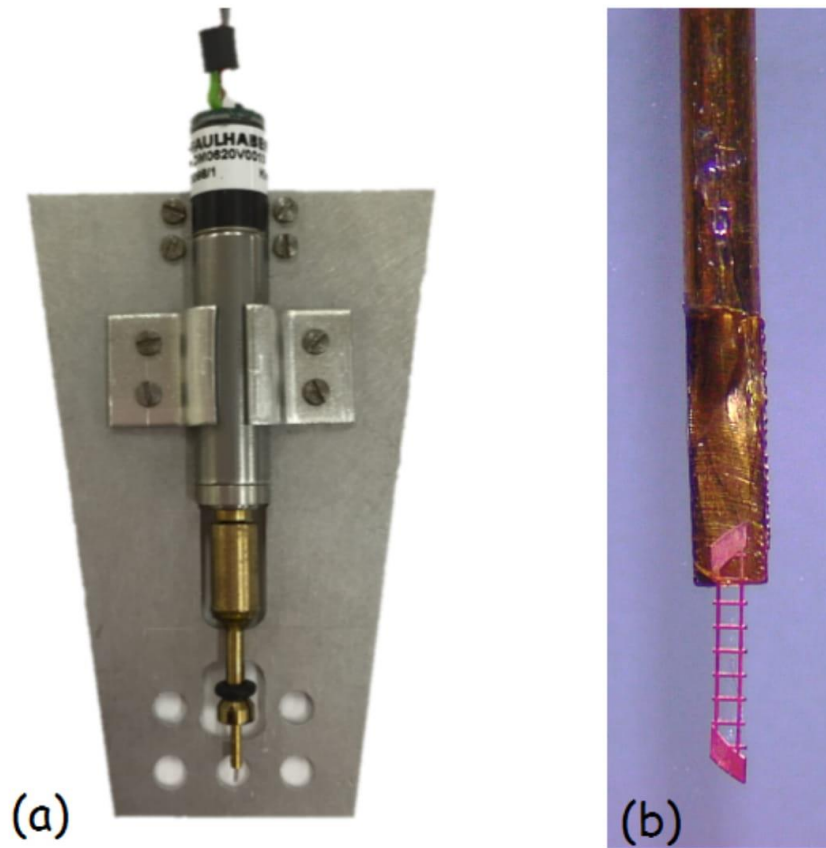


Fig. S-1 (a) rotation stage of STXM tomography, (b) sample strip mounted on brass pin.

S-1 Radiation dose quantification

In order to calculate the radiation dose in STXM, the incident flux (I_0), the x-ray beam diameter (d), and the sample thickness (s) are needed. The absorbed dose (D), in units of mega-grays (MGy) where $1 \text{ MGy} = 10^6 \text{ J/kg}$, is [1] :

$$D = (F \times E \times t) / (k \times m) \quad (2)$$

where F is the absorbed flux, E is the energy of the photon beam, t is the exposure time, k is the detector efficiency, and m is the mass of the volume into which the energy is absorbed [2,3] F is

derived from the incident flux (I_o) and the optical density (OD) of the sample at E by:

$$F = I_o - I = I_o(1 - e^{-OD}) = I_o(1 - e^{-At}) \quad (3)$$

where A is the optical density per nm [1]. In the case of radiation damage to PFSA, there is significant mass loss [4]. After any given exposure, the reduced mass and reduced OD and thus reduced amount of energy absorbed can be calculated by considering the OD and mass that remains at the end of the previous exposure [5]. However, the two factors, reduced mass and reduced OD, roughly compensate, so the difference between a more elaborate dose evaluation taking into account the mass loss [5], and that derived from the above equations (which ignore mass loss) is small. Therefore equations (2) and (3) were used to compute the absorbed doses. An **excel spreadsheet** set up to compute the absorbed dose from the photon energy (E), optical density (OD), incident flux (I_o), thickness (t), X-ray spot diameter (d), sample density, mass in irradiated volume ($m = \pi*d^2*t/4$) and detector efficiency (k) using equations 2 and 3 is provided in the **supplemental information**. More detailed considerations for accurate evaluation of dose for thin polymer films are given elsewhere [5].

One way of estimating the amount of damage expected from an absorbed dose is to compare it to the critical dose for radiation damage to PFSA [4, 6]. For the doses used in this work, which are mostly in the low dose regime where mass loss and chemical transformation is rapid, the relevant critical dose is 40 ± 8 MGy [6]. At this absorbed dose, the amount of a spectral signal from the ionomer ($OD_{694} - OD_{684}$ or $OD_{292.6} - OD_{278}$) is reduced to 63% of the original amount. In order to avoid complications due to differing densities and absorption coefficients of each component in the cathode, all doses reported in this work were evaluated for the membrane region adjacent to the cathode, which is pure PFSA. These values are then assumed to be the same as that absorbed by PFSA ionomer in the cathode. To estimate the dose for the tomography data sets, the OD was taken from on-peak energies, the I_o for F 1s was an average from the two images, I_o for C 1s was taken from the on-peak image, and the thickness of the section was calculated using the average thickness of the PS or TTE embedding media, as measured from a C 1s stack, such as shown in **Figure 3**, or from the membrane, using analysis of a low dose F 1s stack fit on an undamaged region measured before the tomography data acquisition. The density of PFSA was taken as 2 g/cm^3 . While these doses may have systematic errors from various factors they are useful as a tool to discuss the damage effects observed, and to guide the conditions needed for a valid, low damage 4D imaging protocol.

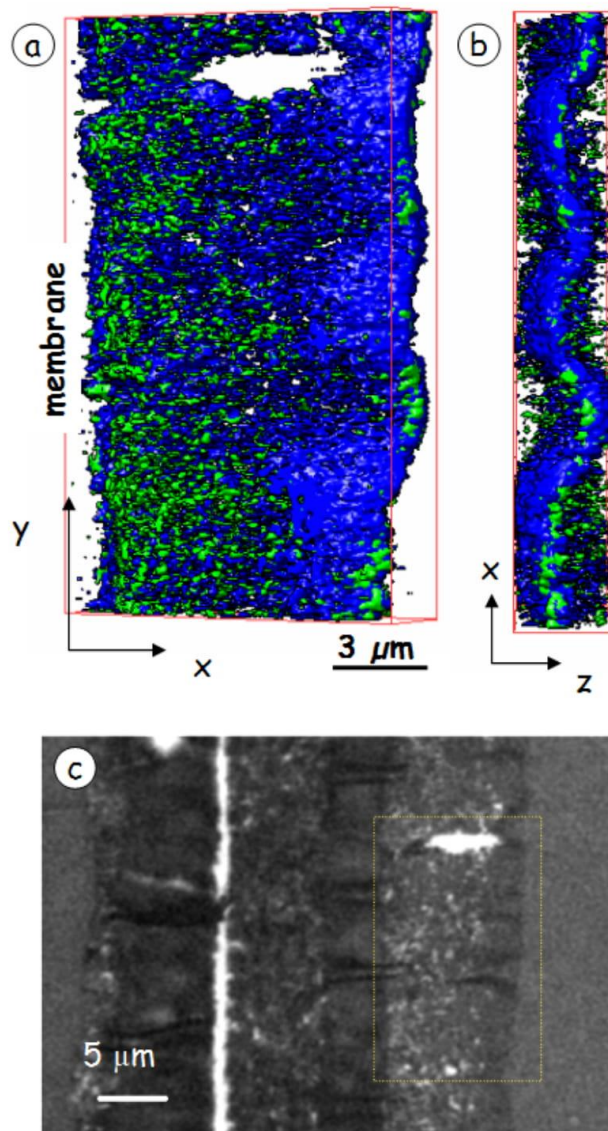


Fig. S-2 3D distributions of the carbon support (blue) and ionomer-in-cathode (green), derived from a 4-energy C 1s and F 1s STXM tomography data set measured from MEA-C, tomography measurement **code B**, reconstructed by compressed sensing (CS). (a) xy view from 30°. (b) xz view from -90°. See table 2 for acquisition details. Threshold for ionomer is 0.036, for carbon support is 0.009. (c) Damage check transmission image at 292.6 eV recorded after tomography. Yellow dotted rectangle indicates area of the tomogram. (measured at ALS 5.3.2.2)

S-2 Evaluation of tomography data for code B and associated radiation damage

Supplemental Figure S-2 present results of a STXM tomography measurement of MEA “C” using many tilt angles (35) and the conditions described for **code B** (table 2 of main paper). At each tilt angle, images at three C 1s energies and 2 F 1s energies were used to determine the 3D distributions of carbon support [OD_{284.5}-OD₂₇₈], PS [OD_{285.3}-OD₂₇₈] and PFSA [OD₆₉₄-OD₆₈₄]. Chemical maps of the carbon support and PFSA were derived at each angle, aligned, and reconstructed in Mantis using the compressed sensing (CS) method [7]. The 2D chemical maps of the carbon support and the ionomer were aligned at each angle; then the same alignment was used for both carbon support and ionomer. Further registry of the carbon support and the ionomer in 4D mapping was performed in Avizo 9.0 [8]. Color coded views of the carbon and ionomer components (PS is not presented for clarity) as projections of the reconstructed volume from the front and the side are shown in **Fig. 2a** and **Fig. S2b**. This 4D imaging shows that the section was not flat, but rather undulating, which is probably a microtoming artifact. The reconstruction also shows a non-uniform distribution of the fluorine signal (i.e. ionomer) in the cathode, consistent with the undamaged section having a gradient of ionomer with more ionomer close to the membrane. The total dose used for these measurements (175 images at 1 ms/pixel and I₀ ~2 MHz) is estimated to be 21 MGy.

After acquiring the **code B** tomography data, the sample was imaged at 292.6 eV over both the tomography area, and a lot of the surrounding area. This damage check image (presented as transmission signal in **Fig. S-2c**) showed no change in contrast between the tomography region and undosed adjacent areas of the cathode or membrane, indicating that there was very little radiation damage, despite a total dose to the tomography area of about half a critical dose for PFSA. In part this is due to reduced visibility of damage in post acquisition 2D image monitoring of a tomography measurement because the region sampled does not have a sharp boundary due to the lack of eucentric adjustment. Damage check images like this are routinely done after tomography studies to monitor the extent of radiation damage.

Section S-3 Three set F 1s spectro-tomography of a thin sample with high dose (code D)

A similar method of conducting three sequential tomography measurements was applied to a ~100 nm sample MEA “A” using measurement conditions **code D** (Table 2), using the STXM on ALS BL 11.0.2. The measured detector efficiency of STXM 11.0.2 is low [62] so the

actual incident flux was much higher than that measured (20 MHz). We estimate the total radiation dose deposited in the full 3-set measurement to be 780 MGy. **Figure S-3a** compares the F 1s spectrum of the cathode in the region of the 3-set tomography measurement, to that from an adjacent region of the cathode which was not irradiated (the regions from which these spectra were acquired are indicated in **Fig. S-3b**, which shows a dramatic change in contrast in the membrane at the right due to the radiation damage). As a consequence of this extremely high dose the characteristic two peak F 1s spectrum of the PFSA has changed to a single broad peak and the F 1s continuum intensity relative to the pre-F 1s edge ($OD_{710} - OD_{684}$) has decreased to only ~25 % of its initial value. There was also significant carbon build-up, which is seen in the increased signal at 684 eV after the tomography measurement (**Fig. S-3a**).

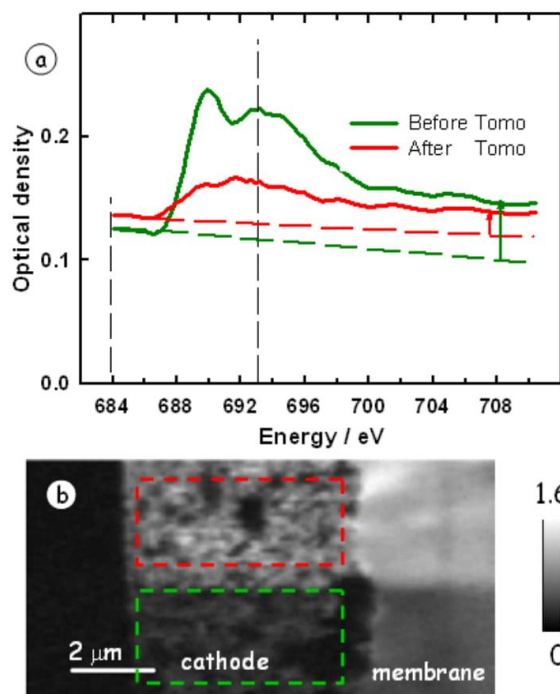


Fig. S-3 (a) Average F 1s spectra of PFSA in cathode of sample MEA-A, **code D** (table 2), before and after 3 set spectro-tomography. **(b)** Fluorine map derived from a F 1s stack (81 images from 678 to 730 eV) measured after 3-set F1s tomography. The rectangular frames indicate the regions of the cathode where the undamaged (green) and damaged (red) spectra were extracted. (measured at ALS 11.0.2)

The much larger dose and thus increased damage is partly because the pixel size was decreased from 50 to 30 nm (thus increasing the dose by $\sim 3\times$); partly because the sample was thinner; and partly because this measurement was made on ALS beamline 11.0.2 which has a much lower detector efficiency [62] and thus use of a nominal 20 MHz incident flux results in an actual incident flux 3-4 times larger than expected.

Ionomer maps ($OD_{694} - OD_{684}$) taken from the -3° , 0° , and 3° tilt angle data for sets 1, 2 and 3 are presented in **Supplemental Figure S-4(a,b,c)**. The F 1s OD signal in the membrane changed from 0.25 to 0.10 from the first angle measured during the first tomography set to the last angle measured in the third tomography set. **Fig. S-4(d,e,f)** are 2D projections from the 3D reconstruction of the F signal. The volume of ionomer, as evaluated from the reconstructed 3D image, decreased by 27% for set 2 and another 35% for set 3. The 3D volume in the region of the yellow box displayed in **Fig. S-4d** is shown for each set in **Figs. S-4(g,h,i)**. The changes in the 3D distribution of the F signal between set 1 and set 2 (**Fig. S-4j**) and between set 1 and set 3 (**Fig. S-4k**) are displayed in red. The changes in both the total volume and the 3D distribution of the F signal are extremely large, not surprising given the extremely high radiation dose. The changes in the 3D ionomer distribution first occur in thin strands distant from the carbon particles, and then spread to regions directly adjacent to carbon particles.

Section S-4 Two-set C 1s and F 1s spectro-tomography at medium dose (code E)

To further reduce dose and thus lessen radiation damage, a much lower incident flux (2 MHz instead of 20 MHz) and a slight defocus (use of 50 nm spot size rather than the fully focused 30 nm spot) was used to measure a 2-set tomography of an MEA-A sample embedded in TTE, using measurement conditions of **code E2** (Table 2). The total radiation dose for the 2-set measurement was 10 MGy, considerably lower than for measurements **C** and **D**. However, that data was measured on the same area than had previously been measured at ALS11.0.2 which has imparted quite a high dose (60 MGy) using conditions of **code E1**.

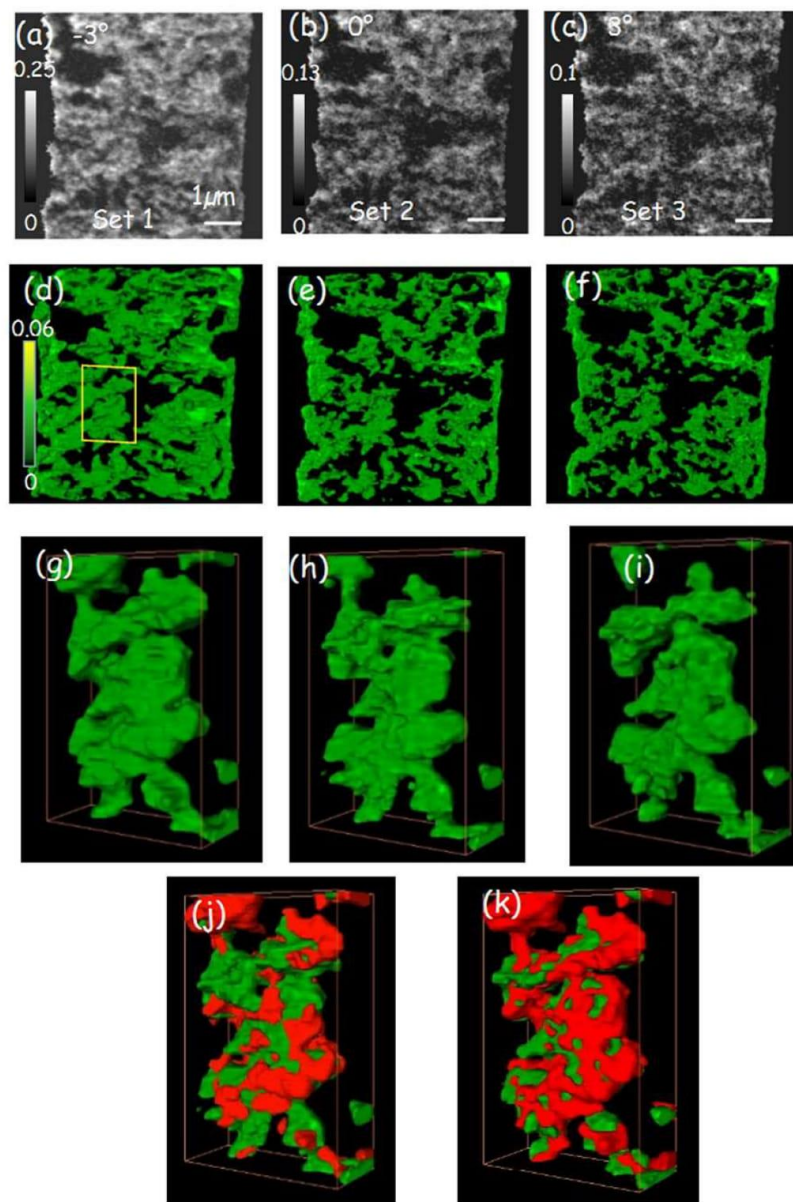


Fig. S-4 2D fluorine maps from cathode of sample MEA-A, **code D**. (a) -3° in set 1, (b) 0° in set 2, (c) 3° in set 3. Projections from 3D reconstruction of PFSA in cathode at 0° : (d) set 1, (e) set 2, (f) set 3. Expanded view of the yellow box (d) with the view changed to 30° : (g) set 1, (h) set 2, (i) set 3. (j) difference of set 1 and set 2 in red (k) difference of set 1 and set 3 in red. Threshold for each tomography set are 0.004, 0.0055, 0.007. (measured at ALS 11.0.2)

As seen in **Supplemental Figure S-5a**, there was substantial damage overall as evidenced by conversion of the two-peak F 1s spectrum to a single peak spectrum and loss of more than 30% of the fluorine, as estimated from $(OD_{694} - OD_{684})$. There was also significant carbon deposition, mostly from the ALS 11.0.2 acquisition, as indicated by a 30% increase in the signal in the pre-F1s region (**Fig. S-5a**). The damage is clearly seen in an image recorded at 694 eV of the area studied by spectro-tomography and an adjacent, undosed area (**Fig. S-5b**) although it is not as severe as for code D.

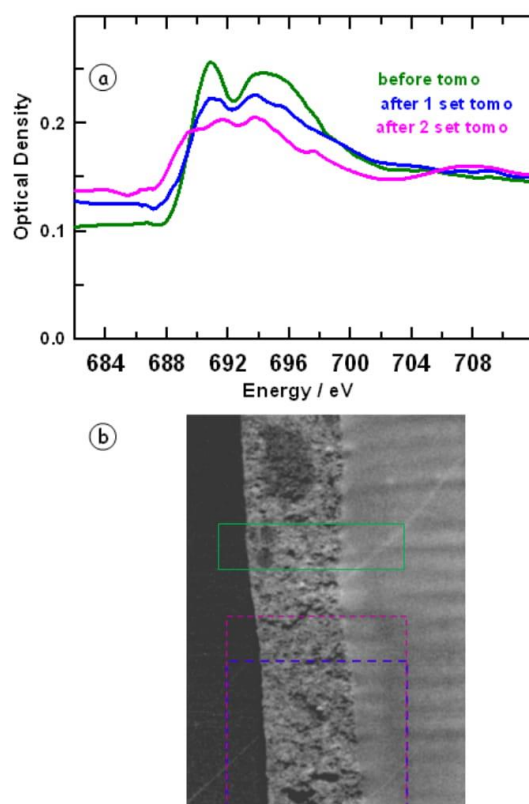


Fig. S-5 (a) F 1s spectra of PFSA (in cathode) before and after each set of 2 set spectro-tomography sample MEA-A, **code E**. The blue curve was recorded after both a C 1s and a F 1s tomography data set was recorded at ALS 11.0.2. The pink curve is after the 3rd tomography data set, F 1s, was measured at CLS. Note that there was extensive carbon build-up as indicated by increase in signal in the pre-F1s region. (b) F map after tomography measurement, the green box, blue box and the purple box indicating the region where the spectra were extracted. (measured at ALS 11.0.2 and CLS 10ID1)

Supplemental Figure S-6 presents views of the carbon support (red) and ionomer (green) as well as maps of the overlap (intersection) of the carbon support and ionomer (in yellow). **Fig. S-6(a,b,c,d)** are the results for set 1, and **Fig. S-6(e,f,g,h)** are the results for set 2. The overlap of carbon support and ionomer is non-physical but rather caused by the limited spatial resolution of STXM tomography. Furthermore, by comparing **Fig.S-6(c)(d)** and **Fig.S6(g)(h)** one can conclude that the fluorine loss happens preferentially in regions that have less ionomer and that the loss starts from the surface of the material and evolves toward thicker regions.

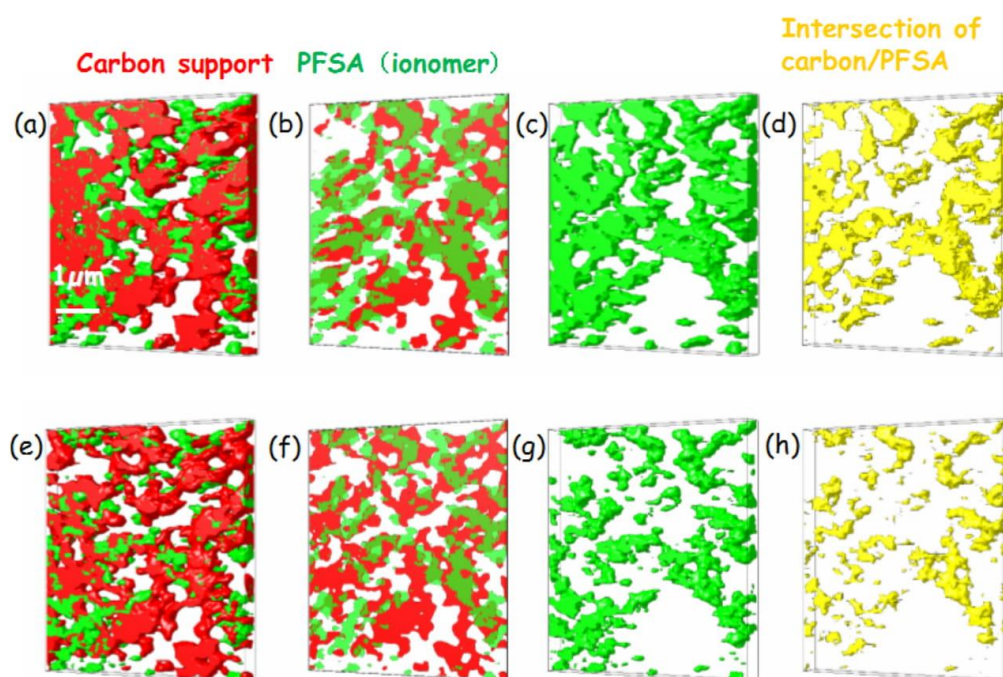


Fig. S-6 3D distributions viewed at a tilt of -30° of carbon support (red) and ionomer in cathode (green) of sample MEA-A, **code E**, low dose cut at a nominal thickness of 100 nm. (a,b,c,d) are from set 1. (e,f,g,h) are from set 2. The yellow display in (d) and (h) is the intersection of the maps of the carbon support and ionomer. Otsu thresholds for set 1 (2) are 0.007 (0.005) for ionomer, and 0.0095 (0.0075) for carbon support. (measured at ALS1102, and CLS 10ID1).

Section S-5 damage evaluation and tomography visualization, code G

The F 1s spectra of the cathode recorded before, during, and after the tomography are presented in **Figure S-7a**. While there was a small reduction in the OD at 694 eV, the shape of the F 1s spectra remained essentially constant. The fluorine loss, as evaluated by $(OD_{705} - OD_{684})$, was only 5%. This, combined with the negligible change of spectral shape, indicates that the 3-set measurement caused negligible changes in the C-F local chemical environment or the amount of ionomer. 2D projection images at 694 eV before the start of the 3-set acquisition and after each set (**Fig. S-7b** through **Fig. S-7e**) are consistent with a very low extent of radiation damage.

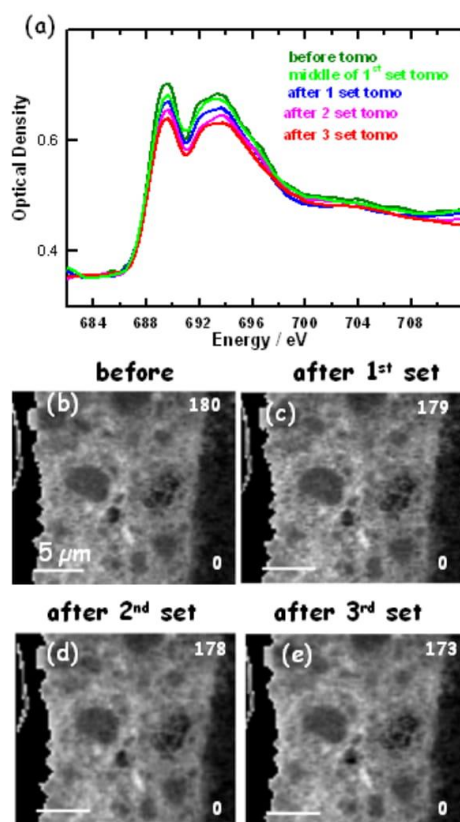


Fig. S-7 (a) F 1s spectra of PFSA (in cathode) measured at the indicated stages of 3 set spectro-tomography of sample MEA 11-GDE, tomography measurement **code G**. (b-e) 2D maps of the ionomer generated by a fit to the F 1s stacks: (b) before tomography, (c) after the 1st set, (d) after the 2nd set, (e) after the 3rd set. The numbers on the right side of each ionomer map are the gray scale limits in nm. (measured at CLS a-STXM, 10ID1)

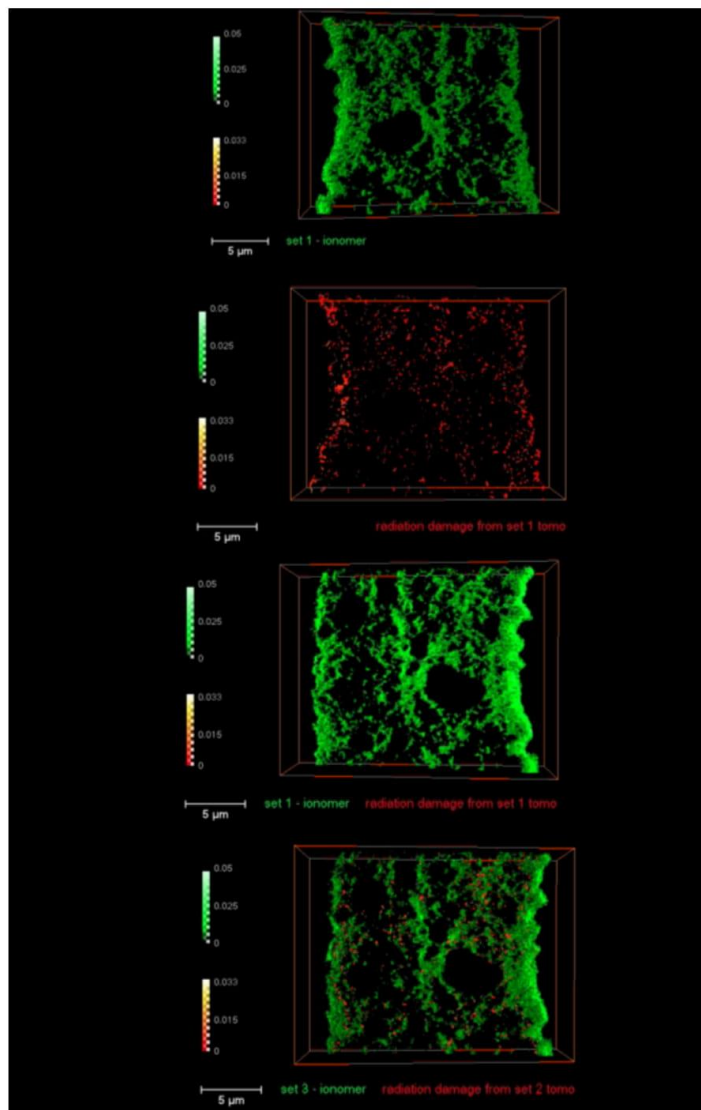


Fig. S-8 & Supplemental Movie: A movie of a rendering of the 3D distribution of the ionomer reconstructed from the **code G** data is presented in supplemental information. Fig. S-6 shows four frames from this movie. The movie was created using Avizo 9.0. The threshold for set 1 is 0.0042, set 2 is 0.0045, and set 3 is 0.0046. Voxel size is 50 nm. The movie shows a 360° rotation around the tilt axis (y), in the sequence of set 1 ionomer (green); difference of set 1 and set 2 = radiation damage caused by set 1 tomography (red); set 2 ionomer (green), difference of set 2 and set 3 = radiation damage caused by set 2 tomography measurement (red); and last, set 3 ionomer (green). The green color scale indicates voxel OD with a max of 0.050, while the red color scale indicates the voxel difference signal, with a max of 0.033.

A **movie** of an Aviso rendering of the 3D distribution of the ionomer reconstructed from the **code G** data is part of the supplemental information (**3sets-scale-17-11-04.mpg**). Several frames from this movie are displayed in **Figure S-8**. The voxels are cubes of 50 nm on a side. In the movie, the ionomer distribution is rotated by 360° about the tilt axis, first as measured from the **first** tilt angle set. It then superimposes in red the differences between set 1 and set 2 (corresponding to ionomer loss due to radiation damage in set 1), plotted on an enhanced intensity scale, relative to that of the ionomer by ~2. This clearly shows preferential loss of ionomer in the thinner regions. It then displays a 360° rotation about the tilt axis of the ionomer distribution as measured from the second tilt angle set. Finally, the differences between set 3 and set 2 ionomer results is superimposed in red, using the same, expanded intensity scale.

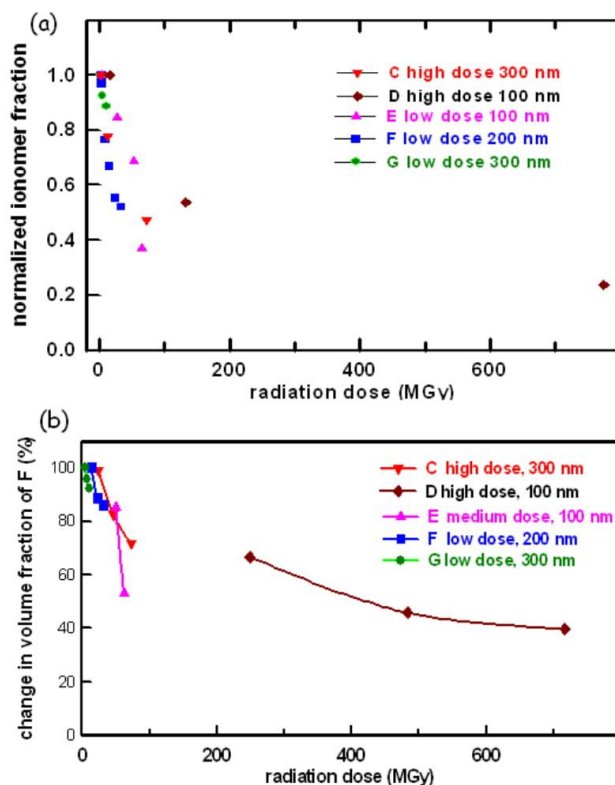


Fig. S-9 (a) Fluorine loss as a function of dose caused by radiation damage in tomography for data sets **C - G**. The fluorine loss was normalized to the F 1s signal from the undamaged sample for each measurement. (b) Change in the volume fraction of ionomer between different sets as a function of radiation dose for data sets **C - G**. (numerical data is presented in table 3).

Section S-6 Quantitative radiation damage overview

Figure S-9a plots the fractional amount of fluorine measured, as a function of the absorbed dose. For each measurement the fluorine loss has been normalized to the signal intensity for undamaged ionomer. **Fig. S-9a** shows that, for all of these measurements - which involved changing incident flux, sample thickness, number of tilt angles, and spot size - the fluorine loss follows an exponential decay as a function of dose. **Fig. S-9b** plots the change in the 3D volume fraction of ionomer after each tomography set as a function of accumulated radiation dose. Use of high incident flux, fully focused beam, and a 100 nm thick sample at ALS BL 11.0.2 (code **D**) resulted in the most extensive radiation damage, consistent with that sample experiencing the highest total dose (780 MGy). When the incident flux was reduced to 2.3 MHz, the radiation dose decreased to only 32 MGy and the change in ionomer volume fraction was reduced (code **F**). The smallest radiation dose used in this study (code **G**, 10 MGy), was <2 % of the largest dose (code **D**, 780 MGy). It is this very significant reduction in total dose, while retaining sufficient statistical quality to have reconstructable tomograms if CS was used, which has enabled meaningful room temperature 4D imaging of ionomer in PEM-FC cathodes.

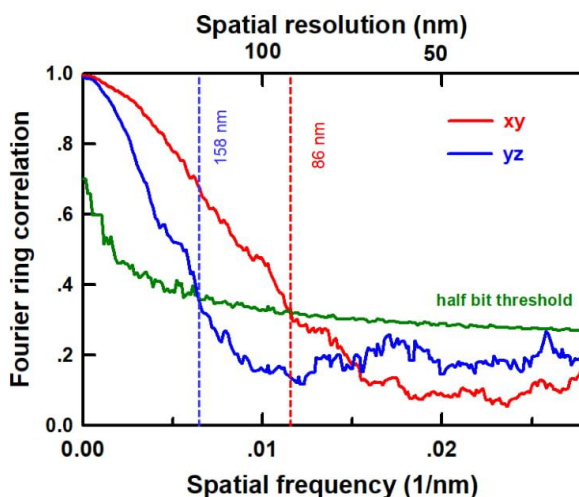


Fig. S-10 Spatial resolution estimated from Fourier ring correlation (FRC) of a slice through the central x-y and y-z directions in the reconstructed tomography results for MEA-A in PS **code F**. (measured at ALS 11.0.2)

Section S-7 Evaluation of 3D spatial resolution

In order to evaluate the spatial resolution of the **code F** tomography results, which were recorded with a 50 nm X-ray spot size, the Fourier Ring correlation (FRC) method [66] was applied to xy, and xz slices extracted from the 3D reconstruction of the ionomer volume (**Supplemental Figure S-10**). If the half bit threshold (green in Fig. S-7) is used, the resolution is estimated to be 86 nm in the xy-direction (red in Fig. S-11), and 158 nm in the z-direction (blue in Fig. S-7). As a result of that limited z-resolution, the tomograms typically show large sub-volumes of mixed carbon support and ionomer (see Figs. 9 and 11), which are somewhat artificial.

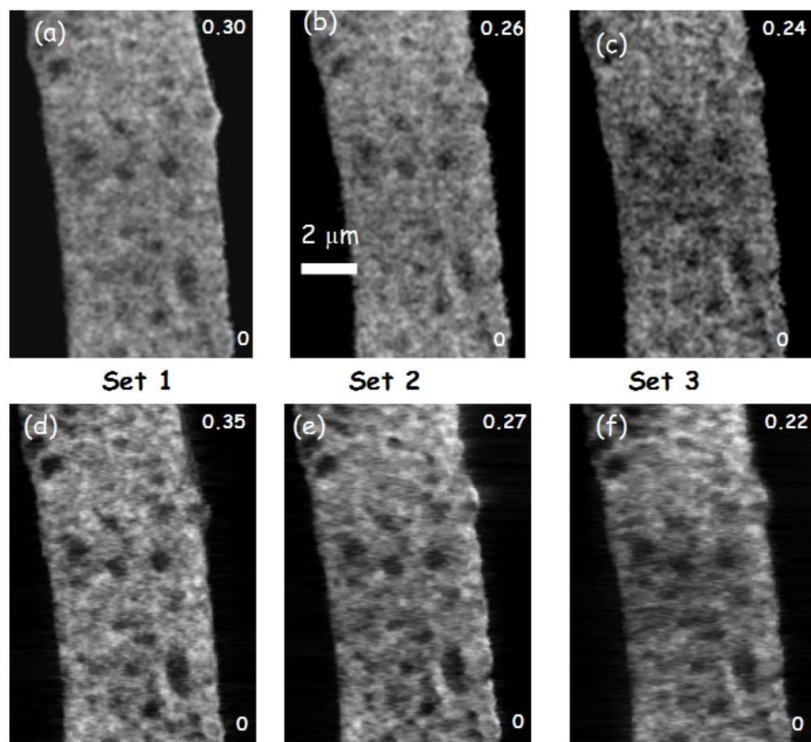


Fig. S-11 2D images of ionomer map of sample MEA-11 GDE, **code F**, at (a) -3° of set 1, (b) 3° of set 2, (c) 0° of set 3. The numbers on the right side of each ionomer map are the gray scale limits in nm. (d-f) 0° projection images of ionomer map from the 3D reconstruction of (d) set 1, (e) set 2, (f) set 3. The numbers on the right side of each projection image are the integrated signal through voxel columns. Threshold for ionomer is 0.007, and that for carbon support is 0.005. (measured at CLS 10ID1)

Section S-8 Comparison of projections of 3D data with 2D measurements, code F

To evaluate the reconstruction quality of the 3D images, projections of 3D images at 0° were compared to the 2D projection images at the lowest angle measured for each tomography set. An example of this is presented for **code F** results in **Supplemental Figure S-11**. There is a good match in the 2D and 3D data, as well as the radiation damage induced morphology changes, over the 3-set measurements. Due to the radiation damage caused by repeated focusing at the center of the area studied, the intensity of the center region of the cathode relative to the surrounding regions systematically decreases. This can be seen in both the 2D images and the 3D image projections at 0° for set 2 and set 3. The optical density scales of the 2D images and the 3D projection in each set are in reasonable agreement, except for the first tomography set.

Supplemental References

1. J. Wang, C. Morin, L. Li, A.P. Hitchcock, X. Zhang, T. Araki, A. Doran and A. Scholl, , J. Electron Spectrosc. Rel. Phenom. 170 (2009) 25-36.
2. A.L.D. Kilcoyne, T. Tylicszak, W.F. Steele, S. Fakra, P. Hitchcock, K. Franck, E. Anderson, B. Harteneck, E.G. Rightor, G.E. Mitchell, A. P. Hitchcock, L. Yang, T. Warwick, H. Ade, J. Synchrotron Radiation 10 (2003) 125-136.
3. A.F.G. Leontowich, A.P. Hitchcock, T. Tylicszak, M. Weigand, J. Wang and C. Karunakaran,, J. Synchrotron Radiation 19 (2012) 976-987
4. L.G. A. Melo, G.A. Botton and A.P. Hitchcock, Microscopy & Microanalysis 21 (2015) 2443-2444.
5. V. Berejnov, B. Rubinstein, L.G.A. Melo and A.P. Hitchcock, J. Synchrotron Rad. (2017) in review
6. L.G.A. Melo, M. West, V. Berejnov and A.P. Hitchcock, Radiation Physics and Chemistry, in preparation.
7. J. Wu, M. Lerotic, S. Collins, R. Leary, Z. Saghi, P Midgley, V. Berejnov, D. Susac, J. Stumper, G. Singh and A.P. Hitchcock, Microscopy & Microanalysis 23 (2017) 951-966.
8. Stalling, M. Westerhoff, and H. Hege, H.-C. Hansen and C.R. Johnson, ed. "*Amira: A Highly Interactive System for Visual Data Analysis*". *The Visualization Handbook*. Elsevier (2005) 749–767.

Screen shot of the STXM-dose-calculator.xls

STXM_dose_calculator.xls (35 kB dated: 05-Nov-2017)

STXM_dose_calculator.xls			
A	B	C	D
Simple dose calculator for STXM measurements			DOSE (energy/mass)
2	STXM-dose-calculator.xls	last changed	n-1
3		05 Nov 2017 (aph)	9-Aug-2017 (lm)
4	Sample	PFSA ionomer MEA-11 GDE	
5		Code G 3-set F 1s edge (CLS)	
6	Fill in the following values:		
7	Parameter	Value	symbol
8	Energy (eV)	690	E
9	OD at this energy	0.55	OD
10	Io (MHz)	2.3	Io
11	spot diameter (nm)	50	2r
12	dwll time (ms)	1	t
13	detector efficiency (0-1)	0.70	ε
14	thickness (nm)	336	d
15	density (g/cc)	1.98	ρ
16	Dose rate (MGy/s)	117	area as circle
17	Absorbed dose/ image (MGy)	0.12	
18	# of images	84	3-sets, 2E; 14 angles
19	TOTAL DOSE	9.87	

E	F	G	H	I
$= \frac{\{(energy\ absorption\ rate)*(time)*(photon\ energy)\}}{(density\ *volume)}$ $= \frac{\{(Io-I)*E*t*ε\}}{(ρ*A*d)} \quad A = \text{spot size area}$				
$\{Io(1-\exp(-OD))*E*t*ε\}/(ρ*π*r*t*d)$				
Notes				
1. Assumes there is no mass loss, thickness change, or change in the OD with dose				
2. Typical detector efficiencies for phosphor/PMT at ALS 5322, and CLS a-STXM are 0.3 at C 1s and 0.7 at F 1s				
3. Typical detector efficiencies for phosphor/PMT at ALS 11.0.2 are 0.15 at C 1s and 0.40 at F 1s				

Movie 3sets-scale-17-11-04.mpg (90,286 kB, dated: 04-Nov-2017)

Description:

A movie of a rendering of the 3D distribution of the ionomer reconstructed from the **code G** data is presented in supplemental information. Fig. S-6 shows four frames from this movie. The movie was created using Avizo 9.0. The threshold for set 1 is 0.0042, set 2 is 0.0045, and set 3 is 0.0046. Voxel size is 50 nm. The movie shows a 360° rotation around the tilt axis (y), in the sequence of set 1 ionomer (green); difference of set 1 and set 2 = radiation damage caused by set 1 tomography (red); set 2 ionomer (green), difference of set 2 and set 3 = radiation damage caused by set 2 tomography measurement (red); and last, set 3 ionomer (green). The green color scale indicates voxel OD with a max of 0.050, while the red color scale indicates the voxel difference signal, with a max of 0.033

Chapter 6

High-Resolution Imaging of Polymer Electrolyte Membrane Fuel Cell Cathode Layers by Soft X-ray Spectro-Ptychography

Juan Wu, Xiaohui Zhu, Marcia M. West, Tolek Tyliczszak, Hung-Wei Shiu, David Shapiro, Viatcheslav Berejnov, Darija Susac, Juergen Stumper, and Adam P. Hitchcock

This chapter presents the results of soft X-ray spectro ptychography studies of Polymer Electrolyte Membrane Fuel Cell cathode layer both in 2 and 3 dimensions.

The samples were provided by Viatcheslav Berejnov, Darija Susac, Juergen Stumper. The samples were microtomed by MMW, the data collection and analysis were done by J. W., XH. Z., A.P.H and D. S. The ptychography measurements on beamline 11.0.2 were carried out by Tolek Tyliczszak, Hung-Wei Shiu, and David Shapiro.. My role in this study was sample preparation and data acquisition. I performed the ptychography reconstruction with XH.Z. supervised by DS. I performed all of the alignment and tomography reconstruction. XH.Z worked on the first draft, and I then expanded it. Further editing was done by APH, XHZ and me, with minor contribution from DS and VB. (Wu et al., 2018) (Reproduced with permission from American Chemical Society)

High-Resolution Imaging of Polymer Electrolyte Membrane Fuel Cell Cathode Layers by Soft X-ray Spectro-Ptychography

Juan Wu,[†] Xiaohui Zhu,[†] Marcia M. West,[‡] Tolek Tyliczszak,[§] Hung-Wei Shiu,^{§,||} David Shapiro,[§] Viatcheslav Berejnov,[⊥] Darija Susac,[⊥] Juergen Stumper,[⊥] and Adam P. Hitchcock^{*,†,Ⓢ}

[†]Dept. of Chemistry and Chemical Biology, McMaster University, Hamilton L8S 4M1, Ontario, Canada

[‡]Electron Microscopy, Dept. of Pathology, McMaster University, Hamilton, Ontario L8N 3Z5, Canada

[§]Advanced Light Source, Berkeley Laboratory, Berkeley, California 94720, United States

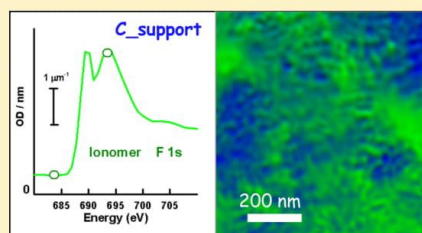
^{||}National Synchrotron Radiation Research Center, Hsinchu, Taiwan 30076, R.O.C.

[⊥]AFCC, 9000 Glenlyon Parkway, Burnaby, British Columbia V5J 5J8, Canada

Supporting Information

ABSTRACT: Polymer electrolyte membrane fuel cells (PEMFCs) are a promising and sustainable alternative to internal combustion engines for automotive applications. Polymeric perfluorosulfonic acid (PFSA) plays a key role in PEMFCs as a proton conductor in the anode and cathode catalyst layers and in the electrolyte membrane. In this study, spectroscopic scanning coherent diffraction imaging (spectro-ptychography) and spectro-ptychographic tomography were used to quantitatively image PFSA ionomers in PEMFC cathodes in both two and three dimensions. We verify that soft X-ray ptychography gives significant spatial resolution improvement on soft matter polymeric materials. A two-dimensional spatial resolution of better than 15 nm was achieved.

With better detectors and brighter and more coherent X-ray beams, radiation-sensitive PFSA ionomers will be visualized with acceptable levels of chemical and structural modification. This work is a step toward visualization of ionomers in PEMFC cathodes at high spatial resolution (presently sub-15 nm, but ultimately below 10 nm), which will be transformative with respect to optimization of PEMFCs for automotive use.



1. INTRODUCTION

Proton exchange membrane fuel cells (PEMFCs) are electrochemical devices, which convert chemical energy to electrical energy.¹ When hydrogen is used as the fuel, the only product is water. Because of their high energy conversion efficiency, high power density, rapid startup, and zero carbon emission,^{1,2} PEMFCs are considered a desirable power conversion technology. They are currently under rapid development for automobile applications, with early introduction in selected markets by Toyota³ and several other manufacturers.

A critical component in a PEMFC is the membrane electrode assembly (MEA), which consists of a proton-conducting membrane coated by anode and cathode catalyst layers (CLs).⁴ The cathode CL is a porous structure composed of platinum nanocatalysts deposited on an electron-conducting carbon black support, a proton conductor, and open spaces for the transport of oxidant (O₂) and product (H₂O).^{5,6} The most commonly used proton conductor in MEA electrodes is perfluorosulfonic acid (PFSA),⁷ which has a high proton conductivity⁸ and also acts as a binder to mechanically stabilize the CL.⁶ Therefore, optimization of the spatial distribution of the PFSA ionomer in CLs relative to the active catalyst, support, and porosity can greatly improve platinum utilization, help to control gas permeability, and potentially achieve higher-

temperature operation.⁹ As with all such goals, the ability to optimize is closely related to the ability to visualize and quantitatively map the chemical components of interest.

However, despite great interest, quantitative imaging of ionomers in PEMFC CLs is poorly developed as it is rather challenging, mainly because of radiation damage issues. Although atomic force microscopy has been used to image the ionomer,^{10,11} it can only provide information about surface topology.¹² Direct visualization of internal morphologies of ionomer with a few nanometer resolution has been claimed with transmission electron microscopy (TEM),¹³ but there was no analytical verification. Typically, the view is that staining techniques are required,¹⁴ but these may not be specific to ionomers and have the potential to modify the material. By targeting water as the signature, isolated hydrophilic domains (3–10 nm) have been observed by TEM in PFSA membranes.^{15–17} In a recent study, Lopez-Haro et al.¹⁸ visualized a Cs⁺-stained ionomer layer deposited on a carbon black via three-dimensional (3D) TEM tomography. However, despite the high resolution and ability to access the 3D

Received: March 27, 2018

Revised: May 10, 2018

Published: May 10, 2018

structure, sample preparation challenges and radiation damage still greatly limit the application of TEM to ionomer materials.¹⁴ Because of the high sensitivity of ionomers to radiation damage, electron beam irradiation causes mass loss, chemical transformation, and displacement of materials,^{19–21} which introduces artifacts.¹⁵

Synchrotron-based scanning transmission X-ray microscopy (STXM) uses the intrinsic X-ray absorption spectral contrast to identify and quantitate chemical species with a spatial resolution of ~ 30 nm.^{22,23} STXM has significant advantages over analytical electron microscopy because of a lower rate of radiation damage relative to useful information obtained, as has been demonstrated in direct comparisons to both TEM–electron energy loss spectroscopy²⁴ and TEM–energy-dispersive X-ray spectroscopy.²⁰ Previously, STXM has been applied to track the changes of chemical constituents during fabrication of fuel cell electrode materials²⁵ and to quantitatively map ionomer distributions in activated CLs^{26,27} and before and after a testing protocol that causes carbon corrosion.²⁸ Most PEMFC STXM studies to date have involved two-dimensional (2D) projection analysis. However, PEMFC CLs have a complex 3D structure. A proper understanding of CL structure and the impact on transport properties will only be achieved with 3D visualization methods. Hard X-ray tomography, using both laboratory²⁹ and synchrotron sources,^{30,31} has been used very effectively for static and operando studies but is essentially blind to the low-molecular-weight, radiation-sensitive PFSA ionomer. We have been developing STXM spectro-tomography specifically for quantitative measurements of the 3D distribution of the PFSA ionomer in CLs. Berejnov et al.³² and Wu et al.²¹ have used room-temperature STXM spectro-tomography at the C 1s and F 1s edges to the 3D image ionomer in a PEMFC cathode. Other STXM spectro-tomography studies of PEMFC materials have been reported by Hitchcock and Toney,³³ Hitchcock²³ and Schmid et al.³⁴ However, the morphological details and ionomer distributions in PEMFCs are still not well-resolved because of a combination of limited spatial resolution [~ 30 nm, dictated by the zone plate (ZP) focusing optic] and the maximum sample thickness (~ 300 nm) which is dictated by X-ray absorption at the F 1s edge.

Ptychography is a scanning coherent diffraction imaging (CDI) technique that can provide high spatial resolution imaging over large fields of view.^{35–37} Unlike conventional X-ray imaging using ZPs (STXM, TXM, etc.), ptychography is not limited by image-forming optics and thus has the potential to reach the Rayleigh limit spatial resolution dictated by the wavelength of X-rays used.^{38,39} Recently, soft X-ray ptychography has been developed by Shapiro et al.,⁴⁰ and ~ 3 nm spatial resolution has been achieved using 1500 eV photons. Soft X-ray ptychography has been applied to magnetotactic bacteria,⁴¹ catalyst particles,⁴² lithium batteries,⁴³ calcium silicate hydrates,⁴⁴ and magnetic films.⁴⁵ The first soft X-ray spectro-ptycho-tomography has recently been reported.⁴⁶

In this study, we report the use of soft X-ray spectro-ptychography to image 2D and 3D distributions of ionomers in PEMFC cathodes. Because ptychography relies on coherent scattering by sample components, there is a real question if noncrystalline soft matter such as the PFSA polymer can be successfully imaged with ptychography. We address this important question by performing ptychography on a model bilayer system consisting of one layer with isolated polytetrafluoroethylene (PTFE) fibers (mimicking PFSA) and a second

layer containing Pt-coated crystalline graphitic fibers (mimicking the catalyst-coated carbon support).

At present, the radiation doses required for ptychographic imaging are typically much larger than those needed for conventional STXM, although one of the data sets reported in this work was measured using very low damage conditions. To track the damage with a view of evolving to minimal damage conditions as done with ambient temperature STXM spectro-tomography,²¹ we have characterized the extent of damage caused by 2D and 3D imaging ptychographic imaging modalities. We also explore the spectroscopic information in ptychography which is richer than that in STXM because both phase and amplitude signals are acquired. In addition, ptychography-based spectro-tomography is used for 4D imaging—probing 3D distributions of ionomer in CLs—with the aim to better understand the organization of all components within PEMFC CLs.

2. EXPERIMENTAL SECTION

2.1. Sample Preparation. PEMFC catalyst-coated membrane (CCM) samples were cut into small rectangular pieces, embedded in an amine epoxy resin, and sectioned using a diamond blade ultramicrotome to a thickness of 100–300 nm. For the tomography measurements, a fresh scalpel was used to cut a single strip of the TEM Cu grid, which contained the CCM section of interest. When performing tomography measurements, the reduced width of the strip (~ 150 μm) allows for sample rotation from -65° to 65° without hitting the order sorting aperture, which is a few hundred microns upstream of the focal point of the ZP.³⁴

The model sample consisted of a two-layer polymer film with Pt-decorated graphitic carbon fibers embedded in an amine resin in one layer and PTFE (Teflon) fibers embedded in an amine resin in the second layer (see Figure 1). STXM tomography measurements on this sample have been presented earlier.^{33,34}

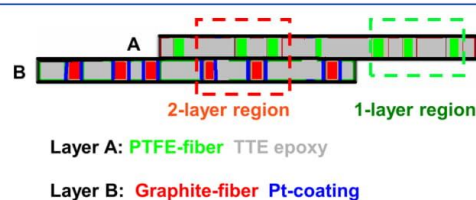


Figure 1. Cartoon of structure of the model sample used to evaluate the resolution improvement when using soft X-ray ptychography to measure noncrystalline soft matter. The dashed boxes indicate the type of areas measured for the data in Figure 2 (1-layer) and Figure 4 (2-layer).

2.2. Data Collection. STXM measurements were carried out using beamlines 11.0.2 and 5.3.2.1 at the Advanced Light Source (ALS), Lawrence Berkeley National Laboratory (LBNL). Instrumentation, STXM operational modes, and data analysis methods have been described in recent reviews.^{22,47} Ptychographic measurements were performed using the STXM on the ALS 11.0.2 undulator beamline, modified by the addition of a Princeton Instruments direct-sense X-ray camera. Ptychography data sets were also obtained using a dedicated ptychography instrument, Nanosurveyor I,⁴⁸ on the ALS 5.3.2.1 bending magnet beamline. A ZP with an

Table 1. Summary of Conditions and Total Dose for Each Measurement Reported

sample	BL—ZP δ_i	spot size (nm) ^a	dwell (ms)	thickness (nm)	OD 694 (eV)	I_0 (MHz)	Det. Eff.	# of images ^b	total dose (MGy) ^c	presented in figure
model, 1-layer	STXM—25 nm	31	4	175	0.75	6.5	0.7	1	12	2a
model, 1-layer	5321 ptycho—60 nm	72	100	175	0.4	3.1	0.7	2 + 1	220	2b
model, 2-layer	5321 ptycho—60 nm	72	100	300	0.4	3.1	0.7	3 angles	220	4
MEA ^d	11.0.2 STXM—60 nm	72	1	130	1.2	9.5	0.4	2	4	S2
MEA	11.0.2 ptycho—60 nm	72	20	130	0.51	9.5	0.4	2	45	5
MEA-11-GDE	5321 STXM—60 nm	72	2	230	1.05	1.7	0.7	74	14	6e
MEA-11-GDE	5321 ptycho 2D—60 nm	72	120	230	(0.4) ^e	2.5	0.7	33	280	6a–e
MEA-11-GDE	5321 ptycho 3D—60 nm	72	100	150	0.3@710 eV	3.1	0.7	2 × (15 angles) = 30	320	7–9

^aCited spot size is the diffraction-limited spot expected for the ZP used (25 or 60 nm outer zone width). ^bWhere two measurements were made, they were measured at 684 and 694 eV. Single measurements were made at 694 eV. ^cThe total dose for the MEA sample was determined from the properties and exposure of the membrane to avoid the influence of Pt/carbon support. The excel program used for the dose calculation is provided in supplementary information of Wu et al.²¹ ^dThis MEA was provided by Ballard. The 25 μm wide, unreinforced, NRE-211 membrane had an equivalent weight of 1100. The cathode, which was fabricated by screen printing, had an ionomer/carbon mass ratio of 1.07 and a Pt loading of 0.65(4) mg/cm^2 . The ionomer was Nafion-117. ^eOD of the sample was changing during the measurement because of fluorine loss. This is an estimate from the spectrum derived from the spectro-ptycho measurement (see Figure 5e).

outer zone width of 60 nm (100 nm) was used to illuminate the sample at beamline 11.0.2 (5.3.2.1). The sample is raster-scanned through the focal point with a step size of 50 nm. This makes the adjacent areas that are sampled overlap with each other, which is an important factor in achieving rapid convergence of the ptychography reconstruction. With the high brightness and coherence of the X-ray sources provided by the undulator at 11.0.2, a very short exposure time (20 ms) was sufficient to achieve good results. Despite this, the clock time to acquire ptychography data sets on beamline 11.0.2 was very long because of the ~ 1 s readout time of the Princeton camera. At beamline 5.3.2.1, a custom, high-frame-rate CCD detector was used to record the diffraction data with single point exposure times of 100–200 ms. A silicon beam stop was used to avoid saturation of the bright-field signal at long dwell time, thereby increasing the dynamic range of the detector. At both 5.3.2.1 and 11.0.2 beamlines, the camera background signal was measured with the beamline shutter closed and removed in subsequent data processing.⁴⁰ Details of the measurements, along with estimates of the radiation dose used for each measurement, are given in Table 1. The doses were estimated using a simplified approach described in Wu et al.²¹

2.3. Ptychography Reconstruction and Data Analysis. Amplitude and phase images were derived from the measured ptychography diffraction patterns using 500 iterations of the relaxed averaged alternating reflection reconstruction algorithm implemented in the SHARP ptychography code⁴⁹ developed by the Center for Applied Mathematics for Energy Research Applications at Berkeley Lab. For spectroscopy data, each set of ptychographic amplitude images was combined into stacks and then aligned using Fourier cross-correlation routines in aXis2000.⁵⁰ The ptychographic amplitude signals were then converted to optical density (OD) signals using the ptychography amplitude signal in a region free of the sample but close to the sample region of interest (ROI). Ptychography OD signal from appropriate sets of image pixels was then extracted from the OD stacks and used for further analysis, such as generating chemical maps. Although we have not performed a detailed analysis of the phase signals, or the combined absorption and phase signals, as performed by Shapiro et al.,⁴⁰ one comparison of ionomer mapping by ptychographic absorption and by ptychographic phase is presented as supplementary information (see Figure S1).

2.4. Ptycho-Tomography Acquisition and Data Analysis.

Ptychographic tomography measurements were performed using a piezo rotation stage, one of the key components of the Nanosurveyor-I instrument.⁴⁸ Eucentric alignment of the rotation axis with the ROI of the sample was achieved by iteratively adjusting the x and z axes of a piezo stage mounted on top of the rotation stage.⁴⁸ 2D coherent diffraction images were then recorded at a range of tilt angles (-57° to $+69^\circ$ with 9° steps). Higher tilt angles could not be achieved because of increasing sample thickness along the beam transmission direction. At each rotation angle, images were measured at 684 eV, below the F 1s onset, and at 710 eV, in the F 1s continuum. The two images were aligned. Maps of PFSA were generated by subtracting the pre-edge (684 eV) OD image from the post-edge (710 eV) OD image. Note that some of the STXM data used for comparative purposes were measured at 684 and 694 eV. While the signal magnitude is larger when the 694 eV signal is used, the fluorine maps are qualitatively similar to those measured at 710 eV. The effect of radiation damage for a given dose is also similar at the two energies because the signal decay rate ($d\text{OD}/d(\text{dose})$) is similar at 694 and 710 eV. Absorption at 684 eV is dominated by the carbon support component. At the time of these measurements, it was not possible to measure ptychography signals at the C 1s edge. Thus, the chemical map of the carbon support (C_{sup}) was extracted by subtracting an appropriately weighted fraction of the PFSA map from the pre-edge image, according to

$$\text{OD}_{C_{\text{sup}}} = \text{OD}_{684} - a \times (\text{OD}_{710} - \text{OD}_{684}) \quad (1)$$

where $\text{OD}_{C_{\text{sup}}}$ is the OD of the carbon support and a is the ratio, $\text{OD}_{1684}(\text{PFSA})/\text{OD}_{1684}(C_{\text{sup}})$, which is 0.21.⁵¹ Here, OD_1 refers to the OD of the component with a thickness of 1 nm. The chemical maps of PFSA and the carbon support at all tilt angles were then aligned in aXis2000 by Fourier correlation methods. The set of aligned chemical maps at all tilt angles was used to generate a 3D reconstruction using a compressed sensing (CS) algorithm^{52,53} implemented in Mantis⁵⁴ (Mantis is available from <http://spectromicroscopy.com>). The 3D models of the two components were merged to generate a 4D model, which shows the quantitative distribution of both components in 3D. Visualization, segmentation, and analysis of the 3D data were performed using Avizo.⁵⁵

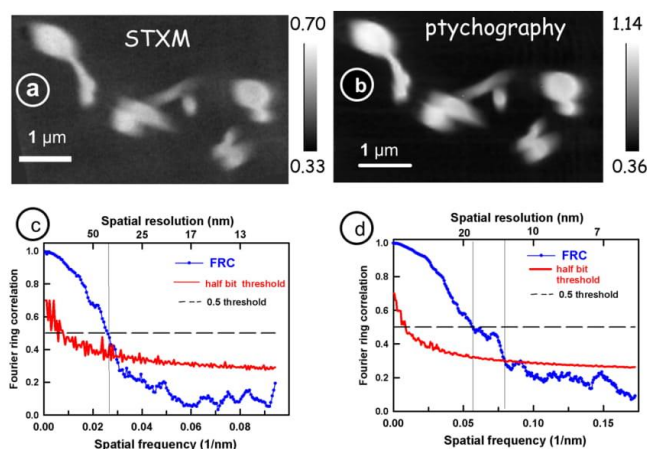


Figure 2. Images of the single layer region of the bilayer model sample (see Figure 1). (a) STXM OD image at 694 eV recorded with 1 ms/pixel sampling, using a ZP with 25 nm outer zone width (recorded after ptychography) (CLS 10ID1). (b) Ptychography absorption image at 694 eV of the same area. (c) FRC analysis of the spatial resolution for the STXM image of (a). (d) FRC analysis for the ptychography image of (b) (ALS 5.3.2.1).

Table 2. Spatial Resolution of Ptychography and STXM Measurements

sample (microscope)	PTFE (CLS)		PTFE (S.3.2.1)		(PTFE, C, Pt) model (S.3.2.1)		MEA (11.0.2)		MEA (S.3.2.1)	
energy		694 eV	694 eV	F-map	694 eV	F map	684 eV	694 eV	F map	F 3d (xy) slice
method	TEM ^a	STXM ^b	ptycho	ptycho	ptycho	ptycho	ptycho	ptycho	ptycho	ptycho-tomo
ZP δ_r (nm) ^a	N/A	25	60	60	60	60	60	60	60	60
resolution (nm) (0.5 metric)	5	35	18	13	9	15	16	13	13	23
resolution (nm) (1/2-bit metric)	4	33	13	11	10	12	14	12	12	20
edge response (nm) 20–80%	11	40	14	16	15	18	18	17	16	35

^aSpatial resolution of a TEM image of a similar region as Figure 2a,b but without radiation damage from X-rays (see Figure 3). Note that the TEM used was operated under conditions where the instrumental resolution was 0.5 nm. ^bSTXM with high-resolution ZP performed on the same area as measured by ptychography. See Figure 2. ^cDiffraction-limited resolution of a ZP is $1.22 \times \delta_r$, where δ_r is the width of the outer zone.

3. RESULTS

3.1. Ptychography of the Model Sample. To validate ptychography for imaging noncrystalline polymers such as PFSA, we measured a bilayer polymer model sample with the structure as shown in Figure 1. Region 1 (green rectangular box) is a single layer consisting of the PTFE fiber cross sections embedded in epoxy. Region 2 (red rectangular box) is two-layers, with the PTFE/epoxy layer on top of the layer containing cross sections of the platinum-coated graphitic fibers embedded in epoxy. Figure 2a shows a conventional STXM OD image at 694 eV of a microtomed cross section of several isolated PTFE fibers from region 1. This image was recorded at 694 eV using a ZP with 25 nm outermost zone width, which produces a theoretical diffraction-limited spot size of 31 nm. Figure 2b presents a ptychography absorption image of the same area measured at the same photon energy. Note that the ptychography amplitude image is recorded by serial sampling of the coherent scattering data with an exposure time of 100 ms at each pixel. Although PTFE is very radiation-sensitive, the morphologies of the PTFE fiber cross sections shown in the ptychography absorption image (Figure 2b) are similar to those in the conventional STXM image (Figure 2a) but with better spatial resolution. These figures indicate that 100 ms ptychographic exposure did not change the morphology of the PTFE fibers. Note that the STXM image

was recorded AFTER the ptychography measurement so that the lower OD in the STXM image reflects fluorine loss caused by the ptychographic measurement.

To quantify the spatial resolution of the STXM and ptychography images, the Fourier ring correlation (FRC) method⁵⁶ was used, with results shown in Figure 2c,d. Single images were evaluated by splitting the image into an even and odd pixel set and measuring the correlation between them, and the associated 2σ , according to the formulae given by Saxton and Baumeister.⁵⁷ The spatial resolution estimates for all of the model bilayer and MEA measurements are summarized in Table 2. For the STXM image in Figure 2a, the intersection of the FRC curve (blue, Figure 2c) and both the 0.5 threshold line (dashed gray line, Figure 2c) and the 1/2-bit curve occur at 0.028 nm^{-1} , which indicates a spatial resolution of 35 nm, consistent with near diffraction-limited performance of the ZP used. The FRC curve of the ptychography image (blue, Figure 2d) drops below the threshold line of 0.5 (dashed gray line, Figure 2d) at a spatial frequency of 0.056 nm^{-1} , which corresponds to a spatial resolution of 18 nm, and crosses the 1/2-bit curve at 0.078 nm^{-1} , which corresponds to a spatial resolution of 13 nm. Sub-10 nm spatial resolution has been achieved previously with soft X-ray ptychography.^{40,41} The spatial resolution of $\sim 15 \text{ nm}$ achieved by ptychography on a soft matter sample is impressive considering that (i) the S.3.2.1

bend magnet beamline has a relatively low coherent fraction compared to that of the 11.0.2 undulator beamline, where the highest resolution data were obtained,^{38,40} and (ii) this is a soft matter polymer sample, which has a very weak coherent scattering signal.

One can speculate that spatial resolution is affected not only by the ability of soft X-ray ptychography to image soft matter but also by the intrinsic properties of the sample, in particular by the abruptness of the PTFE/epoxy interface. To investigate this possibility, the bilayer polymer model sample was imaged using TEM. Figure 3a shows a TEM image of the similar region

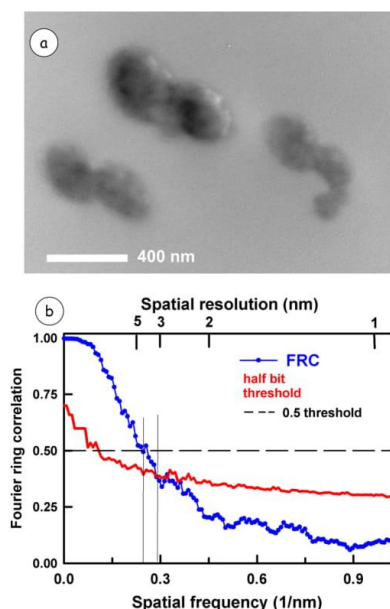


Figure 3. (a) TEM image of a fresh area of the PTFE single layer of the bilayer sample (bright field, 100 keV). (b) FRC analysis of spatial resolution of the TEM image, verifying that the edges of the PTFE fibers are sharp at a spatial scale significantly lower than that measured by ptychography.

but without exposure to any X-rays. It shows that the abruptness of the epoxy–PTFE interface is considerably below 5 nm (Figure 3b), indicating that the intrinsic sharpness of the fiber edges is not limiting the resolution achievable by ptychography. The ~15 nm spatial resolution of ptychography of PTFE fibers (Figure 2b) achieved with a 60 nm ZP is clearly better than that obtained using conventional STXM with a 25 nm ZP (Figure 2a). This is experimental evidence that ptychography can improve the spatial resolution when applied to soft matter samples.

Figure 4a shows a conventional STXM transmission image of region 2 of the two-layer model sample (see Figure 1), recorded at 694 eV using a 60 nm ZP. Figure 4b is the ptychography absorption image of the same region recorded at 694 eV. Figure 4c is a ptychography absorption image of this region at 684 eV below the onset of F 1s absorption. Two different morphologies are apparent in Figure 4b: one has an irregular polygon shape (indicated by yellow arrows) and the other is fuzzy with a spiral shape (indicated by red arrows).

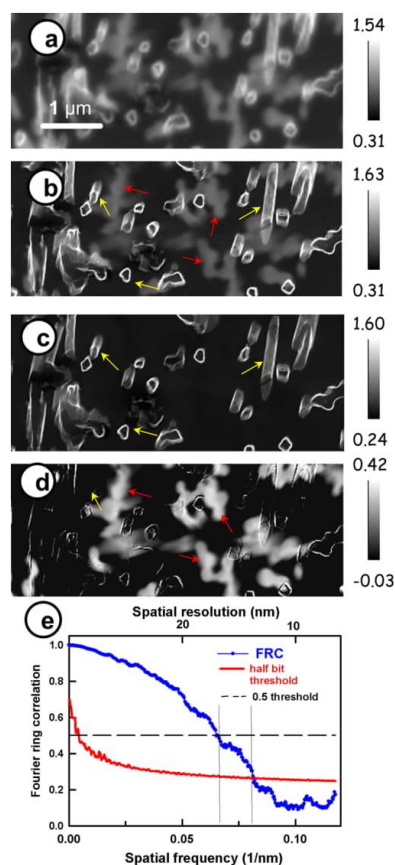


Figure 4. Images of the two-layer region of the bilayer model sample (see Figure 1). (a) STXM transmission image at 694 eV recorded using a ZP with 60 nm outer zone width. Ptychography absorption images at (b) 684 and (c) 694 eV. (d) Fluorine map obtained by taking the difference between ptychography absorption images at 694 eV (Figure 3b) and 684 eV (Figure 3c). (e) FRC analysis of spatial resolution of the ptychography fluorine map. The OD is indicated by a grayscale bar for each image. Yellow and red arrows denote the Pt shells and PTFE fibers, respectively (ALS, 5.3.2.1).

However, the pre-edge image (Figure 4c) only shows the irregular polygon shapes that are the platinum-coated graphite fibers which absorb at all X-ray energies. The lower contrast spiral-shaped structures are cross sections of the PTFE fibers because they are only observed at energies above the F 1s onset. Figure 4d is the difference between the two ptychographic absorption images at 694 eV (Figure 4b) and 684 eV (Figure 4c), which is a map of the fluorine, and thus the PTFE fibers in this region of the sample. Figure 4d also shows some residual signal at the edges of the Pt-coated graphite fibers, which probably is related to imperfect alignment. Figure 4e displays the FRC analysis of the fluorine map in Figure 4d. This analysis indicates a spatial resolution of 15 nm based on the 0.5 threshold or 12 nm based on the 1/2-bit threshold. Figures 2 and 4 clearly demonstrate that soft X-ray ptychography is capable of chemically imaging radiation-sensitive soft materials

with a spatial resolution higher than that provided by conventional STXM. Because PTFE and PFSA have similar radiation damage rates,¹⁹ this model sample study indicates that ptychography is able to characterize the distribution of PFSA in real fuel cell samples.

3.2. Spectro-Ptychography of an MEA CL. Figure S2 presents a STXM OD image at 694 eV (recorded with a 60 nm outer zone ZP) of the cathode region of an MEA. It consists of three regions: embedding epoxy (TTE, left), cathode CL (middle), and membrane (right). Because of the low-resolution ZP used (60 nm outer zone width, thus 72 nm diffraction-limited resolution), the morphology and structure of the cathode are poorly resolved in the conventional STXM image. Figure 5a,b shows ptychography absorption images at 684 and

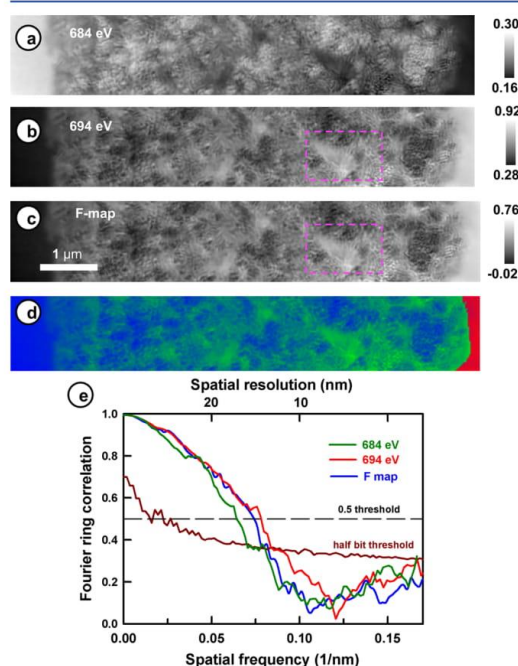


Figure 5. Ptychography absorption images of the MEA cathode (white rectangle in STXM image shown in Figure S3) (a) at 684 eV and (b) at 694 eV. (c) Fluorine map, image difference OD(694 eV) – OD(684 eV). (d) Color-coded composite of the membrane (red), ionomer (green), and carbon (support and epoxy) (blue). The membrane and ionomer maps are threshold masked extracts of the fluorine map. (Note that although the PFSA of the membrane and the PFSA of the ionomer are differentiated based on the signal intensity in this study, the membrane and cathode PFSA can be chemically different, leading to detectable differences in their C 1s and F 1s spectra.⁵¹) The carbon signal is derived from the image at 684 eV. (e) FRC analysis of the fluorine map (c). The OD is indicated by the grayscale bar at the right side of each image (ALS, 11.0.2).

694 eV, measured at the ALS 11.0.2 undulator beamline, of the rectangular region indicated in Figure S2. Figure 5c is the difference between Figure 5b and a, which maps the fluorine signal from PFSA in both the CL and the membrane. Note that the dark regions in the fluorine map (Figure 5c) correspond to the bright regions in Figure 5a, which are carbon-rich. The

PFSA ionomer in the CL (Figure 5c) has a “feather”-like morphology, illustrated by the region in the purple dashed rectangle in Figure 5b,c. Figure 5d is a color-coded composite of the F-map and the carbon support, with the latter derived from the pre-F 1s image and the F-map (carbon support = $OD_{684} - 0.21 \times \text{F-map}$).

The results of FRC analysis of the ptychography absorption images at 684 and 694 eV and the F 1s map are presented in Figure 5e. Table 2 summarizes the spatial resolution of these three images evaluated using the 1/2-bit and 0.5 threshold criteria, along with a visual estimate of the resolution derived from 20 to 80% intensity jumps at sharp interfaces. Generally, the spatial resolution determined with the 0.5 threshold is lower than that with the 1/2-bit threshold. At 684 eV, the resolution (mean of the two FRC criteria) is 15 ± 1 nm, while it is 13 ± 1 nm at 694 eV and for the fluorine map (PFSA). The resolution achieved for the fuel cell cathode is slightly improved relative to that achieved for the model sample, consistent with the stronger scattering ability of the Pt-coated carbon support particles.

A full stack⁵⁸ acquisition (33 energies from 681 to 710 eV) was also measured to explore spectro-ptychography of the CL at the F 1s edge. This provides a high-resolution probe of both the spectroscopy⁵¹ and spatial distribution of the PFSA ionomer in a real cathode CL sample. After reconstructing the ptychographic data for each image and converting the amplitude signal to absorption, the set of 33 OD images was aligned. The aligned stack was then processed using singular value decomposition (SVD)⁵⁹ to derive maps of the PFSA and the non-F-containing components. Figure 6 presents the component maps of the whole PFSA component (Figure 6a) including both the membrane and cathode, the map of only ionomer in cathode (PFSA in the CL, derived by threshold masking and subtracting the membrane signal) (Figure 6b), and the map of nonfluorinated components (Pt-decorated carbon support) (Figure 6c). Figure 6d is a rescaled color composite of the membrane (red), ionomer (green), and carbon support (blue) component maps. Each spot was measured for a total time of ~ 4 s (33×0.12 s) corresponding to an estimated total dose of 280 MGy. Because this is approximately 7 times higher than the critical dose for PFSA damage,¹⁹ PFSA was extensively damaged during the spectro-ptychography measurement. Figure 6e shows the F 1s spectrum of the membrane as measured by STXM after spectro-ptychography (red), compared to that measured prior to the spectro-ptychography (green), in both cases using a 1 ms/pixel dwell time which causes negligible damage. The ptychography data acquisition transforms the characteristic two-peak F 1s spectrum of undamaged PFSA (green in Figure 6e) into a single, broad, asymmetric peak. That change and the reduced F 1s continuum signal indicate a significant reduction of the total fluorine content in the PFSA component. As expected from other studies of radiation damage to PFSA,^{19,21} the spectrum, and thus the chemical structure, is significantly modified by the high X-ray dose used to perform spectro-ptychography. The F 1s edge jump ($OD_{710} - OD_{684}$) after is less than a quarter of that before the spectro-ptychography measurement, indicating that a significant amount of the PFSA has been lost and the remaining fluorine-containing material has been chemically modified. The dashed line in Figure 6e shows that the peak of the F 1s signal after ptychography is at an energy between those of the two peaks of undamaged PFSA, consistent with a disordered system without the well-defined $-(CF_2-CF_2)_n-$

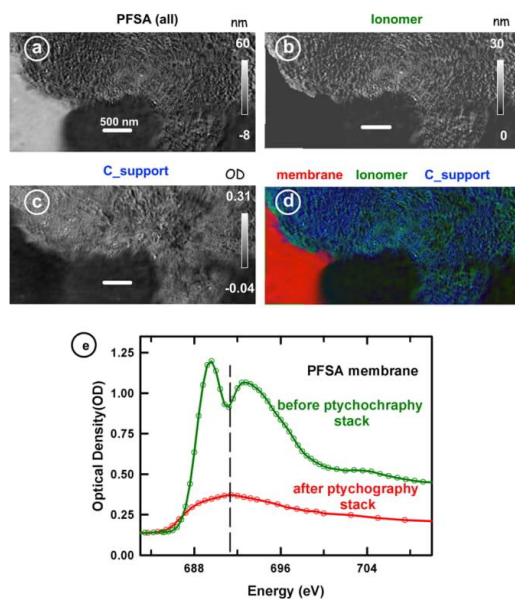


Figure 6. Ptychography F 1s edge full stack (33 energy points) of the fuel cell cathode CL, analyzed using a two-component SVD fit. (a) PFSA component map. (b) Ionomer map in the cathode region only, derived by subtracting the threshold masked membrane signal. (c) Map of nonfluorine components (mainly carbon support). (d) Color-coded composite of component maps of membrane (red), ionomer (green), and carbon support (blue). (e) F 1s spectra of the membrane region recorded before (green) and after (red) ptychography by low-dose (2 ms dwell) STXM. The dashed line indicates the position of the peak of the F 1s signal after the sample was damaged by the ptychography measurement. The intensity scales in (a,b) are nanometer thickness, based on a fit to the F 1s ptychography spectrum displayed in part (e) divided by 60 to match the F 1s continuum of the OD1 spectrum of undamaged PFSA. The intensity scale for (c) is the OD of the constant signal (ALS, 5.3.2.1).

regions which give rise to the characteristic F 1s $\rightarrow \sigma_{C-F}^*$ (\perp) and F 1s $\rightarrow \sigma_{C-F}^*$ (\parallel) transitions at 690 and 694 eV.⁵⁰ Here, σ_{C-F}^* (\perp) and σ_{C-F}^* (\parallel) refer to electronic bands aligned along and perpendicular to the C–C chain. The chemical structure of PFSA after high-dose X-ray damage is known to be able to resist further structural modifications.²⁰ The calculated radiation dose for the ptychography measurement at beamline 11.0.2 (results shown in Figure 5) is 45 MGy. This is similar to the critical dose for radiation damage to PFSA¹⁹ and will have caused about 50% fluorine loss.²¹ For the measurements using beamline 5.3.2.1 (Figures 6–8), the total dose was much larger. However, we find that after ~ 120 MGy, the fluorine loss rate slows considerably, and the remaining modified fluoropolymer is more stable.

3.3. Ptychographic Imaging: Two-Energy Ptychotomography of Ionomers. A PEMFC MEA sample with a thickness of ~ 150 nm was measured by two-energy F 1s ptychographic tomography. The tilt angle range was -57° to $+69^\circ$ with 9° increment. After alignment, conversion to OD, and generation of component maps for the ionomer and the carbon support at each tilt angle, the set of component maps at the 14 tilt angles was aligned and then reconstructed using the

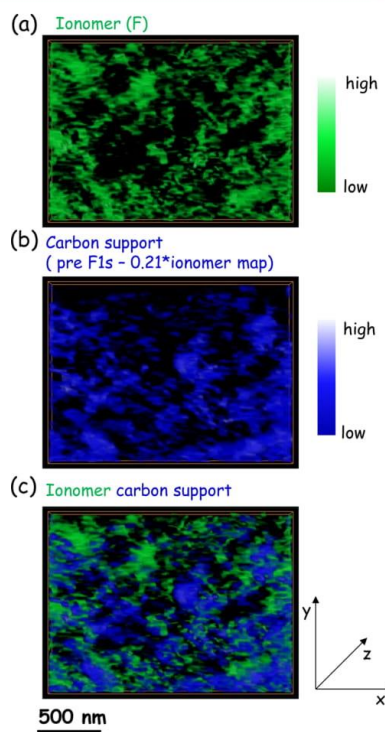


Figure 7. 4D imaging of the fuel cell cathode CL. Volume renderings of the 3D chemical structure of the cathode derived from a CS tomographic reconstruction of two-energy F 1s spectro-ptychotomography data. (a) Ionomer. (b) Carbon support. Threshold values for these renderings are 0.0023 for ionomer and 0.0031 for carbon support. (c) Color composite (ionomer in green, carbon support in blue) (ALS, 5.3.2.1).

CS method implemented in Mantis.⁵³ A β value of 0.1 and 50 iterations were used in the CS reconstruction. Figure 7 presents volume-rendered visualizations of the PEMFC cathode CL based on the ptychographic tomography F 1s stack maps. Figure 7a,b is 3D volume renderings of the ionomer (green, based on an Otsu threshold⁶⁰ of 0.0023) and carbon support (blue, based on an Otsu threshold of 0.0031), on relative color scales, while Figure 7c is a 4D image, that is, a volume rendering of the color composite of the two component volumes. Figure 8 shows three sets of color-coded composite slices in the yz (Figure 8a–c), xz (Figure 8d–f), and xy (Figure 8h–j) planes, which are sliced through the 3D volume at the planes indicated in Figure 8g. The volume fraction of the ionomer is 28%, and the volume fraction of the carbon support is 43%. There is significant overlap of these volume elements because of the finite spatial resolution and reconstruction uncertainty. The total solid fraction of the summed ionomer and carbon support volumes is 57%. Thus, the estimated porosity of the volume is 43%. The average thicknesses of the carbon support particles and PFSA strands are 40 and 22 nm, respectively. The carbon support component typically consists of agglomerations of ~ 50 nm diameter carbon black particles. The ionomer is believed to form a less than 10 nm thick conformal layer on carbon particles decorated with the Pt

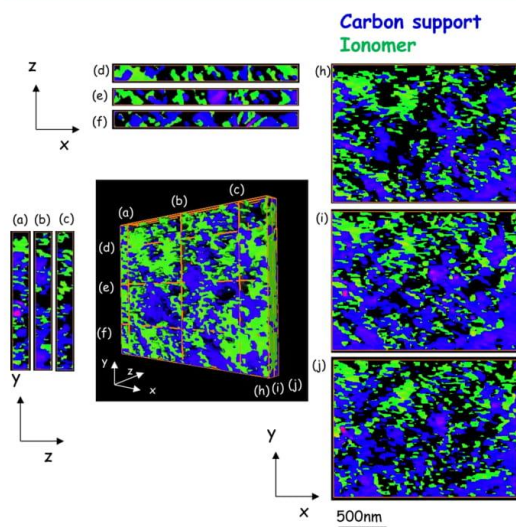


Figure 8. Multiple slices from the 3D rendered volume of the two components derived from F 1s spectro-ptycho-tomography. (a–c) In zy plane, (d–f) in xz plane, and (h–j) in xy plane. (g) indicates the position of each slice in the volume image. Threshold values for the slices are 0.0031 for the ionomer and 0.0023 for the carbon support. See Supporting Information for a movie with a detailed rendering and display of this 4D reconstruction (ALS, 5.3.2.1).

catalyst, but there is no definitive knowledge. Different CL formulation and processing affect both carbon support and ionomer components, resulting in different 4D distributions.²⁷ The spatial resolution of the spectro-ptycho-tomographic 4D imaging (component maps presented in Figure 7) is estimated to be 28 ± 9 nm (Figure 9a, Table 2), as evaluated by applying FRC to several different yz slices.

The F 1s spectrum of PFSA in the cathode after the spectro-ptycho-tomography measurement is shown in Figure 9b (red), compared to the spectrum from a fresh area of ionomer (green). The estimated total radiation dose used to perform the measurement was 320 MGy. At this high radiation dose, the two-peak spectral structure of undamaged PFSA was fully converted to a single peak and there was extensive fluorine loss. The increased pre-F 1s-edge signal indicates that there was also a significant carbon buildup during the measurement.

4. DISCUSSION

This study shows that the spatial resolution of X-ray imaging of soft materials such as PTFE and PFSA can be improved by soft X-ray ptychography. Chemically specific imaging with spectro-ptychography was achieved (Figures 5 and 6), a capability demonstrated in earlier measurements.^{41,61} The measurements at 11.0.2 beamline (Figure 5) exposed each pixel to only ~ 40 ms of X-ray beam. Because the ptychography imaging was performed with a larger beam diameter (70 nm rather than 30 nm), the ~ 40 ms exposure corresponds to ~ 10 ms of conventional STXM, an exposure which does minimal damage. Thus, even with the soft X-ray ptychography system used in this work, it was possible to obtain a scientifically valid high-resolution analysis of ionomers in a cathode CL. One limitation is that a direct-detect X-ray camera for photon energies below

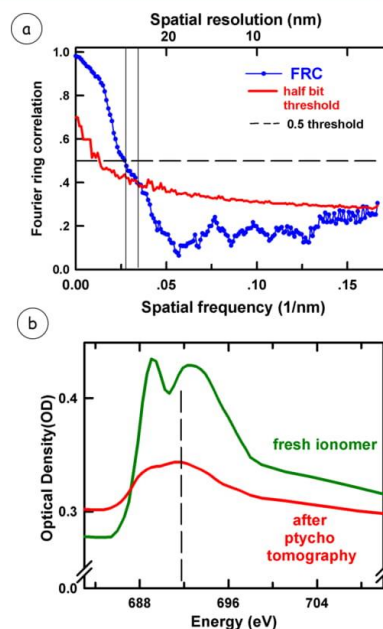


Figure 9. (a) FRC analysis of an yz slice of the 3D reconstruction of the ptycho-tomography PFSA component signal (Figure 8). (b) F 1s spectra of the cathode region extracted from a F 1s stack recorded by conventional STXM after the spectro-ptycho-tomography measurement. The spectrum of the area where ptycho-tomography was performed is in red, while the spectrum of fresh ionomer is in green. The dashed line indicates the position of the peak of the F 1s signal after ptychography (ALS, 5.3.2.1).

~ 500 eV does not exist yet. For best quality 4D imaging of cathodes, it is better to explicitly measure a spectral signal specific to the carbon support, which is usually determined from the difference of OD images measured at 285.1 eV ($C 1s \rightarrow \pi^*$ transition of the graphitic support) and 278 eV (pre-C 1s, dominated by Pt and F).^{26,27}

The improved spatial resolution and thus the potential of spectro-ptycho-tomography for 3D mapping ionomers in PEMFC cathodes were clearly demonstrated (Figures 7–9). As compared to conventional soft X-ray STXM tomography,^{21,53} the higher spatial resolution means there are more differentiable layers of signal in the z-direction (Figure 8). If the dose can be decreased, which seems feasible with a brighter source and thus larger coherence, then room-temperature 3D chemical imaging by spectro-ptycho-tomography will provide 3D ionomer maps, which can help PEM-FC CL optimization. Further improvements are possible if ptychography is performed at cryogenic temperatures to reduce the physical loss of fluorine. A new STXM with cryo-tomography capabilities for both STXM and ptychography has recently been developed at the Canadian Light Source.⁶²

5. CONCLUSIONS

Spectroscopic scanning CDI (spectro-ptychography) was used to image PFSA ionomers in PEMFC cathodes with a 2D spatial resolution better than 15 nm and a 3D spatial resolution better than 30 nm. At present, full spectro-ptychography and spectro-

ptycho-tomography require doses that cause significant radiation damage. However, improved instrumentation, such as the recently commissioned COSMIC⁶³ system at ALS, will reduce the dose required to the point where highly radiation-sensitive soft matter samples, such as PFSA ionomer, can be measured with an acceptable level of chemical and structural modification using few-energy spectro-ptychography mapping and few-tilt-angle spectro-ptycho-tomography.

■ ASSOCIATED CONTENT

■ Supporting Information

The Supporting Information is available free of charge on the ACS Publications website at DOI: 10.1021/acs.jpcc.8b02933.

Ptychography absorption difference compared to ptychography phase difference and STXM OD image of the same region of the sample measured by ptychography (PDF)

Color-coded combination of the renderings of the 3D reconstruction of the carbon support and ionomer derived from spectro-ptychographic tomography (MPG)

■ AUTHOR INFORMATION

Corresponding Author

*E-mail: aph@mcmaster.ca.

ORCID

Adam P. Hitchcock: 0000-0002-1598-7886

Notes

The authors declare no competing financial interest. The data that support the findings of this study are available from the corresponding authors upon reasonable request.

■ ACKNOWLEDGMENTS

We thank Mirna Lerotic (2nd Look consulting), who wrote the CS tomography software. Ptychography and STXM data were measured at beamlines 11.0.2 and 5.3.2.1 at the Advanced Light Source, which is supported by the Director of the Office of Science, Department of Energy, under contract no. DE-AC02-05CH11231. Some STXM data were also measured at the ambient STXM on the Canadian Light Source (CLS) beamline 10ID1. The CLS is supported by the Canadian Foundation for Innovation. Ptychography data analysis was performed using SHARP, which is supported by the Center for Applied Mathematics for Energy Research Applications (CAMERA), a partnership between Basic Energy Sciences (BES) and Advanced Scientific Computing Research (ASRC) at the US Department of Energy.

■ REFERENCES

- (1) Wang, Y.; Chen, K. S.; Mishler, J.; Cho, S. C.; Adroher, X. C. A Review of Polymer Electrolyte Membrane Fuel Cells: Technology, Applications, and Needs on Fundamental Research. *Appl. Energy* **2011**, *88*, 981–1007.
- (2) Gwak, G.; Ju, H. A Rapid Start-up Strategy for Polymer Electrolyte Fuel Cells at Subzero Temperatures Based on Control of the Operating Current Density. *Int. J. Hydrogen Energy* **2015**, *40*, 11989–11997.
- (3) Yoshida, T.; Kojima, K. Toyota MIRAI Fuel Cell Vehicle and Progress Toward a Future Hydrogen Society. *Interface Mag.* **2015**, *24*, 45–49.
- (4) Ji, M.; Wei, Z. A Review of Water Management in Polymer Electrolyte Membrane Fuel Cells. *Energies* **2009**, *2*, 1057–1106.
- (5) Xie, J.; Xu, F.; Wood, D. L.; More, K. L.; Zawodzinski, T. A.; Smith, W. H. Influence of Ionomer Content on the Structure and Performance of PEFC Membrane Electrode Assemblies. *Electrochim. Acta* **2010**, *55*, 7404–7412.
- (6) Eguchi, M.; Baba, K.; Onuma, T.; Yoshida, K.; Iwasawa, K.; Kobayashi, Y.; Uno, K.; Komatsu, K.; Kobori, M.; Nishitani-Gamo, M.; et al. Influence of Ionomer/carbon Ratio on the Performance of a Polymer Electrolyte Fuel Cell. *Polymers* **2012**, *4*, 1645–1656.
- (7) Gottesfeld, S.; Zawodzinski, T. A. *PFSA-Book. In Advances in Electrochemical Science and Engineering*; Alkire, R. C., Gerischer, H., Kolb, D. M., Tobias, C. W., Eds.; Wiley-VCH: Weinheim, Germany, 1997; p 195.
- (8) Li, Q.; He, R.; Jensen, J. O.; Bjerrum, N. Approaches and Recent Development of Polymer Electrolyte Membranes for Fuel Cells Operating above 100 C. *Chem. Mater.* **2003**, *15*, 4896–4915.
- (9) Holdcroft, S. Fuel Cell Catalyst Layers: A Polymer Science Perspective. *Chem. Mater.* **2013**, *26*, 381–393.
- (10) He, Q.; Kusoglu, A.; Lucas, I. T.; Clark, K.; Weber, A. Z.; Kosteckii, R. Correlating Humidity-Dependent Ionically Conductive Surface Area with Transport Phenomena in Proton-Exchange Membranes. *J. Phys. Chem. B* **2011**, *115*, 11650–11657.
- (11) Bass, M.; Berman, A.; Singh, A.; Konovalov, O.; Freger, V. Surface Structure of Nafion in Vapor and Liquid. *J. Phys. Chem. B* **2010**, *114*, 3784–3790.
- (12) Allen, F. I.; Comolli, L. R.; Kusoglu, A.; Modestino, M. A.; Minor, A. M.; Weber, A. Z. Morphology of Hydrated as-Cast Nafion Revealed Through Cryo Electron Tomography. *ACS Macro Lett.* **2015**, *4*, 1–5.
- (13) More, K.; Reeves, S. TEM Specimen Preparation of Partially-Embedded Electrodes From Proton Exchange Membrane Fuel Cell Membrane Electrode Assemblies. *Microsc. Microanal.* **2005**, *11*, 2104–2105.
- (14) Kusoglu, A.; Weber, A. Z. New Insights into Perfluorinated Sulfonic-Acid Ionomers. *Chem. Rev.* **2017**, *117*, 987–1104.
- (15) Yakovlev, S.; Balsara, N. P.; Downing, K. H. Insights on the Study of Nafion Nanoscale Morphology by Transmission Electron Microscopy. *Membranes* **2013**, *3*, 424–439.
- (16) Wang, C.; Krishnan, V.; Wu, D.; Bledsoe, R.; Paddison, S. J.; Duscher, G. Evaluation of the Microstructure of Dry and Hydrated Perfluorosulfonic Acid Ionomers: Microscopy and Simulations. *J. Mater. Chem. A* **2013**, *1*, 938–944.
- (17) Lin, J.; Wu, P.-H.; Wycisk, R.; Pintauro, P. N.; Shi, Z. Properties of Water in Prestretched Recast Nafion. *Macromolecules* **2008**, *41*, 4284–4289.
- (18) Lopez-Haro, M.; Guétaz, L.; Printemps, T.; Morin, A.; Escribano, S.; Jouneau, P.-H.; Bayle-Guillemaud, P.; Chandezon, F.; Gebel, G. Three-Dimensional Analysis of Nafion Layers in Fuel Cell Electrodes. *Nat. Commun.* **2014**, *5*, 5229.
- (19) Melo, L. G. A.; Botton, G. A.; Hitchcock, A. P. Quantification of the Critical Dose for Radiation Damage to Perfluorosulfonic Acid Membranes Using Soft X-Ray Microscopy. *Microsc. Microanal.* **2015**, *21*, 2443–2444.
- (20) Melo, L. G. d. A.; Hitchcock, A. P.; Jankovic, J.; Stumper, J.; Susac, D.; Berejnov, V. Quantitative Mapping of Ionomer in Catalyst Layers by Electron and X-Ray Spectromicroscopy. *ECS Trans.* **2017**, *80*, 275–282.
- (21) Wu, J.; Melo, L. G. A.; Zhu, X.; West, M. M.; Berejnov, V.; Susac, D.; Stumper, J.; Hitchcock, A. P. 4D Imaging of Polymer Electrolyte Membrane Fuel Cell Catalyst Layers by Soft X-Ray Spectro-Tomography. *J. Power Sources* **2018**, *381*, 72–83.
- (22) Hitchcock, A. P. Soft X-Ray Imaging and Spectromicroscopy. In *Handbook of Nanoscopy*; Van Tendeloo, G., Van Dyck, D., Pennycook, J. S., Eds.; Wiley, 2012; Vol. II, pp 745–792.
- (23) Hitchcock, A. P. Soft X-Ray Spectromicroscopy and Ptychography. *J. Electron Spectrosc. Relat. Phenom.* **2015**, *200*, 49–63.
- (24) Wang, J.; Botton, G. A.; West, M. M.; Hitchcock, A. P. Quantitative Evaluation of Radiation Damage to Polyethylene Terephthalate by Soft X-Rays and High-Energy Electrons. *J. Phys. Chem. B* **2009**, *113*, 1869–1876.

- (25) Lee, V.; Berejnov, V.; West, M.; Kundu, S.; Susac, D.; Stumper, J.; Atanasoski, R. T.; Debe, M.; Hitchcock, A. P. Scanning Transmission X-Ray Microscopy of Nano Structured Thin Fi Lm Catalysts for Proton-Exchange-Membrane Fuel Cells. *J. Power Sources* **2014**, *263*, 163–174.
- (26) Susac, D.; Berejnov, V.; Hitchcock, A. P.; Stumper, J. STXM Study of the Ionomer Distribution in the PEM Fuel Cell Catalyst Layers. *ECS Trans.* **2011**, *41*, 629–635.
- (27) Susac, D.; Berejnov, V.; Hitchcock, A. P.; Stumper, J. STXM Characterization of PEM Fuel Cell Catalyst Layers. *ECS Trans.* **2012**, *50*, 405–413.
- (28) Hitchcock, A. P.; Berejnov, V.; Lee, V.; West, M.; Colbow, V.; Dutta, M.; Wessel, S. Carbon Corrosion of Proton Exchange Membrane Fuel Cell Catalyst Layers Studied by Scanning Transmission X-Ray Microscopy. *J. Power Sources* **2014**, *266*, 66–78.
- (29) Epting, W. K.; Gelb, J.; Litster, S. Resolving the Three-Dimensional Microstructure of Polymer Electrolyte Fuel Cell Electrodes Using Nanometer-Scale X-Ray Computed Tomography. *Adv. Funct. Mater.* **2012**, *22*, 555–560.
- (30) Schneider, A.; Wieser, C.; Roth, J.; Helfen, L. Impact of Synchrotron Radiation on Fuel Cell Operation in Imaging Experiments. *J. Power Sources* **2010**, *195*, 6349–6355.
- (31) Eller, J.; Marone, F.; Büchi, F. N. Operando Sub-Second Tomographic Imaging of Water in PEFC Gas Diffusion Layers. *ECS Trans.* **2015**, *69*, 523–531.
- (32) Berejnov, V.; Susac, D.; Stumper, J.; Hitchcock, A. P. 3D Chemical Mapping of PEM Fuel Cell Cathodes by Scanning Transmission Soft X-Ray Spectroscopy. *ECS Trans.* **2013**, *50*, 361–368.
- (33) Hitchcock, A. P.; Toney, M. F. Spectromicroscopy and Coherent Diffraction Imaging: Focus on Energy Materials Applications. *J. Synchrotron Radiat.* **2014**, *21*, 1019–1030.
- (34) Schmid, G.; Obst, M.; Wu, J.; Hitchcock, A. 3D Chemical Imaging of Nanoscale Biological, Environmental, and Synthetic Materials by Soft X-Ray STXM Spectroscopy. In *X-ray and Neutron Techniques for Nanomaterials Characterization*; Kumar, C. S. S. R., Ed.; Springer: Berlin, 2016; pp 43–94.
- (35) Thibault, P.; Guizar-Sicairos, M.; Menzel, A. Coherent Imaging at the Diffraction Limit. *J. Synchrotron Radiat.* **2014**, *21*, 1011–1018.
- (36) Rodenburg, J. M.; Faulkner, H. M. L. A Phase Retrieval Algorithm for Shifting Illumination. *Appl. Phys. Lett.* **2004**, *85*, 4795–4797.
- (37) Pfeiffer, F. X-Ray Ptychography. *Nat. Photonics* **2018**, *12*, 9–17.
- (38) Miao, J.; Ishikawa, T.; Robinson, I. K.; Murnane, M. M. Beyond Crystallography: Diffractive Imaging Using Coherent X-Ray Light Sources. *Science* **2015**, *348*, 530–535.
- (39) Edo, T. B.; Batey, D. J.; Maiden, A. M.; Rau, C.; Wagner, U.; Pešić, Z. D.; Waigh, T. A.; Rodenburg, J. M. Sampling in X-Ray Ptychography. *Phys. Rev. A: At, Mol, Opt. Phys.* **2013**, *87*, 053850.
- (40) Shapiro, D. A.; Yu, Y.-S.; Tyliczszak, T.; Cabana, J.; Celestre, R.; Chao, W.; Kaznatcheev, K.; Kilcoyne, A. L. D.; Maia, F.; Marchesini, S.; et al. Chemical Composition Mapping with Nanometre Resolution by Soft X-Ray Microscopy. *Nat. Photonics* **2014**, *8*, 765–769.
- (41) Zhu, X.; Hitchcock, A. P.; Bazylinski, D. A.; Denes, P.; Joseph, J.; Lins, U.; Marchesini, S.; Shiu, H.-W.; Tyliczszak, T.; Shapiro, D. A. Measuring Spectroscopy and Magnetism of Extracted and Intracellular Magnetosomes Using Soft X-Ray Ptychography. *Proc. Natl. Acad. Sci. U.S.A.* **2016**, *113*, E8219–E8227.
- (42) Wise, A. M.; Weker, J. N.; Kalirai, S.; Farmand, M.; Shapiro, D. A.; Meirer, F.; Weckhuysen, B. M. Nanoscale Chemical Imaging of an Individual Catalyst Particle with Soft X-Ray Ptychography. *ACS Catal.* **2016**, *6*, 2178–2181.
- (43) Yu, Y.-S.; Kim, C.; Shapiro, D. A.; Farmand, M.; Qian, D.; Tyliczszak, T.; Kilcoyne, A. L. D.; Celestre, R.; Marchesini, S.; Joseph, J.; et al. Dependence on Crystal Size of the Nanoscale Chemical Phase Distribution and Fracture in Li_xFePO_4 . *Nano Lett.* **2015**, *15*, 4282–4288.
- (44) Bae, S.; Taylor, R.; Shapiro, D.; Denes, P.; Joseph, J.; Celestre, R.; Marchesini, S.; Padmore, H.; Tyliczszak, T.; Warwick, T.; et al. Soft X-Ray Ptychographic Imaging and Morphological Quantification of Calcium Silicate Hydrates (C – S – H). *J. Am. Ceram. Soc.* **2015**, *98*, 4090–4095.
- (45) Shi, X.; Fischer, P.; Neu, V.; Elefant, D.; Lee, J. C. T.; Shapiro, D. A.; Farmand, M.; Tyliczszak, T.; Shiu, H.-W.; Marchesini, S.; et al. Soft X-Ray Ptychography Studies of Nanoscale Magnetic and Structural Correlations in Thin SmCo_5 Films. *Appl. Phys. Lett.* **2016**, *108*, 094103.
- (46) Yu, Y.-S.; Farmand, M.; Kim, C.; Liu, Y.; Grey, C. P.; Strobbridge, F. C.; Tyliczszak, T.; Celestre, R.; Denes, P.; Joseph, J.; Krishnan, H.; Maia, F. R. N. C.; Kilcoyne, A. L. D.; Marchesini, S.; Leite, T. P. C.; Warwick, T.; Padmore, H.; Cabana, J.; Shapiro, D. A. Three-dimensional Localization of Nanoscale Battery Reactions Using Soft X-Ray Tomography. *Nat. Commun.* **2018**, *9*, 921.
- (47) Ade, H.; Hitchcock, A. P. NEXAFS Microscopy and Resonant Scattering: Composition and Orientation Probed in Real and Reciprocal Space. *Polymer* **2008**, *49*, 643–675.
- (48) Shapiro, D. A.; Celestre, R.; Denes, P.; Farmand, M. Ptychographic Imaging of Nano-Materials at the Advanced Light Source with the Nanosurveyor Instrument. *J. Phys.: Conf. Ser.* **2016**, *849*, 012028.
- (49) Marchesini, S.; Krishnan, H.; Daurer, B. J.; Shapiro, D. A.; Perciano, T.; Sethian, J. A.; Maia, F. R. N. C. SHARP: A Distributed GPU-Based Ptychographic Solver. *J. Appl. Crystallogr.* **2016**, *49*, 1245–1252.
- (50) Hitchcock, A. P. aXis2000 Is Written in Interactive Data Language (IDL). It Is Available Free for Non-Commercial Use from <http://unicorn.mcmaster.ca/aXis2000.html> (accessed Feb 21, 2018).
- (51) Yan, Z. B.; Hayes, R.; Melo, L. G. A.; Goward, G. R.; Hitchcock, A. P. X-Ray Absorption and Solid-State NMR Spectroscopy of Fluorinated Proton Conducting Polymers. *J. Phys. Chem. C* **2018**, *122*, 3233–3244.
- (52) Saghi, Z.; Divitini, G.; Winter, B.; Leary, R.; Spiecker, E.; Ducati, C.; Midgley, P. A. Compressed Sensing Electron Tomography of Needle-Shaped Biological Specimens - Potential for Improved Reconstruction Fidelity with Reduced Dose. *Ultramicroscopy* **2016**, *160*, 230–238.
- (53) Wu, J.; Lerotic, M.; Collins, S.; Leary, R.; Saghi, Z.; Midgley, P.; Berejnov, S.; Susac, D.; Stumper, J.; Singh, G.; et al. Optimization of Three-Dimensional (3D) Chemical Imaging by Soft X-Ray Spectro-Tomography Using a Compressed Sensing Algorithm. *Microsc. Microanal.* **2017**, *23*, 951–966.
- (54) Lerotic, M.; Mak, R.; Wirick, S.; Meirer, F.; Jacobsen, C. MANTIS: A Program for the Analysis of X-Ray Spectromicroscopy Data. *J. Synchrotron Radiat.* **2014**, *21*, 1206–1212.
- (55) Stalling, D.; Westerhoff, M.; Hege, H.-C. *Amira: A Highly Interactive System for Visual Data Analysis*; Zuse Institute Berlin, 2004.
- (56) Banterle, N.; Bui, K. H.; Lemke, E. A.; Beck, M. Fourier Ring Correlation as a Resolution Criterion for Super-Resolution Microscopy. *J. Struct. Biol.* **2013**, *183*, 363–367.
- (57) Saxton, W. O.; Baumeister, W. The Correlation Averaging of a Regularly Arranged Bacterial Cell Envelope Protein. *J. Microsc.* **1982**, *127*, 127–138.
- (58) Jacobsen, C.; Wirick, S.; Flynn, G. J.; Zimba, C. Soft X-Ray Spectroscopy from Image Sequences with Sub-100 nm Spatial Resolution. *J. Microsc.* **2000**, *197*, 173–184.
- (59) Koprinarov, I. N.; Hitchcock, A. P.; McCrory, C. T.; Childs, R. F. Quantitative Mapping of Structured Polymeric Systems Using Singular Value Decomposition Analysis of Soft X-Ray Images. *J. Phys. Chem. B* **2002**, *106*, 5358–5364.
- (60) Otsu, N. A threshold Selection Method from Gray-Level Histograms. *IEEE Trans. Syst. Man Cybern. B Cybern.* **1979**, *9*, 62–66.
- (61) Beckers, M.; Senkbeil, T.; Gorniak, T.; Reese, M.; Giewekemeyer, K.; Gleber, S.-C.; Salditt, T.; Rosenhahn, A. Chemical Contrast in Soft X-Ray Ptychography. *Phys. Rev. Lett.* **2011**, *107*, 208101.
- (62) Leontowich, A. F. G.; Berg, R.; Regier, C. N.; Taylor, D. M.; Wang, J.; Beauregard, D.; Geilhufe, J.; Swirsky, J.; Wu, J.; Karunakaran,

C.: et al. Cryo Scanning Transmission X-Ray Microscope Optimized for Spectrotomography. *Rev. Sci Instruments*, submitted.
(63) Shapiro, D.; Roy, S.; Celestre, R.; Chao, W.; Doering, D.; Howells, M.; Kevan, S.; Kilcoyne, D.; Kirz, J.; Marchesini, S.; et al. Development of Coherent Scattering and Diffractive Imaging and the COSMIC Facility at the Advanced Light Source. *J. Phys.: Conf. Ser.* **2013**, *425*, 192011.

Supplemental Information for
High resolution imaging of polymer electrolyte membrane fuel cell cathode
layers by soft X-ray spectro-ptychography

Juan Wu,¹ Xiaohui Zhu¹, Marcia M. West,² Tolek Tyliczszak,³ Hung-Wei Shiu,^{3,4} David
Shapiro,³ Viatcheslav Berejnov,⁵ Darija Susac,⁵ Juergen Stumper⁵ and Adam P.
Hitchcock^{1*}

1. Chemistry & Chemical Biology, McMaster University, Hamilton, ON Canada L8S 4M1
2. Electron Microscopy, Pathology, McMaster University, Hamilton, ON Canada L8N 3Z5
3. Advanced Light Source, Berkeley Lab, Berkeley, CA, USA 94720
4. National Synchrotron Radiation Research Center, Hsinchu, Taiwan, R.O.C. 30076
5. AFCC, 9000 Glenlyon Parkway, Burnaby, BC Canada V5J 5J8

J. Phys. Chem C

(*) corresponding author: aph@mcmaster.ca

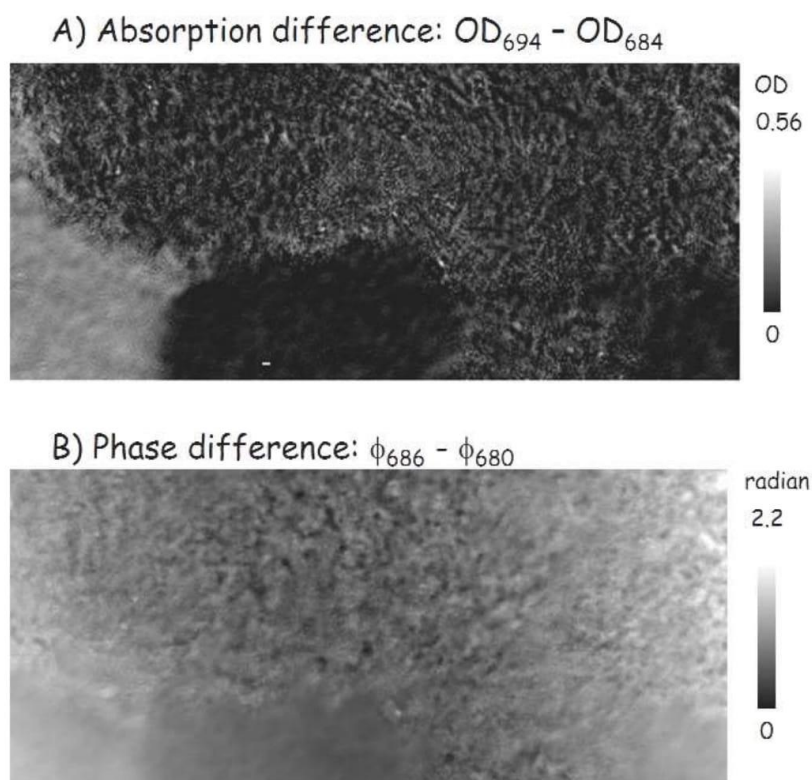


Figure S-1 (a) Ptychography absorption difference image ($OD_{694} - OD_{684}$). **(b)** Phase difference image (phase(686 eV) – phase(680 eV)) derived from the same ptychography stack data set.

Phase in the energy range just below onset of F 1s absorption gives contrast from the ionomer in the cathode.

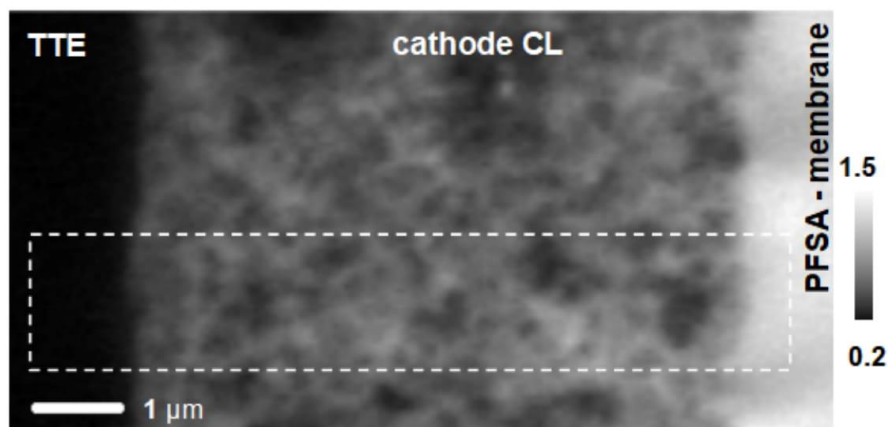


Figure S-2. STXM optical density image at 694 eV of the cathode region of a PEMFC membrane electrode assembly (MEA), recorded using a zone plate with 60 nm outer zone width. (ALS, 11.0.2)

Supplemental Movie *ptycho-PEMFC-SI-movie.mpg*

In addition to the movie of the reconstructed spectro-ptycho-tomography data set, renderings are given in Figures 7 and 8, while an evaluation of the 3D spatial resolution is given in Figure 9.

Chapter 7

4D Imaging of ZnO Coated Alumina Aerogels by Scanning Transmission X-Ray Microscopy and Ptychographic Tomography

This chapter presents the results of scanning transmission X-ray microscopy (STXM), STXM tomography, spectro-ptychography, and spectro-ptycho-tomography of Al₂O₃ aerogel samples coated with ZnO by atomic layer deposition. 2D and 3D spatial resolution was evaluated by Fourier ring correlation methods. Quantitative 4D images in the form of ZnO and Al₂O₃ 3D spatial distributions, and their correlations are reported. Comparisons are made to electron microscopy imaging of the same material. This work is a collaboration with Xiaohui Zhu, David A. Shapiro, Jonathan R. I. Lee, Tony Van Buuren, Monika M. Biener, Stuart A. Gammon, Tian T. Li, Theodore F. Baumann, and Adam P. Hitchcock. The synthesis of the sample and the morphology analysis by transmission electron microscopy images were provided by JRIL, TVB, MMB, SAG, TTL and TFB. XHZ wrote the python FRC code. The data was collected and analyzed by me, XHZ and APH. DAS helped with data collection and gave suggestions for data analysis and interpretation.

7.1 Introduction

Functional porous materials are attracting increasing attention for applications in energy conversion and storage, catalysis, and sensing (Biener et al. 2011a; Bagge-Hansen et al. 2014; Qiu et al. 2016). From the viewpoint of material development for these

applications, it is often preferable to introduce the desired functionality by creating a hetero-structured system in which a functional species (e.g. catalytic nanoparticle) is deposited on the inner surface area of a porous bulk substrate that is prepared by an existing and robust synthetic approach. This strategy can greatly simplify materials optimization in that structural properties of the porous support, such as mechanical stability, thermal stability, and architecture, can be tailored independently from the desired properties of the added functionality. A number of gas-phase and liquid-phase deposition techniques have been developed to uniformly distribute a desired functional material within a porous support material. These include atomic layer deposition (ALD) (Biener et al. 2011a; Ye et al. 2015; Biener et al. 2013), wet impregnation (Ge et al. 2014), galvanic replacement (Zhao et al. 2018), and electrodeposition (S. Yang et al. 2014). Previous work has demonstrated the utility of ALD on porous substrates to create functional hetero-structured materials with applications ranging from catalysis (King et al. 2008; Biener et al. 2011b) and energy storage (Ye et al. 2015), to laser-induced X-ray sources (Biener et al. 2013). Three dimensional (3D) characterization of the nanoscale structure and chemistry of these materials is of critical importance because it enables: (i) evaluation of synthetic pathways designed to generate heterostructures with targeted architectures and compositions; and (ii) correlation between their structure and performance, which, in turn, can inform the rational design of materials with enhanced properties and behavior.

Four-dimensional (4D) imaging - in this case, quantitative chemical mapping in 3D - is a powerful approach for material characterization (Torruella et al. 2016), which is often the key to fully understand the physical and chemical properties of hetero-structured systems. Recently there have been significant advances in 4D imaging. Electron

tomography in electron microscopy (ET) has been used to acquire the 3D structure of samples (Goris et al. 2014). Tilt series tomography has been combined with energy dispersive X-ray spectroscopy (EDS) (Slater et al. 2016) and electron energy loss spectroscopy (EELS) (Jarausch et al. 2009, Horl et al. 2013, Goris et al. 2014, Torruella et al. 2016, Wang et al. 2015a) to provide 4D characterization. These EM methods are extremely powerful and provide outstanding spatial resolution.

Synchrotron-based microscopies (Thibault et al. 2014), with variable incident photon energy or EDS detection, provide 4D imaging capabilities which complement EM methods, with certain advantages in terms of accessible sample thickness and ability to measure beam sensitive samples. Soft X-ray scanning transmission x-ray microscopy (STXM) characterizes electronic and chemical structure by imaging with near edge X-ray absorption fine structure (NEXAFS) spectral contrast at better than 30 nm spatial resolution (Hitchcock et al. 2012, Hitchcock et al. 2015). STXM provides more analytical information per unit radiation dose than TEM-EELS (Wang et al. 2009) or TEM-EDS (Melo et al. 2016) so it is particularly useful for characterizing radiation sensitive materials (Zhu et al. 2015). In order to perform 3D and 4D imaging by STXM, several methods have been developed, including laminography (Xu et al. 2012b), serial sectioning (Hitchcock et al. 2003), and tilt-series tomography (Schmid et al. 2014). Soft X-ray STXM tilt-series tomography on gold patterns was first performed at the STXM on the UV-ring of NSLS-I (Haddad et al. 1994). The first 4D soft X-ray STXM imaging (tomography at multiple photon energies) was a study of acrylate polyelectrolyte-filled polystyrene microspheres in water (Johansson et al. 2007). In recent years, STXM tomography has become a mature technique providing useful

information on environmental, biological, biogeochemical, and material science samples in both dry and wet conditions (Schmid et al. 2016; Hitchcock et al. 2003).

One of the limitations of soft X-ray STXM tomography is spatial resolution, typically 30-60 nm, which is much lower than EM tomography. The resolution is largely limited by the quality of zone plate focusing optics. Recent advances in zone plate fabrication have pushed the record spatial resolution for 2D imaging of high contrast test objects to sub-10 nm (Chao et al. 2012), but further progress in that direction seems to be very slow. For practical studies 4D soft X-ray STXM imaging only provides 25 nm spatial resolution at best.

Ptychography is a coherent diffraction imaging (CDI) technique (Miao et al. 2012), which has achieved spatial resolutions well below 10 nm in the soft X-ray region (Shapiro et al. 2014; Zhu et al. 2016). In addition, ptychography can be combined with tomography to produce high-resolution 3D nanostructure characterization. More information about ptychography was given in Chapter 2. This chapter reports a 4D spectro-ptychotomography study of two different samples of a model hetero-structured material, Al_2O_3 aerogels coated with nanoscale ZnO via ALD. Ptychographic images recorded at energies above and below the Zn L-edges enabled 4D spectro-ptycho-tomography to be successfully reconstructed. Direct comparison of these measurements with conventional STXM spectro-tomography data recorded on the same samples reveal dramatic improvements in spatial resolution. Comparisons to TEM imaging and EDS analysis of the same materials give valuable insights into the ALD of ZnO on alumina aerogels.

7.2 Materials and Methods

7.2.1 Samples

As mentioned in Chapter 2, samples for STXM and ptychography were prepared by two different methods. The sample made from water dispersion was labeled as **sample A**, and the sample made from FIB milling was labeled as **sample B**. **Table 7.1** summarizes properties of all samples for which we report results in this paper. Samples were prepared for TEM measurements by pressing copper grids against fragments of the ZnO-coated Al₂O₃ aerogels obtained via crushing with a scalpel blade.

Table 7.1 Sample and measurement details

CODE	Details	sample	Run	measure
A	6 cycle ALD	FIB cube	May 17 CLS aSTXM	STXM spectro-tomography at the Zn and Al edges Zn 2p, Al 1s spectra
B	25 cycle ALD	Cast from a water suspension	Nov 16 ALS 5321	Ptychographic Zn 2p spectro-tomography

7.2.2 Measurements

STXM measurements were carried out using the ambient STXM at beamline 10ID-1 at the Canadian Light Source (CLS) (Kaznatcheev et al. 2007). For conventional 2D STXM, a Al K edge stack with 91 images was recorded from 1546-1631 eV and a Zn L_{2,3}-edge stack with 105 images was recorded from 1006-1124 eV. For conventional STXM tomography measurements, images were collected at each angle for energies below and above absorption edges of Zn (1015 eV and 1055 eV for the Zn L-edge) and Al (1555 eV

and 1571 eV for the Al K-edge). In total, images were collected at 18 angles from 0° to 180° with a step size of 10° at each energy of interest.

7.2.3 Ptychographic tomography and reconstruction

Ptychographic measurements were carried out using Nanosurveyor I (Shapiro et al. 2016) at the 5.3.2.1 bending magnet beamline at the ALS. A zone plate (ZP) with outer zone width of 60 nm was used to illuminate the sample. The sample was raster scanned through the ~75 nm focus spot with a step size of 50 nm (~30 % overlap, possibly higher than the nominal geometric overlap since there is a lot of power outside of the central beam of the zone plate focus). The high-frame-rate CCD detector of Nanosurveyor I was used to record diffraction images with a single point exposure time of 150 ms. Ptychographic images were measured at energies below and above the Zn L₃-edge, at 1010 eV and 1026.8 eV respectively, from -65° to +65° with a step size of 10° (14 tilt angles). The ptychography measurements were only performed at the Zn L-edge because the coherent flux on the beamline 5.3.2.1 bend magnet is low at the Al K edge (1570 eV) energy, and a Si bright field filter, used to allow a single time exposure, was overly transparent at the Al K-edge energy. At each energy point and tilt angle, the camera background signal is measured with the beamline shutter closed, and the background is removed in subsequent data processing (Farmand et al. 2017; Shapiro et al. 2014). Ptychographic images were reconstructed using 500 iterations of the relaxed averaged alternating reflection (RAAR) reconstruction algorithm implemented in the SHARP ptychography code developed by the Center for Applied Mathematics for Energy Research Applications (Marchesini et al. 2016).

The spatial resolution of both STXM and ptychography was evaluated by Fourier ring correlation (FRC) analysis. Images or slices from the reconstruction were split into two subsets using even and odd pixel indices to generate two independent images. The FRC was calculated between the two images as described in (Banterle et al. 2013).

7.2.4 Tomographic reconstruction

Energy image alignment was usually done using the ‘Zimba’ routine in aXis2000. For the ptychographic tomography measurements, further alignment of energy images using an auto affine transformation in ImageJ (Thevenaz et al. 1998) has been done to correct for image distortion. The STXM chemical maps at each tilt angle were generated as the difference of the aligned 2-energy OD images. For ptychography, the ZnO map was generated as the difference of ptychographic absorption images below (1015 eV) and in the Zn L edge (1026.8 eV). For the ptychographic data, an Al₂O₃ map at each angle was derived from the pre-Zn edge OD image, by subtracting 69 % of the ZnO map, to correct for the absorption at 1010 eV by ZnO. Alignment of the angle stacks for different components was done manually in axis2000.

A compressed sensing (CS) algorithm (Wu et al. 2017) was used for the tomographic reconstruction. The version used is based on the FISTA code for total variation (TV) (Beck and Teboulle 2009) which is implemented in the Mantis analysis package (Lerotic et al. 2014). CS reconstruction methods are more robust than alternatives such as the simultaneous iterative reconstruction technique (SIRT), which allowed us to greatly reduce the number of tilt angles measured, while obtaining excellent reconstruction quality (Beck and Teboulle 2009). The motivation for developing CS methods for tomography was to reduce the overall radiation dose and thus allow tomography of

radiation sensitive materials (Beck and Teboulle 2009). Although the metal oxide aerogel system in this study is relatively resistant to radiation damage, it is important to note that the total measurement time was dramatically reduced via use of CS, which is significant because STXM-tomography and ptycho-tomography are relatively slow methods. The 18 angle, 4 energy STXM tomography measurement of FIB aerogel sample A took 20 hours while the 14 angle, 2-energy ptychography tomography measurement of aerogel sample B took 9 hours.

7.3 Results

7.3.1 Spectroscopy of the aerogel samples

Figure 7.1a presents the Zn $L_{2,3}$ X-ray absorption spectrum (XAS) of a ZnO/Al₂O₃ aerogel (**sample A**), prepared by focused ion beam (FIB) milling. Details of the sample and measurements are given in **Table 7.1**. The inset shows an expansion of the L_3 region. In the Zn²⁺ ground state the 3D orbital is fully occupied so the lowest unoccupied Zn levels are 4s, followed by 4p and 4d (Chen et al. 2011). Therefore, the lowest energy features of the Zn L_3 XAS correspond to Zn $2p_{3/2} \rightarrow 4s$ excitations. Peak A is attributed to Zn $2p_{3/2} \rightarrow 4s$ excitations while peaks B and C are Zn $2p_{3/2} \rightarrow 4d$ excitations (Yuste et al. 2012; Wang et al. 2015b; Cho et al. 2010). **Figure 7.1b** presents the Al K XAS of the FIB ZnO/Al₂O₃ aerogel sample. The inset shows an expansion of the Al K edge. The Al K XAS of the aerogel is similar to that of the θ phase of Al₂O₃ (Kato et al. 2001). It has three distinct features, shoulder A at 1566 eV, peak B at 1568 eV and peak C at 1572 eV, which are assigned to excitations associated with the tetrahedral AlO₄ (A) and octahedral AlO₆ (B,C) local coordination environments (Cabaret et al. 1996; Kato et al. 2001). The intensity scales of the Zn L-edge and Al K-edge spectra in Fig. 7.1 are quantitative, with their vertical scale

expressed in terms of optical density per nm thickness. This was established by matching the pre- and post-edge intensities to that predicted for the elemental compositions from standard tabulations (Henke, Gullikson, and Davis 1993), and the density of the bulk materials ($\text{ZnO } d= 5.61 \text{ g/cm}^3$; $\text{Al}_2\text{O}_3, d= 3.95 \text{ g/cm}^3$).

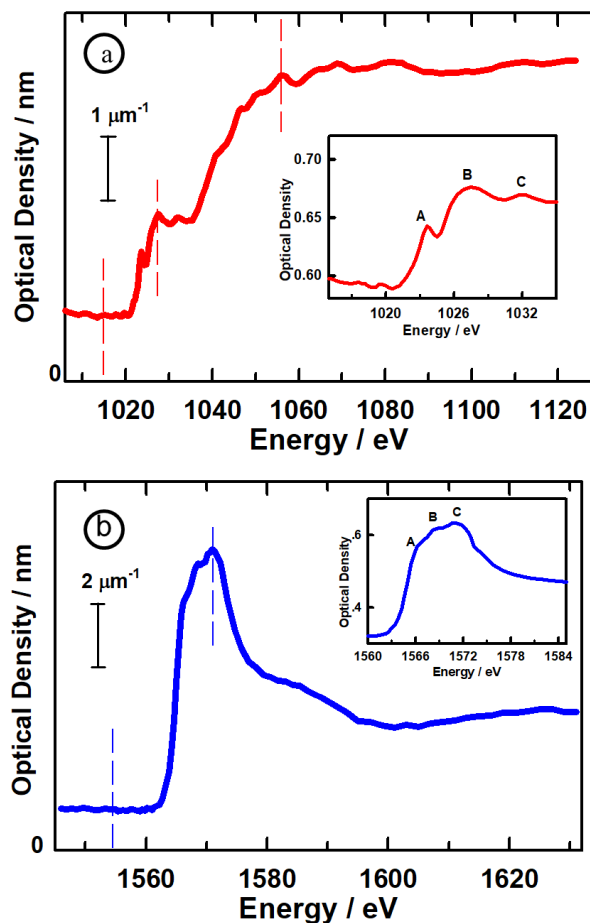


Figure 7.1 (a) X-ray absorption spectra (XAS) of ZnO/Al₂O₃ aerogel (**sample A**). (a) Zn L_{2,3} edge, converted to optical density per nm (OD1). The inset shows an expanded view of the near edge L₃ region. (b) Al K edge, converted to optical density per nm (OD1). The inset shows an expanded view of the near edge.

A two energy stack map was used to measure the Zn and Al distributions in the ZnO/Al₂O₃ aerogel sample. **Figure 7.2a, 7.2b** present 2D maps of the ZnO and Al₂O₃ derived from the difference between aligned and OD-converted STXM images at 1055/1015 eV (Zn), and 1571/1555 eV (Al). The gray scale in Figs. 2a, and 2b indicate the thickness in nm, determined by taking the ratio of the difference in OD at the above and below-edge energies, to that of the difference in the OD1 values at the same 2 energies (see **Fig. 7.1**), where OD1 is the OD of ZnO or Al₂O₃ at standard density and a thickness of 1 nm. **Figure 7.2c** is a re-scaled color composite of the ZnO (red) and Al₂O₃ (blue) stack maps in Figure 7.2a and 7.2b, which presents the spatial correlation of these two elements. If both species were uniformly distributed over the whole of the FIB section all pixels would be a uniform shade of purple, since the sample is very thick (~20 μm) and thus has many overlapping regions. In fact, the lower part of the section is predominantly blue, indicating substantial ion beam depletion of the Zn in the FIB sample preparation.

7.3.2 Conventional STXM spectro-tomography of ZnO/Al₂O₃ aerogel, sample A

Figure 7.3 presents results from 4D STXM imaging of the FIB prepared ZnO/Al₂O₃ aerogel, **sample A**, in the form of volume renderings of the Zn and Al 3D maps. The voxel size is 40 nm. The blue color is Al₂O₃, and the red color is ZnO. **Fig. 7.3a** and **Fig. 7.3b** are the front view while **Fig. 7.3c** and **7.3d** are the top view. When examining the two 3D chemical maps from the front view (**Figs. 7.3a, 7.3b**), one observes that the bottom and right edges of the sample are heavily damaged in terms of depletion of ZnO, which was caused by the FIB milling. A similar situation is seen in **Figs. 7.3c and 7.3d**, where ZnO depletion damage is evident at the top and bottom. The 4D chemical representation (**Fig.**

7.3e) clearly shows the spatial correlation of the two chemical maps, and the zones of mass loss of ZnO. The relatively large scale of the sample required extensive milling to obtain the desired sample size. The porous structure of the aerogel allowed energetic ions in the FIB process to penetrate into the interior of the structure. As a result, ZnO relatively far from the milling surface was damaged.

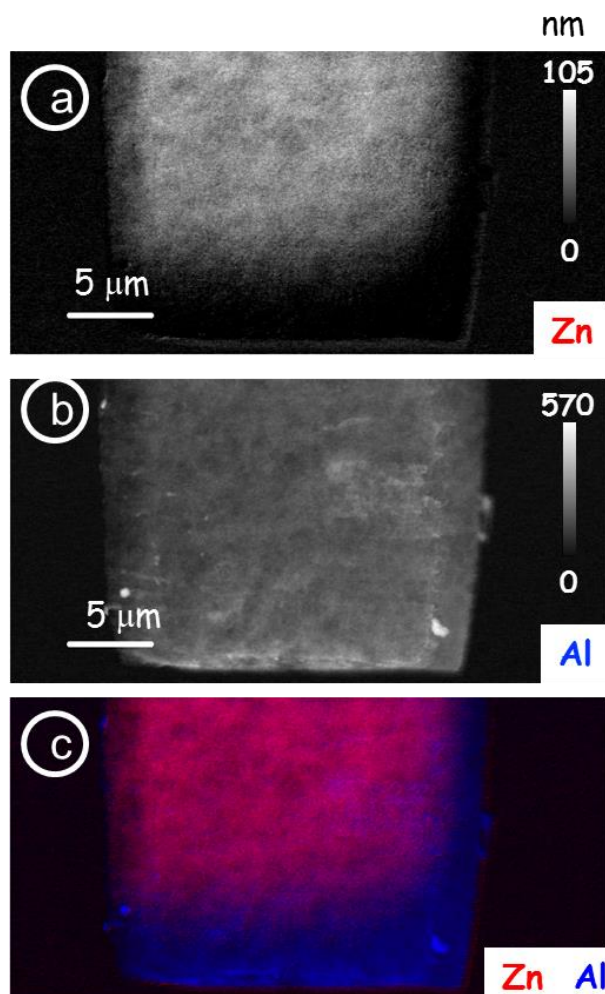


Figure 7.2 STXM 2D chemical maps at 0° tilt angle of a ZnO/Al₂O₃ aerogel (**sample A**).
(a) Al₂O₃. (b) ZnO. (c) color coded composite map of Al₂O₃ (blue), ZnO (red).

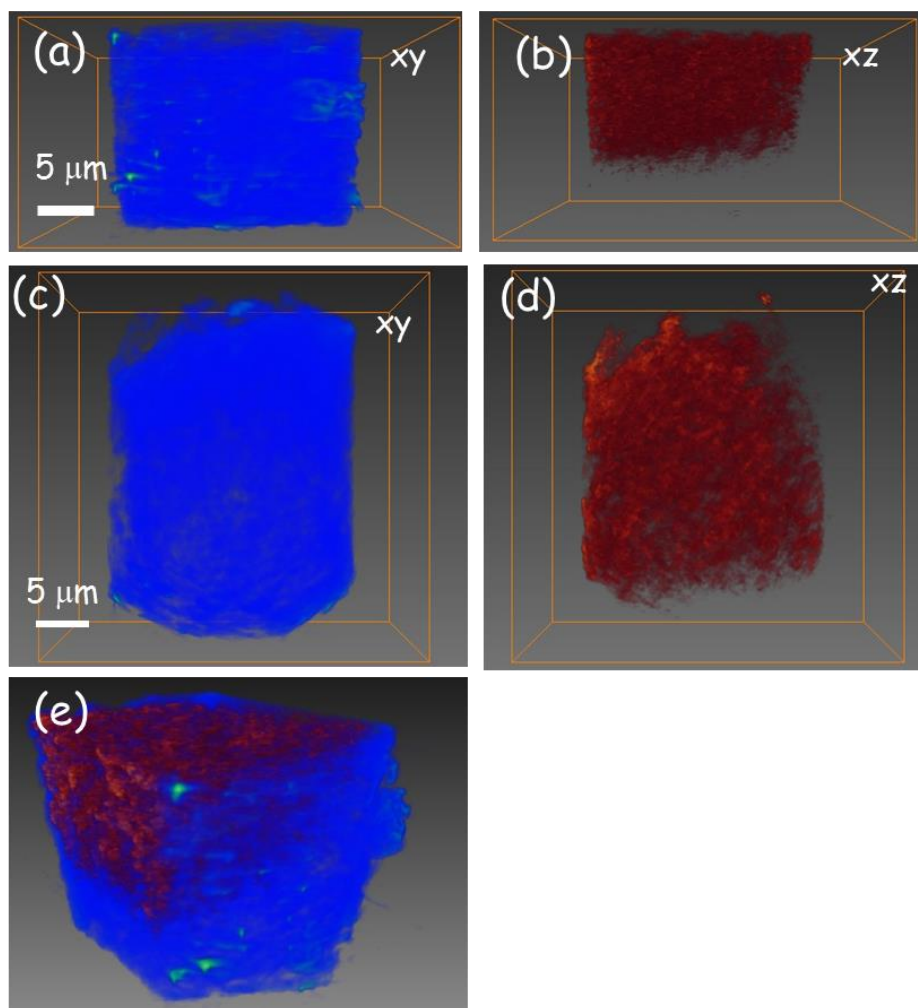


Figure 7.3 STXM spectro-tomography derived, 3D volume rendering of Al₂O₃ (blue) and ZnO (red) in the ZnO/Al₂O₃ aerogel FIB **sample A**. (a, b) xy views. (c,d) xz views. (z is direction of X-ray beam). (e) 4D image, a color coded composite of the two components with Al₂O₃ in blue and ZnO in red. Otsu threshold for ZnO is 0.0004, for Al₂O₃ is 0.0001.

Figure 7.4a shows a surface rendering of the center ($5\ \mu\text{m} \times 5\ \mu\text{m} \times 5\ \mu\text{m}$) volume of the FIB sample, a region where there appears to be negligible ion beam damage. Red in **Fig. 7.4a** indicates ZnO, selected using an Otsu threshold of 0.0004, while blue represents Al₂O₃ selected using an Otsu threshold of 0.0001. For comparison, the voxel intensity range of the region shown in **Fig. 7.4** runs from 0.0000 to 0.0015 for ZnO and 0.0000 to 0.0019

for Al_2O_3 . In order to quantitatively evaluate the distributions of Al_2O_3 and ZnO in the composite, the relative elemental concentration (REC) (Yang et al. 2014) of Al_2O_3 and ZnO in the aerogel was calculated as a function of distance from the sample surface (xy). Here, the REC is defined as the ratio of the amounts of the species (Al_2O_3 or ZnO) relative to that of the sum of all species ($\text{Al}_2\text{O}_3 + \text{ZnO}$). **Figure 7.4b** plots the relative elemental concentration of only Al_2O_3 (blue), only ZnO (red), and both ZnO and Al_2O_3 ('colocalization', green) as a function of the distance across the central $(5 \mu\text{m})^3$ volume. While the Al_2O_3 spatial distribution is relatively uniform and unstructured, that of the ZnO shows larger spatial variations in the REC, which suggests that much of the ZnO is present as "de-localized" nanoclusters rather than a conformal thin film. This interpretation is confirmed by complementary TEM and TEM-EDS measurements (see below). Nevertheless, the distribution of the two components generally follows the same trend, indicating a significant uniformity of the aerogel sample prepared via ALD, on the ~ 30 nm spatial scale of STXM spectro-tomography.

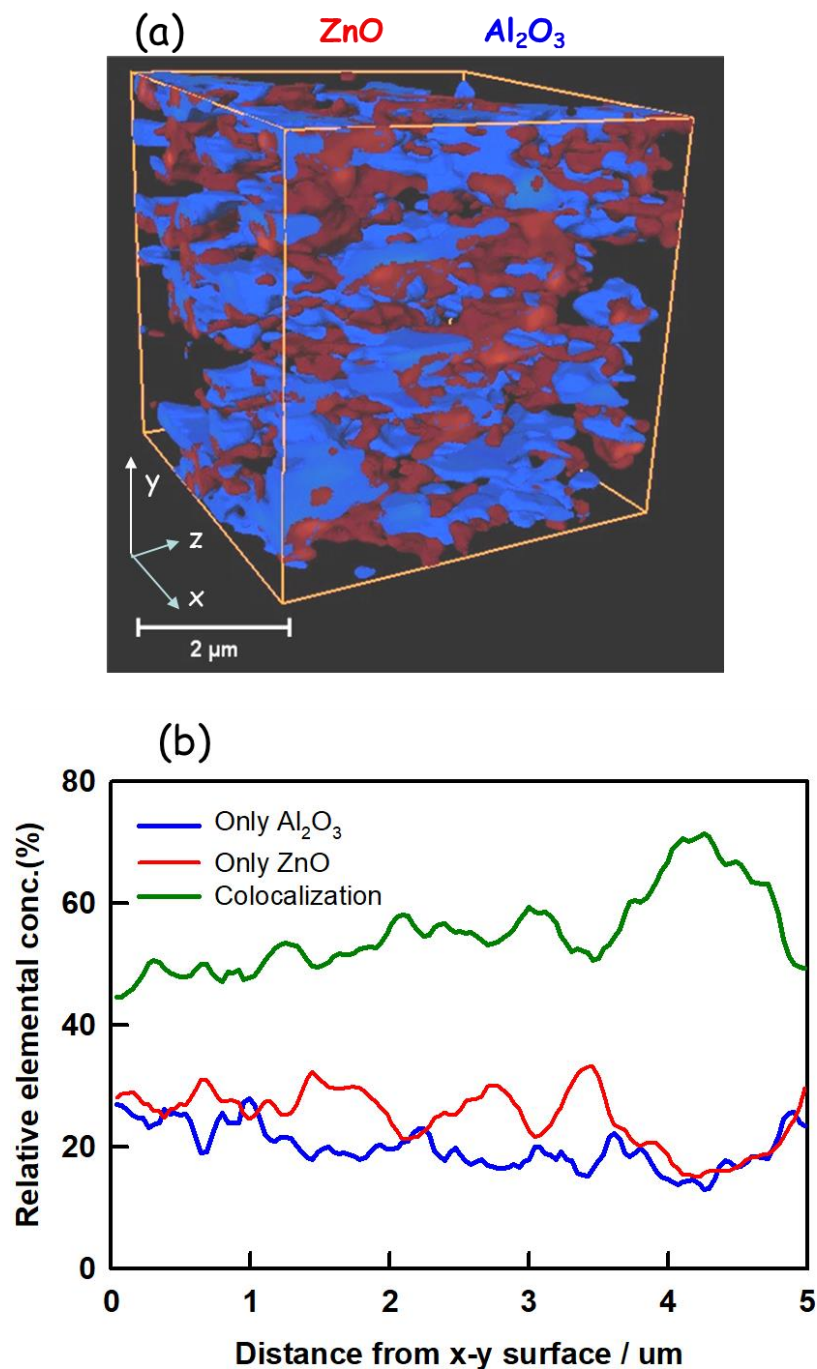


Figure 7.4 (a) Surface rendering of color coded composite of the ZnO (red) and Al₂O₃ (blue) 3D distributions from reconstruction of STXM spectro-tomography on ZnO/Al₂O₃ aerogel (**sample A**), in a 5*5*5 μm³ cube from the center of Fig. 3 (e). (b) Relative elemental concentration (REC) curves of the two components derived for xy slices averaged through the z direction. Otsu threshold for ZnO is 0.0004, for Al₂O₃ is 0.0001.

7.3.3 Spectro-ptychography and spectro-ptycho-tomography of ZnO/Al₂O₃ aerogel

Figure 7.5a and **7.5b** show the ptychography 2D absorption images of the ZnO/Al₂O₃ aerogel, **sample B**, at 1010 eV and 1026.8 eV, which correspond to the pre-edge and Zn L₃ absorption resonance energy of ZnO (see **Fig. 7.1a**). The ptychography absorption image is generated from $-\ln(A_{py}/I_o)$, where A_{py} is the amplitude of the reconstruction of a 2D ptychographic image and I_o is the incident photon intensity. **Figure 7.5c** is the ZnO distribution in the ZnO/Al₂O₃ sample, derived from the difference between the ptychography absorption images in **Fig. 7.5a** and **7.5b**. The Al₂O₃ distribution was extracted from the pre-edge signal at 1010 eV by subtracting the ZnO signal [OD(1026.8) – OD(1010)], weighted by 0.17 from OD 1010 eV. The factor of 0.68 is the ratio [OD(1026.8) – OD(1010)]/OD(1010) for ZnO (see **Fig. 7.1**). This estimate of the Al₂O₃ signal is presented in **Fig. 7.5d**. **Figure 7.5e** is a scaled color composite of the ZnO (red) and estimated Al₂O₃ (blue) signals in the ZnO/Al₂O₃ aerogel sample. The purple colored pixels correspond to columns where there is both ZnO and Al₂O₃. The existence of relatively pure red and blue areas, in addition to purple, indicates there is a non-uniform coating of ZnO. However, 3D maps of the two chemical components are needed to determine if the ZnO and Al₂O₃ are in contact, or are spatially separated and only accidentally at the same point of the 2D image.

Figure 7.6a and **7.6c** shows the projection at -5° tilt angle of the reconstructed 3D images of ZnO and Al₂O₃ respectively. These regenerated 2D chemical images can be directly compared to the 2D projection chemical maps of ZnO and Al₂O₃ at about the same tilt angle, displayed in **Fig. 5c** and **Fig. 5d**. The difference between the 2D chemical maps and the projections at the same tilt angle from the 3D reconstruction are presented as **Fig.**

7.6b and **Fig. 7.6d**. The results indicate a good match of the reconstruction especially for Al_2O_3 . For ZnO the difference may be related to spatial distortion of the sample in the ptychography images, caused by the high dose used.

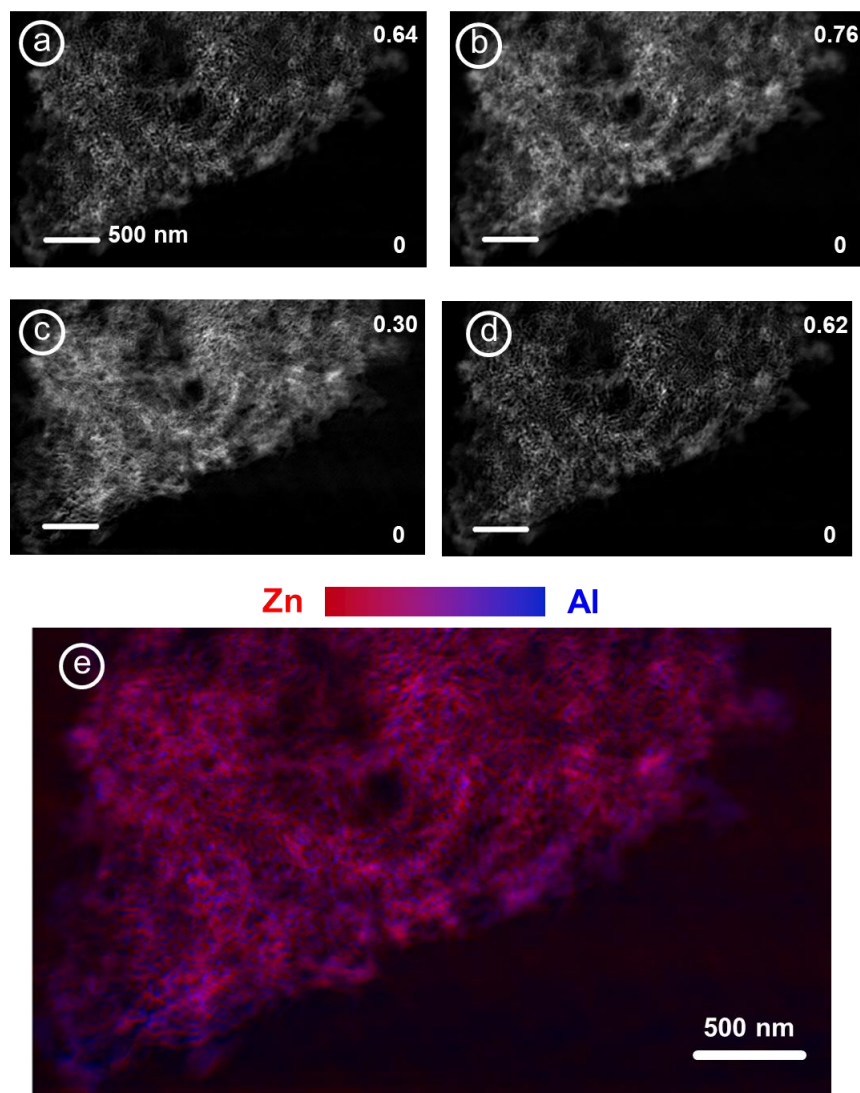


Figure 7.5 Ptychography absorption images of ZnO/ Al_2O_3 aerogel (**sample B**) at (a) 1010 eV, (b) 1026.8 eV. (c) ZnO chemical map ($\text{OD}(1026.8 \text{ eV}) - \text{OD}(1010 \text{ eV})$). (d) Derived Al_2O_3 chemical map (see text). (e) 4D image color composite of the two component maps, ZnO in red, Al_2O_3 in blue.

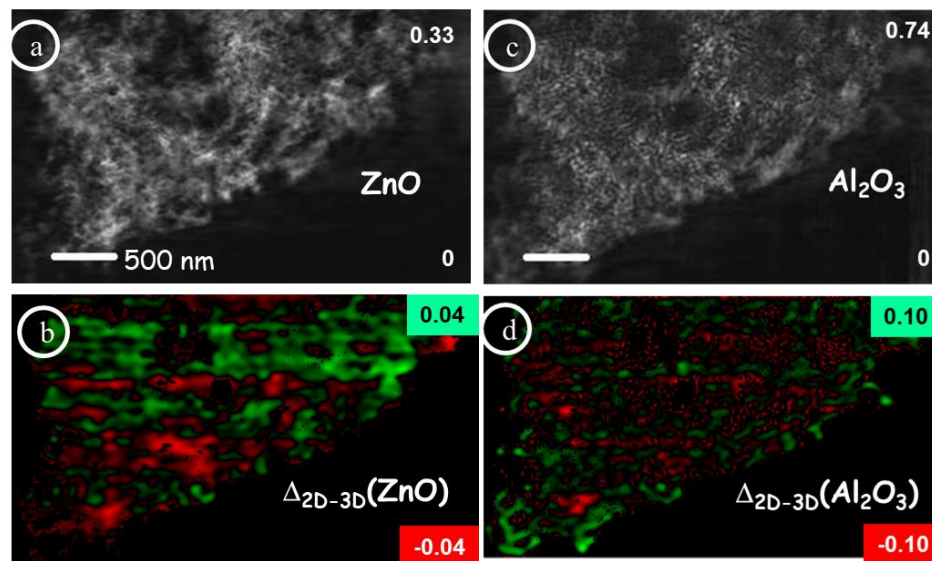


Figure 7.6 Check on precision of the reconstruction of the ptychographic tomography data set (**sample B**). (a) 2D map of ZnO derived from ptychography images at 1010 eV and 1026.8 eV, at -5° tilt angle. (b) Difference between the 2D ZnO map and that generated from the reconstruction of the ptychographic stack map tomography data at -5° (green is +ve and red is -ve difference). (c) 2D map of Al_2O_3 at 5° tilt angle, derived from the ptychography image at 1010 eV, corrected for ZnO contribution (see main text). (d) Difference between the 2D Al_2O_3 map and that generated from the reconstruction of the ptychographic stack map tomography data at -5° (green is +ve and red is -ve difference). Note the change in scales from the 2D maps (a,c) to the difference signals (b,d).

Figure 7.7 shows surface renderings of the compressed sensing (CS) reconstruction of the 3D distributions of Al_2O_3 and ZnO derived from the spectro-ptycho-tomography measurement of the irregular water cast **sample B**. Thresholds of 0.0018 (Al) and 0.0026 (Zn), derived using the Otsu auto threshold procedure (Otsu 1975) were used to derive these distributions. For comparison, the voxel intensity ranges of the region shown in Fig. 7.4 runs from 0 to 0.0103 for Al_2O_3 and 0 to 0.011 for ZnO. With the high spatial resolution provided by spectro-ptycho-tomography, the Al_2O_3 and ZnO spatial distributions are more clearly defined than with STXM tomography (**Fig. 7.4**). The overall morphology

is generally very similar, indicating that the ZnO is attached to the Al₂O₃ aerogel framework. However the ZnO distribution is clearly ‘clumpier’, suggesting less uniform distributions and a non-uniform coating of the Al₂O₃ framework by the ZnO ALD.

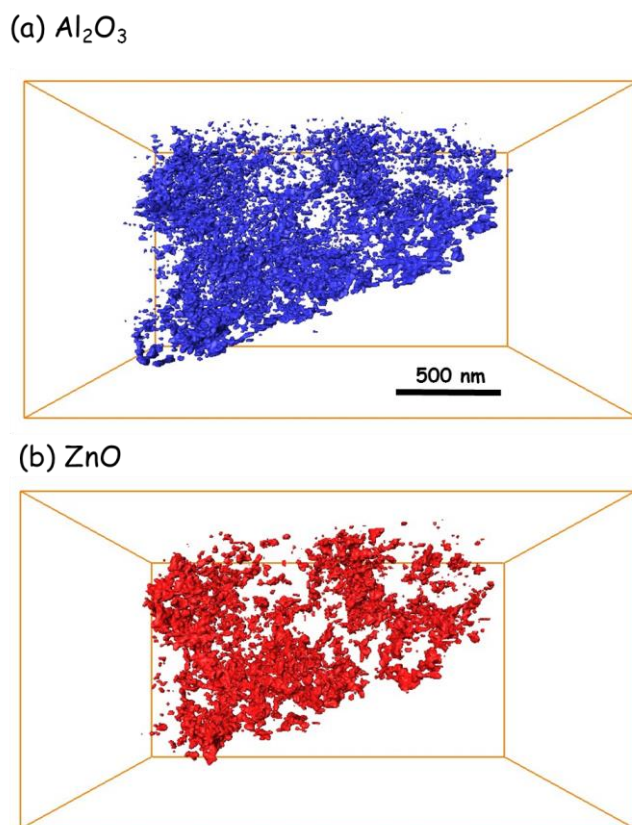


Figure 7.7 3D surface rendering of ZnO and Al₂O₃ from ptychography of ZnO/Al₂O₃ aerogel (**sample B**). View at 0° of (a) Al₂O₃ (blue), derived from the signal at 1010 eV minus 17 % of the ZnO signal. (b) ZnO (red) (OD(1026.8 eV) – OD(1010 eV)). The voxel size is (5.6*5.6*5.6) nm³. The Otsu thresholds used were 0.0018 for the Al₂O₃ signal and 0.0026 for the ZnO signal.

The results of Fourier Ring Correlation (FRC) evaluation of spatial resolution of the 2D ptychography stack maps (**Figs. 7.5c & 7.5d**) are displayed in **Fig. 7.8**. For the ZnO ptychographic stack map (**Fig. 7.5c**), the FRC analysis (red, **Fig. 7.8**) indicates a spatial resolution of 16.7 nm, using the 0.5 threshold (dashed black line, **Fig. 7.8**), or 14.6 nm if

the conventional half-bit threshold (dark red line, **Fig. 7.8**) is used. For the Al₂O₃ ptychographic stack map (**Fig. 7.5d**), the FRC analysis (blue, **Fig. 7.8**) indicates a spatial resolution of 15.4 nm (0.5 threshold), or 13.7 nm (1/2-bit threshold). In other evaluations of the spatial resolution of ptychography using Nanosurveyor I on beamline 5.3.2.1, the resolution is typically higher on resonance than off-resonance, whereas the opposite is the case for this data. The similarity of the estimated resolution evaluated from off- and on-resonance images suggests that this type of aerogel sample is a special case because it has a nano-structure which diffracts strongly at all photon energies so it is really ideal for ptychographic imaging. Compared with the ZnO and Al₂O₃ stack maps measured with conventional STXM (**Fig. 7.2a, 7.2b** for 2D, and **Fig. 7.4a** for 3D), it is clear that the spatial resolution of the ptychography maps and 3D spectro-ptycho-tomography 4D imaging is significantly higher than that of the corresponding STXM results.

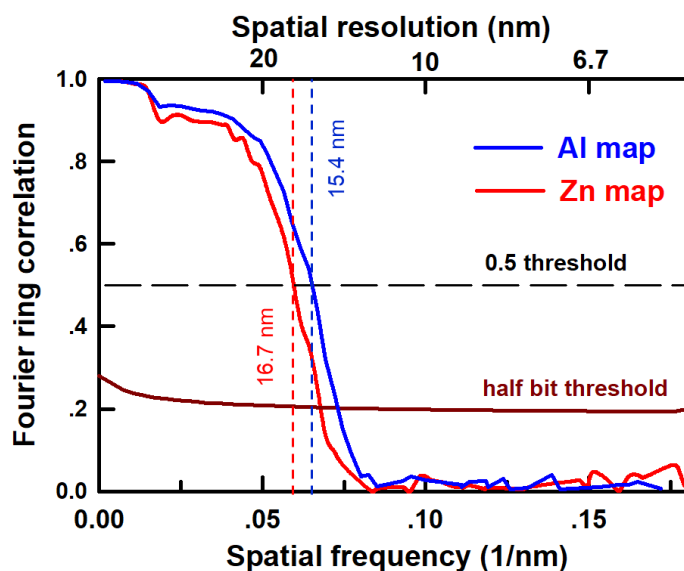


Figure 7.8 Spatial resolution estimated from Fourier Ring Correlation (FRC) of the ZnO and Al₂O₃ ptychography maps (Figs. 5c and 5d). (**sample B**).

In order to further evaluate the structural properties of the $\text{Al}_2\text{O}_3/\text{ZnO}$ composite, the distributions of the thickness of Al_2O_3 and ZnO were quantified from the tomography results using the open source ‘Bone J’ plugin in Image J software (Doubé et al. 2010). This software first measures the distance of each solid voxel to the nearest empty surface. It then measures the radius of the largest sphere centered on that voxel which fits inside the structure. It then removes all redundant spheres. The diameter of the sphere with the largest radius is considered as the thickness. **Figure 7.9a** and **7.9b** present histograms of the distributions of thicknesses of the Al_2O_3 and ZnO components, with a lower value thickness cut-off of 10 nm. The black squares and curve in Figure 8 correspond to the cumulative probability of the thickness of Al_2O_3 and ZnO in the composite. This analysis shows that the thickness of the $\text{Al}_2\text{O}_3/\text{ZnO}$ composite ranges from 10 nm to 60 nm with a thicknesses below 40 nm at a cumulative probability of 95%. The average thickness of the Al_2O_3 component is 32 ± 9 nm while that of the ZnO component is 36 ± 12 nm.

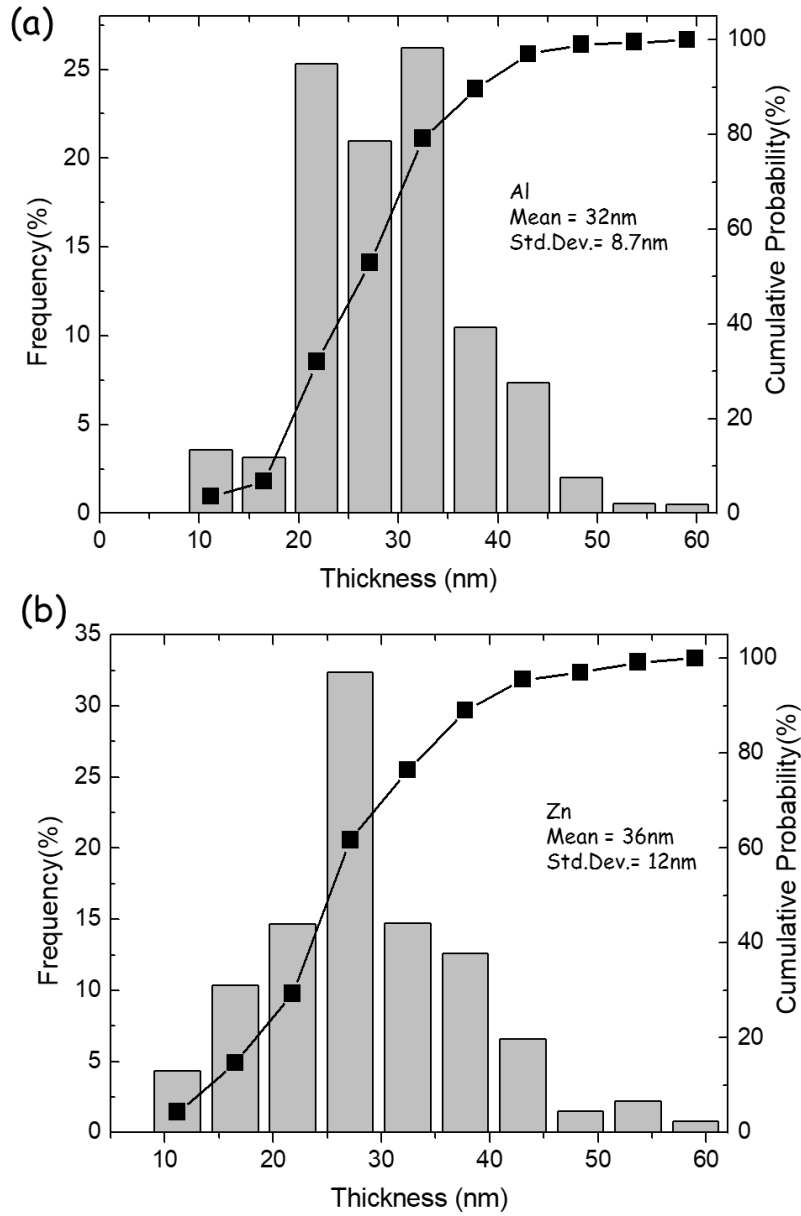


Figure 7.9 Histogram of the thickness distribution of (a) Al₂O₃ signal and (b) ZnO signal, in the aerogel sample measured by ptychography (**sample B**), derived using the ‘Bone J’ plugin in Image J. The square data points and curve are the cumulative probability of the thickness distributions.

Figure 7.10a presents a surface rendering of the ptychographic 4D reconstruction of the Al₂O₃/ZnO composite with Al₂O₃ in blue and ZnO in red, derived using Otsu thresholds of 0.0018 for the Al₂O₃ signal and 0.0026 for the ZnO signal. In order to investigate the detailed distribution of Al₂O₃ and ZnO components in the aerogel, the relative elemental concentrations (REC) of Al₂O₃ and ZnO in the aerogel were calculated as a function of distance from the sample surface (xy). Similarly to Figure 4b, the REC (Yang et al. 2014) is defined as the ratio of the amounts of each species (Al₂O₃ or ZnO) relative to that of the sum of both species. **Figure 7.10b** plots the relative elemental concentration of only Al₂O₃ (blue), only ZnO (red), and both ZnO and Al₂O₃ ('colocalization', green), as a function of distance from the surface. The elemental concentration that presented in y axis is relative to the solid component on each slice. In this volume, there is more Al₂O₃ towards the surface and less Al₂O₃ in the middle region (50~250 nm from the surface of the 1.5³ μm³ volume), where the Al₂O₃ is distributed more uniformly. The distribution of ZnO is almost opposite to that of Al₂O₃, with more ZnO in the middle region and less ZnO toward the surface. The 'colocalization' volume (green in **Fig. 7.10b**), where both Al₂O₃ and ZnO components are present, has a similar distribution as that of ZnO. It is clear that the ZnO does not fully cover the Al₂O₃ phase, as ~30% of the Al₂O₃ (blue) is not coated by ZnO. However, the volume fraction of the colocalization is depend on the threshold value that used for Al₂O₃ and ZnO. With a smaller threshold value, the colocalization volume fraction will increase. More surface rendered views of the 4D maps at different tilt angles are shown in **Fig. 7.11**. These views show that the aerogel piece deposited from the water suspension has an irregular shape. To estimate the porosity of the sample, a 1.5 μm³ cube in the center of the sample has been extracted, as shown in **Fig. 7.12**. The threshold values were the same as in

Fig. 7.10. Images of ~20 nm thick xy planes at different depths along the z direction are presented in **Fig. 7.12b**. The volume fractions of the two components in the xy planes along the z direction are plotted in **Fig. 7.12c**. The porosity of the cube is 89(4) %, which is reduced from the uncoated Al₂O₃, as expected. The volume fraction of ZnO is 6.3(0.8) %, and the Al₂O₃ is 5.6(0.8) %.

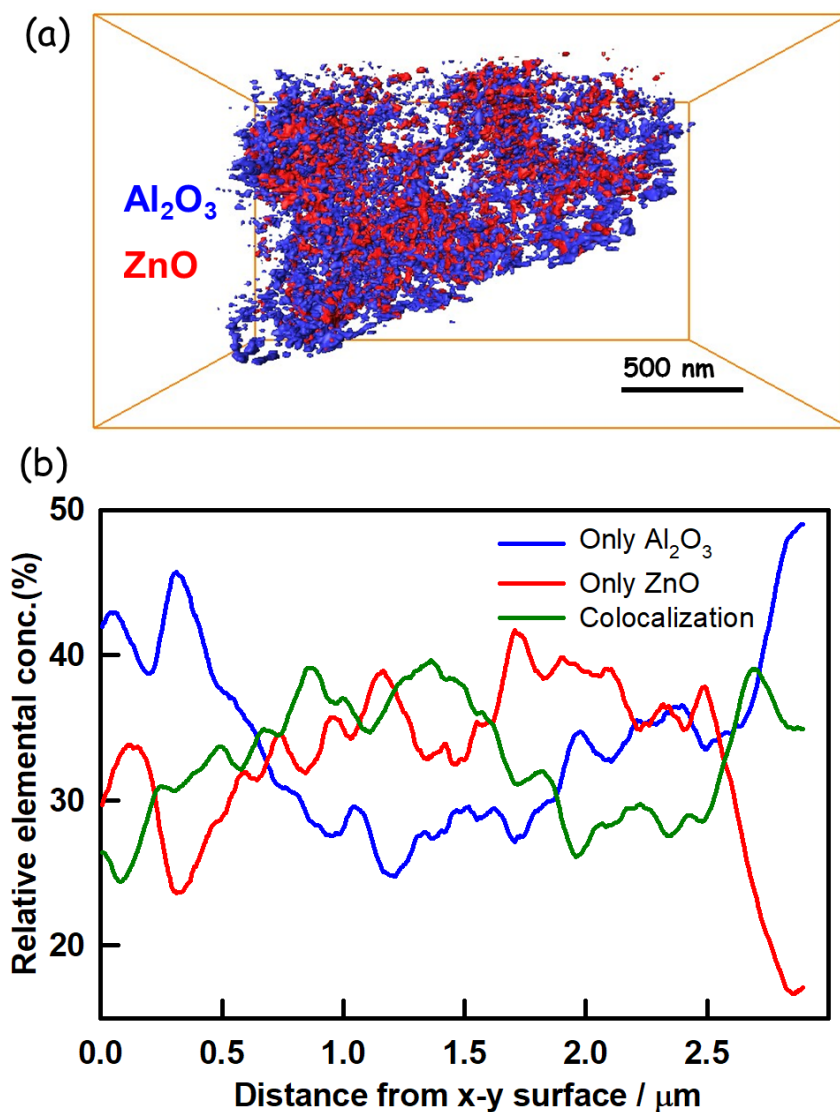


Figure 7.10 a) Surface rendered color coded composite of the 3D distributions of ZnO and Al₂O₃ from ptychography of ZnO/Al₂O₃ aerogel (**sample B**). (b) Volume fraction of the two components and their co-localized amounts in the solid portion of xy slices through the

z direction of the same volume as Figure 8. The Otsu thresholds used were 0.0018 for the Al_2O_3 signal and 0.0026 for the ZnO signal.

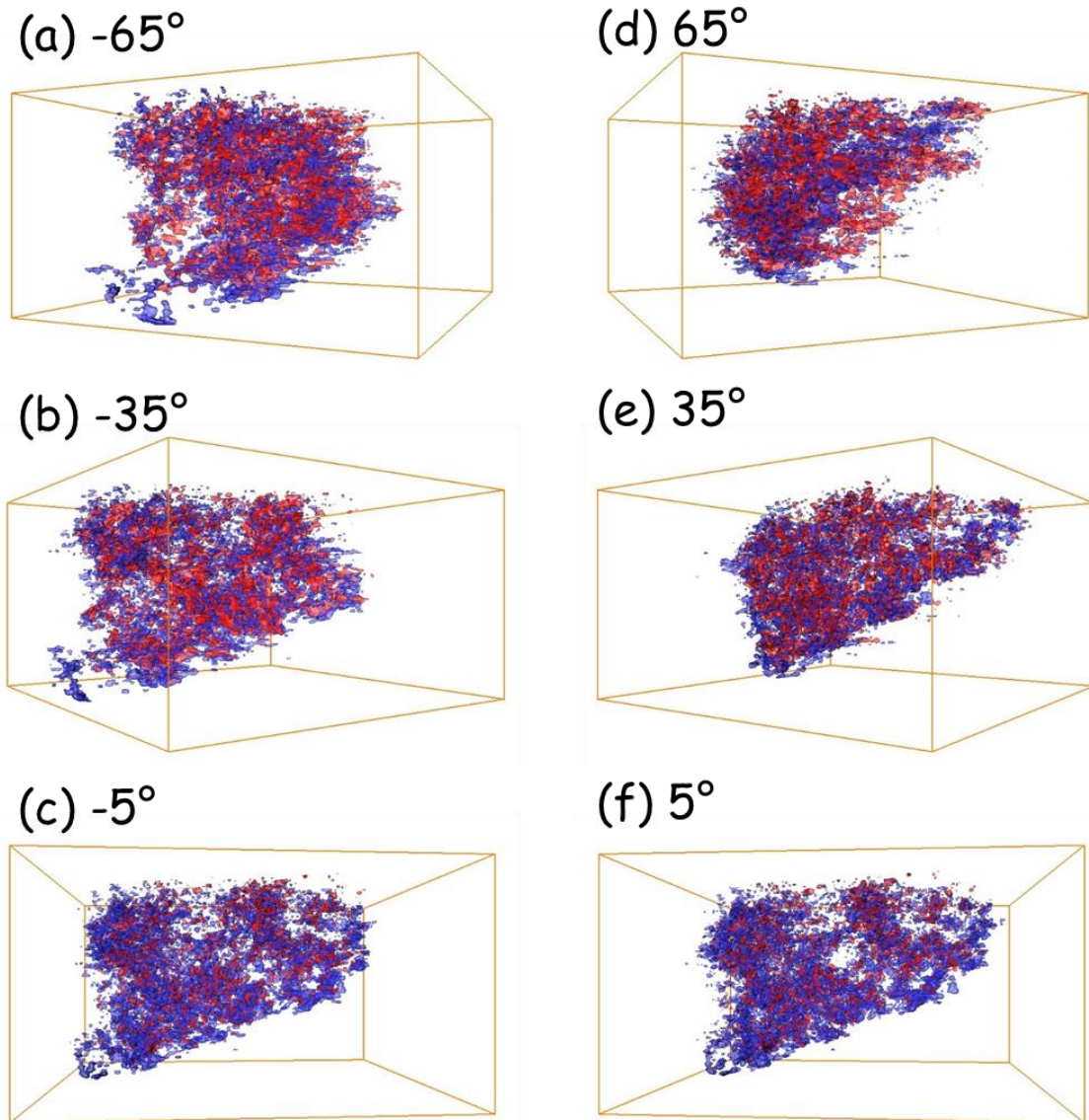


Figure 7.11 Views at 6 different tilted angles of the reconstruction of the ptycho tomography **sample B**. (a) -65°, (b) -35°, (c) -5°, (d) 5°, (e) 35° and (f) 65°.

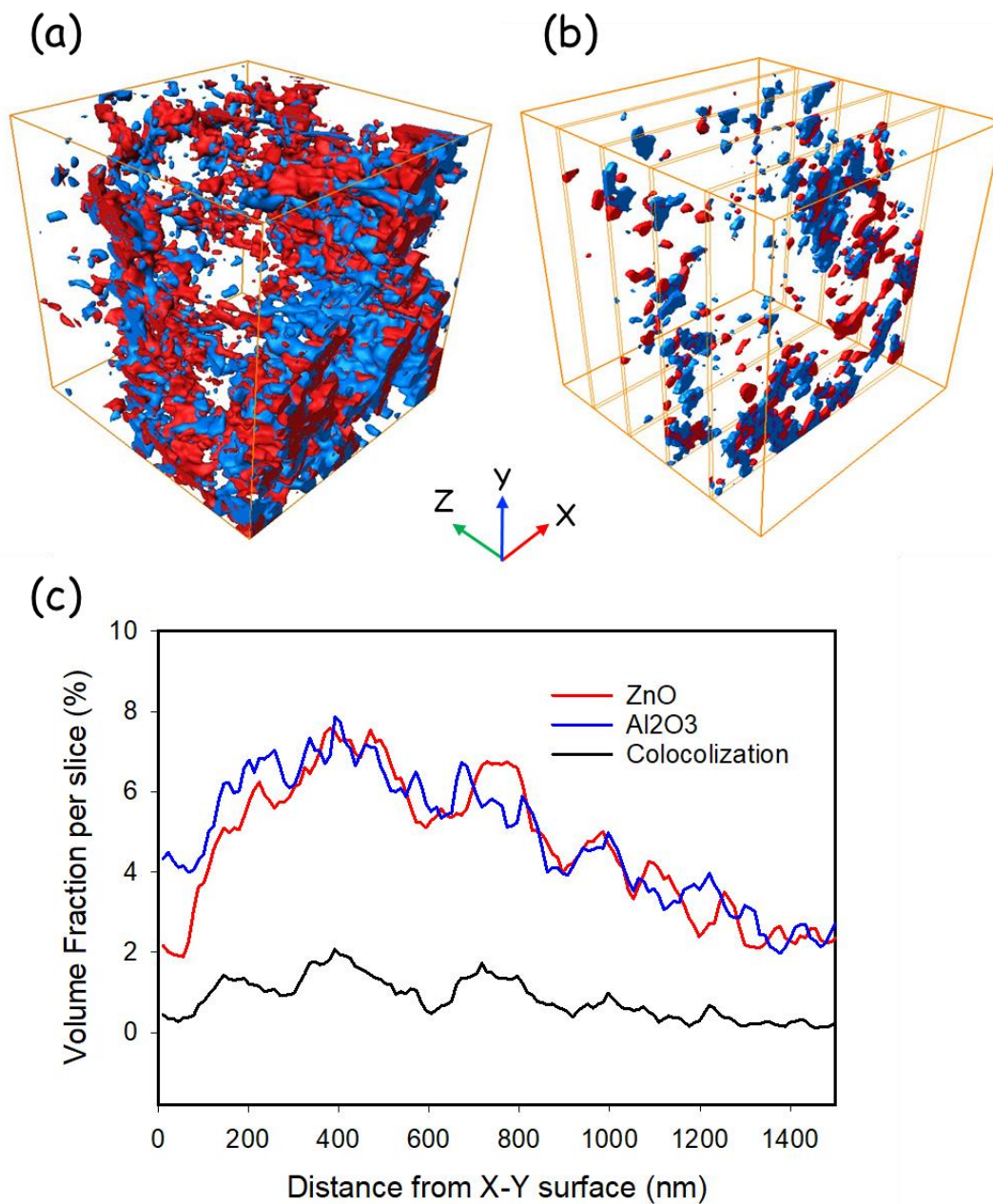


Figure 7.12 (a) Surface rendering of $(1.5 \mu\text{m})^3$ center cube of the reconstructed ptychographic spectro tomography data (**sample B**). (b) single slices at 0.3 μm , 0.6 μm , 0.9 μm and 1.2 μm depth of the cube. c) plot of the volume fraction per slice, as a function of depth from the xy surface.

A **movie** of various renderings of the 4D ptychography result (color coded composite of the ZnO and Al₂O₃ reconstructions) is available for viewing at <https://drive.google.com/drive/u/2/my-drive?ogsrc=32>. The movie shows the 3D chemical structure of the composite imaged from a number of angles and with detailed interior views. It clearly shows the presence of non-conformal ZnO coatings (red) on the Al₂O₃ aerogel framework (blue). Using a 10–90% intensity metric, and measuring profiles at 3 locations in each of the xy and yz planes, the spatial resolution is estimated to be 18 nm (3 pixels) for the xy plane, and 24 nm (4 pixels) for the yz plane.

7.3.4 Transmission Electron Microscopy (TEM) of ZnO/Al₂O₃ Aerogel

In order to verify the unexpected poor coverage and aggregated ZnO coating, TEM studies were performed by the Lawrence Livermore Lab collaborators using a Titan 80-300 (Scanning) Transmission Electron Microscope (STEM) operated at 300 kV for both TEM images and STEM-EDS measurements. **Figures 7.13a** and **7.13b** display high resolution transmission electron microscopy (HR-TEM) images of the ZnO-coated Al₂O₃ aerogel. Needle- and leaf-like motifs are readily observed in **Fig. 7.13a** for the aerogel framework, which are consistent with the structures reported for Al₂O₃ aerogels prepared via the synthetic pathway used to make the samples of this study (Poco et al. 2001). The surfaces of the Al₂O₃ aerogel are decorated by nanoparticles with dimensions ranging from a few nanometers to more than 30 nm. Z-contrast imaging (**Fig. 7. 13c**) reveals that these nanoparticles contain a higher-Z element than the aerogel scaffold, which strongly indicates that they arise from the ZnO ALD coating. This interpretation is further supported by

energy dispersive spectroscopy (EDS) measurements (data not shown) that indicate the presence of only Al, O, and Zn in the sample (Cu from the TEM sample grid was also observed). The EDS data also reveals that the relative concentration of each of these elements varies as a function of position within the sample. Significantly, the ZnO nanoparticles are highly crystalline and typically observed to be single crystals, as demonstrated by **Fig. 7.13b**. Attempts to obtain atomic resolution images of the Al₂O₃ network were unsuccessful as the sample fragments reacted to the incident electron beam by moving on to the Cu grid, which is attributed to charging of the Al₂O₃.

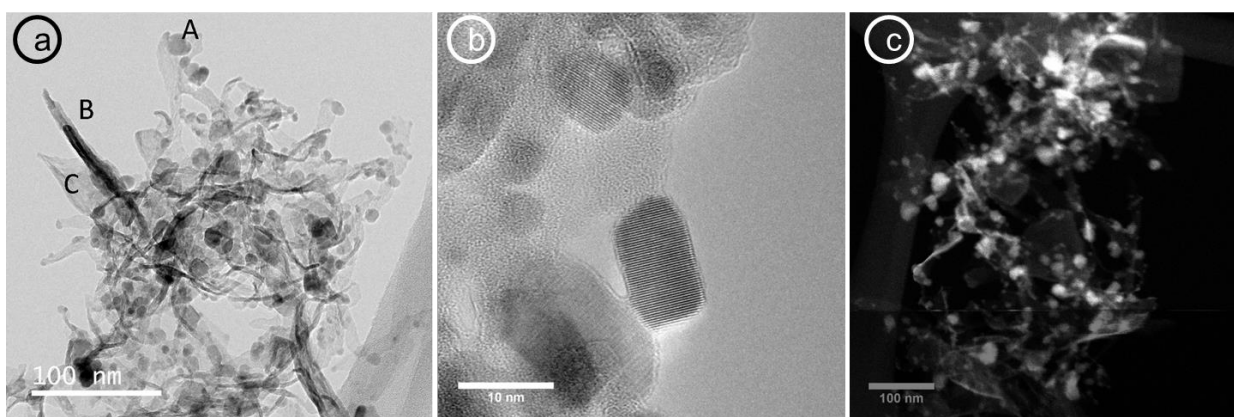


Figure 7.13 (a) Transmission electron micrograph of an Al₂O₃ aerogel coated with 25 ALD cycles of ZnO. Three morphologies are indicated: ~10 – 30 nm strongly scattering, square/spherical clusters of single crystals (ZnO); elongated, strongly scattering rods (ZnO); and weakly scattering sheet-like material (alumina). (b) High resolution TEM showing crystal planes of ZnO. (c) a Z-contrast scanning transmission electron micrograph of the same material in which the higher-Z ZnO coating appears white and the Al₂O₃ appears grey.

7.4 Discussion

As observed in other soft X-ray STXM /ptychography comparisons (Miao et al. 2012, Shapiro et al. 2014), ptychography provides significantly improved spatial resolution

relative to STXM in both 2D and 3D. Although the spectro-ptycho-tomography data was only measured at the Zn L-edge due to technical reasons, this was sufficient to determine images and quantitative maps of both the ZnO and Al₂O₃ components. From detailed analyses of the 3D distributions it was possible to estimate the degree to which the ALD deposited ZnO covered the Al₂O₃ aerogel framework. In the ptychography measurement of **sample B** the ZnO coverage of the Al₂O₃ aerogel was estimated to be 33(5) %. A similar co-localization analysis of the STXM spectro-tomography reconstruction gave a derived ZnO coverage of 55(8) %. This somewhat larger value is likely due to the lower spatial resolution of STXM than ptychography.

The ability to derive the surface coverage of the ALD coating, combined with the structural and spectroscopic information available for the aerogel scaffold and ALD layer using spectro-ptycho-tomography, provides significant new insights about ZnO ALD on porous Al₂O₃ frameworks. It has been reported that the mode of ZnO ALD growth on Al₂O₃ (specifically sapphire) is dependent on the sample temperature during deposition – island growth is encountered at 150°C on a planar substrate, while layer-by-layer growth occurs at 220°C (Baji et al. 2012). The measurements performed in this study conclusively demonstrate that island (/nanoparticle) formation occurs on the Al₂O₃ for at least the first 25 ALD cycles at a sample temperature of 110°C, suggesting that the lower-temperature growth mode extends from planar surfaces to the curved framework of the Al₂O₃ aerogel. Furthermore, the dimensions of the ZnO nanocrystals (tens of nm) are also shown to dramatically exceed the thicknesses one would predict based upon the reported deposition rates during the initial stages of ALD (~0.2 nm/cycle, for an expected thickness of ≤ 5nm). This behavior is consistent with a growth mechanism in which adsorbates migrate across

the substrate surface to form larger nanoparticles, thereby minimizing interfacial and surface energies.

Comparison with the TEM data for the $\text{Al}_2\text{O}_3/\text{ZnO}$ material further illustrates the value of spectro-ptycho-tomography as a complementary or alternative method for high resolution materials characterization. There is clearly strong qualitative and quantitative agreement between the structures derived from the two techniques. Such close correlation confirms that the formation of ZnO nanocrystals is not an artifact of irradiation with the electron beam, i.e., via beam damage/heating, and thus greater weight can be placed on the TEM data. Without the complementary spectro-ptycho-tomography measurements, beam damage could have remained a concern if one was attempting to distinguish between layer-by-layer and island growth using only TEM, particularly given that the sample reacted by moving under the electron beam during HR-TEM measurements of the Al_2O_3 scaffold. This movement of the sample has additional significance in that it precluded high spatial resolution diffraction or spectroscopy studies to identify the phase and bonding of the aerogel using TEM. The X-ray based methods were able to address this gap in knowledge via assignment of the θ phase of Al_2O_3 and identification of both tetrahedral (AlO_4) and octahedral (AlO_6) bonding environments of Al within the aerogel. The combination of techniques also indicate that the structure of the Al_2O_3 aerogel remains unchanged through formation of the ZnO layer, which demonstrates the robustness of the aerogel as a scaffold for functionalization by ALD.

Spectro-ptycho-tomography has far broader applicability than this study of ZnO ALD on an Al_2O_3 aerogel. The enhanced spatial resolution of spectro-ptycho-tomography versus conventional STXM spectro-tomography, combined with the localized structural and

chemical information derived from the technique, has the potential for significant impact on development of improved nanoscale and nanostructured functional materials. This study demonstrates that 4D spectro-ptycho-tomography can provide quantitative information regarding the size, distribution, and electronic structure (and, by extension, local bonding and phase) of nanoscale coatings, the exposed surface area of both template and coating, the amount of interface between them, and the pore architecture. Such information is of direct value in understanding relationships between the structure and properties/performance of nanostructured systems including catalysts, e.g. for identifying active sites, the efficiency of specific architectures, mass transport through the material, degradation pathways, etc.. Furthermore, assignment of the material structure and bonding can be used in a feedback loop to improve synthetic pathways for generating designer materials. Significantly, spectro-ptycho-tomography does not impose as stringent limits over sample thickness and radiation sensitivity as does comparable electron beam techniques, making it a powerful complementary or alternative 4D analysis method.

With the development of near diffraction limited synchrotron radiation (DLSR) facilities like Max IV in Sweden and Sirius in Brazil, as well as DLSR upgrade activities and plans at many 3rd generation facilities, it is clear that the types of dramatic improvements in 4D imaging presented in this work will become routinely available in the near future (Hitchcock and Toney 2014). The recently commissioned COSMIC beamline at the ALS, which is dedicated to ptychography, will be an outstanding facility to continue this type of 4D imaging.

7.5 Summary

STXM spectro-tomography and ptychography spectro-tomography were performed on several different Al_2O_3 aerogel samples, and 4D images were generated by reconstruction. The spatial resolution calculated by FRC shows that the 2D and 3D spatial resolution in the ptychography results was significantly improved relative to corresponding conventional STXM measurements. A quantitative analysis of both the STXM and ptychography tomography results gave detailed information about the atomic layer deposition coatings. Non-uniform coating of ZnO by atomic layer deposition was documented by both STXM and ptychography 4D imaging. The quantitative and qualitative structural information provided by the x-ray methods have direct value for evaluating and optimizing the ZnO ALD process and illustrate their broad applicability for characterizing heterostructures on nanometer length scales.

This chapter has demonstrated the advantage of ptychography compared to conventional STXM that described in Chapter 5. The disadvantage is the high radiation damage. The radiation damage can be reduced by cryo STXM which is discussed in Chapter 8.

Chapter 8

Summary and Future Work

This chapter provides a summary of the main scientific results of this thesis. Results from cryo-STXM tomography measurements carried out toward the end of my thesis research are presented. Ideas are provided for future research in 4D imaging based on scanning X-ray microscopy methods, including STXM, ptychography and laminography.

8.1 Summary

Soft X-ray scanning transmission X-ray microscopy (STXM) was used to characterize the 3D distributions of ionomer and carbon support in the catalyst layer of proton exchange membrane fuel cell (PEMFC) cathodes. The compressed sensing (CS) algorithm was adapted for reconstruction of STXM and ptychography tomography data sets. I demonstrated the superior performance of CS relative to SIRT and FBP reconstruction methods when applied to STXM tomography data set. CS was used extensively for efficient 3D reconstruction. I studied the changes in the amounts and 3D spatial distributions of ionomer due to radiation damage in STXM tomography and ptychography. Soft X-ray ptychography was used to improve the spatial resolution of 4D imaging and applied to both PEMFC cathodes and to ZnO/Al₂O₃ aerogels.

(chapter 4) This collaboration with members the Cambridge electron microscopy group (Sean Collins, Rowan Leary, Zineb Saghi, Paul Midgley) and Mirna Lerotic (2nd Look Consulting) implemented and tested compressed sensing as a tool for reconstructing tilt angle tomography data sets. My role was to test the software, which was written by Mirna

Lerotic with help from the Midgley group. I applied the CS code in Mantis to a number of different electron and X-ray tomography data sets during its development, and for the paper. I made suggestions on how to improve the user interface and extensively explored the dependence of the results on the CS parameters and the nature of the data set. The CS method implemented in Mantis (Lerotic et al. 2014) was then used extensively in the remainder of my studies, and has also been used by other groups (Luo et al. 2017). Given the ongoing interest and adoption of compressed sensing methods in both data acquisition (Gurbuz et al., 2009) and data analysis, this paper and the Mantis implementation will be of great value to the 3D and 4D imaging communities.

(Chapter 5) 4D imaging of PEMFC cathode catalyst layers was used to measure the distribution of ionomer relative to carbon support, in order to optimize the fabrication of the cathode catalyst. 2-set and 3-set experiments were used to guide modification of acquisition procedures in order to minimize radiation damage in 4D. With the use of CS, fewer tilt angles are needed and radiation damage during tomography measurement was reduced. This study showed that STXM tomography at room temperature can be used to quantify 3D distributions of ionomer in PEMFC cathodes with negligible radiation damage. With this approach, it is possible to systematically measure MEA samples with different loading of ionomer, and combine the 4D results with performance analysis results, in order to optimize the cathode catalyst layer formulation, fabrication and nanostructure.

(Chapter 6) PEMFC MEA cathodes were measured by ptychography tomography to improve the 3D spatial resolution compared to STXM tomography. A model sample was used to demonstrate that ptychography can provide significant resolution enhancements even for soft matter samples which do not scatter strongly. Significant improvements in the

spatial resolution were achieved for both 2D and 3D distributions. A full F 1s ptychographic stack of the catalyst layer was also successfully recorded. Although excessively damaging, this provided a high-resolution probe of both the spectroscopy and spatial distribution of PFSA ionomer in a real cathode CL sample. COSMIC beamline and ptychography end stations are now available at the ALS. With the fast detector of COSMIC, 4D imaging of ionomer in PEMFC electrodes with spectro-ptycho-tomography with acceptable doses and extent of radiation damage will be achieved.

(**Chapter 7**) STXM spectro-tomography and soft X-ray ptychography spectro-tomography were performed on Al₂O₃ aerogel samples with ZnO ALD coating. I developed a water dispersion sample preparation method which provided a variable size range for tomography measurements. This study showed that, compared to conventional STXM measurements, the 2D and 3D spatial resolution in the ptychography results was significantly improved. The technique can be used to evaluate and optimize the ALD process and illustrate their broad applicability for characterizing heterostructures on nanometer length scales.

8.2 Suggestions for future research

8.2.1 Ambient STXM of PEMFC MEAs at the S 1s edge

One of the major limitations of the 4D imaging of PEMFC cathodes is the limited Z-dimension that can be measured, due to the requirement of X-ray transmission, which limits sample thickness to less than 300 nm for F 1s measurements and 150 nm for C1s measurements. Even with the ~15 nm spatial resolution achieved with ptychography that places a significant restriction on the spatial extent of true 3D information, namely spatial distribution and ionomer pathway connectivity in the Z-direction. One way to greatly expand the Z-range over which STXM and ptychographic 4D imaging of MEA samples can

be performed would be to measure at the S 1s edge (2460 eV) where the X-ray penetration depth is much greater. Although the amount of S in PFSA is very low (the formula for Nafion-117 is $C_{21}F_{41}O_5SH$), the sulfonate group has a very prominent transition at 2477 eV. Perhaps more significantly with respect to probing the proton conducting capability of ionomer in pristine and electrochemically tested samples, the sulfur signal is a direct measure of the ionomer proton conduction capability whereas the F 1s edge is only indirectly related. This aspect has already been explored using S 2p measurements in a study of carbon corrosion of PEMFC MEAs (Hitchcock et al 2016).

Figure 8.1a plots the S 1s spectra of sulfate and sulfite species, illustrating the excellent sensitivity of this edge to the oxidation state of sulfur (Hay et al. 2004). **Figure 8.1b** plots a calculated spectrum of 1 μm thickness of nafion-117 in the 1900 – 2600 eV region, based on the typical composition of a cathode (40 % ionomer, 10 % Pt and 50 % carbon support). At 1 μm thickness the peak S 1s OD of pure ionomer is 0.1 in the S 1s region, while the contribution of all species in the simulated cathode at the same energy is 0.65, and is dominated by the strong Pt 3D absorption. These OD values are suitable to avoid absorption saturation and get good statistics. S 1s studies of liquid crystal display materials (Kaznatcheev et al., 2007) and biological systems (Norlund et al 2009) have been performed at the CLS ambient STXM. Based on these considerations, all components of the MEA could be measured with chemical specificity by making tomography measurements at 2465 eV (pre S-edge) and 2482 eV ($S\ 1s \rightarrow \sigma^*_{S=O}$ peak), 2100 eV (pre-Pt), 2170 eV (Pt $3d_{5/2}$). The PFSA chemical map would be obtained from $OD_{2482} - OD_{2465}$ with a quantitative response of 0.034 OD/ μm . The Pt catalyst map can be obtained from $OD_{2170} - OD_{2100}$ with a quantitative response of 3.8 OD/ μm . The carbon support map would not be

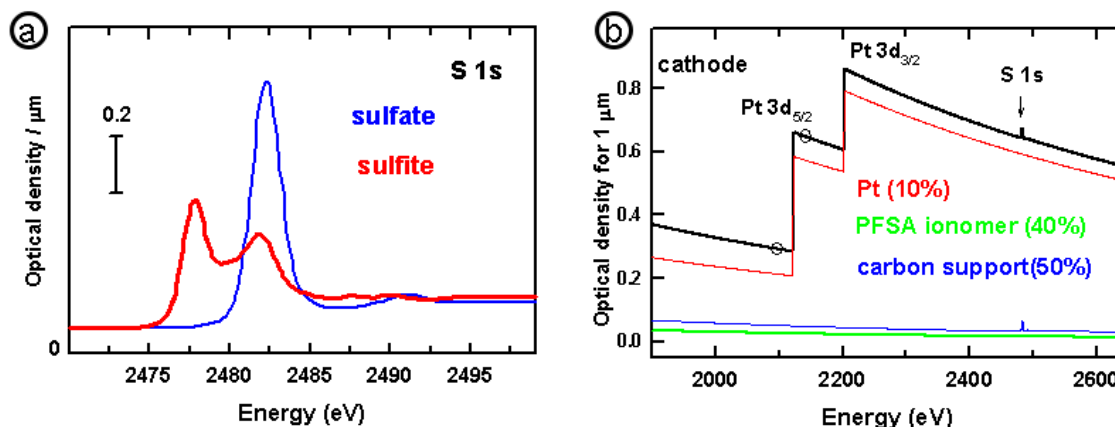


Fig. 8.1 Evaluation of S 1s STXM of cathodes. (a) S 1s spectra of sulfate and sulfite species (Hay et al 2004). (b) Simulation of Pt 3d and S 1s region of the X-ray absorption spectra of a cathode, consisting of 10 % Pt (red), 50 % carbon support (blue), and 40 % PFSA ionomer (green).

obtained directly, but it could be estimated from OD_{2100} by subtracting weighted contributions of the PFSA and Pt signals. This evaluation indicates S 1s would be feasible, and the 1-2 μm thickness of the microtomed MEA section would allow STXM spectro-tomography to provide very extensive information in the z-direction. However the SM beamline has relatively low flux at the S 1s edge (typically less than 1 MHz), and the energy scale is not very stable. As part of the CLS-SM upgrade there is funding to replace the monochromator and improve flux in the 2000 – 3000 eV range by as much as a factor of 40 through the use of multilayer coated mirror and grating optics. This is expected to be completed by 2020 or 2021. S 1s ptychography measurements can also be done of the new COSMIC beamline in ALS and this should be expected in the near future.

8.2.2 Cryo STXM tomography

A new cryo-STXM has been designed, built and commissioned as part of a CFI-funded upgrade of the SM beamline Canadian Light Source (CLS). Cryogenic sample

temperatures suppress mass loss radiation damage. A JEOL goniometer and Gatan cryo transfer system, (donated to CLS by Dr. Chris Jacobson, Northwestern University) is used, allowing load-lock transfer of samples into the STXM vacuum tank. My part in this instrument development was testing the goniometer rotation and developing procedures for eucentric adjustment of the sample position such that the region of interest stays at the X-ray focal point over the full angle range (-70° to $+70^{\circ}$). Although this has not yet been achieved, cryo-tomography data sets have been recorded in an automated fashion by oversampling the spatial region to compensate for motion of the region of interest with rotation.

MEA samples were used for commissioning the cryo-STXM, including 2D imaging, full stacks and cryo-tomography measurements. **Figure 8.2(a-d)** shows chemical maps at different tilt angles from cryo-tomography of an MEA sample. Images were measured at 684 and 694 eV from -70° to $+65^{\circ}$ with 10° increments, with the sample maintained at -180°C . A volume rendering of the reconstruction is presented in **Fig. 8.2(e)**. In order to demonstrate that the cryo conditions actually do reduce radiation damage, a cryo-tomography data set of an MEA sample must be measured with higher dose. C 1s and F 1s spectra should be recorded with the sample cold, before and after the tomographic data set. The commissioning paper (Leontowich et al. 2018) already presents evidence that cooling reduces mass loss damage, as shown in **Fig. 8.3**.

During PEMFC operation, the cathode side is at high temperature and high relative humidity (RH) (typically 80 % RH and 80°C). It would be desirable to measure the MEA as close to the real operating conditions as possible. With cryo-STXM, “wet” tomography with Luxel windows (see **Fig. 3.6c**) would be possible, although at present it is not

possible to flash freeze samples and thus the crystallization of water during cooling (which takes ~10 min) would likely alter the cathode morphology. I tried wet tomography of MEAs using the CLS ambient-STXM. However, the experiments failed because the Luxel window samples dried before or during the measurement. Another sample that was tried using the Luxel window cell was magnetotactic bacteria (MTB) cells in water, a collaboration with group member, Xiaohui Zhu. **Figure 8.4a** shows TEM images of the MTB cells (dried). **Figure 8.4b** is a STXM image of the Luxel window with the MTB cell solution inside. A color coded composite chemical map, derived from STXM measurements at the O 1s and Fe 2p edge, is shown in **Fig. 8.4c**, with the cell in green, the water in blue and the magnetosomes in red. A tomography data set was measured for this sample. However, the sample dried out during the measurement and there was extensive reconstruction artefacts. Also the MTB cells were dry and dead before the sample preparation, so the shape of the cell and the magnetosome chain may have been changed from its structure in the cell when the cell was live. If a plunge freeze apparatus is acquired at the CLS it would be possible to measure 2D and 3D of MTB cells and other biological samples (Lepault et al. 1983, Gros et al. 2005) with the water still present as amorphous ice.

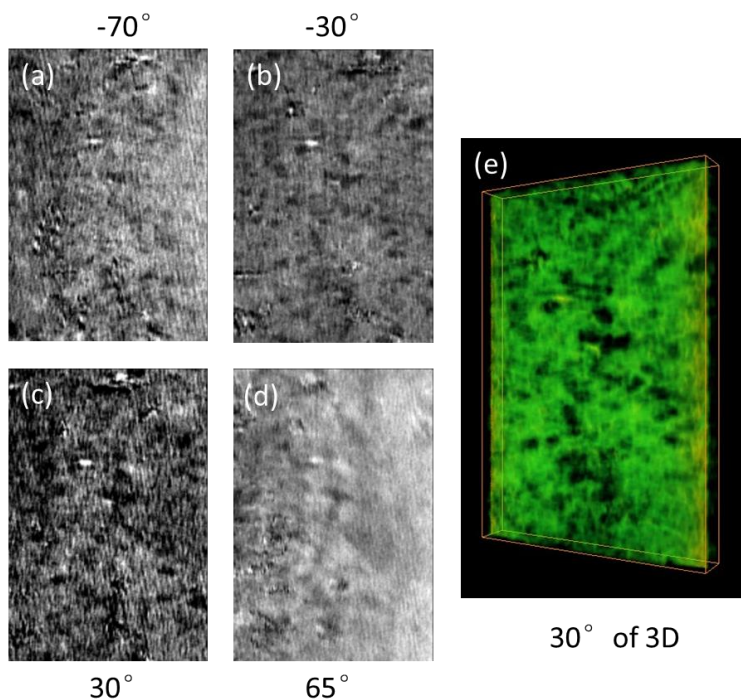


Figure 8.2 2D chemical maps of PFSA of an MEA sample under cryo conditions (-181°C) at different tilted angles, derived from images measured at 684eV and 694 eV. (a) -70° , (b) -30° , (c) 30° , (d) 65° . (e) 30° tilted view of the 3D reconstructed volume.

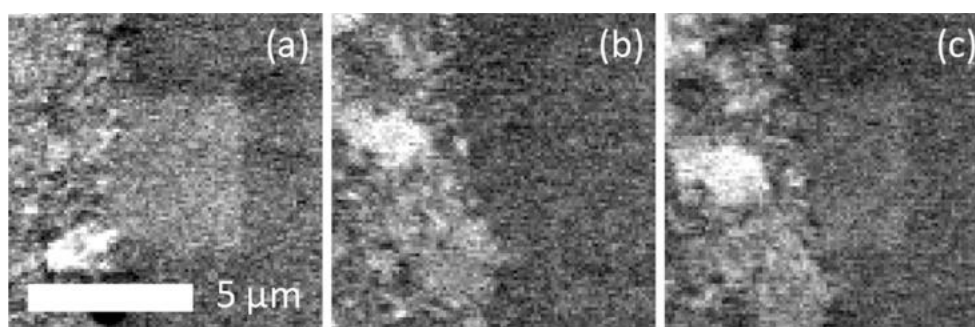


Figure 8.3 X-ray transmission images at 694.0 eV of 100 ± 14 nm thick PEM fuel cell sample. The membrane region is on the right and the cathode is on the left for all images, which are all on the same spatial scale. (a) Image of a sample region immediately after X-ray exposure at 296 K. (b) Image of a different sample region immediately after X-ray exposure at 95 K, using otherwise identical exposure conditions as a). (c) Same region as b), imaged after allowing the sample to warm up to 296 K

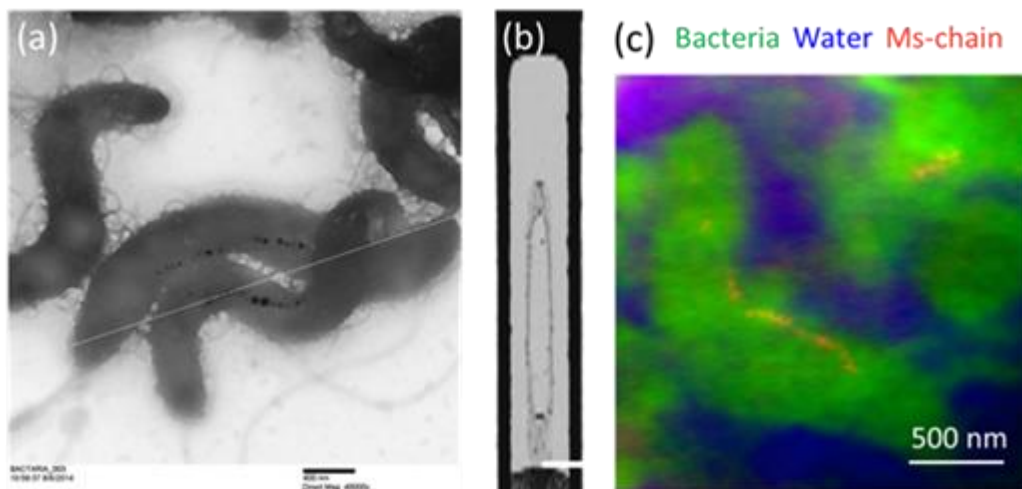


Figure 8.4 (a) TEM image of MV-1 magnetotactic bacteria cells. The scale bar is 400 nm; (b) STXM image of the sample in a Luxel tomography holder. Scale bar is 200 μm (c) color composite of component maps of a wet MT sample, measured at O1s edge (OD₅₂₅-OD₅₅₀) and Fe 2p edge (OD₇₁₀). The bacteria cell is in green, water in blue, and magnetosome chain in red.

8.2.3 Cryo soft X-ray ptychography tomography

Another goal for the new CLS cryo-STXM could be to develop other techniques that are currently available in the CLS ambient-STXM, including: total electron yield detection for surface studies (Behyan et al. 2011); X-ray fluorescence detection for trace level studies (Hitchcock et al. 2010) and ptychography (Wang et al. 2017). As a continuation of my thesis work, cryo soft X-ray spectro-ptycho- tomography is of greatest interest since it would combine low radiation damage, chemical sensitivity, high spatial radiation and 4D visualization. Applications may include radiation sensitive biomaterials, bacteria, flu virus, proteins and lipids assembles, and different polymer nanocomposites.

8.2.4 Other STXM 4D imaging applications

Cellulose is an organic compound that exists in the cell walls of plants. It is widely

used to make paper, plastic, and various fibres and fabrics. Nanocrystalline cellulose is a newly developed product which can be used to produce nanocomposites with superior thermal and mechanical properties (Pranger et al. 2008, Cai et al. 2009). **Figure 8.5** shows an anatase-titania–cellulose hydrogel deposited with 20-layer titania gel films (Luo et al. 2014). The high-magnification field emission scanning electron microscopy (FE-SEM) image (**Fig. 8.5b**) indicates that each microfibre is composed of fine nanofibres. The TEM image (**Fig. 8.5c**) indicates that the diameter of the anatase titania nanoparticles varies from 20 nm to 50 nm. STXM 4D measurements could be taken at the Ti 2p or the O 1s edge to differentiate the two components. A nanocellulose hydrogel from Prof. Emily Cranston (McMaster University) was measured by ambient STXM at the C1s edge at CLS in 2015. However, the signal was saturated at the peak energy. To avoid the saturation problem, the sample thickness can be controlled by FIB. Another possible sample preparation method is to crush the sample into fine powder and disperse into water, then plunge freeze the liquid and measure by cryo soft X-ray spectro-ptychography.

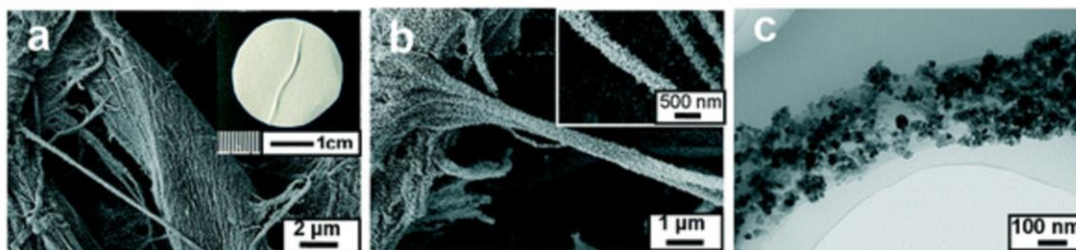


Figure 8.5 (a) Low-magnification FE-SEM image; (b) high-magnification FE-SEM image; (c) TEM of an individual anatase-titania–cellulose composite nanofibre isolated from the assembly (Luo et al. 2014) (Reproduced with permission from Royal Society of Chemistry)

REFERENCE

- Abrams, H.L. and McNeil, B.J. (1978) Medical Implications of Computed Tomography (Cat Scanning). *New England Journal of Medicine* 298(6), 310-318.
- Ade, H. and Hitchcock, A.P. (2008) NEXAFS microscopy and resonant scattering: Composition and orientation probed in real and reciprocal space. *Polymer* 49(3), 643-675.
- Ade, H., Kirz, J., Hulbert, S.L., Johnson, E.D., Anderson, E. and Kern, D. (1990) X - ray spectromicroscopy with a zone plate generated microprobe. *Applied Physics Letters* 56(19), 1841-1843.
- Ade, H., Zhang, X., Cameron, S., Costello, C., Kirz, J. and Williams, S. (1992) Chemical contrast in X-ray microscopy and spatially resolved XANES spectroscopy of organic specimens. *Science* 258(5084), 972.
- Allen, F.I., Comolli, L.R., Kusoglu, A., Modestino, M.A., Minor, A.M. and Weber, A.Z. (2015) Morphology of Hydrated As-Cast Nafion Revealed through Cryo Electron Tomography. *ACS Macro Letters* 4(1), 1-5.
- Anand, A., Savery, D. and Hall, C. (2007) Three-dimensional spatial and temporal temperature imaging in gel phantoms using backscattered ultrasound. *IEEE Transactions on Ultrasonics, Ferroelectrics, and Frequency Control* 54(1), 23-31.
- Andrews, J.C., Almeida, E., van der Meulen, M.C.H., Alwood, J.S., Lee, C., Liu, Y., Chen, J., Meirer, F., Feser, M., Gelb, J., Rudati, J., Tkachuk, A., Yun, W. and Pianetta, P. (2010) Nanoscale X-Ray Microscopic Imaging of Mammalian Mineralized Tissue. *Microscopy and Microanalysis* 16(3), 327-336.

- Aramburo, L.R., Liu, Y., Tyliczszak, T., de Groot, F.M.F., Andrews, J.C. and Weckhuysen, B.M. (2013) 3D Nanoscale Chemical Imaging of the Distribution of Aluminum Coordination Environments in Zeolites with Soft X-Ray Microscopy. *ChemPhysChem* 14(3), 496-499.
- Awaji, M., Suzuki, Y., Takeuchi, A., Takano, H., Kamijo, N., Tamura, S. and Yasumoto, M. (2002) Zernike-type X-ray imaging microscopy at 25 keV with Fresnel zone plate optics. *J Synchrotron Radiat* 9(3), 125-127.
- Bae S, et al. (2015) Soft X-ray Ptychographic Imaging and Morphological Quantification of Calcium Silicate Hydrates (C–S–H). *J Am Ceram Soc* 4095(36679):4090–4095.
- Bagge-Hansen, M.; Wichmann, A.; Wittstock, A.; Lee, J. R. I.; Ye, J.; Willey, T. M.; Kuntz, J. D.; Van Buuren, T.; Biener, J.; Bäumer, M.; et al. (2014) Quantitative phase composition of TiO₂-coated nanoporous Au monoliths by X-ray absorption spectroscopy and correlations to catalytic behavior. *J Phys Chem C* 118(8):4078–4084.
- Baji, Z., Lábadi, Z., Horváth, Z.E., Molnár, G., Volk, J., Bársony, I., Barna, P. (2012) Nucleation and growth modes of ALD ZnO. *Cryst. Growth Des.* 12, 5615–5620.
- Banterle N., Bui K.H., Lemke E.A., and Beck M. (2013) Fourier ring correlation as a resolution criterion for super-resolution microscopy. *J Struct Biol* 183(3):363–367.
- Bassim, N.D., De Gregorio, B.T., Kilcoyne, A.L.D., Scott, K., Chou, T., Wirick, S., Cody, G. and Stroud, R.M. (2012) Minimizing damage during FIB sample preparation of soft materials. *Journal of Microscopy* 245(3), 288-301.

- Beck A and Teboulle M (2009) Fast gradient-based algorithms for constrained total variation image denoising and deblurring problems. *IEEE Trans Image Process* 18(11):2419–2434.
- Beckers M, et al. (2011) Chemical contrast in soft X-ray ptychography. *Phys Rev Lett* 107(20):1–4.
- Beckhaus, P., Dokupil, M., Heinzl, A., Souzani, S. and Spitta, C. (2005) On-board fuel cell power supply for sailing yachts. *Journal of Power Sources* 145(2), 639-643.
- Beddar, A.S., Briere, T.M., Balter, P., Pan, T., Tolani, N., Ng, C., Szklaruk, J. and Krishnan, S. (2008) 4D-CT imaging with synchronized intravenous contrast injection to improve delineation of liver tumors for treatment planning. *Radiotherapy and Oncology* 87(3), 445-448.
- Beetz, T. and Jacobsen, C. (2003) Soft X-ray radiation-damage studies in PMMA using a cryo-STXM. *J. Synchrotron Rad.*, 10: 280-283.
- Berejnov, V., D. Susac, J. Stumper and A. P. Hitchcock (2011). Nano to Micro Scale Characterization of Water Uptake in The Catalyst Coated Membrane Measured by Soft X-ray Scanning Transmission X-ray Microscopy. *ECS Transactions* 41(1): 395-402.
- Berejnov, V., Susac, D., Stumper, J. and Hitchcock, A.P. (2013) 3D Chemical Mapping of PEM Fuel Cell Cathodes by Scanning Transmission Soft X-ray SpectroTomography. *ECS Transactions* 50(2), 361-368.
- Behyan, S., Haines, B., Karanukaran, C., Wang, J., Obst, M., Tyliczszak, T., and Urquhart, S.G., (2011) Surface Detection in a STXM Microscope. *AIP Conf. Proc.* 1365, 184–187.

- Biener, J., Stadermann, M., Suss, M., Worsley, M. A., Biener, M. M., Rose, K. A., and Baumann, T. F. (2011b) Advanced carbon aerogels for energy applications. *Energy Environ Sci* 4(3):656.
- Biener, M. M.; Biener, J., Wichmann, A., Wittstock, A., Baumann, T. F., Bäumer, M., and Hamza, A. V. (2011a) ALD functionalized nanoporous gold: Thermal stability, mechanical properties, and catalytic activity. *Nano Lett* 11(8):3085–3090.
- Biener, M.M., Biener, J., Wang, Y.M., Shin, S.J., Tran, I.C., Willey, T.M., Pérez, F.N., Poco, J.F., Gammon, S.A., Fournier, K.B., van Buuren, A.W., Satcher, J.H. and Hamza, A.V. (2013) Atomic Layer Deposition-Derived Ultra-Low-Density Composite Bulk Materials with Deterministic Density and Composition. *ACS Applied Materials & Interfaces* 5(24), 13129-13134.
- Bilbao-Castro, J.R., Carazo, J.M., García, I. and Fernández, J.J. (2006) Parallelization of reconstruction algorithms in three-dimensional electron microscopy. *Applied Mathematical Modelling* 30(8), 688-701.
- Boerckel, J.D., Mason, D.E., McDermott, A.M. and Alsberg, E. (2014) Microcomputed tomography: approaches and applications in bioengineering. *Stem Cell Research & Therapy* 5(6), 144.
- Bonanno, G., Coppo, S., Modregger, P., Pellegrin, M., Stuber, A., Stampanoni, M., Mazzolai, L., Stuber, M. and van Heeswijk, R.B. (2015) Ultra-high-resolution 3D imaging of atherosclerosis in mice with synchrotron differential phase contrast: a proof of concept study. *Scientific Reports* 5, 11980.
- Brenner, D.J. and Hall, E.J. (2007) Computed Tomography — An Increasing Source of Radiation Exposure. *New England Journal of Medicine* 357(22), 2277-2284.

- Brune, C. (2010) 4D imaging in tomography and optical nanoscopy. Dissertation, PhD Thesis, Münster (Westfalen) University.
- Bunk, O., Dierolf, M., Kynde, S., Johnson, I., Marti, O. and Pfeiffer, F. (2008) Influence of the overlap parameter on the convergence of the ptychographical iterative engine. *Ultramicroscopy* 108(5), 481-487.
- Burghardt, A.J., Link, T.M., and Majumdar, S. (2011) High-resolution Computed Tomography for Clinical Imaging of Bone Microarchitecture. *Clin. Orthop. Relat. Res.* 469, 2179-2193.
- C. Jacobsen, Wirick, S., Flynn, G. and Zimba, C. (2000) Soft X-ray Spectroscopy from Image Sequences with Sub-100 nm Spatial Resolution. *J. Microscopy* 197, 10.
- Cabaret D, Sainctavit P, Ildefonse P, and Flank A-M (1996) Full multiple-scattering calculations on silicates and oxides at the Al K edge. *J Phys: Condes Matter* 8:3691.
- Cai, J., S. Kimura, M. Wada and S. Kuga (2009). Nanoporous Cellulose as Metal Nanoparticles Support. *Biomacromolecules* 10(1): 87-94.
- Campbell, S. (2002) 4D, or not 4D: that is the question. *Ultrasound in Obstetrics & Gynecology* 19(1), 1-4.
- Chao, W., Fischer, P., Tyliczszak, T., Rekawa, S., Anderson, E. and Naulleau, P. (2012) Real space soft x-ray imaging at 10 nm spatial resolution. *Optics Express* 20(9), 9777-9783.
- Chao, W., Harteneck, B.D., Liddle, J.A., Anderson, E.H. and Attwood, D.T. (2005) Soft X-ray microscopy at a spatial resolution better than 15 nm. *Nature* 435, 1210.

- Chen C.Y., Lai K.Y., Lo J.W., Lin C.A., Chiu S.H., Chao Y.C., and He J.H. (2011) Electronic structures of well-aligned Er-doped ZnO nanorod arrays. *J Nanosci Nanotechnol* 11(12):10615–10619.
- Chen, J., Yang, Y., Zhang, X., Andrews, J.C., Pianetta, P., Guan, Y., Liu, G., Xiong, Y., Wu, Z. and Tian, Y. (2010) 3D nanoscale imaging of the yeast, *Schizosaccharomyces pombe*, by full-field transmission X-ray microscopy at 5.4 keV. *Anal Bioanal Chem* 397(6), 2117-2121.
- Cho, D.Y., Kim, J.H., Na, K.D., Song, J., Hwang, C.S., Park, B.G., Kim, J.Y., Min, C.H., and Oh, S.J. (2009) Spectroscopic evidence for limited carrier hopping interaction in amorphous ZnO thin film. *Appl. Phys. Lett.* 95, 261903:1–4.
- Colgan, R., McClelland, J., McQuaid, D., Evans, P.M., Hawkes, D., Brock, J., Landau, D. and Webb, S. (2008) Planning lung radiotherapy using 4D CT data and a motion model. *Physics in Medicine & Biology* 53(20), 5815.
- Cosmidis, J., Benzerara, K., Nassif, N., Tyliczszak, T. and Bourdelle, F. (2015) Characterization of Ca-phosphate biological materials by scanning transmission X-ray microscopy (STXM) at the Ca L_{2,3}-, P L_{2,3}- and C K-edges. *Acta Biomaterialia* 12, 260-269.
- Cosslett, V.E. (1978) Radiation damage in the high resolution electron microscopy of biological materials: A review. *Journal of Microscopy* 113(2), 113-129.
- Cretoiu, D., Hummel, E., Zimmermann, H., Gherghiceanu, M. and Popescu, L.M. (2014) Human cardiac telocytes: 3D imaging by FIB - SEM tomography. *Journal of Cellular and Molecular Medicine* 18(11), 2157-2164.

- Cullen, D.A., Koestner, R., Kukreja, R.S., Liu, Z.Y., Minko, S., Trotsenko, O., Tokarev, A., Guetaz, L., Meyer, H.M., Parish, C.M. and More, K.L. (2014) Imaging and Microanalysis of Thin Ionomer Layers by Scanning Transmission Electron Microscopy. *Journal of The Electrochemical Society* 161(10), F1111-F1117.
- David, A.S., Rich, C., Peter, D., Maryam, F., John, J., Kilcoyne, A.L.D., Stefano, M., Howard, P., Singanallur, V.V., Tony, W. and Young-Sang, Y. (2017) Ptychographic Imaging of Nano-Materials at the Advanced Light Source with the Nanosurveyor Instrument. *Journal of Physics: Conference Series* 849(1), 012028.
- De Chiffre, L., Carmignato, S., Kruth, J.P., Schmitt, R. and Weckenmann, A. (2014) Industrial applications of computed tomography. *CIRP Annals* 63(2), 655-677.
- Denes, P., Doering, D., Padmore, H.A., Walder, J.P. and Weizeorick, J. (2009) A fast, direct x-ray detection charge-coupled device. *Review of Scientific Instruments* 80(8), 083302.
- Dierolf, M., Menzel, A., Thibault, P., Schneider, P., Kewish, C.M., Wepf, R., Bunk, O. and Pfeiffer, F. (2010) Ptychographic X-ray computed tomography at the nanoscale. *Nature* 467(7314), 436-439.
- Doube M, Kłosowski M.M., Arganda-Carreras I, Cordelières F.P., Dougherty R.P., Jackson J.S., Schmid B., Hutchinson J.R., and Shefelbine S.J. (2010) BoneJ: Free and extensible bone image analysis in ImageJ. *Bone* 47(6):1076–1079.
- Dynes, J.J., Lawrence, J.R., Korber, D.R., Swerhone, G.D.W., Leppard, G.G., Hitchcock, A.P. (2006a) Quantitative mapping of chlorhexidine in natural river biofilms. *Sci. Total Environ.* 369, 369–383.

- Dynes, J.J., Tyliczszak, T., Araki, T., Lawrence, J.R., Swerhone, G.D.W., Leppard, G.G., Hitchcock, A.P. (2006b) Speciation and Quantitative Mapping of Metal Species in Microbial Biofilms Using Scanning Transmission X-ray Microscopy. *Environ. Sci. Technol.* 40, 1556–1565.
- Edo TB, et al. (2013) Sampling in x-ray ptychography. *Phys Rev A - At Mol Opt Phys* 87(5):1–8.
- Egerton, R.F. (2013) Control of radiation damage in the TEM. *Ultramicroscopy* 127, 100-108.
- Egerton, R.F., Li, P. and Malac, M. (2004) Radiation damage in the TEM and SEM. *Micron* 35(6), 399-409.
- Epting, W.K., Gelb, J. and Litster, S. (2012) Resolving the Three-Dimensional Microstructure of Polymer Electrolyte Fuel Cell Electrodes using Nanometer-Scale X-ray Computed Tomography. *Advanced Functional Materials* 22(3), 555-560.
- Esmaeili, M., Fløystad, J.B., Diaz, A., Høydalsvik, K., Guizar-Sicairos, M., Andreasen, J.W. and Breiby, D.W. (2013) Ptychographic X-ray Tomography of Silk Fiber Hydration. *Macromolecules* 46(2), 434-439.
- Farmand, M., Celestre, R., Denes, P., Kilcoyne, A.L.D., Marchesini, S., Padmore, H., Tyliczszak, T., Warwick, T., Shi, X., Lee, J., Yu, Y.S., Cabana, J., Joseph, J., Krishnan, H., Perciano, T., Maia, F.R.N.C., and Shapiro, D.A. (2017) Near-edge X-ray refraction fine structure microscopy. *Appl. Phys. Lett.* 110: 063101.
- Fathabadi, H. (2018) Fuel cell hybrid electric vehicle (FCHEV): Novel fuel cell/SC hybrid power generation system. *Energy Conversion and Management* 156, 192-201.

- Fishman, Z., Hinebaugh, J. and Bazylak, A. (2010) Microscale Tomography Investigations of Heterogeneous Porosity Distributions of PEMFC GDLs. *Journal of The Electrochemical Society* 157, B1643-B1650.
- Folkesson, A., Andersson, C., Alvfors, P., Alaküla, M. and Overgaard, L. (2003) Real life testing of a Hybrid PEM Fuel Cell Bus. *Journal of Power Sources* 118(1–2), 349-357.
- Garzon, F.H., Lau, S.H., Davey, J.R. and Borup, R. (2007) Micro And Nano X-Ray Tomography Of PEM Fuel Cell Membranes After Transient Operation. *ECS Transactions* 11(1), 1139-1149.
- Ge, X., Chen, L., Zhang, L., Wen, Y., Hirata, A. and Chen, M. (2014) Nanoporous metal enhanced catalytic activities of amorphous molybdenum sulfide for high-efficiency hydrogen production. *Adv Mater* 26(19):3100–3104.
- George, M.G., Wang, J., Banerjee, R. and Bazylak, A. (2016) Composition analysis of a polymer electrolyte membrane fuel cell microporous layer using scanning transmission X-ray microscopy and near edge X-ray absorption fine structure analysis. *Journal of Power Sources* 309, 254-259.
- Giewekemeyer K, et al. (2010) Quantitative biological imaging by ptychographic x-ray diffraction microscopy. *Proc Natl Acad Sci U S A* 107(2):529–534.
- Glaeser R. M. and Taylor K. A. (1978) Radiation damage relative to transmission electron microscopy of biological specimens at low temperature: a review. *Journal of Microscopy* 112(1), 127-138.
- Gontard, L.C., Dunin-Borkowski, R.E. and Ozkaya, D. (2008) Three-dimensional shapes and spatial distributions of Pt and PtCr catalyst nanoparticles on carbon black. *Journal of Microscopy* 232(2), 248-259.

- Goris B., Turner S., Bals S., and Tendeloo G Van (2014) Three-dimensional valency mapping in ceria nanocrystals. *ACS Nano* (10):10878–10884.
- Gros, M.A., McDermott, G., Larabell, C.A. (2005) X-ray tomography of whole cells. *Curr. Opin. Struct. Biol.* 15, 593–600.
- Grothausmann, R., Zehl, G., Manke, I., Fiechter, S., Bogdanoff, P., Dorbandt, I., Kupsch, A., Lange, A., Hentschel, M.P., Schumacher, G. and Banhart, J. (2011) Quantitative Structural Assessment of Heterogeneous Catalysts by Electron Tomography. *Journal of the American Chemical Society* 133(45), 18161-18171.
- Gurbuz, A. C., J. H. McClellan and W. R. Scott (2009). A Compressive Sensing Data Acquisition and Imaging Method for Stepped Frequency GPRs. *IEEE Transactions on Signal Processing* 57(7): 2640-2650.
- Haberfehlner, G., Orthacker, A., Albu, M., Li, J. and Kothleitner, G. (2014) Nanoscale voxel spectroscopy by simultaneous EELS and EDS tomography. *Nanoscale* 6(23), 14563-14569.
- Haddad, W.S., McNulty, I., Trebes, J.E., Anderson, E.H., Levesque, R.A. and Yang, L. (1994) Ultrahigh-Resolution X-ray Tomography. *Science* 266(5188), 1213.
- Hagen, C., Werner, S., Carregal-Romero, S., N. Malhas, A., G. Klupp, B., Guttman, P., Rehbein, S., Henzler, K., C. Mettenleiter, T., J. Vaux, D., J. Parak, W., Schneider, G. and Grünewald, K. (2014) Multimodal nanoparticles as alignment and correlation markers in fluorescence/soft X-ray cryo-microscopy/tomography of nucleoplasmic reticulum and apoptosis in mammalian cells. *Ultramicroscopy* 146, 46-54.
- Hay, S. J.; Metson, J. B. and Hyland, M. M. (2004) Sulfur speciation in aluminum smelting anodes. *Ind. Eng. Chem. Res.* 43 (7), 1690–1700.

- Haydel, M.J., Preston, C.A., Mills, T.J., Luber, S., Blaudeau, E. and DeBlieux, P.M.C. (2000) Indications for Computed Tomography in Patients with Minor Head Injury. *New England Journal of Medicine* 343(2), 100-105.
- He, Q., Chen, J., Keffer, D.J. and Joy, D.C. (2014) Electron beam induced radiation damage in the catalyst layer of a proton exchange membrane fuel cell. *Scanning* 36(3), 338-346.
- Helfen, L., Baumbach, T., Mikulík, P., Kiel, D., Pernot, P., Cloetens, P. and Baruchel, J. (2005) High-resolution three-dimensional imaging of flat objects by synchrotron-radiation computed laminography. *Applied Physics Letters* 86(7), 071915.
- Helfen, L., Myagotin, A., Mikulík, P., Pernot, P., Voropaev, A., Elyyan, M., Di Michiel, M., Baruchel, J. and Baumbach, T. (2011) On the implementation of computed laminography using synchrotron radiation. *Rev Sci Instrum* 82(6), 063702.
- Henke B.L., Gullikson E.M., and Davis J.C. (1993) X-ray interactions: Photoabsorption, scattering, transmission, and reflection at $E = 50\text{-}30,000$ eV, $Z = 1\text{-}92$. *At Data Nucl Data Tables* 54(2):181–342.
- Herdem, M.S., Farhad, S. and Hamdullahpur, F. (2015) Modeling and parametric study of a methanol reformat gas-fueled HT-PEMFC system for portable power generation applications. *Energy Conversion and Management* 101, 19-29.
- Hernández-Cruz, D., Hitchcock, A.P., Tyliczszak, T., Rousseau, M.-E., Pézolet, M., 2007. In situ azimuthal rotation device for linear dichroism measurements in scanning transmission x-ray microscopy. *Rev. Sci. Instrum.* 78, 33703.
- Higier, A., Hsu, L., Oiler, J., Phipps, A., Hooper, D. and Kerber, M. (2017) Polymer electrolyte fuel cell (PEMFC) based power system for long-term operation of leave-in-

- place sensors in Navy and Marine Corps applications. *International Journal of Hydrogen Energy* 42(7), 4706-4709.
- Hilhorst, J., van Schooneveld, M.M., Wang, J., de Smit, E., Tyliczszak, T., Raabe, J., Hitchcock, A.P., Obst, M., de Groot, F.M. and Petukhov, A.V. (2012) Three-dimensional structure and defects in colloidal photonic crystals revealed by tomographic scanning transmission X-ray microscopy. *Langmuir* 28(7), 3614-3620.
- Hitchcock AP (2012) Soft X-ray Imaging and Spectromicroscopy. *Handbook of Nanoscopy*, eds Van Tendeloo G, Van Dyck D, Pennycook JS (Wiley), pp 745–792.
- Hitchcock AP (2015) Soft X-ray spectromicroscopy and ptychography. *J Electron Spectros Relat Phenomena* 200:49–63.
- Hitchcock AP (2018) aXis2000 is written in Interactive Data Language (IDL). It is available free for non-commercial use from <http://unicorn.mcmaster.ca/aXis2000.html>.
- Hitchcock AP, Araki T, Ikeura-Sekiguchi H, Iwata N, Tani K (2003) 3-Dimensional chemical mapping of toners by serial section scanning transmission X-ray microscopy. *J Phys IV* 104(X-Ray Microscopy):509–512.
- Hitchcock AP, Wu, J., Lee, V., Appathurai, N., Tyliczszak, T., Shiu, H.-W., Shapiro, D. A., Berejnov, V., Susac, D., and Stumper, J. (2016) Progress in soft X-ray microscopy characterization of PEM fuel cell catalyst layers. *Microsc Microanal* 22(S3):1290–1291.
- Hitchcock AP, and Toney MF (2014) Spectromicroscopy and coherent diffraction imaging: Focus on energy materials applications. *J Synchrotron Radiat* 21(5):1019–1030.

- Hitchcock, A., Tyliczszak, T., Obst, M., Swerhone, G., & Lawrence, J. (2010). Improving Sensitivity in Soft X-ray STXM Using Low Energy X-ray Fluorescence. *Microscopy and Microanalysis*, 16(S2), 924-925.
- Hitchcock, A.P. (2015) Soft X-ray spectromicroscopy and ptychography. *Journal of Electron Spectroscopy and Related Phenomena* 200, 49-63.
- Hitchcock, A.P., Araki, T., Ikeura-Sekiguchi, H., Iwata, N. and Tani, K. (2003) 3D chemical mapping of toners by serial section scanning transmission X-ray microscopy. *J. Phys. IV France* 104, 509-512.
- Hitchcock, A.P., Johansson, G.A., Mitchell, G.E., Keefe, M.H. and Tyliczszak, T. (2008) 3-d chemical imaging using angle-scan nanotomography in a soft X-ray scanning transmission X-ray microscope. *Applied Physics A* 92(3), 447-452.
- Hitchcock, A.P., Morin, C., Zhang, X., Araki, T., Dynes, J., Stöver, H., Brash, J., Lawrence, J.R. and Leppard, G.G. (2005) Soft X-ray spectromicroscopy of biological and synthetic polymer systems. *Journal of Electron Spectroscopy and Related Phenomena* 144–147, 259-269.
- Hitchcock, A.P., Wang, J. and Obst, M. (2010) 3D Chemical Imaging with STXM Spectro-Tomography. *Microscopy and Microanalysis* 16(S2), 850-851.
- Holler, M., Diaz, a, Guizar-Sicairos, M., Karvinen, P., Färm, E., Härkönen, E., Ritala, M., Menzel, a, Raabe, J., Bunk, O. (2014) X-ray ptychographic computed tomography at 16 nm isotropic 3D resolution. *Sci Rep* 4:3857.
- Holzer, L. and Cantoni, M. (2012) Review of FIB-tomography. In *Nanofabrication Using Focused Ion and Electron Beams: Principles and Applications*, eds Utke I. Moshkalev S.A. Russell Ph., Oxford University Press, New York, NY.

- Horl A, Trugler A, Hohenester U (2013) Tomography of particle plasmon fields from electron energy loss spectroscopy. *Phys Rev Lett* 111(7):1–5.
- Hoshino, M., Uesugi, K., Takeuchi, A., Suzuki, Y. and Yagi, N. (2011) Development of x-ray laminography under an x-ray microscopic condition. *Rev Sci Instrum* 82(7), 073706.
- Howells, M., Jacobsen, C., Kirz, J., Feder, R., McQuaid, K. and Rothman, S. (1987) X-ray holograms at improved resolution: a study of zymogen granules. *Science* 238(4826), 514.
- Hwang, J.J., Wang, D.Y. and Shih, N.C. (2005) Development of a lightweight fuel cell vehicle. *Journal of Power Sources* 141(1), 108-115.
- Hwang, J.J., Wang, D.Y., Shih, N.C., Lai, D.Y. and Chen, C.K. (2004) Development of fuel-cell-powered electric bicycle. *Journal of Power Sources* 133(2), 223-228.
- Inkson, B.J., Mulvihill, M. and Möbus, G. (2001) 3D determination of grain shape in a FeAl-based nanocomposite by 3D FIB tomography. *Scripta Materialia* 45(7), 753-758.
- Jacobsen C, Wirick S, Flynn GJ, Zimba C (2000) Soft x-ray spectroscopy from image sequences with sub-100 nm spatial resolution. *J Microsc* 197:173–184.
- Jankovic, J., Susac, D., Soboleva, T. and Stumper, J. (2013) Electron Tomography Based 3D Reconstruction of Fuel Cell Catalysts. *ECS Transactions* 50(2), 353-359.
- Jarausch K, Thomas P, Leonard DN, Twesten R, Booth CR (2009) Four-dimensional STEM-EELS: enabling nano-scale chemical tomography. *Ultramicroscopy* 109(4):326–337.
- Jinnai, H. and Spontak, R.J. (2009) Transmission electron microtomography in polymer research. *Polymer* 50(5), 1067-1087.

- Johansson, G.A., Dynes, J.J., Hitchcock, A.P., Tyliczszak, T., Swerhone, G.D.W. and Lawrence, J.R. (2006) Chemically sensitive 3D imaging at sub 100 nm spatial resolution using tomography in a scanning transmission x-ray microscope, *Proc. SPIE* 6318, *Developments in X-Ray Tomography V.* 63181I-63186.
- Johansson, G.A., Tyliczszak, T., Mitchell, G.E., Keefe, M.H. and Hitchcock, A.P. (2007) Three-dimensional chemical mapping by scanning transmission X-ray spectromicroscopy. *J Synchrotron Radiat* 14(Pt 5), 395-402.
- Kato, Y., Shimizu, K., Matsushita, N., Yoshida, T., Yoshida, H., Satsuma, A., Hattori, T. (2001) Quantification of aluminium coordinations in alumina and silica – alumina by Al K-edge XANES. *Phys Chem Chem Phys* 3:1925–1929.
- Kaznachejev, K., Osanna, A., Jacobsen, C., Plashkevych, O., Vahtras, O., Ågren, Carravetta, V., Hitchcock, A.P. (2002) Innershell Absorption Spectroscopy of Amino Acids. *J. Phys. Chem. A* 106, 3153–3168.
- Kaznatcheev, K. V., Karunakaran, C., Lanke, U.D., Urquhart, S.G., Obst, M., Hitchcock, A.P. (2007) Soft X-ray spectromicroscopy beamline at the CLS: Commissioning results. *Nucl Instruments Methods Phys Res Sect A Accel Spectrometers, Detect Assoc Equip* 582(1):96–99.
- Khadivi K. O. (2006) *Computed Tomography: Fundamentals, System Technology, Image Quality, Applications*, 2nd edition. *Medical Physics* 33(8), 3076-3076.
- Kilcoyne, A.L.D., Tyliczszak, T., Steele, W.F., Fakra, S., Hitchcock, P., Franck, K., Harteneck, B., Rightor, E.G., Mitchell, G.E., Hitchcock, A.P., Yang, L. and Ade, H. (2003) Interferometer-controlled scanning transmission X-ray microscopes at the Advanced Light Source. *J. Synchrotron Radiation* 10, 125-136.

- Kim, B.M., Murray, T. and Bau, H.H. (2005) The fabrication of integrated carbon pipes with sub-micron diameters. *Nanotechnology* 16(8), 1317.
- Kimoto, K., Asaka, T., Nagai, T., Saito, M., Matsui, Y. and Ishizuka, K. (2007) Element-selective imaging of atomic columns in a crystal using STEM and EELS. *Nature* 450, 702.
- Kirz, J. and Jacobsen, C. (2009) The history and future of X-ray microscopy. *J. Phys. Conf. Ser.* 186, 12001..
- Koprinarov, I.N., Hitchcock, A.P., McCrory, C.T., Childs, R.F. (2002) Quantitative mapping of structured polymeric systems using singular value decomposition analysis of soft X-ray images. *J. Phys. Chem. B* 106, 5358–5364.
- Kyle, J.R. and Ketcham, R.A. (2015) Application of high resolution X-ray computed tomography to mineral deposit origin, evaluation, and processing. *Ore Geology Reviews* 65, 821-839.
- Lasagni, F., Lasagni, A., Engstler, M., Degischer, H.P. and Mücklich, F. (2008) Nano - characterization of Cast Structures by FIB - Tomography. *Advanced Engineering Materials* 10(1 - 2), 62-66.
- Lasagni, F., Lasagni, A., Marks, E., Holzapfel, C., Mücklich, F. and Degischer, H.P. (2007) Three-dimensional characterization of ‘as-cast’ and solution-treated AlSi12(Sr) alloys by high-resolution FIB tomography. *Acta Materialia* 55(11), 3875-3882.
- Lee Jin, H., Hargreaves Brian, A., Hu Bob, S. and Nishimura Dwight, G. (2003) Fast 3D imaging using variable - density spiral trajectories with applications to limb perfusion. *Magnetic Resonance in Medicine* 50(6), 1276-1285.

- Lee, V., D. Susac, S. Kundu, V. Berejnov, R. T. Atanasoski, A. P. Hitchcock and J. Stumper (2013). STXM Characterization of Nanostructured Thin Film Anode Before and After Start-Up Shutdown and Reversal Tests. *ECS Transactions* 58(1): 473-479.
- Leontowich A. F. G., Berg R., Regier C. N., Taylor D. M., Wang J., Beaugard D., Geilhufe J., Swirsky J., Wu J., Karunakaran C., Hitchcock A. P., and Urquhart S. G. (2018) Cryo scanning transmission X-ray microscope optimized for spectrotomography. *Review of Scientific Instruments*. In press.
arXiv:1808.05702
- Lepault, J. , Booy, F. P. and Dubochet, J. (1983), Electron microscopy of frozen biological suspensions. *Journal of Microscopy*, 129: 89-102.
- Lerotic, M., Mak, R., Wirick, S., Meirer, F. and Jacobsen, C (2014). Mantis: A Program for the Analysis of X-Ray Spectromicroscopy Data. *Journal of Synchrotron Radiation* 21 (5): 1206–1212.
- Li, J., Hitchcock, A.P., Stöver, H.D.H. and Shirley, I. (2009) A New Approach to Studying Microcapsule Wall Growth Mechanisms. *Macromolecules* 42(7), 2428-2432.
- Lin, M., Cheng, Y., Lin, M. and Yen, S. (2005) Evaluation of PEMFC power systems for UPS base station applications. *Journal of Power Sources* 140(2), 346-349.
- Litster, S. and McLean, G. (2004) PEM fuel cell electrodes. *Journal of Power Sources* 130(1–2), 61-76.
- Lockwood, G.R., Talman, J.R. and Brunke, S.S. (1998) Real-time 3-D ultrasound imaging using sparse synthetic aperture beamforming. *IEEE Transactions on Ultrasonics, Ferroelectrics, and Frequency Control* 45(4), 980-988.

- Lopez-Haro, M., Guétaz, L., Printemps, T., Morin, A., Escribano, S., Jouneau, P.H., Bayle-Guillemaud, P., Chandezon, F. and Gebel, G. (2014) Three-dimensional analysis of Nafion layers in fuel cell electrodes. *Nat Commun* 5.
- Lučić, V., Rigort, A. and Baumeister, W. (2013) Cryo-electron tomography: The challenge of doing structural biology in situ. *The Journal of Cell Biology* 202(3), 407-419.
- Luo, D., Y.-P. Deng, X. Wang, G. Li, J. Wu, J. Fu, W. Lei, R. Liang, Y. Liu, Y. Ding, A. Yu and Z. Chen (2017). Tuning Shell Numbers of Transition Metal Oxide Hollow Microspheres toward Durable and Superior Lithium Storage. *ACS Nano* 11(11): 11521-11530.
- Luo, Y., J. Xu and J. Huang (2014). Hierarchical nanofibrous anatase-titania-cellulose composite and its photocatalytic property. *CrystEngComm* 16(3): 464-471.
- Mack, F., Klages, M., Scholta, J., Jörissen, L., Morawietz, T., Hiesgen, R., Kramer, D. and Zeis, R. (2014) Morphology studies on high-temperature polymer electrolyte membrane fuel cell electrodes. *Journal of Power Sources* 255, 431-438.
- Marchesini S, et al. (2016) SHARP: A distributed GPU-based ptychographic solver. *J Appl Crystallogr* 49(4):1245–1252.
- Mark A Le Gros, Gerry McDermott, Carolyn A Larabell (2005) X-ray tomography of whole cells, *Current Opinion in Structural Biology*, 15 (5), 593-600.
- Markötter, H., Manke, I., Kuhn, R., Arlt, T., Kardjilov, N., Hentschel, M.P., Kupsch, A., Lange, A., Hartnig, C., Scholta, J. and Banhart, J. (2012) Neutron tomographic investigations of water distributions in polymer electrolyte membrane fuel cell stacks. *Journal of Power Sources* 219, 120-125.

- Maser J., Osanna A., Wang Y., Jacobsen C., Kirz J., Spector S., Winn B. and Tennant D. (2000) Soft X-ray microscopy with a cryo scanning transmission X-ray microscope: I. Instrumentation, imaging and spectroscopy. *Journal of Microscopy* 197(1), 68-79.
- McDermott, G., Le Gros, M.A. and Larabell, C.A. (2012) Visualizing Cell Architecture and Molecular Location Using Soft X-Ray Tomography and Correlated Cryo-Light Microscopy. *Annual Review of Physical Chemistry* 63(1), 225-239.
- McNulty, I., Kirz, J., Jacobsen, C., Anderson, E.H., Howells, M.R. and Kern, D.P. (1992) High-Resolution Imaging by Fourier Transform X-ray Holography. *Science* 256(5059), 1009.
- Medalia, O., Weber, I., Frangakis, A.S., Nicastro, D., Gerisch, G. and Baumeister, W. (2002) Macromolecular Architecture in Eukaryotic Cells Visualized by Cryoelectron Tomography. *Science* 298(5596), 1209-1213.
- Melo L.G.A. (2014) Characterization of Catalyst Coated Membranes using Electron and X-ray Microscopy. McMaster University.
- Melo L.G.A., Vincent Lee, Darija Susac, Viatcheslav Berejnov, Juergen Stumper, Gianluigi A. Botton, and Adam P. Hitchcock (2014) Effects of Sample Preparation Technique on Quantitative Analysis of Automotive Fuel Cell Catalyst Layers. *Microscopy and Microanalysis* 20, no. S3: 472–73.
- Melo, L.G.A., Hitchcock, A.P., Berejnov, V., Susac, D., Stumper, J., Botton, G.A., 2016. Evaluating focused ion beam and ultramicrotome sample preparation for analytical microscopies of the cathode layer of a polymer electrolyte membrane fuel cell. *J. Power Sources* 312, 23–35.

- Melo, L.G.A., Hitchcock, A.P., Jankovic, J., Stumper, J., Susac, D. and Berejnov, V. (2017) Quantitative Mapping of Ionomer in Catalyst Layers by Electron and X-ray Spectromicroscopy. *ECS Transactions* 80(8), 275-282.
- Miao J, Ishikawa T, Robinson IK, Murnane MM (2015) Beyond crystallography: Diffractive imaging using coherent x-ray light sources. *Science* 348(6234):530–535.
- Miao J, Sandberg RL, Song C (2012) Coherent X-ray diffraction imaging. *IEEE J Sel Top Quantum Electron* 18(1):399–410.
- Minutillo, M., Forcina, A., Jannelli, N. and Lubrano Lavadera, A. (2018) Assessment of a sustainable energy chain designed for promoting the hydrogen mobility by means of fuel-cell powered bicycles. *Energy* 153, 200-210.
- Möbus, G., Doole, R.C. and Inkson, B.J. (2003) Spectroscopic electron tomography. *Ultramicroscopy* 96(3), 433-451.
- Moffat, A.J., Wright, P., Helfen, L., Baumbach, T., Johnson, G., Spearing, S.M. and Sinclair, I. (2010) In situ synchrotron computed laminography of damage in carbon fibre–epoxy [90/0]s laminates. *Scripta Materialia* 62(2), 97-100.
- Mor-Avi, V., Sugeng, L., Weinert, L., MacEneaney, P., Caiani, E.G., Koch, R., Salgo, I.S. and Lang, R.M. (2004) Fast Measurement of Left Ventricular Mass With Real-Time Three-Dimensional Echocardiography. *Circulation* 110(13), 1814.
- Morin, C., Ikeura-Sekiguchi, H., Tyliczszak, T., Cornelius, R., Brash, J.L., Hitchcock, A.P., Scholl, A., Nolting, F., Appel, G., Winesett, D.A., Kaznacheyev, K. and Ade, H. (2001) X-ray spectromicroscopy of immiscible polymer blends: polystyrene–poly(methyl methacrylate). *Journal of Electron Spectroscopy and Related Phenomena* 121(1–3), 203-224.

- Murphy, G.E. and Jensen, G.J. (2007) Electron Cryotomography. *Biotech* 43(4), 5.
- Nan, F., Song, C., Zhang, J., Hui, R., Chen, J., Fairbridge, C. and Botton, G.A. (2011) STEM HAADF Tomography of Molybdenum Disulfide with Mesoporous Structure. *ChemCatChem* 3(6), 999-1003.
- Nelson, G.J., Harris, W.M., Lombardo, J.J., Izzo, J.R., Chiu, W.K.S., Tanasini, P., Cantoni, M., Van herle, J., Comninellis, C., Andrews, J.C., Liu, Y., Pianetta, P. and Chu, Y.S. (2011) Comparison of SOFC cathode microstructure quantified using X-ray nanotomography and focused ion beam–scanning electron microscopy. *Electrochemistry Communications* 13(6), 586-589.
- Norlund, K.L.I., Southam, G., Tyliczszak, T., Hu, Y. Karunakaran, C. , Obst, M., Hitchcock, A.P. and Warren, L.A. (2009) A novel syntrophic microbial sulphur metabolising consortia: new evidence for microbial global carbon cycling, *Environmental Science & Technology* 43 8781–8786.
- Obst, M. and Schmid, G. (2014) Electron Microscopy. Kuo, J. (ed), pp. 757-781, Humana Press.
- Obst, M., Wang, J. and Hitchcock, A.P. (2009a) 3-d chemical imaging with STXM tomography. *Journal of Physics: Conference Series* 186, 012045.
- Obst, M., Wang, J. and Hitchcock, A.P. (2009b) Soft X-ray spectro-tomography study of cyanobacterial biomineral nucleation. *Geobiology* 7(5), 577-591.
- Ohigashi, T., Inagaki, Y., Ito, A., Shinohara, K. and Kosugi, N. (2017) Investigation of Measurement Condition for 3-Dimensional Spectroscopy by Scanning Transmission X-ray Microscopy. *Journal of Physics: Conference Series* 849, 012044.

- Osanna, A., Jacobsen, C.J., Kirz, J., Sheynkin, Y.R. (2001) Cryogenic scanning transmission microscopy for biochemical analysis of the sperm. *Fertil. Steril.* 76, S265.
- Ortiz, J.O., Brandt, F., Matias, V.R.F., Sennels, L., Rappsilber, J., Scheres, S.H.W., Eibauer, M., Hartl, F.U. and Baumeister, W. (2010) Structure of hibernating ribosomes studied by cryoelectron tomography in vitro and in situ. *The Journal of Cell Biology* 190(4), 613-621.
- Otón, J., Sorzano, C.O.S., Chichón, F.J., Carrascosa, J.L., Carazo, J.M. and Marabini, R. (2014) Computational Methods for Three-Dimensional Microscopy Reconstruction. Herman, G.T. and Frank, J. (eds), pp. 187-220, Springer New York, New York, NY.
- Otsu N (1975) A threshold selection method from gray-level histograms. *Automatica* 11:23–27.
- Otsu, N. (1979) A Threshold Selection Method from Gray-Level Histograms. *IEEE Transactions on Systems, Man and Cybernetics* 9, 62-66.
- Pan, T., Lee, T.Y., Rietzel, E. and Chen George, T.Y. (2004) 4D - CT imaging of a volume influenced by respiratory motion on multi - slice CT. *Medical Physics* 31(2), 333-340.
- Papadopoulos, N., Tsourlos, P.I., Tsokas, G.N. and Sarris, A. (2007) Efficient ERT Measuring and Inversion Strategies for 3D Imaging of Buried Antiquities.
- Parkinson, D.Y., McDermott, G., Etkin, L.D., Le Gros, M.A. and Larabell, C.A. (2008) Quantitative 3-D imaging of eukaryotic cells using soft X-ray tomography. *Journal of Structural Biology* 162(3), 380-386.

- Pettersen, E.F., Goddard, T.D., Huang, C.C., Couch, G.S., Greenblatt, D.M., Meng, E.C. and Ferrin, T.E. (2004) UCSF Chimera—A visualization system for exploratory research and analysis. *Journal of Computational Chemistry* 25(13), 1605-1612.
- Plauche F. (1978) Fuel Cells Power the Space Shuttle Orbiter. *Electrical Review* 202.
- Poco, J.F., Satcher, J.H. and Hrubesh, L.W. (2001) Synthesis of high porosity, monolithic alumina aerogels. *Journal of Non-Crystalline Solids* 285(1), 57-63.
- Porat, Z.e., Fryer, J.R., Huxham, M. and Rubinstein, I. (1995) Electron Microscopy Investigation of the Microstructure of Nafion Films. *The Journal of Physical Chemistry* 99(13), 4667-4671.
- Pranger, L. and R. Tannenbaum (2008). Biobased Nanocomposites Prepared by In Situ Polymerization of Furfuryl Alcohol with Cellulose Whiskers or Montmorillonite Clay. *Macromolecules* 41(22): 8682-8687.
- Prieto, G. (2015) Encyclopedia of Membranes. Drioli, E. and Giorno, L. (eds), pp. 1-3, Springer Berlin Heidelberg, Berlin, Heidelberg.
- Putz, A.M.V., Susac, D., Berejnov, V., Wu, J., Hitchcock, A.P., Stumper, J. (2016) (Plenary) Doing More with Less: Challenges for Catalyst Layer Design. *ECS Trans.* 75, 3–23.
- Qiu S, Zhao F, Zenasni O, Li J, Shih WC (2016) Nanoporous Gold Disks Functionalized with Stabilized G-Quadruplex Moieties for Sensing Small Molecules. *ACS Appl Mater Interfaces* 8(44):29968–29976.
- Rightor, E.G., Hitchcock, A.P., Ade, H., Leapman, R.D., Urquhart, S.G., Smith, A.P., Mitchell, G., Fischer, D., Shin, H.J. and Warwick, T. (1997) Spectromicroscopy of Poly(ethylene terephthalate): Comparison of Spectra and Radiation Damage Rates in

- X-ray Absorption and Electron Energy Loss. *The Journal of Physical Chemistry B* 101(11), 1950-1960.
- Rodenburg JM, Hurst AC, Cullis AG, Dobson BR, Pfeiffer F, Bunk O, David C, Jefimovs K, Johnson I.. (2007) Hard-X-ray lensless imaging of extended objects. *Phys Rev Lett* 98(3):1–4.
- Rodenburg, J.M. (2008) Ptychography and Related Diffractive Imaging Methods. *Advances in Imaging and Electron Physics*. Hawkes (ed), pp. 87-184, Elsevier.
- Ruijiang, L., John, H.L., Laura, I.C. and Steve, B.J. (2009) 4D CT sorting based on patient internal anatomy. *Physics in Medicine & Biology* 54(15), 4821.
- Rustin, G.J., Mead, G.M., Stenning, S.P., Vasey, P.A., Aass, N., Huddart, R.A., Sokal, M.P., Joffe, J.K., Harland, S.J., Kirk, S.J. and National Cancer Research Institute Testis Cancer Clinical Studies, G. (2007) Randomized trial of two or five computed tomography scans in the surveillance of patients with stage I nonseminomatous germ cell tumors of the testis: Medical Research Council Trial TE08, ISRCTN56475197--the National Cancer Research Institute Testis Cancer Clinical Studies Group. *J Clin Oncol* 25(11), 1310-1315.
- Saida, T., Sekizawa, O., Ishiguro, N., Hoshino, M., Uesugi, K., Uruga, T., Ohkoshi, S., Yokoyama, T. and Tada, M. (2012) 4D visualization of a cathode catalyst layer in a polymer electrolyte fuel cell by 3D laminography-XAFS. *Angew Chem Int Ed Engl* 51(41), 10311-10314.
- Salvemini, F., Grazzi, F., Kardjilov, N., Manke, I., Civita, F. and Zoppi, M. (2015) Neutron computed laminography on ancient metal artefacts. *Anal. Methods* 7(1), 271-278.

- Salvo, L., Suéry, M., Marmottant, A., Limodin, N. and Bernard, D. (2010) 3D imaging in material science: Application of X-ray tomography. *Comptes Rendus Physique* 11(9), 641-649.
- Sansoni, G. and Docchio, F. (2004) Three-dimensional optical measurements and reverse engineering for automotive applications. *Robotics and Computer-Integrated Manufacturing* 20(5), 359-367.
- Sansoni, G., Trebeschi, M. and Docchio, F. (2009) State-of-The-Art and Applications of 3D Imaging Sensors in Industry, Cultural Heritage, Medicine, and Criminal Investigation. *Sensors* 9(1).
- Schmid, G., Zeitvogel, F., Hao, L., Ingino, P., Kuerner, W., Dynes, J.J., Karunakaran, C., Wang, J., Lu, Y., Ayers, T., Schietinger, C., Hitchcock, A.P., Obst, M. (2014) Synchrotron-Based Chemical Nano-Tomography of Microbial Cell-Mineral Aggregates in their Natural, Hydrated State. *Microsc. Microanal.* 20, 531–536.
- Schmid G, Obst M, Wu J, Hitchcock AP (2016) 3D Chemical Imaging of Nanoscale Biological, Environmental, and Synthetic Materials by Soft X-Ray STXM Spectrotomography. *X-Ray and Neutron Techniques for Nanomaterials Characterization*, ed C.S.S.R. Kumar (Springer-Verlag, Berlin Heidelberg), pp 43–94.
- Segars, W.P., Mahesh, M., Beck, T.J., Frey, E.C. and Tsui, B.M.W. (2008) Realistic CT simulation using the 4D XCAT phantom. *Medical Physics* 35(8), 3800-3808.
- Seynaeve PC, B.J. (1995) The history of tomography. *J Belge Radiol.* 78(5), 5.
- Shalaby, W.A., Saad, W., Shokair, M. and Dessouky, M. (2017) Efficient Parameters for Compressed Sensing Recovery Algorithms. *Wireless Personal Communications* 94(3), 1715-1736.

- Shapiro DA, Celestre R, Denes P, Farmand M (2016) Ptychographic Imaging of Nano-Materials at the Advanced Light Source with the Nanosurveyor Instrument. *J Phys Conf Ser* 849:12028-1–5.
- Shapiro, D., Thibault, P., Beetz, T., Elser, V., Howells, M., Jacobsen, C., Kirz, J., Lima, E., Miao, H., Neiman, A.M. and Sayre, D. (2005) Biological imaging by soft x-ray diffraction microscopy. *Proceedings of the National Academy of Sciences* 102(43), 15343.
- Shapiro, D.A., Yu, Y.-S., Tyliczszak, T., Cabana, J., Celestre, R., Chao, W., Kaznatcheev, K., Kilcoyne, A.L.D., Maia, F., Marchesini, S., Meng, Y.S., Warwick, T., Yang, L.L. and Padmore, H.A. (2014) Chemical composition mapping with nanometre resolution by soft X-ray microscopy. *Nat. Photonics* 8(10), 765-769.
- She, F.H., Nihara, K., Gao, W.M., Hodgson, P.D., Jinnai, H. and Kong, L.X. (2010) 3-Dimensional characterization of membrane with nanoporous structure using TEM tomography and image analysis. *Desalination* 250(2), 757-761.
- Sinha, P.K., Halleck, P. and Wang, C.-Y. (2006) Quantification of Liquid Water Saturation in a PEM Fuel Cell Diffusion Medium Using X-ray Microtomography. *Electrochemical and Solid-State Letters* 9(7), A344-A348.
- Slater TJA, et al. (2016) STEM-EDX tomography of bimetallic nanoparticles: A methodological investigation. *Ultramicroscopy* 162(5):61–73.
- Slowko, W. and Krysztof, M. (2014) Detector System for Three-Dimensional Imaging in the Variable Pressure/Environmental SEM. *Acta Phys. Pol A* 123: 877-879.

- Star, A.G. and Fuller, T.F. (2017) FIB-SEM Tomography Connects Microstructure to Corrosion-Induced Performance Loss in PEMFC Cathodes. *Journal of The Electrochemical Society* 164(9), F901-F907.
- Stöhr, J. (1992) *NEXAFS Spectroscopy*, Springer-Verlag, Berlin.
- Sun, S., Yao, Y., Zou, X., Fan, S., Zhou, Q., Dai, Q., Dong, F., Liu, M., Nie, X., Tan, D. and Li, S. (2014) Nano-Scale Spatial Assessment of Calcium Distribution in Coccolithophores Using Synchrotron-Based Nano-CT and STXM-NEXAFS. *International Journal of Molecular Sciences* 15(12).
- Susac, D., Berejnov, V., Hitchcock, A.P. and Stumper, J. (2013) STXM Characterization of PEM Fuel Cell Catalyst Layers. *ECS Transactions* 50(2), 405-413.
- Susac, D., V. Berejnov, A. P. Hitchcock and J. Stumper (2011). STXM Study of the Ionomer Distribution in the PEM Fuel Cell Catalyst Layers. *ECS Transactions* 41(1): 629-635.
- Takahashi, Y., Suzuki, A., Zettsu, N., Kohmura, Y., Senba, Y., Ohashi, H., Yamauchi, K. and Ishikawa, T. (2011) Towards high-resolution ptychographic x-ray diffraction microscopy. *Physical Review B* 83(21), 214109.
- Thevenaz P, Ruttimann UE, and Unser M (1998) A pyramid approach to subpixel registration based on intensity. *IEEE Trans Image Process* 7(1):27–41.
- Thibault P, Dierolf M, Bunk O, Menzel A, and Pfeiffer F (2009) Probe retrieval in ptychographic coherent diffractive imaging. *Ultramicroscopy* 109(4):338–343.
- Thibault P, Guizar-Sicairos M, and Menzel A (2014) Coherent imaging at the diffraction limit. *J Synchrotron Radiat* 21(5):1011–1018.

- Thiele, S., Fürstehaupt, T., Banham, D., Hutzenlaub, T., Birss, V., Ziegler, C. and Zengerle, R. (2013) Multiscale tomography of nanoporous carbon-supported noble metal catalyst layers. *Journal of Power Sources* 228, 185-192.
- Tkachuk, A., Duerwer, F., Cui, H., Feser, M., Wang, S. and Yun, W. (2009) X-ray computed tomography in Zernike phase contrast mode at 8 keV with 50-nm resolution using Cu rotating anode X-ray source. *Crystalline Materials* 222(11/2007), 6.
- Torruella, P., Arenal, R., de la Peña, F., Saghi, Z., Yedra, L., Eljarrat, A., López-Conesa, L., Estrader, M., López-Ortega, A., Salazar-Alvarez, G., Nogués, J., Ducati, C., Midgley, P.A., Peiró, F., and Estradé, S. (2016) 3D Visualization of the iron oxidation state in FeO/Fe₃O₄ core – shell nanocubes from electron energy loss tomography. *Nano Lett* 16(6):5068–5073.
- Tüber, K., Zobel, M., Schmidt, H. and Hebling, C. (2003) A polymer electrolyte membrane fuel cell system for powering portable computers. *Journal of Power Sources* 122(1), 1-8.
- Tyliszczak, T., Warwick, T., Kilcoyne, A.L.D., Fakra, S., Shuh, D.K., Yoon, T.H., Brown, G.E., Andrews, S., Chembrolu, V., Strachan, J. and Acremann, Y. (2004) Soft X - ray Scanning Transmission Microscope Working in an Extended Energy Range at the Advanced Light Source. *AIP Conference Proceedings* 705(1), 1356-1359.
- Venkatakrishnan, S. V., Farmand, M., Yu, Y.S., Majidi, H., Van Benthem, K., Marchesini, S., Shapiro, D.A., Hexemer, A. (2016) Robust X-Ray Phase Ptycho-Tomography. *IEEE Signal Process Lett* 23(7):944–948.
- Vivet, N., Chupin, S., Estrade, E., Piquero, T., Pommier, P.L., Rochais, D. and Bruneton, E. (2011) 3D Microstructural characterization of a solid oxide fuel cell anode

- reconstructed by focused ion beam tomography. *Journal of Power Sources* 196(18), 7541-7549.
- Wang, C., Xu, Z., Liu, H., Wang, Y., Wang, J., Tai, R. (2017) Background noise removal in x-ray ptychography. *Appl. Opt.* 56, 2099–2111.
- Wang, M., Ren, F., Zhou, J., Cai, G., Cai, L., and Hu, Y. (2015b) N Doping to ZnO Nanorods for photoelectrochemical water splitting under visible light: engineered impurity distribution and terraced band structure. *Sci Rep* 5(12925):1–13.
- Wang X, Langelier B, Palmquist A, Grandfield K (2015a) Biomineralization at Interfaces Revealed with 4D Electron and Atom Probe Tomographies. *Microsc Microanal* 21(S3):83–84.
- Wang, C., Mao, Z., Bao, F., Li, X. and Xie, X. (2005) Development and performance of 5 kw proton exchange membrane fuel cell stationary power system. *International Journal of Hydrogen Energy* 30(9), 1031-1034.
- Wang, J., Botton, G.A., West, M.M. and Hitchcock, A.P. (2009b) Quantitative Evaluation of Radiation Damage to Polyethylene Terephthalate by Soft X-rays and High-energy Electrons. *The Journal of Physical Chemistry B* 113(7), 1869-1876.
- Wang, J., Hitchcock, A.P., Karunakaran, C., Prange, A., Franz, B., Harkness, T., Lu, Y., Obst, M. and Hormes, J. (2011c) 3D Chemical and Elemental Imaging by STXM Spectrotomography. *AIP Conference Proceedings* 1365(1), 215-218.
- Wang, J., Morin, C., Li, L., Hitchcock, A.P., Scholl, A. and Doran, A. (2009a) Radiation damage in soft X-ray microscopy. *Journal of Electron Spectroscopy and Related Phenomena* 170(1–3), 25-36.

- Wang, Jacobsen, Maser and Osanna (2000) Soft X-ray microscopy with a cryo scanning transmission X-ray microscope: II. Tomography. *Journal of Microscopy* 197(1), 80-93.
- Wang, Y., Chen, K.S., Mishler, J., Cho, S.C. and Adroher, X.C. (2011a) A review of polymer electrolyte membrane fuel cells: Technology, applications, and needs on fundamental research. *Applied Energy* 88(4), 981-1007.
- Wee, J.-H. (2007) Applications of proton exchange membrane fuel cell systems. *Renewable and Sustainable Energy Reviews* 11(8), 1720-1738.
- Westenberger, P. (2008) Avizo—Three-Dimensional Visualization Framework, p. 13—14.
- Weyland, M. and Midgley, P.A. (2004) Electron tomography. *Materials Today* 7(12), 32-40.
- Wildenschild, D., Vaz, C.M.P., Rivers, M.L., Rikard, D. and Christensen, B.S.B. (2002) Using X-ray computed tomography in hydrology: systems, resolutions, and limitations. *Journal of Hydrology* 267(3–4), 285-297.
- Willi, A.K. (2006) X-ray computed tomography. *Physics in Medicine and Biology* 51(13), R29.
- Wise, A.M., Weker, J.N., Kalirai, S., Farmand, M., Shapiro, D.A., Meirer, F., Weckhuysen, B.M., et al. (2016) Nanoscale chemical imaging of an individual catalyst particle with soft X-ray ptychography. *ACS Catal* 6:2178-2181.
- Wu, J., Lerotic, M., Collins, S., Leary, R., Saghi, Z., Midgley, P., Berejnov, S., Susac, D., Stumper, J., Singh, G., and Hitchcock, A. P. (2017) Optimization of Three-Dimensional (3D) Chemical Imaging by Soft X-Ray Spectro-Tomography Using a Compressed Sensing Algorithm. *Microscopy and Microanalysis* 23, no. 5: 951–966.

- Wu, J., Melo, L.G.A., Zhu, X., West, M.M., Berejnov, V., Susac, D., Stumper, J. and Hitchcock, A.P. (2018) 4D imaging of polymer electrolyte membrane fuel cell catalyst layers by soft X-ray spectro-tomography. *Journal of Power Sources* 381, 72-83.
- Xia, J., Ip, H.H.S., Samman, N., Wang, D., Kot, C.S.B., Yeung, R.W.K. and Tideman, H. (2000) Computer-assisted three-dimensional surgical planning and simulation: 3D virtual osteotomy. *International Journal of Oral and Maxillofacial Surgery* 29(1), 11-17.
- Xiao-chen Bai, Greg McMullan, Sjors H.W Scheres (2015) How cryo-EM is revolutionizing structural biology, *Trends in Biochemical Sciences*, 40 (1), 49-57.
- Xu, F., Helfen, L., Baumbach, T. and Suhonen, H. (2012a) Comparison of image quality in computed laminography and tomography. *Opt. Express* 20, 13.
- Xu, F., Helfen, L., Suhonen, H., Elgrabli, D., Bayat, S., Reischig, P., Baumbach, T., Cloetens, P., (2012b) Correlative Nanoscale 3D Imaging of Structure and Composition in Extended Objects. *PLoS One* 7(11):1–6.
- Yang, F., Liu, Y., Martha, S.K., Wu, Z., Andrews, J.C., Ice, G.E., Pianetta, P., and Nanda, J. (2014) Nanoscale morphological and chemical changes of high voltage lithium-manganese rich NMC composite cathodes with cycling. *Nano Lett* 14(8):4334–4341.
- Yang, S.; Deng, B.; Ge, R.; Zhang, L.; Wang, H.; Zhang, Z.; Zhu, W.; Wang, G. (2014) Electrodeposition of porous graphene networks on nickel foams as supercapacitor electrodes with high capacitance and remarkable cyclic stability. *Nanoscale Res Lett* 9(1):672.

- Ye J, Baumgaertel AC, Wang YM, Biener J, Biener MM (2015) Structural optimization of 3D porous electrodes for high-rate performance lithium ion batteries. *ACS Nano* 9(2):2194–2202.
- Yedra, L., Eljarrat, A., Rebled, J.M., Lopez-Conesa, L., Dix, N., Sanchez, F., Estrade, S. and Peiro, F. (2014) EELS tomography in multiferroic nanocomposites: from spectrum images to the spectrum volume. *Nanoscale* 6(12), 6646-6650.
- Yu, Y., Xin, H.L., Hovden, R., Wang, D., Rus, E.D., Mundy, J.A., Muller, D.A. and Abruña, H.D. (2012) Three-Dimensional Tracking and Visualization of Hundreds of Pt–Co Fuel Cell Nanocatalysts During Electrochemical Aging. *Nano Letters* 12(9), 4417-4423.
- Yu, Y.S., Farmand, M., Kim, C., Liu, Y., Grey, C.P., Strobridge, F.C., Tyliszczak, T., Celestre, R., Denes, P., Joseph, J., Krishnan, H., Maia, F.R.N.C., Kilcoyne, A.L.D., Marchesini, S., Leite, T.P.C., Warwick, T., Padmore, H., Cabana, J., and Shapiro, D.A. (2018) Three dimensional localization of nanoscale battery reactions using soft X-ray tomography. *Nat Comm* 9(921):1–7.
- Yu, Y.S., Kim, C., Shapiro, D.A., Farmand, M., Qian, D., Tyliszczak, T., Kilcoyne, A.L.D., Celestre, R., Marchesini, S., Joseph, J., Denes, P., Warwick, T., Strobridge, F.C., Grey, C.P., Padmore, H., Meng, Y.S., Kostecki, R. and Cabana, J. (2015) Dependence on Crystal Size of the Nanoscale Chemical Phase Distribution and Fracture in Li_xFePO_4 . *Nano Letters* 15(7), 4282-4288.
- Yuste M, Escobar Galindo R, Caretti I, Torres R, and Sanchez O (2012) Influence of the oxygen partial pressure and post-deposition annealing on the structure and optical

- properties of ZnO films grown by dc magnetron sputtering. *J Phys D Appl Phys* 45:25303.
- Zenyuk, I.V., Parkinson, D.Y., Hwang, G. and Weber, A.Z. (2015) Probing water distribution in compressed fuel-cell gas-diffusion layers using X-ray computed tomography. *Electrochemistry Communications* 53, 24-28.
- Zewail, A.H. (2010) Four-Dimensional Electron Microscopy. *Science* 328 (5975), 187.
- Zhang, T., Orton Nigel, P. and Tomé Wolfgang, A. (2005) On the automated definition of mobile target volumes from 4D - CT images for stereotactic body radiotherapy. *Medical Physics* 32(11), 3493-3502.
- Zhao, Z. L.; Wang, Q.; Zhang, L. Y.; An, H. M.; Li, Z.; Li, C. M. (2018) Galvanic exchange-formed ultra-low Pt loading on synthesized unique porous Ag-Pd nanotubes for increased active sites toward oxygen reduction reaction. *Electrochim Acta* 263:209–216.
- Zhu X, et al. (2016) Measuring spectroscopy and magnetism of extracted and intracellular magnetosomes using soft X-ray ptychography. *Proc Natl Acad Sci U S A* 113:E8219–E8227.
- Zhu X, Hitchcock AP, Bittencourt C, Umek P, Krüger P (2015) Individual titanate nanoribbons studied by 3D-resolved polarization dependent X-ray absorption spectra measured with scanning transmission X-ray microscopy. *J Phys Chem C* 119(42):24192–24200.
- Ziegler, C., Thiele, S. and Zengerle, R. (2011) Direct three-dimensional reconstruction of a nanoporous catalyst layer for a polymer electrolyte fuel cell. *Journal of Power Sources* 196(4), 2094-2097.

Appendix I List of software

This appendix lists all the softwares that used for this thesis.

1. AUTOCAD 2013

AUTOCAD 2013 was used for the design of the modification of Laminography sample rotator.

2. Avizo 9.0

Avizo 9.0 was used for the visualization, volume rendering, segmentation, and quantification of the 3D/4D volumes.

3. aXis2000

aXis2000 was used to analysis all the STXM data.

4. ImageJ (FIJI)

ImageJ was used for image visualization, calculation, alignment, and 3D reconstruction.

5. Mantis v.2.3

Mantis (by Mirna Lerotic) was used for 3D reconstruction, and 4D reconstruction.

6. SigmaPlot 6.0

SigmaPlot was used to plot spectroscopy and graphs.

7. STXM rotator v.3.5

STXM rotator was used to control the tomography/laminography step rotation.

8. UCSF Chimera

Chimera was used for visualization, volume rendering, segmentation of 3D/4D volumes.

Appendix II Laminography

This appendix presents the progress of soft X-ray microscopy laminography.

STXM laminography measurements has been done for several different samples. The experiments are listed in **Table A.1**. A magnetite sample was measured at 704 eV and 709.6 eV. The tilt angle was 20°, and the rotation range is 0° to 360° with 4° increment. The Fe maps were generated by subtracting the pre edge signal at 704 eV from the peak signal at 709.6 eV (**Fig. A.1**). **Figure A.2** shows the Fe maps at different rotation positions.

Laminography of a PEMFC cathode catalyst sample was measured at CLS STXM with a rotation axis tilt of 30°. Two energies (278 eV, 284.5 eV) were used at the C1s edge, and 684 eV, 693 eV were used at the F 1s edge. The angle scan range was from 0° to 360° with 10° increment. **Figure A.3** shows some of the carbon support maps at different rotation positions. A change of the shape around the center hole can be seen, which indicates sensitivity to the 3D structure. The chemical maps of carbon support (blue) and ionomer (green) are shown in **Figure A.4**. However, both the magnetite sample and the PEMFC cathode catalyst sample are flat samples, so the change of structure at different rotation positions is not significant.

Table A.1 List of STXM laminography experiment

date	sample	energies	angle	unicorn/data/xrm/stxm-cls
Jan-17	ZnO/Al ₂ O ₃ aerogel	1018eV/1060eV /1562eV/1568.2eV	0° -360° /10°	/2017/17-01B/laminography-analysis
Feb-16	TiO ₂ / Al ₂ O ₃ aerogel	450eV/520eV /1570eV/1560eV	0° -360° /10°	/2016/16-02/laminography-analysis
Jan-16	TiO ₂ / Al ₂ O ₃ aerogel	450eV/520eV	0° -360° /10°	/2016/16-01/lami-analysis
Sep-15	TiO ₂ / Al ₂ O ₃ aerogel	1560eV/1570eV	0° -360° /10°	/2015/15-09/laminography-analysis
Jun-15	TiO ₂ / Al ₂ O ₃ aerogel	1558eV/1567eV	0° -360° /10°	/2015/15-06/laminography/aerogel-lami-data
Mar-15	MEA Sample C in PS	278eV/284.5eV /684eV/693eV	210° -360° /10°	/2015/15-03/MEA-laminography
Dec-14	MEA Sample C in PS	278eV/284.5eV /684eV/693eV	0° -210° /10°	/2014/14-12/laminography-pemfc-gif
Oct-14	MEA Sample C in PS	684eV/693.3eV	0° -300° /60°	/2014/14-10/laminography
Aug-14	magnitite	704eV/709.6eV	220°-360° / 4°	/2014/14-08/magnitite-lami
Jun-14	magnitite	704eV/709.6eV	0°-220° / 4°	/2014/14-06/laminography-analysis-06-21

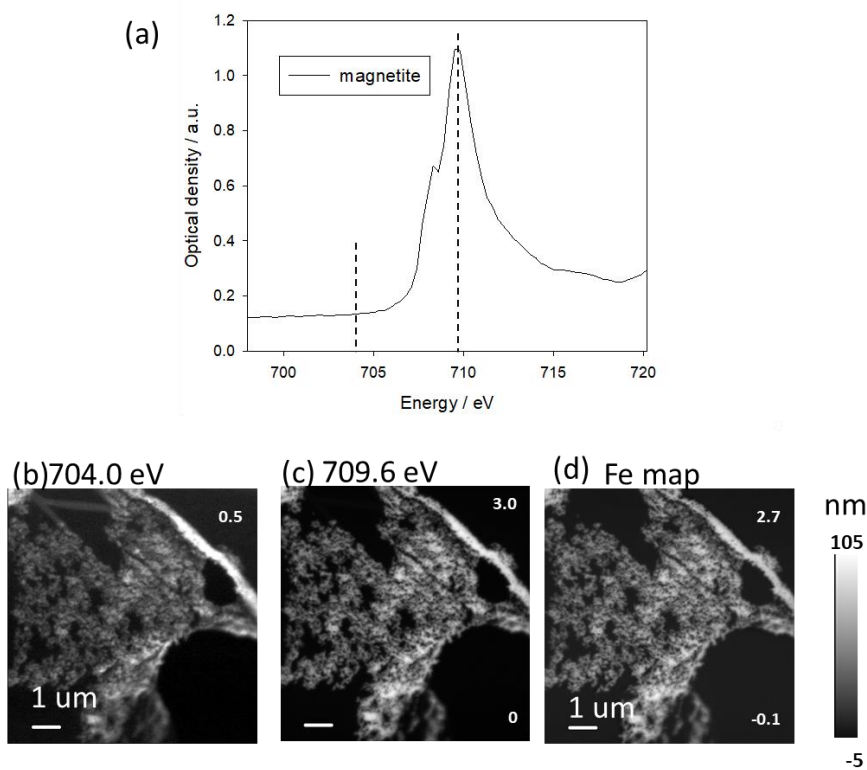


Figure A.1 (a) Fe 2p_{3/2} spectrum of magnetite; (b) 2D images at 704 eV; (c) 2D images at 709.6 eV; (d) Fe map generated by OD_{709.6}-OD₇₀₄

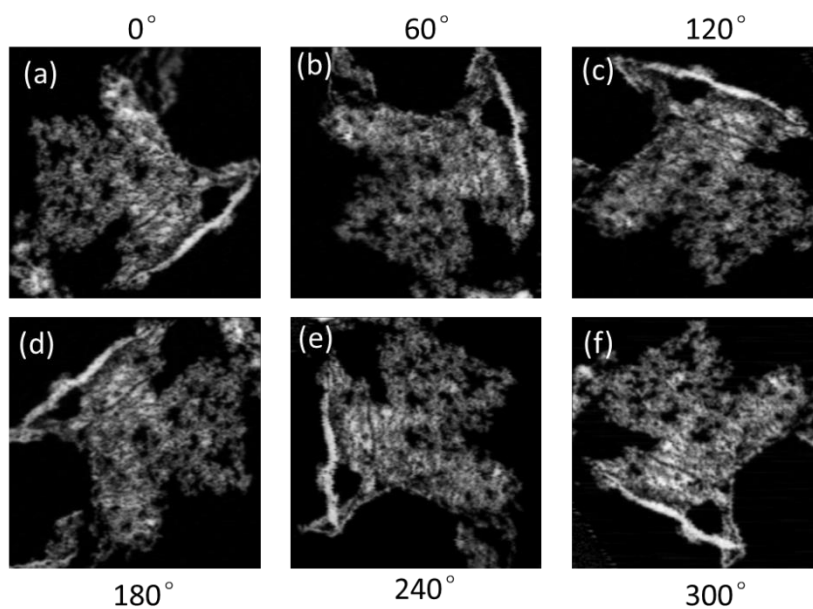


Figure A.2 Fe map of magnetite at 0°, 60°, 120°, 180°, 240°, 300°

To test the capabilities of STXM laminography, a sample which is porous, with 3D chemical structure, and low density was sought. The aerogels provided by Jonathan Lee (Lawrence Livermore National Laboratory) were measured by STXM laminography. The details of the aerogel sample have been described in Chapter 7. The $\text{TiO}_2/\text{Al}_2\text{O}_3$ aerogel was composed of an Al_2O_3 aerogel substrate coated with TiO_2 by atomic layer deposition (ALD). The diameter of pores is around 200 nm, while the sub-pores are about 30~50 nm. The spectrum of TiO_2 at the Ti 2p edge and Al_2O_3 at the Al 1s edge are shown in **Fig. A.5**. The TiO_2 spectrum was saturated at the Ti 2p edge. A Ti 2p continue pre-O1s energy 520eV was used to derive the TiO_2 map. The TiO_2 map was generated by $\text{OD}_{520}-\text{OD}_{450}$, and the Al_2O_3 was generated by $\text{OD}_{1570}-\text{OD}_{1560}$ (see **Fig. A.6**). The 4-energy laminography angle set was acquired from 0° to 360° with 10° increment. The rotation axis tilt was 30° . **Figure A.7** shows the chemical maps of Al_2O_3 (blue) and TiO_2 (red) at different rotation angles. The 3D structure changes are more clear.

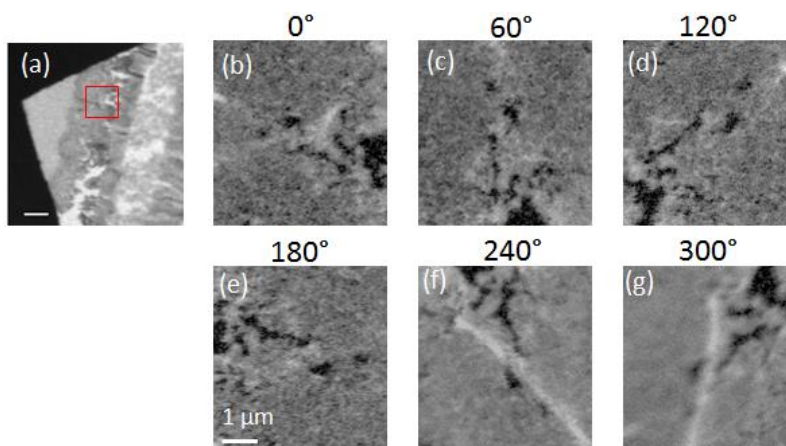


Figure. A.3 (a) Laminography measurement region in red box, (b-g) 2D laminography carbon support maps at 0° , 60° , 120° , 180° , 240° , 300° from the cathode region of a PEMFC.

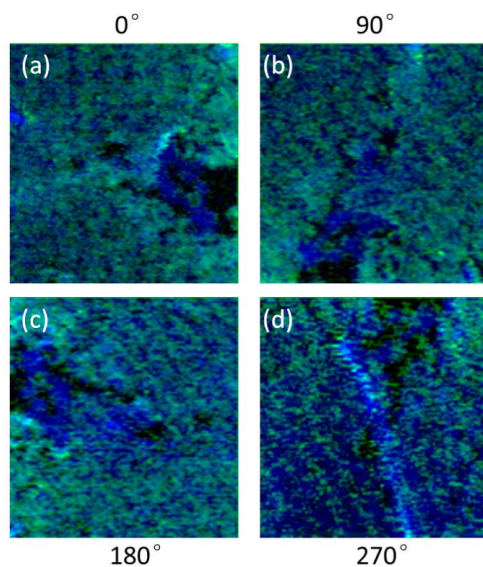


Figure A.4 Chemical maps of carbon support (blue) and ionomer (green) at (a) 0° , (b) 90° , (c) 180° , (d) 270°

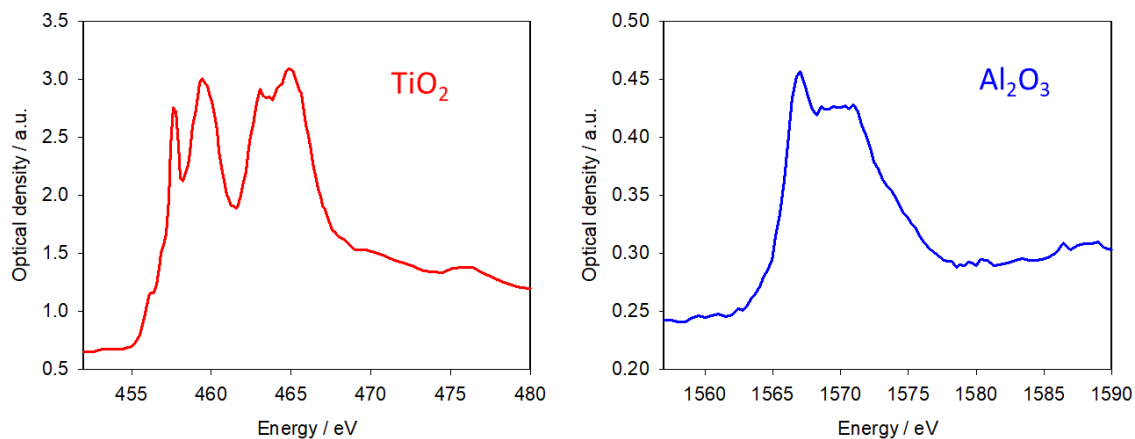


Figure A.5 X-ray absorption spectrum of $\text{TiO}_2/\text{Al}_2\text{O}_3$ aerogel: (a) TiO_2 at Ti 2p edge, (b) Al_2O_3 at Al 1s edge

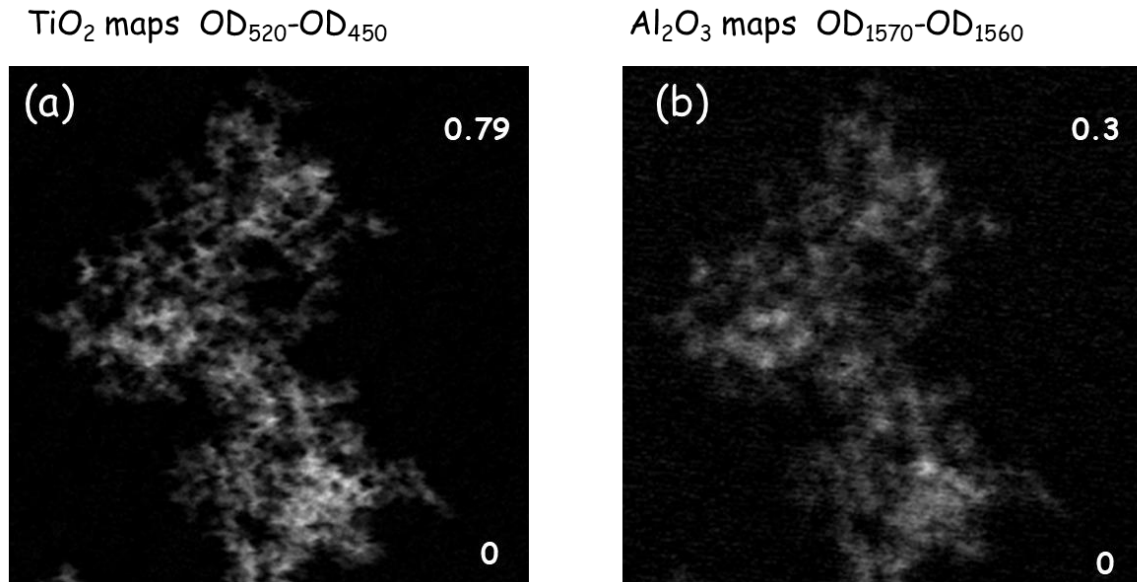


Figure A.6 Chemical maps of (a) TiO₂ generated by OD₅₂₀-OD₄₅₀ (b) Al₂O₃ generated by OD₁₅₇₀-OD₁₅₆₀

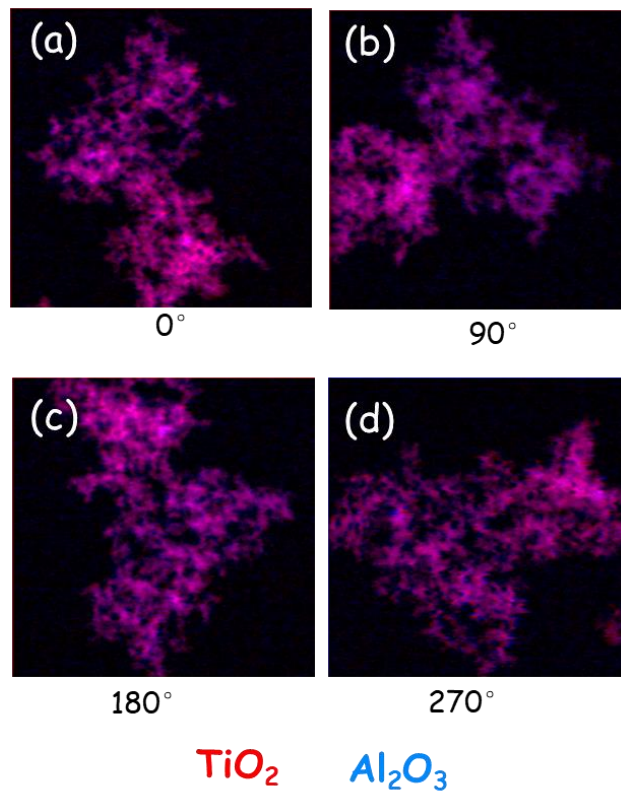


Figure A.7 Chemical maps of TiO₂ (red) Al₂O₃ (blue) at rotation position (a) 0°, (b) 90°, (c) 180°, (d) 270°

The laminography reconstruction is still under development. **Figure A.8** was the laminography reconstruction of the magnetite sample done by the Helfen group with the filtered back-projection (FBP) algorithm. The same FBP algorithm was implanted by Mirna Lerotic in python code she developed to analysis my data. The geometry is shown in **Fig. A.9**. The tilt angle between x and x' (after tilt) (z and z') is θ . The laminography rotation angle is ϕ . However, the code is not working properly (see **Fig. A.10**). Compared to the 2D image of the magnetite at 0° (**Fig. A.10(a)**), the 0° projection of the reconstructed volume (**Fig. 8.10(b)**) has a different shape. The reasons for failure may include: (1) The number of rotation angles is not enough for the FBP algorithm. (2) The calculation geometry is not correct. (3) The laminography alignment is not done properly. Improvement has to be done in future: (1) Check the calculation geometry. (2) Find a better auto alignment method for laminography data set. (3) Develop a Compressed Sensing algorithm for lanimography reconstruction. Furthermore, another difference between our data set and Helfen's data sets is the tilted angle θ . The tilted angle θ equals to 60° , while in our setup, the angle θ is 30° . This is another reason for the fail. The tilted angel has to be increase to reduce the missing wedge.

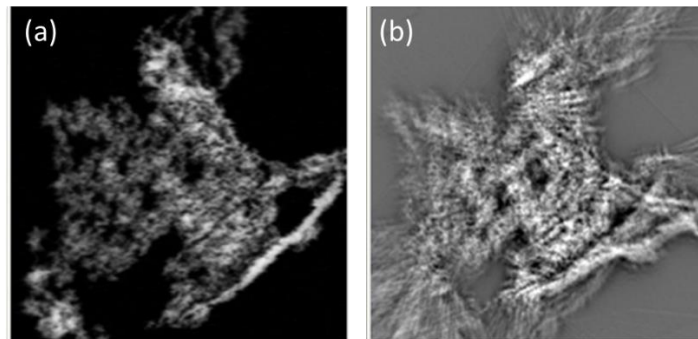


Figure A.8 (a) 2D images of the magnetite at 0° ; (b) 0° view of the 3D reconstructed volume

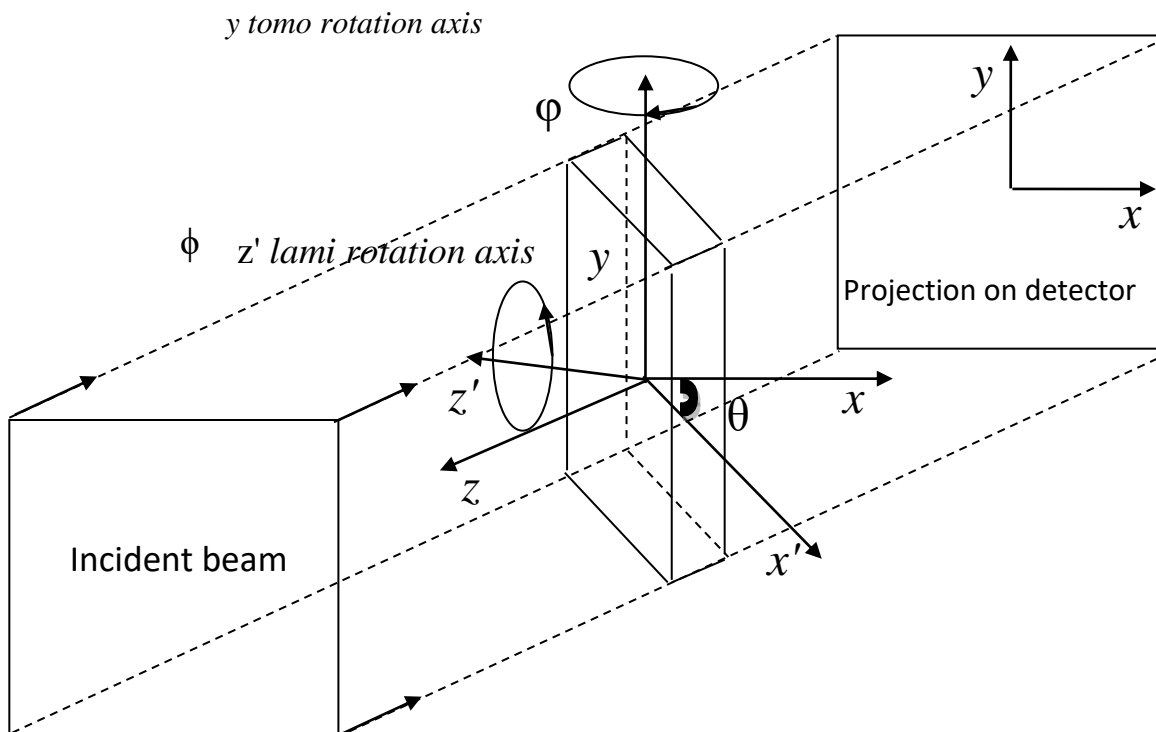


Figure A.9 STXM laminography geometry

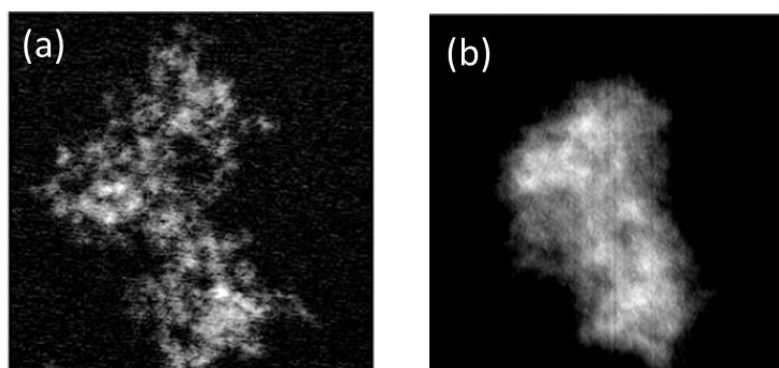


Figure A.10 (a) 2D images of the TiO₂ / Al₂O₃ aerogel sample at 0°; (b) 0° view of the 3D reconstructed volume